



CFD Transient Simulation of an Isolator Shock Train in a Scramjet Engine

DISSERTATION

Troy Christopher Hoeger, Lieutenant Colonel, USAF

AFIT/DS/ENY/12-18

DEPARTMENT OF THE AIR FORCE
AIR UNIVERSITY

AIR FORCE INSTITUTE OF TECHNOLOGY

Wright-Patterson Air Force Base, Ohio

The views expressed in this dissertation are those of the author and do not reflect the official policy or position of the United States Air Force, Department of Defense, or the United States Government. This material is declared a work of the U.S. Government and is not subject to copyright protection in the United States.

AFIT/DS/ENY/12-18

**CFD TRANSIENT SIMULATION OF AN ISOLATOR SHOCK TRAIN IN A
SCRAMJET ENGINE**

DISSERTATION

Presented to the Faculty

Graduate School of Engineering and Management

Air Force Institute of Technology

Air University

Air Education and Training Command

In Partial Fulfillment of the Requirements for the

Degree of Doctor of Philosophy

Troy Christopher Hoeger, BS, MS

Lieutenant Colonel, USAF

September, 2012

APPROVED FOR PUBLIC RELEASE; DISTRIBUTION UNLIMITED

CFD TRANSIENT SIMULATION OF AN ISOLATOR SHOCK TRAIN IN A
SCRAMJET ENGINE

Troy C. Hoeger, BS, MS
Lieutenant Colonel, USAF

Approved:

Paul I. King

Date

Douglas D. Decker

Date

Jeffrey M. Donbar

Date

Robert B. Greendyke

Date

William F. Bailey

Date

Accepted:

M. U. Thomas
Dean, Graduate School of
Engineering and Management

Date

Abstract

For hypersonic flight, the scramjet engine uses an isolator to contain the pre-combustion shock train formed by the pressure difference between the inlet and the combustion chamber. If this shock train were to reach the inlet, it would cause an engine unstart, disrupting the flow through the engine and leading to a loss of thrust and potential loss of the vehicle. Prior to this work, a Computational Fluid Dynamics (CFD) simulation of the isolator was needed for simulating and characterizing the isolator flow and for finding the relationship between back pressure and changes in the location of the leading edge of the shock train. In this work, the VULCAN code was employed with back pressure as an input to obtain the time history of the shock train leading location. Results were obtained for both transient and steady-state conditions. The simulation showed a relationship between back-to-inlet pressure ratios and final locations of the shock train. For the 2-D runs, locations were within one isolator duct height of experimental results while for 3-D runs, the results were within two isolator duct heights.

Acknowledgments

I would like to express my sincere appreciation to my faculty advisor, Dr. Paul I. King, for his guidance and support, and Dr. Jeffrey M. Donbar from the Air Force Research Laboratory for both the help and encouragement he provided me in this endeavor. I would also like to thank the other members of my research committee for their support: Dr. Robert B. Greendyke, Dr. William F. Bailey, and Dr. Douglas D. Decker.

I give special thanks to Dr. Susan Cox-Stouffer for her help, insight, and experience with the VULCAN code throughout the course of this effort, and Drs. Douglas Davis, Mark Hagenmaier, and Dean Eklund for their assistance with computers, accounts, and access. Finally, to my wife, son, and the rest of my family, thanks for the love and support.

Troy C. Hoeger

Table of Contents

	Page
Abstract	v
Acknowledgments	vi
List of Figures	ix
List of Tables	xviii
List of Symbols	xix
 I. Introduction	 1
Background.....	1
Ram/Scram Modes and Shock Trains	2
Problem Statement.....	5
Chapter Summary	7
 II. Literature Review	 8
The Isolator.....	8
Governing Equations	10
Turbulence Modeling	17
Previous Work on Isolators and CFD.....	22
 III. Methodology	 29
Computational Fluid Dynamics (CFD)	29
Grid Generation	32
VULCAN Code	37
Computer Runtimes	38
 IV. Two-Dimensional CFD Results.....	 40
Introduction	40
Transient 2-D Simulation	41
Grid Convergence Study	41
Temporal Resolution Study	43
Turbulence Model Comparison	44
Instantaneous application of backpressure	46
Gradual application of backpressure	71
Summary of 2-D Results	93
 V. Three-Dimensional CFD Results	 95
Introduction	95
Transient 3-D Simulation	95

Grid Convergence Study	96
Temporal Resolution Study	98
Turbulence Model Comparison	99
Gradual application of backpressure	100
Ramped application of backpressure	139
VI. Analysis	152
Billig's Correlation	152
Shock Speed	154
Off-Centerline Analysis	159
Friction Stress Analysis	162
CFD and Experiment Comparison	169
Distortion Analysis	182
Summary	186
VII. Conclusions and Recommendations	188
Conclusions	188
Recommendations	193
Bibliography	196

List of Figures

Figure	Page
Figure 1. Schematic of a scramjet engine	2
Figure 2. Schematic of isolator pre-combustion shock train (PCST) for ram, early scram, and late scram modes	4
Figure 3. Normal shock train	4
Figure 4. Oblique shock train.....	4
Figure 5. Maximum pressure capability of isolator	23
Figure 6. 2D comparisons of static pressure along isolator baseline and initial shock location	26
Figure 7. AFIT isolator test facility	30
Figure 8. Nozzle/isolator grid: (top) overview, (bottom) nozzle closeup	36
Figure 9. Boundary layer profile for Mach 1.8 nozzle/isolator	42
Figure 10. Grid comparison for nozzle/isolator (89.6 kPa back pressure)	43
Figure 11. 2-D Temporal Resolution Results	44
Figure 12. Comparison of Turbulence Models in 2-D.....	46
Figure 13. Evolution of PCST solution for instant 89.6 kPa back pressure	48
Figure 14. Evolution of PCST solution for instant 89.6 kPa back pressure continued.....	49
Figure 15. CFD static pressures along floor of nozzle/isolator	50
Figure 16. Time history of static pressures after 89.6 kPa back pressure applied	52
Figure 17. Close-up view of static pressures after 89.6 kPa back pressure applied	53
Figure 18. Time history of static pressure after 89.6 kPa back pressure applied	54
Figure 19. Solution evolution to shock stability for 89.6 kPa back pressure applied	55

Figure 20. Evolution of PCST solution for instant 85.0 kPa back pressure	56
Figure 21. Evolution of PCST solution for instant 85.0 kPa back pressure continued.....	57
Figure 22. Time history of static pressure after 85.0 kPa back pressure applied	58
Figure 23. Evolution of PCST solution for instant 75.0 kPa back pressure	59
Figure 24. Evolution of PCST solution for instant 75.0 kPa back pressure continued.....	60
Figure 25. Time history of static pressure after 75.0 kPa back pressure applied	61
Figure 26. Evolution of PCST solution for instant 75.0 kPa back pressure (140.6 kPa inflow)	63
Figure 27. Evolution of PCST solution for instant 75.0 kPa back pressure continued (140.6 kPa inflow)	64
Figure 28. Time history of static pressure after 75.0 kPa back pressure applied (140.6 kPa inflow)	65
Figure 29. Evolution of PCST solution for instant 71.1 kPa back pressure	66
Figure 30. Evolution of PCST solution for instant 71.1 kPa back pressure continued.....	67
Figure 31. Time history of static pressure after 71.1 kPa back pressure applied	68
Figure 32. Evolution of PCST solution for instant 62.78 kPa back pressure	69
Figure 33. Evolution of PCST solution for instant 62.78 kPa back pressure continued...	70
Figure 34. Time history of static pressure after 62.78 kPa back pressure applied	71
Figure 35. Simulation of back flap in isolator for 85.0 kPa case	72
Figure 36. Evolution of PCST solution with back pressure stepped to 89.6 kPa	73
Figure 37. Evolution of PCST solution with back pressure stepped to 89.6 kPa	74
Figure 38. Time history of static pressure for stepped 89.6 kPa back pressure.....	75
Figure 39. Evolution of PCST solution with back pressure stepped to 85.0 kPa	77

Figure 40. Time history of static pressure for stepped 85.0 kPa back pressure.....	78
Figure 41. Time history of static pressure from 0.008 to 0.012 seconds.....	79
Figure 42. Evolution of PCST solution with back pressure stepped to 75.0 kPa	80
Figure 43. Evolution of PCST solution with back pressure stepped to 75.0 kPa continued	81
Figure 44. Time history of static pressure for stepped 75.0 kPa back pressure.....	82
Figure 45. Evolution of PCST solution with back pressure stepped to 75.0 kPa (140.6 kPa inflow).....	83
Figure 46. Evolution of PCST solution with back pressure stepped to 75.0 kPa continued (140.6 kPa inflow).....	84
Figure 47. Time history of static pressure for stepped 75.0 kPa back pressure (140.6 kPa inflow)	85
Figure 48. Evolution of PCST solution with back pressure stepped to 71.1 kPa	87
Figure 49. Time history of static pressure for stepped 71.1 kPa back pressure.....	88
Figure 50. Evolution of PCST solution with back pressure stepped to 62.78 kPa	89
Figure 51. Evolution of PCST solution with back pressure stepped to 62.78 kPa continued	90
Figure 52. Time history of static pressure for stepped 62.78 kPa back pressure.....	91
Figure 53. Boundary layer profile for 3-D Mach 1.8 nozzle/isolator	97
Figure 54. Grid comparison for 3-D nozzle/isolator for 89.6 kPa back pressure	98
Figure 55. 3-D Temporal Resolution Results	99
Figure 56. Comparison of Turbulence Models in 3-D.....	100
Figure 57. Evolution of PCST solution for 89.6 kPa back pressure	102

Figure 58. Evolution of PCST for 89.6 kPa back pressure continued	103
Figure 59. Lines of time history read for back pressure	104
Figure 60. Time history for 89.6 kPa back pressure along line S1 (bottom) in the nozzle/isolator.	104
Figure 61. Time history for 89.6 kPa back pressure along line S2 (top) in the nozzle/isolator	105
Figure 62. Time history for 89.6 kPa back pressure along line S3 (left) in the nozzle/isolator	106
Figure 63. Time history for 89.6 kPa back pressure along line S4 (right) in the nozzle/isolator	107
Figure 64. Evolution of PCST solution for 85.0 kPa back pressure	108
Figure 65. Evolution of PCST solution for 85.0 kPa back pressure continued	109
Figure 66. Time history for 85.0 kPa back pressure along line S1 (bottom) in the nozzle/isolator	110
Figure 67. Time history for 85.0 kPa back pressure along line S2 (top) in the nozzle/isolator	111
Figure 68. Time history for 85.0 kPa back pressure along line S3 (left) in the nozzle/isolator	112
Figure 69. Time history for 85.0 kPa back pressure along line S4 (right) in the nozzle/isolator	113
Figure 70. Evolution of PCST solution for 75.0 kPa back pressure	114
Figure 71. Evolution of PCST solution for 75.0 kPa back pressure continued	115

Figure 72. Time history for 75.0 kPa back pressure along line S1 (bottom) in the nozzle/isolator	116
Figure 73. Time history for 75.0 kPa back pressure along line S2 (top) in the nozzle/isolator	117
Figure 74. Time history for 75.0 kPa back pressure along line S3 (left) in the nozzle/isolator	118
Figure 75. Time history for 75.0 kPa back pressure along line S4 (right) in the nozzle/isolator	119
Figure 76. Evolution of PCST solution for 75.0 kPa back pressure (140.6 kPa inflow)	120
Figure 77. Evolution of PCST solution for 75.0 kPa back pressure (140.6 kPa inflow) continued	121
Figure 78. Time history for 75.0 kPa back pressure (140.6 kPa inflow) along line S1 (bottom) in the nozzle/isolator	122
Figure 79. Time history for 75.0 kPa back pressure (140.6 kPa inflow) along line S2 (top) in the nozzle/isolator	123
Figure 80. Time history for 75.0 kPa back pressure (140.6 kPa inflow) along line S3 (left) in the nozzle/isolator	124
Figure 81. Time history for 75.0 kPa back pressure (140.6 kPa inflow) along line S4 (right) in the nozzle/isolator	125
Figure 82. Evolution of PCST solution for 71.1 kPa back pressure	126
Figure 83. Evolution of PCST solution for 71.1 kPa back pressure continued	127
Figure 84. Time history for 71.1 kPa back pressure along line S1 (bottom) in the nozzle/isolator	128

Figure 85. Time history for 71.1 kPa back pressure along line S2 (top) in the nozzle/isolator	129
Figure 86. Time history for 71.1 kPa back pressure along line S3 (left) in the nozzle/isolator	130
Figure 87. Time history for 71.1 kPa back pressure along line S4 (right) in the nozzle/isolator	131
Figure 88. Evolution of PCST solution for 62.78 kPa back pressure	132
Figure 89. Evolution of PCST solution for 62.78 kPa back pressure continued	133
Figure 90. Time history for 62.78 kPa back pressure along line S1 (bottom) in the nozzle/isolator	134
Figure 91. Time history for 62.78 kPa back pressure along line S2 (top) in the nozzle/isolator	135
Figure 92. Time history for 62.78 kPa back pressure along line S3 (left) in the nozzle/isolator	136
Figure 93. Time history for 62.78 kPa back pressure along line S4 (right) in the nozzle/isolator	137
Figure 94. Plot of the location of the leading edge of PCST vs. time	139
Figure 95. Rise in back pressure and ramp angle during the AFIT experiment for 85.0 kPa back pressure (Hutzel, 2011).....	140
Figure 96. Evolution of PCST solution for 85.0 kPa back pressure ramp case.....	141
Figure 97. Time history for 85.0 kPa back pressure ramp case along line S1 (bottom) in the nozzle/isolator	142

Figure 98. Time history for 85.0 kPa back pressure ramp case along line S2 (top) in the nozzle/isolator	143
Figure 99. Time history for 85.0 kPa back pressure ramp case along line S3 (left) in the nozzle/isolator	144
Figure 100. Time history for 85.0 kPa back pressure ramp case along line S4 (right) in the nozzle/isolator	145
Figure 101. Rise in back pressure and ramp angle during the AFIT experiment for 56.5 kPa back pressure	146
Figure 102. Evolution of PCST solution for 56.5 kPa back pressure ramp case	147
Figure 103. Time history for 56.5 kPa back pressure ramp case along line S1 (bottom) in the nozzle/isolator	148
Figure 104. Time history for 56.5 kPa back pressure ramp case along line S2 (top) in the nozzle/isolator	149
Figure 105. Time history for 56.5 kPa back pressure ramp case along line S3 (left) in the nozzle/isolator	150
Figure 106. Time history for 56.5 kPa back pressure ramp case along line S4 (right) in the nozzle/isolator	151
Figure 107. Billig comparison with 2-D and 3-D back pressure ratios	153
Figure 108. Pressure rise correlation for rectangular ducts (Billig, 1993).....	153
Figure 109. Shock speed for 0.533 ratios	155
Figure 110. Shock speed for 0.506 ratios	157
Figure 111. Shock speed for 0.446 ratios	158

Figure 112. Time history for 89.6 kPa back pressure 0.25 inches from the S1 / S4 corner	159
Figure 113. Time history for 89.6 kPa back pressure 0.5 inches from the S1 / S4 corner	161
Figure 114. Time history for 89.6 kPa back pressure 1 inch from the S1 / S4 corner....	162
Figure 115. Friction Stress along bottom centerline (S1) for 89.6 kPa back pressure ...	164
Figure 116. Friction Stress along bottom centerline (S1) for 85.0 kPa back pressure ...	165
Figure 117. Friction Stress along bottom centerline (S1) for 75.0 kPa back pressure ...	166
Figure 118. Friction Stress along bottom centerline (S1) for 75.0 kPa back pressure (140.6 kPa inflow).....	167
Figure 119. Friction Stress along bottom centerline (S1) for 71.1 kPa back pressure ...	168
Figure 120. Friction Stress along bottom centerline (S1) for 62.78 kPa back pressure .	169
Figure 121. Comparison of CFD (0.533) with AFIT Experiment (0.527)	171
Figure 122. Comparison of CFD (0.506) with AFIT Experiment (0.494)	172
Figure 123. Comparison of CFD (0.446) with AFIT Experiment (0.452)	173
Figure 124. Comparison of CFD (0.533) with AFIT Experiment (0.520)	174
Figure 125. Comparison of CFD (0.506) with AFIT Experiment (0.492)	175
Figure 126. Comparison of CFD (0.446) with AFIT Experiment (0.442)	177
Figure 127. Comparison of final locations based on back to inflow pressure ratio.....	180
Figure 128. Pitot pressure, total pressure and Mach number for 168.2 kPa inflow with no back pressure	183
Figure 129. Close up of Figure 128	184

Figure 130. Pitot pressure, total pressure and Mach number for 140.6 kPa inflow with no back pressure	185
Figure 131. Close up of Figure 130	186

List of Tables

Table	Page
Table 1. Reference conditions / pressure ratios for simulation sets.....	7
Table 2. Set of model constants for switching function in Menter model.....	20
Table 3. 2-D Results of instantaneous back pressure method	93
Table 4. 2-D Results of gradual (stepped) back pressure method	93
Table 5. Results of the six 3-D back pressure cases	138
Table 6. Comparison of final location between CFD results and experimental results..	178

List of Symbols

Acronyms

2-D	=	Two-Dimensional
3-D	=	Three-Dimensional
AFIT	=	Air Force Institute of Technology
AFRL	=	Air Force Research Laboratory
CFD	=	Computational Fluid Dynamics
CPU	=	Central Processing Unit
DoD	=	Department of Defense
DSRC	=	DoD Shared Resource Center
ERDC	=	Engineering Research and Development Center
FANS	=	Favre Averaged Navier-Stokes
GB	=	Gigabyte
GHz	=	GigaHertz
HPC	=	High Performance Computing
KB	=	Kilobyte
LES	=	Large Eddy Simulation
LHS	=	Left Hand Side
MB	=	Megabyte
MPP	=	Massively Parallel Processor
NASA	=	National Aeronautics and Space Administration
ORS	=	Operationally Responsive Spacelift
PCST	=	Pre-Combustion Shock Train
PDE	=	Partial Differential Equation
RANS	=	Reynolds Averaged Navier-Stokes
RDT&E	=	Research, Development, Test, and Evaluation
RHS	=	Right Hand Side
RLV	=	Reusable Launch Vehicle
SST	=	Shear-Stress Transport
TB	=	Terabyte
TFLOPS	=	Teraflops
USAF	=	United States Air Force
VULCAN	=	Viscous Upwind aLgorithm for Complex flow ANalysis

Symbols

e	=	internal energy per unit mass (J/kg)
F_1, F_2	=	switching functions (no units)
f	=	conserved quantity (no units)
K	=	bulk viscosity (kg/m·s)
k	=	turbulent kinetic energy (J)
M	=	Mach number (no units)
M_i	=	inlet Mach number (no units)
P_b	=	back pressure (Pa)
P_i	=	inflow pressure (Pa)

P_k	=	production of turbulence (no units)
p	=	pressure (Pa)
q	=	heat release per unit mass (J/kg)
t	=	time (sec)
u,v,w	=	velocity vectors (m/sec)
y^+	=	distance to wall (non-dimensional)

Greek

ε	=	rate of dissipation of turbulent kinetic energy (m^2/s^3)
κ	=	thermal conductivity coefficient ($W/m^2 \cdot K$)
λ	=	second viscosity conductivity ($kg/m \cdot s$)
ϕ_1, ϕ_2	=	constants (Menter SST model) (no units)
ρ	=	density (kg/m^3)
σ, τ	=	viscous stress tensors (N/m^2)
θ	=	function for viscous stresses and heat conduction ($W/m \cdot K$)
μ	=	laminar viscosity coefficient ($kg/m \cdot s$)
μ_t	=	turbulent viscosity coefficient ($kg/m \cdot s$)
Ω	=	vorticity (s^{-1})
ω	=	turbulence frequency (s^{-1})

CFD TRANSIENT SIMULATION OF AN ISOLATOR SHOCK TRAIN IN A SCRAMJET ENGINE

I. Introduction

Background

Ramjet and scramjet engines have long been seen as the answer for high-speed air breathing propulsion systems. A ramjet engine allows for freestream air at high subsonic or supersonic speeds to enter the inlet, be compressed and slowed to low subsonic Mach numbers at the entrance of the combustor where burning takes place subsonically. In the Mach number regime of two to five, such conventional ramjets have propulsion advantages over the standard gas turbine engines. For higher flight Mach number, supersonic combustion is required to maintain a lower combustor entrance gas temperature. The scramjet utilizes external and internal shock structures to achieve inlet air compression (Le, 2005) and allows for the required supersonic combustion. Such an engine can be subject to engine unstart when transitioning from sub- to supersonic flight or when combustion perturbations evolve a shock system that discharges the flow from the engine inlet.

A classical schematic of the scramjet is shown in Figure 1 with four main sections: inlet, isolator, combustor and exit nozzle. The inlet captures the air, the isolator passes the air to the combustor while separating the inlet from the combustor's effects, the combustor mixes fuel with the air and burns the fuel-air mixture, and the exit nozzle expands the exhaust gases to produce vehicle thrust (Le, 2005). One approach used in research is the computer simulation of fluid transport processes by solving the

approximations of the mathematical description of the fluid flow. Computational Fluid Dynamics (CFD) enables detailed analysis of complex flow fields such as those found in the components of a scramjet engine. (Tu, et al., 2008)

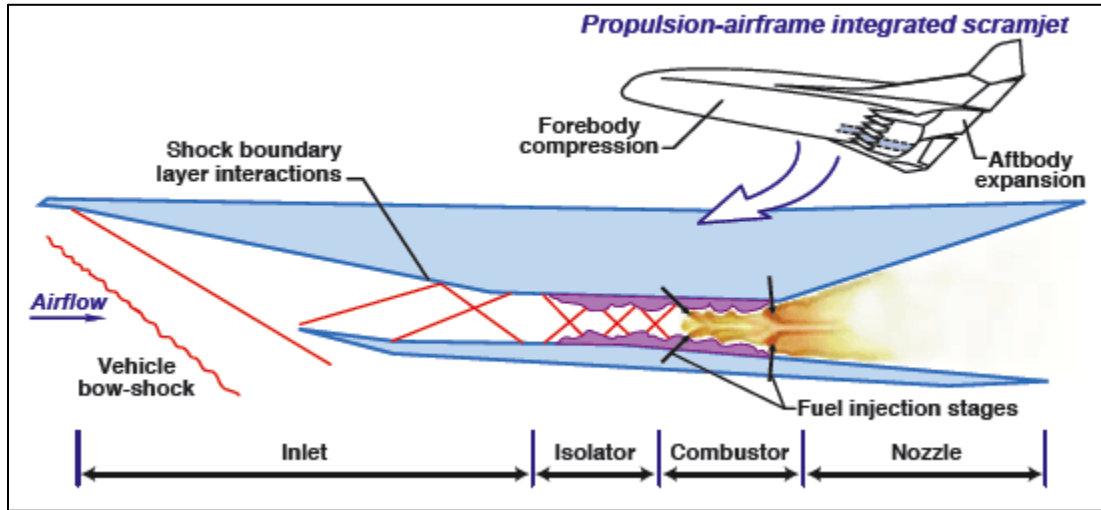


Figure 1. Schematic of a scramjet engine (NASA Fact Sheet, 2006)

Ram/Scram Modes and Shock Trains

There are three modes of the dual-mode scramjet operating at supersonic speed, as shown in Figure 2. In ram mode (Figure 2a, Torrez, et al., 2008) freestream air is compressed and slowed in the inlet and isolator to a subsonic Mach number at the entrance of the combustor. Shock waves in the isolator form a pre-combustion shock train (PCST) that creates an adverse pressure gradient and may cause boundary layer separation. Heat is added in the combustor until the flow is thermally choked. An increase in flight Mach number decreases the static pressure in the isolator. The boundary layer will reattach at the end of the isolator and remain attached in the combustor. For a flight Mach number between five and seven, the dual-mode scramjet engine is in early scramjet mode (Figure 2b). Definitions of scram mode vary, but generally the combustor

is considered predominately supersonic. Subsonic combustion may occur near the walls, within flame holders and in other areas of separated flow. The combustor cannot produce a thermal choke at these higher flight Mach numbers, and the PCST is much weaker. The separated boundary layer is thinner, but there is an adverse pressure gradient in the isolator. Constant pressure combustion is expected to occur because the separated boundary layer creates a new effective wall shape (Torrez, et al., 2008). A thinner separated boundary layer means a larger effective flow area which causes the static pressure to decrease. This decrease is offset by the increase in static pressure due to the heat addition in the combustor. In scramjet mode (Figure 2c) the flight Mach number is greater than seven and there is only supersonic combustion. There is no thermal choking, and the PCST here has disappeared with only supersonic flow through the isolator into the combustor (Torrez, et al., 2008).

Two types of shock trains that can form in the isolator are the normal shock train and oblique shock train. The normal shock train, shown in Figure 3, tends to occur at lower inlet Mach numbers (M_i) and with thicker inlet boundary layers. The oblique shock train, shown in Figure 4, tends to occur at higher inlet Mach numbers, and develops thinner inlet boundary layers. A rough but useful rule of thumb is that the dividing line between normal and oblique shock trains is in the range $2 < M_i < 3$ (Heiser, et al., 1994).

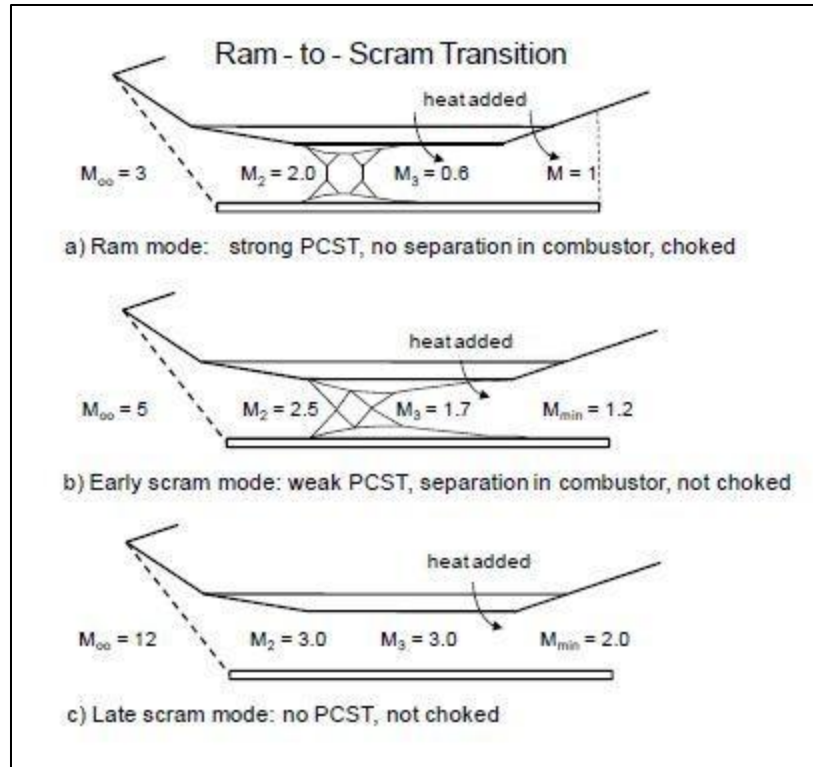


Figure 2. Schematic of isolator pre-combustion shock train (PCST) for ram, early scram, and late scram modes (Torrez, et al. 2008)

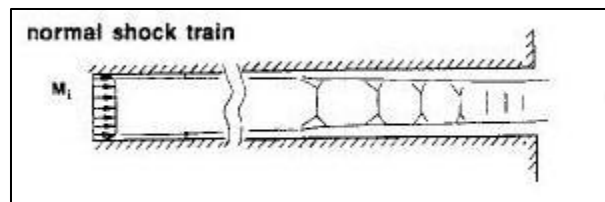


Figure 3. Normal shock train (Lin, et al. 1991)

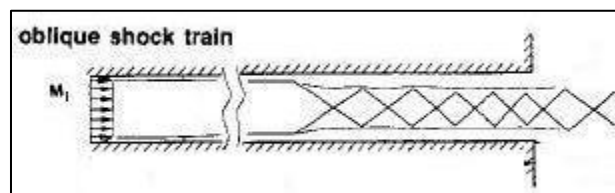


Figure 4. Oblique shock train (Lin, et al. 1991)

Problem Statement

The focus of this research is on CFD used to simulate complex flow fields in the isolator and develop a rationale for dynamic shock train movement. The primary function of the isolator is to contain the PCST and prevent interaction between the combustor and the inlet (Le, et al., 2006). Perturbations in combustion or inlet flow may cause a shock train to develop. A forward location of the leading edge of a PCST in the isolator may cause an engine unstart, and thus detection and control of the PCST in the isolator is critical to the advancement of scramjets (McDaniel, et al., 2005). Previous CFD simulations of the isolator done to characterize the shock train structure (Lin, et al., 2006) or study the influence of the boundary conditions (Tam, et al., 2008), were steady-state flow calculations where an equilibrium condition is reached for all the flow variables involved. Changes or perturbations in internal pressures result in transient conditions and possibly unstable dynamics (Chang, et al., 2010). Transient simulations can predict the extent of a shock overshoot or the time for a steady state condition and changes in the location of the leading edge of the PCST in the isolator.

The focus of this work was to create a transient CFD simulation to understand the dynamics of PCST formation and to compare results. The fundamental input to the CFD simulation is back pressure and the most important output is the time history of the leading edge of the PCST. 2-D and 3-D simulations were accomplished. 2-D simulations were used to determine the functionality of the VULCAN code and to provide a quick (compared to the 3-D simulations), reasonable transient simulation for varying inputs (such as the back pressure and inflow pressure values) while modifying different variables in the VULCAN code (such as the time step, turbulence model, and grid

density). Additionally, the output of the 2-D simulations with varying back pressures approximate the type of response expected in 3-D simulations. For example, if 2-D simulations show forward movement of the PCST with increasing back pressure, then similar results should occur in 3-D simulations too.

Six simulations were accomplished: three cases with inflow stagnation pressure of 168.2 kPa and three with 140.6 kPa, both at an inlet Mach number of 1.8. The 168.2 kPa inflow pressure represents the maximum inflow pressure in an AFIT experiment. For 168.2 kPa inflow pressure, the three back pressure cases chosen represent allowable upper (89.6 kPa) and lower (75.0 kPa) and mid value back pressure limits. Higher backpressures than 89.6 kPa would cause an unstart, while any lower backpressures than 75.0 kPa would result in no PCST forming. A third, intermediate backpressure, 85.0 kPa, case was chosen equal to that in early runs done in the AFIT experiment. The three back pressures represent back-to-inlet pressure ratios of 0.533, 0.506, and 0.446. Back pressures for the 140.6 kPa stagnation inflow were adjusted to achieve the same ratios (See Table 1). Since this simulation was compared to a cold flow experiment, the temperature was set to the measured room temperature in the experiment, with ratio of specific heats held constant. The 168.2 kPa inflow pressure corresponds to a Reynolds/meter number of 2.3×10^7 and the 140.6 kPa inflow pressure corresponds to a Reynolds/meter number of 1.9×10^7 . Table 1 has the reference conditions, back pressures, and ratios used in each simulation set.

Table 1. Reference conditions / pressure ratios for simulation sets

Inflow Mach Number (M)	1.8	1.8
Inflow Total Pressure (P_0)	168,185 Pa	140,625 Pa
Inflow Total Temperature (T_0)	288.89 K	288.89 K
Reynolds number/m	2.3×10^7	1.9×10^7
Ratio of Specific Heats (Gamma)	1.4	1.4
Back Pressure (P_{BP}) / Ratio of Back Pressure to Inflow Total Pressure (P_{BP} / P_0)	89,600 Pa / 0.533 85,000 Pa / 0.506 75,000 Pa / 0.446	75,000 Pa / 0.533 71,100 Pa / 0.506 62,780 Pa / 0.446

Chapter Summary

Chapter II presents the Literature Review, and Chapter III presents the Methodology. Chapter IV presents the Two-Dimensional Results, and Chapter V presents the Three-Dimensional results. Chapter VI presents the Analysis, and finally, Chapter VII presents the Conclusions and Recommendations.

II. Literature Review

The Isolator

The isolator between the inlet and the combustion chamber in a scramjet is a long duct placed ahead of the combustor that helps maintain a stable supersonic airflow from the inlet to the combustor and improves the homogeneity of the flow. When combustion takes place, there is an increase over time in pressure, which is considerably higher than the inlet pressure (Le, 2005). The pressure rise generates a PCST inside the isolator to elevate the pressure from the isolator entrance to the combustion zone (Lin, et al., 2007). The PCST allows the pressure to rise through the isolator while decreasing the flow speed before it enters the combustor. The rise in pressure and decrease in flow speed reduces the ignition time (by both increasing the static temperature and pressure of the air stream), and increases the residence time (by decelerating the flow), which aids flame stabilization (Tam, et al., 2008). From a vehicle performance point-of-view, the isolator flow path should maximize the static pressure rise across the isolator (without inlet unstart), maximize stagnation pressure recovery, and minimize flow distortion. (Bagaveyev, et al., 2010). The length of the shock train in the isolator varies with operating conditions and such factors as isolator geometry and the combustor-to-inlet pressure ratio (Le, et al., 2006). Other factors, such as surface roughness, which can significantly increase flow boundary layer thickness and growth, also play an important role in defining isolator performance (Lin, et al., 2006). The length required in the isolator to contain the PCST is one of two methods to measure isolator performance. The other is to measure the uniformity of the flow exiting the isolator. The gradient of the

flow properties across the isolator exit plane decreases and the flow becomes more uniform at the exit of the isolator as the PCST moves forward in the isolator. A uniform exit flow is desired for efficient mixing and burning in the combustor (Rice, 2003).

The isolators main function in the scramjet is to contain the PCST and prevent the PCST from reaching the inlet. If the combustor back pressure increases, the length of the PCST in the isolator will also increase, and the PCST will move towards the isolator entrance and the inlet. A PCST near the isolator entrance is very sensitive to any pressure variation, and any small increase in back pressure can easily push the shock train out of the isolator into the inlet (Lin, et al., 2006). If the shock train were to reach the inlet, there would be a loss of air mass capture, increased pressure and thermal loads, increased drag and decreased thrust. The shock train reaching the inlet would result in mission and/or vehicle failure and is known as an engine “unstart” (Le, 2005). Various methods have been proposed to stop an unstart before it fully develops: flow path geometry (inlet, throat, or nozzle area) changes, mass bleeding, fuel flow changes, vehicle angle of attack changes, or sideslip changes. The choice of the means would reflect the type of unstart that is impending. Recent works have indicated that an unstart can develop very quickly, from several milliseconds to tens of milliseconds (Chang, et al., 2010).

The lack of understanding that currently exists about how an unstart occurs is compensated for in scramjet engines by prescribing extra isolator length (Donbar, 2010). A longer isolator means more weight on the engine, which in turn means more fuel used in flight and less range capability for the vehicle. The isolator should be short enough to minimize weight, but long enough to isolate the inlet from the disturbances caused by combustion (Lin, et al., 1991). In other words, the isolator needs to be long enough to

contain the PCST and prevent its leading edge from reaching the inlet and causing an unstart. One approach to solve this problem is to create a CFD simulation that detects and describes the behavior of the shock train in the isolator. This simulation can be used to complement and augment a parallel experimental effort to investigate the shock train dynamics using a test apparatus at the Air Force Institute of Technology (AFIT). The combined efforts will help to develop a dynamic simulation for research to create a feedback controller capable of actively placing the shock train at a desired location within the isolator, allowing for a short isolator in the engine and preventing an unstart.

Governing Equations

CFD is fundamentally based on the governing equations of fluid dynamics (Tu, et al., 2008). The equations include the conservations of mass, momentum, and energy (Hoffman and Chang, 2004). For fluids like air or water, the shear stress is assumed linearly proportional to the velocity gradient (a Newtonian fluid). In such a fluid, the fluid dynamic equations are called the Navier-Stokes equations (Blazek, 2005). For 3-D flow, the continuity equation is (Hoffman and Chang, 2004):

$$\frac{\partial \rho}{\partial t} + \frac{\partial}{\partial x}(\rho u) + \frac{\partial}{\partial y}(\rho v) + \frac{\partial}{\partial z}(\rho w) = 0 \quad (1)$$

The x-component of the momentum equation is:

$$\frac{\partial}{\partial t}(\rho u) + \frac{\partial}{\partial x}(\rho u^2 + p) + \frac{\partial}{\partial y}(\rho uv) + \frac{\partial}{\partial z}(\rho uw) = \frac{\partial}{\partial x}(\sigma_{xx}) + \frac{\partial}{\partial y}(\tau_{xy}) + \frac{\partial}{\partial z}(\tau_{xz}) \quad (2)$$

The y-component of the momentum equation is:

$$\frac{\partial}{\partial t}(\rho v) + \frac{\partial}{\partial x}(\rho uv) + \frac{\partial}{\partial y}(\rho v^2 + p) + \frac{\partial}{\partial z}(\rho vw) = \frac{\partial}{\partial x}(\tau_{xy}) + \frac{\partial}{\partial y}(\sigma_{yy}) + \frac{\partial}{\partial z}(\tau_{yz}) \quad (3)$$

The z-component of the momentum equation is:

$$\frac{\partial}{\partial t}(\rho w) + \frac{\partial}{\partial x}(\rho uw) + \frac{\partial}{\partial y}(\rho vw) + \frac{\partial}{\partial z}(\rho w^2 + p) = \frac{\partial}{\partial x}(\tau_{xz}) + \frac{\partial}{\partial y}(\tau_{yz}) + \frac{\partial}{\partial z}(\sigma_{zz}) \quad (4)$$

Finally, the energy equation is:

$$\frac{\partial}{\partial t}(\rho e) + \frac{\partial}{\partial x}(\rho ue + pu) + \frac{\partial}{\partial y}(\rho ve + pv) + \frac{\partial}{\partial z}(\rho we + pw) = \frac{\partial}{\partial x}(\theta_x) + \frac{\partial}{\partial y}(\theta_y) + \frac{\partial}{\partial z}(\theta_z) \quad (5)$$

where ρ is the density, p is the pressure, e is the internal energy per unit mass, and u, v , and w are the x, y, and z components, respectively, of the velocity vector. The viscous stress tensors (σ_{ii} and τ_{ij}) are defined as

$$\sigma_{xx} = \lambda \left(\frac{\partial u}{\partial x} + \frac{\partial v}{\partial y} + \frac{\partial w}{\partial z} \right) + 2\mu \frac{\partial u}{\partial x} \quad (6)$$

$$\sigma_{yy} = \lambda \left(\frac{\partial u}{\partial x} + \frac{\partial v}{\partial y} + \frac{\partial w}{\partial z} \right) + 2\mu \frac{\partial v}{\partial y} \quad (7)$$

$$\sigma_{zz} = \lambda \left(\frac{\partial u}{\partial x} + \frac{\partial v}{\partial y} + \frac{\partial w}{\partial z} \right) + 2\mu \frac{\partial w}{\partial z} \quad (8)$$

$$\tau_{xy} = \mu \left(\frac{\partial u}{\partial y} + \frac{\partial v}{\partial x} \right) \quad (9)$$

$$\tau_{xz} = \mu \left(\frac{\partial w}{\partial x} + \frac{\partial u}{\partial z} \right) \quad (10)$$

$$\tau_{yz} = \mu \left(\frac{\partial w}{\partial y} + \frac{\partial v}{\partial z} \right) \quad (11)$$

where μ is the dynamic viscosity coefficient and λ represents the second viscosity coefficient. The functions θ_x , θ_y , and θ_z are defined as:

$$\theta_x = u\sigma_{xx} + v\tau_{xy} + w\tau_{xz} + \kappa \frac{\partial T}{\partial x} \quad (12)$$

$$\theta_y = u\tau_{xy} + v\sigma_{yy} + w\tau_{yz} + \kappa \frac{\partial T}{\partial y} \quad (13)$$

$$\theta_z = u\tau_{xz} + v\tau_{yz} + w\sigma_{zz} + \kappa \frac{\partial T}{\partial z} \quad (14)$$

Functions θ_x , θ_y , and θ_z are the terms describing the work of the viscous stresses and of the heat conduction in the fluid (with κ as the thermal conductivity coefficient) (Blazek, 2005). The combination of μ and λ in the following form is known as the bulk viscosity K , i.e.,

$$K = \lambda + \frac{2}{3}\mu \quad (15)$$

If bulk viscosity of a fluid is assumed negligible, then

$$\lambda = -\frac{2}{3}\mu \quad (16)$$

Equation (16) is known as the Stokes hypothesis (Hoffman and Chang, 2004). When the hypothesis is inserted into the viscous stress tensor equations, we have:

$$\sigma_{xx} = \frac{2}{3}\mu \left(2\frac{\partial u}{\partial x} - \frac{\partial v}{\partial y} - \frac{\partial w}{\partial z} \right) \quad (17)$$

$$\sigma_{yy} = \frac{2}{3}\mu \left(2\frac{\partial v}{\partial y} - \frac{\partial u}{\partial x} - \frac{\partial w}{\partial z} \right) \quad (18)$$

$$\sigma_{zz} = \frac{2}{3}\mu \left(2\frac{\partial w}{\partial z} - \frac{\partial u}{\partial x} - \frac{\partial v}{\partial y} \right) \quad (19)$$

In order to include and account for the effect of turbulence in a flow field, the equations of fluid motion are amended by turbulence models. There are two approaches

to reformulate the Navier-Stokes equations for this purpose. In both approaches, an averaging process is used (Hoffman and Chang, 2000). The first approach was presented by Osborne Reynolds in 1895 (Blazek, 2005). The flow variables used are decomposed into a mean and a fluctuating part. The governing equations are then solved for the mean values. Mathematically, Reynolds' averaging is expressed as:

$$f = \bar{f} + f' \quad (20)$$

where the mean value is denoted by a bar over the variable and the time-dependent fluctuating value is denoted by a prime (Hoffman and Chang, 2000). The mean value is defined as:

$$\bar{f} = \frac{1}{\Delta t} \int_{t_o}^{t_o + \Delta t} f dt \quad (21)$$

The time averaging of a fluctuating quantity over a time interval, Δt , results in:

$$\overline{f'} = \frac{1}{\Delta t} \int_{t_o}^{t_o + \Delta t} f' dt = 0 \quad (22)$$

The time interval, Δt , used above must be larger than the period of fluctuating quantities but smaller than the time interval associated with the unsteady flow. Thus the time interval is problem dependent, i.e., depends on the geometry and physics of the flow-field being investigated. The rules for Reynolds averaging are as follows:

$$\overline{\bar{f}} = \bar{f} \quad (23)$$

$$\overline{f + g} = \bar{f} + \bar{g} \quad (24)$$

$$\overline{fg} = \bar{f} \bar{g} \quad (25)$$

$$\frac{\partial \bar{f}}{\partial x} = \frac{\partial \bar{f}}{\partial x} \quad (26)$$

$$\overline{f'^2} \neq 0 \quad (27)$$

$$\overline{f'g'} \neq 0 \quad (28)$$

$$\overline{(\bar{f} + f')^2} = \bar{f}^2 + \overline{f'^2} \quad (29)$$

When Reynolds-averaging and its rules are applied to the Navier-Stokes equations, the results are the mean values, which are formally identical to the Navier-Stokes equations above with nine new additional terms in the equations:

$$\frac{\partial \bar{\rho}}{\partial t} + \frac{\partial}{\partial x}(\bar{\rho}\bar{u}) + \frac{\partial}{\partial y}(\bar{\rho}\bar{v}) + \frac{\partial}{\partial z}(\bar{\rho}\bar{w}) = 0 \quad (30)$$

$$\begin{aligned} \frac{\partial}{\partial t}(\bar{\rho}\bar{u}) + \frac{\partial}{\partial x}(\bar{\rho}\bar{u}^2 + \bar{p}) + \frac{\partial}{\partial y}(\bar{\rho}\bar{u}\bar{v}) + \frac{\partial}{\partial z}(\bar{\rho}\bar{u}\bar{w}) = \\ \frac{\partial}{\partial x}(\bar{\sigma}_{xx} - \rho\overline{u'u'}) + \frac{\partial}{\partial y}(\bar{\tau}_{xy} - \rho\overline{u'v'}) + \frac{\partial}{\partial z}(\bar{\tau}_{xz} - \rho\overline{u'w'}) \end{aligned} \quad (31)$$

$$\begin{aligned} \frac{\partial}{\partial t}(\bar{\rho}\bar{v}) + \frac{\partial}{\partial x}(\bar{\rho}\bar{u}\bar{v}) + \frac{\partial}{\partial y}(\bar{\rho}\bar{v}^2 + \bar{p}) + \frac{\partial}{\partial z}(\bar{\rho}\bar{v}\bar{w}) = \frac{\partial}{\partial x}(\bar{\tau}_{xy} - \rho\overline{v'u'}) \\ + \frac{\partial}{\partial y}(\bar{\sigma}_{yy} - \rho\overline{v'v'}) + \frac{\partial}{\partial z}(\bar{\tau}_{yz} - \rho\overline{v'w'}) \end{aligned} \quad (32)$$

$$\begin{aligned} \frac{\partial}{\partial t}(\bar{\rho}\bar{w}) + \frac{\partial}{\partial x}(\bar{\rho}\bar{u}\bar{w}) + \frac{\partial}{\partial y}(\bar{\rho}\bar{v}\bar{w}) + \frac{\partial}{\partial z}(\bar{\rho}\bar{w}^2 + \bar{p}) = \frac{\partial}{\partial x}(\bar{\tau}_{xz} - \rho\overline{w'u'}) \\ + \frac{\partial}{\partial y}(\bar{\tau}_{yz} - \rho\overline{w'v'}) + \frac{\partial}{\partial z}(\bar{\sigma}_{zz} - \rho\overline{w'w'}) \end{aligned} \quad (33)$$

$$\begin{aligned} \frac{\partial}{\partial t}(\bar{\rho}\bar{e}) + \frac{\partial}{\partial x}(\bar{\rho}\bar{u}\bar{e} + \bar{p}\bar{u}) + \frac{\partial}{\partial y}(\bar{\rho}\bar{v}\bar{e} + \bar{p}\bar{v}) + \frac{\partial}{\partial z}(\bar{\rho}\bar{w}\bar{e} + \bar{p}\bar{w}) = \\ \frac{\partial}{\partial x}(\bar{\theta}_x) + \frac{\partial}{\partial y}(\bar{\theta}_y) + \frac{\partial}{\partial z}(\bar{\theta}_z) \end{aligned} \quad (34)$$

The nine new terms in the momentum equations ($\overline{\rho u'u'}$, $\overline{\rho u'v'}$, $\overline{\rho u'w'}$, $\overline{\rho v'u'}$, $\overline{\rho v'v'}$, $\overline{\rho v'w'}$, $\overline{\rho w'u'}$, $\overline{\rho w'v'}$, and $\overline{\rho w'w'}$) are referred to as the Reynolds stresses (Hirsch, 2007). (Actually, there are only six new terms because $\overline{\rho u'v'} = \overline{\rho v'u'}$, $\overline{\rho u'w'} = \overline{\rho w'u'}$, and $\overline{\rho v'w'} = \overline{\rho w'v'}$). The new terms contribute overall to the Reynolds-stress tensor (Blazek, 2005). More equations are needed to model the Reynolds stress terms (Hirsch, 2007).

In cases where the density is not constant, the density (mass) weighted or Favre decomposition can be applied instead of Reynolds averaging. A Favre averaged quantity is defined by,

$$f = \frac{\overline{\rho f}}{\overline{\rho}} \quad (35)$$

where ρ is the density, f is any conserved variable, and the over bar represents a Reynolds-averaged quantity. All properties are then defined as an average quantity plus a fluctuation, either,

$$f = \overline{f} + f' \quad (36)$$

for Reynolds averaging, or,

$$f = \overline{f} + f'' \quad (37)$$

for Favre averaging, where f' and f'' are the respective fluctuations (Corbin, 2008).

Now the system of equations, composed as the Favre-Averaged Navier-Stokes (FANS) equations, are written in a vector form as

$$\frac{\partial \overline{\rho}}{\partial t} + \frac{\partial}{\partial x}(\overline{\rho \tilde{u}}) + \frac{\partial}{\partial y}(\overline{\rho \tilde{v}}) + \frac{\partial}{\partial z}(\overline{\rho \tilde{w}}) = 0 \quad (38)$$

$$\begin{aligned} \frac{\partial}{\partial t}(\bar{\rho}\tilde{u}) + \frac{\partial}{\partial x}(\bar{\rho}\tilde{u}^2 + \bar{p}) + \frac{\partial}{\partial y}(\bar{\rho}\tilde{u}\tilde{v}) + \frac{\partial}{\partial z}(\bar{\rho}\tilde{u}\tilde{w}) = \\ \frac{\partial}{\partial x}(\tilde{\sigma}_{xx}) + \frac{\partial}{\partial y}(\tilde{\tau}_{xy}) + \frac{\partial}{\partial z}(\tilde{\tau}_{xz}) \end{aligned} \quad (39)$$

$$\begin{aligned} \frac{\partial}{\partial t}(\bar{\rho}\tilde{v}) + \frac{\partial}{\partial x}(\bar{\rho}\tilde{u}\tilde{v}) + \frac{\partial}{\partial y}(\bar{\rho}\tilde{v}^2 + \bar{p}) + \frac{\partial}{\partial z}(\bar{\rho}\tilde{v}\tilde{w}) = \\ \frac{\partial}{\partial x}(\tilde{\tau}_{xy}) + \frac{\partial}{\partial y}(\tilde{\sigma}_{yy}) + \frac{\partial}{\partial z}(\tilde{\tau}_{yz}) \end{aligned} \quad (40)$$

$$\begin{aligned} \frac{\partial}{\partial t}(\bar{\rho}\tilde{w}) + \frac{\partial}{\partial x}(\bar{\rho}\tilde{u}\tilde{w}) + \frac{\partial}{\partial y}(\bar{\rho}\tilde{v}\tilde{w}) + \frac{\partial}{\partial z}(\bar{\rho}\tilde{w}^2 + \bar{p}) = \\ \frac{\partial}{\partial x}(\tilde{\tau}_{xz}) + \frac{\partial}{\partial y}(\tilde{\tau}_{yz}) + \frac{\partial}{\partial z}(\tilde{\sigma}_{zz}) \end{aligned} \quad (41)$$

$$\begin{aligned} \frac{\partial}{\partial t}(\bar{\rho}\tilde{e}) + \frac{\partial}{\partial x}(\bar{\rho}\tilde{u}\tilde{e} + \bar{p}\tilde{u}) + \frac{\partial}{\partial y}(\bar{\rho}\tilde{v}\tilde{e} + \bar{p}\tilde{v}) + \frac{\partial}{\partial z}(\bar{\rho}\tilde{w}\tilde{e} + \bar{p}\tilde{w}) = \\ \frac{\partial}{\partial x}(\tilde{\theta}_x) + \frac{\partial}{\partial y}(\tilde{\theta}_y) + \frac{\partial}{\partial z}(\tilde{\theta}_z) \end{aligned} \quad (42)$$

where

$$\sigma_{xx} = (\mu + \mu_t) \left[2 \frac{\partial u}{\partial x} - \frac{2}{3} \nabla \cdot \bar{V} \right] - \frac{2}{3} \bar{\rho} k \quad (43)$$

$$\sigma_{yy} = (\mu + \mu_t) \left[2 \frac{\partial \tilde{v}}{\partial y} - \frac{2}{3} \nabla \cdot \bar{V} \right] - \frac{2}{3} \bar{\rho} k \quad (44)$$

$$\sigma_{zz} = (\mu + \mu_t) \left[2 \frac{\partial w}{\partial z} - \frac{2}{3} \nabla \cdot \bar{V} \right] - \frac{2}{3} \bar{\rho} k \quad (45)$$

$$\tilde{\tau}_{xy} = (\mu + \mu_t) \left(\frac{\partial u}{\partial y} + \frac{\partial \tilde{v}}{\partial x} \right) \quad (46)$$

$$\tilde{\tau}_{xz} = (\mu + \mu_t) \left(\frac{\partial u}{\partial z} + \frac{\partial w}{\partial x} \right) \quad (47)$$

$$\tilde{\tau}_{yz} = (\mu + \mu_t) \left(\frac{\partial \tilde{v}}{\partial z} + \frac{\partial \tilde{w}}{\partial y} \right) \quad (48)$$

where u , \tilde{v} , and w are the Favre-averaged velocity vectors (for Cartesian coordinates x , y , and z , respectively), q_x , q_y , and q_z are the Favre-averaged heat release from conduction and Favre-averaged energy release from diffusion (again, for x , y , and z), \tilde{e} , $\tilde{\sigma}$, $\tilde{\tau}$, and μ are the Favre-averaged total energy, molecular stress tensors, and laminar viscosity, μ_t is the turbulent viscosity coefficient and $\bar{\rho}$ and \bar{p} are the Reynolds-averaged density and pressure, respectively (Hoffman and Chang, 2000). Therefore, the most convenient way to use both approaches is to employ Reynolds averaging for density and pressure, and Favre averaging for other variables such as velocity, internal energy, enthalpy, and temperature (Blazek, 2005).

Turbulence Modeling

A turbulence model is an equation relating the fluctuating correlation to mean flow variables with various constants provided from experimental investigations. Many types of models have been developed to predict turbulence. Zero-equation models, like Cebeci-Smith or Baldwin-Lomax, are algebraic equations. Zero-equation models are mathematically simple, but their underlying assumption is that local turbulent production and dissipation are always in equilibrium, and they do not include the convection of turbulence (Hoffman and Chang, 2000). The half-equation model, like that of Johnson-King, employs an ordinary differential equation to account for transport of turbulence. Half-equation models are not commonly used, and have no clear advantage over the

algebraic models. Partial differential equations (PDE) are referred to as one-equation or two-equation models, depending on the number of PDE utilized (Hoffman and Chang, 2000). In CFD, different types of turbulent flows require different applications of turbulence models. In the event that insufficient knowledge precludes the selection of an appropriate model, a two-equation model is strongly encouraged as a starting point for turbulent analysis (Tu, et al., 2008). Two-equation models have the capability of predicting more complex flows than zero and one-equation models (Kim, et al., 2005). The most widely used two-equation turbulence model today is the k- ϵ model, which solves both the turbulent kinetic energy (k) and the rate of dissipation of the turbulent kinetic energy (ϵ). The first low Reynolds number k- ϵ model was developed by Jones and Launder (Jones, et al., 1973) and has subsequently been modified by many investigators (Menter, 1993). The k- ϵ model is mathematically defined by the following two equations:

$$\begin{aligned} \frac{\partial \rho k}{\partial t} + \frac{\partial \rho u k}{\partial x} + \frac{\partial \rho v k}{\partial y} + \frac{\partial \rho w k}{\partial z} = \frac{\partial}{\partial x} \left[\left(\mu + \sigma_k \mu_t \right) \frac{\partial k}{\partial x} \right] \\ + \frac{\partial}{\partial y} \left[\left(\mu + \sigma_k \mu_t \right) \frac{\partial k}{\partial y} \right] + \frac{\partial}{\partial z} \left[\left(\mu + \sigma_k \mu_t \right) \frac{\partial k}{\partial z} \right] + P_k - \rho \epsilon \end{aligned} \quad (49)$$

$$\begin{aligned} \rho \left(\frac{\partial \epsilon}{\partial t} + u \frac{\partial \epsilon}{\partial x} + v \frac{\partial \epsilon}{\partial y} + w \frac{\partial \epsilon}{\partial z} \right) = \frac{\partial}{\partial x} \left[\left(\mu + \frac{\mu_t}{\sigma_\epsilon} \right) \frac{\partial \epsilon}{\partial x} \right] + \frac{\partial}{\partial y} \left[\left(\mu + \frac{\mu_t}{\sigma_\epsilon} \right) \frac{\partial \epsilon}{\partial y} \right] \\ + \frac{\partial}{\partial z} \left[\left(\mu + \frac{\mu_t}{\sigma_\epsilon} \right) \frac{\partial \epsilon}{\partial z} \right] + c_{\epsilon 1} P_k \frac{\epsilon}{k} - c_{\epsilon 2} \rho \frac{\epsilon^2}{k} \end{aligned} \quad (50)$$

where $c_{\epsilon 1}=1.44$, $c_{\epsilon 2}=1.92$, $\sigma_k=1.0$, and $\sigma_\epsilon=1.3$. The term, μ_t , is the turbulent viscosity

defined as $\mu_t = \rho c_\mu k^2 / \epsilon$ where $c_\mu=0.09$, and P_k is the production of turbulence, defined as:

$$P_k = \tau_{ij} \left(\frac{\partial u_i}{\partial x_j} \right) \quad (51)$$

A second model is the k- ω model, which solves for both the turbulent kinetic energy and the specific turbulent dissipation rate (or turbulence frequency), ω . There are several versions of the k- ω model, but the best known is the model developed by David C. Wilcox (Hoffman and Chang, 2000). The k- ω model's two equations are:

$$\begin{aligned} \frac{\partial \rho k}{\partial t} + \frac{\partial \rho u k}{\partial x} + \frac{\partial \rho v k}{\partial y} + \frac{\partial \rho w k}{\partial z} = \frac{\partial}{\partial x} \left[(\mu + \sigma_k \mu_t) \frac{\partial k}{\partial x} \right] \\ + \frac{\partial}{\partial y} \left[(\mu + \sigma_k \mu_t) \frac{\partial k}{\partial y} \right] + \frac{\partial}{\partial z} \left[(\mu + \sigma_k \mu_t) \frac{\partial k}{\partial z} \right] + P_k - \beta^* \rho k \omega \end{aligned} \quad (52)$$

$$\begin{aligned} \rho \left(\frac{\partial \omega}{\partial t} + u \frac{\partial \omega}{\partial x} + v \frac{\partial \omega}{\partial y} + w \frac{\partial \omega}{\partial z} \right) = \frac{\partial}{\partial x} \left[(\mu + \sigma_\omega \mu_t) \frac{\partial \omega}{\partial x} \right] + \frac{\partial}{\partial y} \left[(\mu + \sigma_\omega \mu_t) \frac{\partial \omega}{\partial y} \right] \\ + \frac{\partial}{\partial z} \left[(\mu + \sigma_\omega \mu_t) \frac{\partial \omega}{\partial z} \right] + \alpha_1 \frac{\omega}{k} P_k - \beta_1 \rho \omega^2 \end{aligned} \quad (53)$$

where μ_t is redefined as $\mu_t = \rho k / \omega$ and $\varepsilon = \beta^* \omega k$ where $\beta^* = 0.09$ (a constant).

The k- ε and the k- ω turbulence models both have strengths and weaknesses. The k- ε model does very well in regions away from the wall surface, but cannot be typically integrated to the wall. The k- ω model, on the other hand, performs very well in viscous sub layers, but is very sensitive to freestream values. A turbulence model which combines the best features of both the k- ω and k- ε models was created by F.R. Menter (Menter, 1993). Menter's model would switch from the k- ω model at the wall surface to the k- ε model for free shear flow with blending in the wake region of the boundary layer (Kim and Song, 2005). Menter's original model is defined in Eq. (52) above and the following equation:

$$\begin{aligned} \rho \left(\frac{\partial \omega}{\partial t} + u \frac{\partial \omega}{\partial x} + v \frac{\partial \omega}{\partial y} + w \frac{\partial \omega}{\partial z} \right) = \frac{\partial}{\partial x} \left[(\mu + \sigma_\omega \mu_t) \frac{\partial \omega}{\partial x} \right] + \frac{\partial}{\partial y} \left[(\mu + \sigma_\omega \mu_t) \frac{\partial \omega}{\partial y} \right] \\ + \frac{\partial}{\partial z} \left[(\mu + \sigma_\omega \mu_t) \frac{\partial \omega}{\partial z} \right] + \frac{\gamma \rho}{\mu_t} P_k - \beta \rho \omega^2 + 2 \rho (1 - F_1) \sigma_{\omega^2} \frac{1}{\omega} \left[\frac{\partial k}{\partial x} \frac{\partial \omega}{\partial x} + \frac{\partial k}{\partial y} \frac{\partial \omega}{\partial y} + \frac{\partial k}{\partial z} \frac{\partial \omega}{\partial z} \right] \end{aligned} \quad (54)$$

where F_1 is a switching function designed to switch from k - ω to k - ε . The switching function is defined as $F_1 = \tanh(\arg_1^4)$ where (Kim and Song, 2005):

$$\arg_1 = \min \left[\max \left(\frac{\sqrt{k}}{0.09\omega y}; \frac{500\mu}{\rho\omega y^2} \right); \frac{4\rho\sigma_{\omega 2}k}{CD_{k\omega}y^2} \right] \quad (55)$$

and

$$CD_{k\omega} = \max \left(2\rho\sigma_{\omega 2} \frac{1}{\omega} \left[\frac{\partial k}{\partial x} \frac{\partial \omega}{\partial x} + \frac{\partial k}{\partial y} \frac{\partial \omega}{\partial y} + \frac{\partial k}{\partial z} \frac{\partial \omega}{\partial z} \right]; 10^{-20} \right) \quad (56)$$

The constants appearing in equations (52) and (54) above can be expressed in a general compact form by $\phi = F_1\phi_1 + (1-F_1)\phi_2$ where ϕ_1 represents the constants of the k - ω model and ϕ_2 represents the same constants for the k - ε model. Table 2 has the two sets of model constants used in the switching function of the Menter model.

Table 2. Set of model constants for switching function in Menter model

Constant Set	σ_k	σ_ω	β	κ	γ
ϕ_1	0.5	0.5	0.075	0.41	$\beta_1/\beta^* - \sigma_{\omega 1}\kappa^2/(\beta^*)^{0.5}$
ϕ_2	1.0	0.856	0.0828	0.41	$\beta_2/\beta^* - \sigma_{\omega 2}\kappa^2/(\beta^*)^{0.5}$

Menter (Menter, 1993) was later able to modify this baseline model to account for the transport of the principal turbulent shear stress in adverse pressure gradient boundary layers. Menter's modified model is called the Shear-Stress Transport (SST) model. In the SST model, the turbulent viscosity is defined as:

$$\nu_t = \frac{a_1 k}{\max(a_1\omega, \Omega F_2)} \quad (57)$$

where $a_1 = 0.31$ (a constant), Ω is the absolute vorticity:

$$\Omega = \left| \frac{\partial w}{\partial y} - \frac{\partial v}{\partial z} \right| + \left| \frac{\partial u}{\partial z} - \frac{\partial w}{\partial x} \right| + \left| \frac{\partial v}{\partial x} - \frac{\partial u}{\partial y} \right| \quad (58)$$

and $F_2 = \tanh(\arg_2^2)$ where:

$$\arg_2 = \max \left[2 \frac{\sqrt{k}}{0.09 \omega y}, \frac{500 \nu}{\omega y^2} \right] \quad (59)$$

The constants for ϕ_1 and ϕ_2 are the same as the baseline model above, except for

$\sigma_{k1}=0.85$.

For this research, the turbulence model used must be able to work well with a turbulent boundary layer interacting with a shock wave. According to Wilcox, the $k-\omega$ model is of “satisfactory accuracy” for both attached boundary layers and mildly separated flows (Wilcox, 2001). In the VULCAN CFD code used in this research, there are three turbulence model choices available that use the $k-\omega$ model: the $k-\omega$ model itself, Menter, and Menter-SST. As shown later in the 2-D and 3-D simulation sections, runs were accomplished with different turbulence models to determine the differences among them. The choice of turbulence model does affect the final location of the shock train in both the 2-D and 3-D simulations. For the 2-D runs, the Menter-SST model had the shock train furthest upstream in the isolator, followed by $k-\omega$ and Menter. The results with the Menter-SST model were closest to the AFIT experimental runs, so Menter-SST was used for the 2-D runs. For the 3-D runs, Menter-SST was the furthest upstream again, this time followed by Menter and then $k-\omega$. In the 3-D cases, the results with the $k-\omega$ model were closest to the AFIT experimental runs so $k-\omega$ was used for the 3-D runs.

Previous Work on Isolators and CFD

There have been several numerical studies done in the past on the performance and capabilities of an isolator. Billig in 1993 found an experimental correlation for the pressure ratio to the length of the shock train in the isolator. The correlation is defined in the following equation:

$$50(P_s/P_4 - 1) + 170(P_s/P_4 - 1)^2 = S_t(M_4 - 1) \text{Re } \theta^{1/4} / h(\theta/h)^{1/2} \quad (60)$$

where S_t is the measured shock train length (from the leading edge of the shock train to the end of the isolator), M_4 is the Mach speed at the leading edge of the shock train, θ is the momentum thickness of the boundary layer, h is the height of the isolator height, P_s is the static pressure measured at points along the shock train, and P_4 is the pressure at the shock train's leading edge. Billig's correlation is adequate for an engineering design model (Billig, 1993). A comparison of the results with Billig's work will be shown and discussed more in the Analysis section. Other related topics have also been investigated. For example, one study (Lin, et al. 1991) focused on the numerical analysis of a normal PCST in a 2-D, constant area isolator and its comparison with a previously computed oblique PCST. The numerical analysis, done by the Rocketdyne Division of the Rockwell International Corporation, showed that the length of both normal and oblique PCSTs increases when the momentum thickness increases at high back pressures (Ratio of back pressure to inflow pressure, or $P_b/P_i = 3.0$ and 3.2). Any change in momentum thickness produced no change in PCST length at low back pressures ($P_b/P_i = 2.5$ and 2.0). Another similarity was that the length of both PCSTs decreases with increasing Mach number for the same back pressure. The two flows for the normal and oblique PCSTs were different in that the pressure plateaus in an oblique

PCST at lower Mach numbers are not seen in a normal PCST (except for the case of thin boundary layers). Since this research will include work using inlet Mach numbers that would create both normal and oblique PCSTs, the results of Rocketdyne's work (Lin, et al. 1991) will be compared with the results from this research to determine if they show the same patterns.

Other numerical studies have focused on certain performance parameters of the isolator. Balu et al. (2005) computed the maximum back pressure to inflow pressure ratio for unstart (shown in Figure 5) in a 2-D, constant area isolator (with a length to height ratio of 5) with an intake attached.

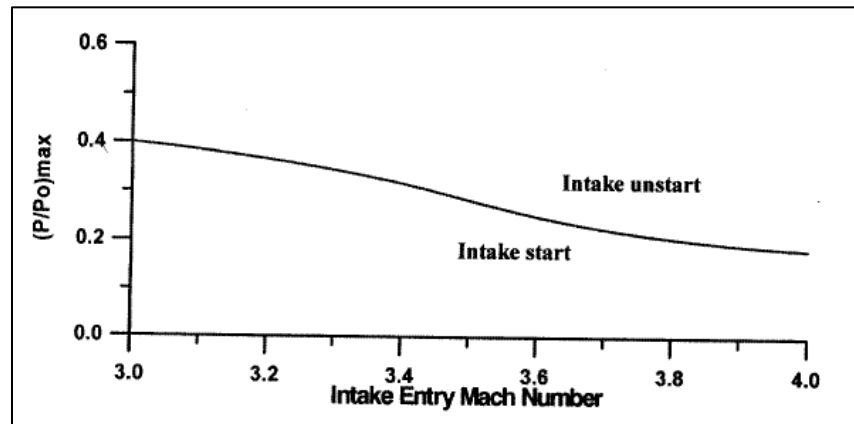


Figure 5. Maximum pressure capability of isolator (Balu, et al. 2005)

Many studies have been done on isolators using VULCAN as the CFD code. K.-C. Lin, et al. (2006) computed 3-D shock train structures inside constant area isolators. They investigated the effects of back pressure, isolator configuration, and flow Mach number, and drew the following conclusions:

1. Surface roughness plays an important role in defining isolator performance. It affects the boundary layer thickness and growth, and determines the pressure rise across the length of the isolator. In these simulations, surface roughness

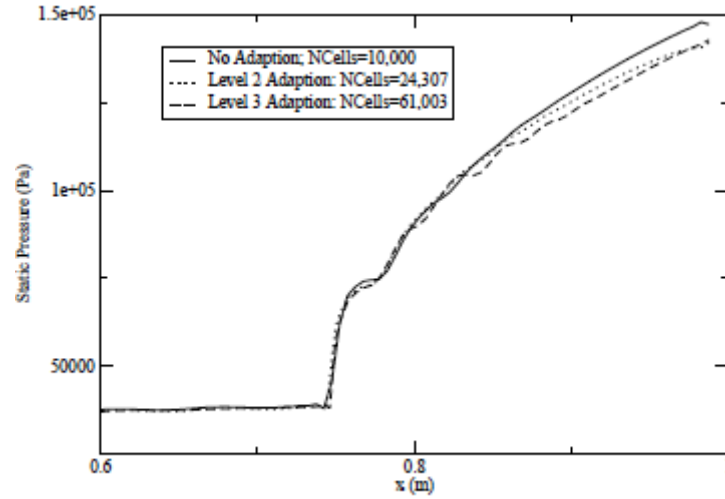
was factored in. Since the walls of the experimental isolator these simulations are based on are smooth, the walls in these simulations were smooth also.

2. The PCST moves toward the isolator entrance as the back pressure increases. The movement based on an increased back pressure is expected based on the previous developed correlations by Waltrup and Billig (1973).
3. The PCST near the isolator entrance is very sensitive to any pressure variation. When a shock train is positioned in the upstream section of the isolator, a small increase in back pressure can easily cause an engine unstart by pushing the shock train out of the isolator. With these simulations, the backpressure values must be chosen so that they are large enough to form a PCST, but not too large as to cause an unstart and make the simulations crash.
4. As the PCST moves forward, the gradient of flow properties across the isolator exit plane decreases. At the exit plane, the Mach number decreases, the temperature increases, and the flow become more uniform.

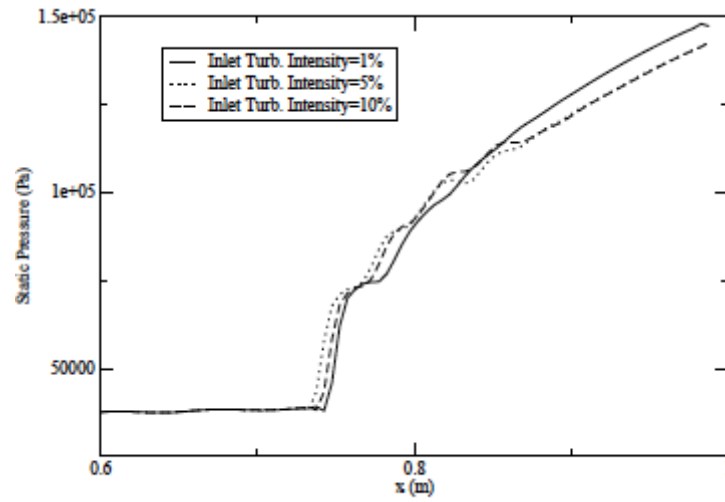
These conclusions about the movement and location of the PCST were used in this research, just like the results for normal and oblique PCSTs mentioned previously in this section.

Allen, et al. (2007) used FLUENT with 2-D geometries to arrive at simplifying assumptions prior to the use of the more computationally expensive 3-D geometries. The 2-D results, shown in Figure 6, indicate that neither the inlet turbulence intensity nor adaptive grid refinement is critical to the PCST location, but the PCST location is influenced by the turbulence model used. A further comparison of these FLUENT results showed that the Reynolds-Averaged Navier-Stokes (RANS) approach showed the least

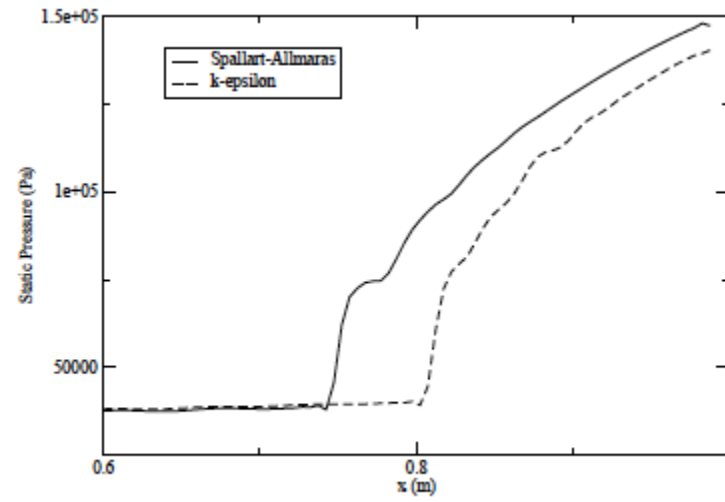
disparity with experimental values, while the Large Eddy Simulation (LES) showed the greatest disparity from the experiment. The difference between RANS and LES results is expected since RANS, complemented with a turbulence model, is the most basic method of computing turbulent flows and most practical in engineering applications while LES is computationally expensive, inherently unstable, and used mostly as a research tool in CFD. The fact that RANS showed the least disparity with experimental results works well since the VULCAN code uses RANS to run the simulations.



(a) Effect of Grid Refinement



(b) Effect of Inlet Turbulence Intensity



(c) Effect of Turbulence Model

Figure 6. 2D comparisons of static pressure along isolator baseline and initial shock location. (Allen, et al. 2007)

Based on the previous work presented, there are two conclusions that can be drawn regarding isolators and CFD. First, simulations with varying turbulence models need validation. Second, of the two CFD approaches available for use, RANS is the best approach for CFD work with comparison to experimental results for this research. LES, as mentioned previously, is computationally expensive, though providing better accuracy. The transient simulation will incorporate both steady-state and transient conditions, but will react to changes in certain variables such as back pressure and turbulence model.

There are other challenges that must also be considered in hypersonic simulation. The University of Tennessee Space Institute evaluated CFD codes for hypersonic flow simulations (Maicke and Majdalani, 2010). The Space Institute identified some general challenges in hypersonic simulations, such as combustion modeling and multiphase flow (fuel mixing with incoming air and pre-existing combustion products). For an isolator, there are some specific challenges the Space Institute identified that need to be addressed. One challenge is using the best turbulence model for these simulations, which was already mentioned. Another challenge is boundary layer effects. Because hypersonic engines are integrated with the air frame, boundary layer transition simulations are also of key importance in CFD applications. Accurate prediction of boundary layer transitions can have a profound effect on the efficiency of the scramjet. In CFD, wall functions can be used to provide near-wall boundary conditions for the momentum and turbulence transport equations. Normally, a transition study would be appropriate, but for this research, it cannot be done because of lack of data from the experiment.

The Space Institute's evaluation also included a comparison of some well known CFD codes, identifying strengths and weaknesses. The best code for isolator work in this

research is VULCAN. VULCAN's strengths are: Designed for internal flows in scramjet engines, runs on both Unix or Linux (which was available for this research) platforms, can run on a single machine or in parallel using MPI, has a number of turbulence models to choose from, and employs a probability density function approach for reacting species fluctuations. VULCAN's weaknesses are: Not suited for lower speed flows due to degradation in convergence (without modifications), and requires structured grids. There have been some time-accurate simulations done that show a transient simulation is possible. Benson et al. (1993) ran 2-D simulations of unsteady inlet unstarts to study the effects of turbulence. A second paper by Neaves et al. (2001) used an adaptive grid algorithm to calculate 3-D time-accurate simulations for high-speed inlet unstarts. The results of the previous works mentioned in this section, along with addressing the challenges of turbulence models and boundary layers identified above, show an accurate, transient isolator simulation using VULCAN is possible.

III. Methodology

Computational Fluid Dynamics (CFD)

To successfully solve problems of fluid dynamics and heat transfer, there are three approaches: Experimental, Analytical, and Computational Fluid Dynamics (CFD). Experimental involves models, experiments, and flight testing. Analytical involves the closed form solution. CFD is the computer simulation of fluid transport processes by solving approximations to the mathematical description of fluid flow. The experimental approach can be very expensive and can put pilots and vehicles at greater risk. The analytical approach is both safer and cheaper, but is very time-consuming and is not good for complex flow problems where the closed form solution may not exist. The final approach, CFD, is the best one for this research. CFD is cost-effective, reduces risks to pilots and vehicles, and enables detailed analysis of the flow field (Tu, et al., 2008). CFD can complement the scramjet flow path design process and provide insight into complex flow phenomena by using parametric studies of various design configurations. The parametric studies can identify and estimate the sensitivity of changes to flow path performance (Bagaveyev, et al., 2010). The CFD solution process consists of three main elements: Pre-processor, solver, and post-processor. The first step in the pre-process is to define and create the geometry of the flow region, or computational domain, for the CFD calculations. The computational domain is a representation of the physical domain that defines the actual flow problem. For this research, the physical domain is based on a test cell located at AFIT with a convergent/divergent nozzle providing flow to the entrance of a constant area isolator (60.96 cm x 6.35 cm x 6.35 cm). Figure 7 is a picture of the laboratory set-up of the AFIT test cell.

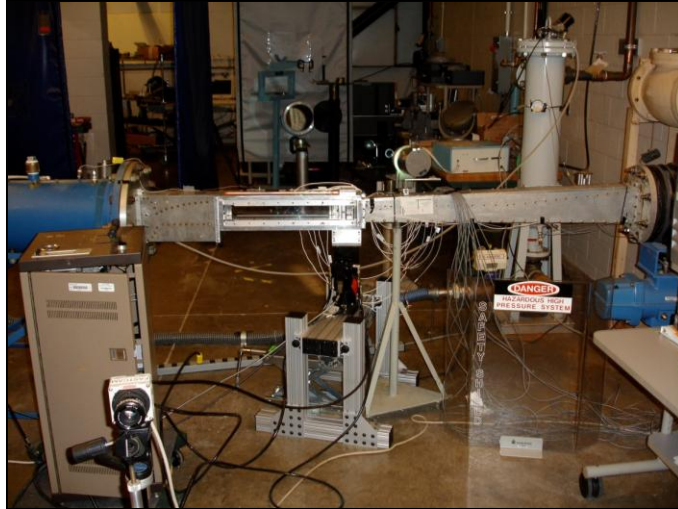


Figure 7. AFIT isolator test facility

The second step is grid (or mesh) generation. Grid generation is considered one of the most important steps of the pre-process stage, where the computational domain is broken down into a smaller number of non-overlapping sub domains. The result is a grid of nodes and cells. The fluid variables (such as pressure, temperature, and velocity) will be solved at each node or in each cell. The quality and resolution of the grid will determine the accuracy of the solution, so a majority of the time is spent on this step. The CFD nozzle/isolator grid used in this research was a cell-centered, structured grid with regularly shaped cells, with easily addressed indices (explicit neighbors), and good boundary layers with stretched grid cells near the walls. The grid was created using Gridgen™, a commercial product of Pointwise, Inc. used for geometry creation and grid generation (Pointwise, 2003). More details are provided in the next section, Grid Generation.

The third step is the selection of which properties and which models to use. CFD requires solutions to very complex physical processes such as heat transfer and combustion. The properties and models chosen will affect the flow properties, so a CFD

user must decide what to include in the calculations. When the simulations were run, several different turbulence models were tested and compared to determine which one works best. The fourth step includes a choice of boundary conditions that mimic the real physical flow system. These conditions include the inflow and outflow boundaries, and other boundary conditions such as solid walls or open boundaries. The fifth step in the CFD process, initialization and solution control, marks the beginning of the solver phase. CFD usually requires iterative solutions to simulation complex flow processes. Initialization is an initial guess of the flow properties in the process. A good guess will lead to shorter computational time to solve the problem, and aid in stability in the problem. Solution control is where the CFD user decides what iterative solver and interpolation (or discretization) scheme to use for the problem. The choices made for steps three, four, and five in this research are discussed more in the VULCAN Code section. The sixth step is to monitor convergence. The sixth step is used to determine when the solution is finished. It includes both grid independence and numerical convergence. Grid independence is where the grid is refined to the point where there is no appreciable change in the key results. Grid independence can be applied to both steady-state and transient simulations. Numerical convergence is where the imbalance in the equations used are tracked in terms of residuals to see if the residuals increase or decrease and to check and see if the residuals reach an acceptable tolerance level when they decrease. For a transient simulation, the numerical convergence normally used in steady-state simulations will not work. Instead, stopping criteria must be established for ending the simulations. In this research, there were two criteria set for stopping the criteria. The first criteria is no further movement of the leading edge location of the shock train

(indicating the final location of the leading edge which can be compared to the AFIT experiment) and the second criteria is a mass flow imbalance of less than one percent, which is calculated by VULCAN in its output file. The mass imbalance is defined as the difference of mass flow rate in minus the mass flow rate out divided by the mass flow rate in ($[\dot{m}_{in} - \dot{m}_{out}] / \dot{m}_{in}$). Finally, the post-processing phase of flow visualization is completed, where meaningful information and physical insight to the flow are extracted from the solution. Post-processing can include plots, particle tracking, data reports, and animation (Tu, et al., 2008).

Grid Generation

Grid generation is the process where the space of the flow to be computed – the physical space, is divided into a large number of geometrical elements called grid cells. Grid generation can be viewed as placing grid points in the physical space and then connecting them by straight lines called grid lines (Blazek, 2005). Grids are used to adequately resolve the important physics and to capture all the geometric details of the domain within the flow region. The quality of such a grid affects the solution's accuracy, stability, and convergence rate. For these simulations, VULCAN only uses a structured grid. A structured grid has the defining characteristics mapped to a Cartesian mesh in computational space. A structured grid has regularly shaped cells, is easily addressed by indices, and is good for boundary layers when stretched grid cells near the walls are used. The grid generation process is 1) determine the domain of interest (the experiment's nozzle and isolator), 2) define the geometry (measurements), 3) decompose the domain and plan the topology (build the grid), 4) build the surface meshes (the walls of the

experimental isolator), and 5) build the volume meshes (for the flow in the nozzle and isolator). Grid generation requirements for a given problem depend on two things: problem and solver considerations. The problem considerations include the objective (identifying the PCST leading edge and determining how the back pressure changes its location in transient conditions), the flow conditions (unsteady and supersonic) and the geometry (grid clustering, grid topology). The solver considerations include the grid types supported, where the flow variables are stored (in the cells), the boundary conditions supported, the numerical scheme, and adaptation (Tu, et al., 2008).

Once a grid is created, a grid independence study was performed to analyze the suitability of the grid and yield an estimate of the numerical errors (Tu, et al., 2008). The definition of grid independence is a converged solution obtained from a CFD calculation is independent of the grid's density. The number of cells in a grid-independent CFD simulation would not (ideally) change the flow field solution and integrated quantities. Only when further mesh refinement yields small, insignificant changes is grid independence indicated (FLUENT, 2001). Grid independence here was accomplished for both 2-D and 3-D using three grids. The first grid was the original grid (called the medium grid in this dissertation). The second grid was a fine grid, with twice as many cells in both directions and one-half the wall spacing as the medium grid. The third grid was a coarse grid, with half the cells and twice the wall spacing as the medium grid. A comparison of the same simulations (under the same conditions and same length of time) using these different grids was accomplished to determine if grid independence was achieved.

Another grid adaptation, local refinement, is used to capture important flow features. One local refinement technique that is widely used in many CFD applications is the concept of a stretched grid in the near vicinity of domain walls. A large number of small cells clustered within the physical boundary layer will minimize the truncation error with closely spaced grid points, and capture the actual flow physics (Tu, et al., 2008). Stretched cells will give sufficient grid resolution to capture the large velocity gradients that are characterized in a boundary layer, including the use of wall functions based on the non-dimensional distance to the walls (y^+), instead of solving the turbulent flow at or near the walls dominated by shear stress.

Both the 2-D and 3-D CFD nozzle/isolator grid used were created with Gridgen™. For this problem, the isolator was truncated at the location where the backpressure was experimentally measured (53.31 cm from the nozzle exit), so the backpressure can be applied instead as a subsonic outflow boundary condition. The grid used for the simulation must have enough cells to provide the level of detail needed for analysis. Figure 8 is the 2-D grid for the nozzle/isolator used in this simulation, consisting of 88,173 cells (873 cells in the stream wise direction and 101 cells in the vertical direction.). The horizontal spacing, vertical spacing and grid stretching were accomplished through a hyperbolic tangent distribution function giving the spacing in the nozzle an Δx of 0.2578 mm and a Δy of 0.4913 mm and in the isolator an Δx of 0.5334 mm and a Δy of 0.3175 mm. This leads to a maximum y^+ spacing of 218.5 in the nozzle, but a y^+ less than 100 in the isolator, which is acceptable when using a wall matching function (Wilcox, 1989). The 3-D grid was identical to the 2-D grid with 101 cells in the z-direction (8,905,473 total cells), giving the spacing in the nozzle a Δz of 0.4913 mm,

and the isolator a Δz of 0.3715 mm.. A fine grid with twice as many cells in all directions (352,692 cells in 2-D and 70,580,547 cells in 3-D) and one-half the wall spacing and a coarse grid with half the cells (22,261 cells in 2-D and 1,131,435 cells in 3-D) and twice the wall spacing were also created. Both grid convergence and temporal resolution studies were performed on both the 2-D and the 3-D grids. The results are presented in Chapters 4 and 5, respectively.

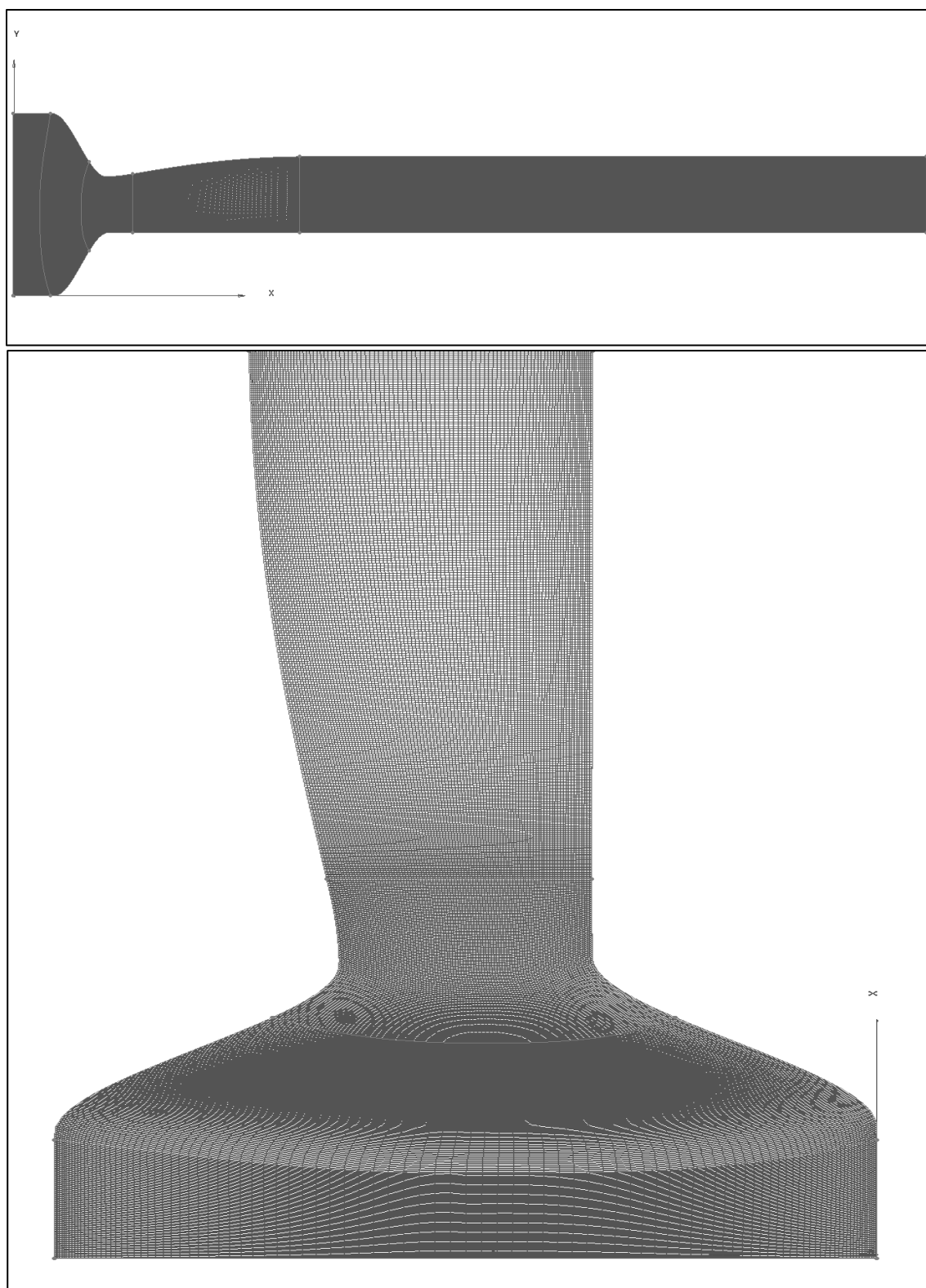


Figure 8. Nozzle/isolator grid: (top) overview, (bottom) nozzle close up

VULCAN Code

The simulations for the isolator will be accomplished using VULCAN (Viscous Upwind Algorithm for Complex flow Analysis), a Navier-Stokes flow solver code that is currently maintained and distributed by the Hypersonic Air Breathing Propulsion Branch of the NASA Langley Research Center (VULCAN Home Page, 2009). The code solves the conservation equations (both Reynolds-averaging and Favre-averaging as described earlier in Section II) governing inviscid and viscous flows appropriate for calorically or thermally perfect gases with a cell-centered, structured-grid, finite-volume scheme. The inviscid fluxes are computed using the MUSCL (Monotone Upstream Centered Scheme for Conservation Laws) scheme (Van Leer, 1979), with either Roe's approximate Riemann solver (Roe, 1986) or Edwards' LDFSS (Low Dissipation Flux Splitting Scheme) (Edwards, 1997). Viscous fluxes are based on a central difference scheme, with options to include cross-derivative terms for accuracy in highly three-dimensional flows or to neglect them for computational efficiency. VULCAN can simulate 2-D, axisymmetric, or 3-D flows. A variety of implicit and explicit time-integration strategies are available for advancing the solution in time, including a pseudo-time iterative approach for parabolic flows and time-accurate (or unsteady, which is needed in a transient simulation) schemes such as a multi-stage Runge-Kutta scheme and several approximate factorization methods. A variety of one-equation and two-equation turbulence models are available to describe the turbulent velocity field, including the Menter SST turbulence model. VULCAN has full multi-grid capabilities, allowing rapid convergence for steady-state problems (Baurle, et al., 2001). MPI (Message Passing Interface) routines using an SPMD (Single Program, Multiple Data) paradigm take

advantage of the parallelism of modern supercomputers, and arbitrary block-to-block connectivity allows the easy removal or addition of grid-points at zonal interfaces (White, et al., 1999).

VULCAN is executed in command line mode, using both input and output files. The input file controls how VULCAN runs and provides many options for defining a computational domain, setting boundary conditions, initializing the flow, controlling the solution process, and selecting the information to be post-processed for plotting. The output file is where the VULCAN run stream is written and includes the time step, the flow variables calculated in each time step, and a summary on the residuals, y^+ , and other information used in VULCAN. In addition, VULCAN creates post-processed Plot3d format files for viewing on TecPlot 360™, a CFD software program for plotting simulation results (TecPlot, 2011).

Computer Runtimes

Since the time steps required to reach the stopping criteria will be on the order of hundreds of thousands, multiple processors are needed for the complex calculations involved with VULCAN. The best way to accomplish this is through a supercomputer. The DoD Supercomputer Resource Centers (DSRCs) are high performance computing (HPC) facilities that were utilized for this research. To run the 2-D transient simulation, a Cray XT4 supercomputer using eighteen 2.1 GHz AMD Opteron 64-bit quad-core processors was used. The Cray XT4 required 1 hour and 3 minutes to complete 10,000 time steps of a simulation (including both pre-processing and post-processing) The time required to run the longest 2-D simulation from beginning (start of simulation) to end

(meeting stopping criteria) was just under 39 hours. For the 3-D simulations, a Cray XE6 using one hundred and fifty 2.4 GHz AMD Opteron 64-bit 8-core processors was used. The 3-D simulation required 5 hours and 9 minutes to complete 10,000 time steps of a simulation. The time required to run the longest 3-D simulation from beginning to end was approximately 216 hours (9 days).

IV. Two-Dimensional CFD Results

Introduction

This section presents the 2-D, time-accurate, CFD results using VULCAN for a mechanically back-pressured, cold flow isolator with an inflow Mach number of 1.8. These results mimic the experimental efforts used to investigate shock train dynamics with the test apparatus at AFIT. As stated in the Objectives section of Chapter 1, the 2-D simulations allowed the user to try different values (like the back pressure and the inflow pressure) and variables (like time step and the turbulence model), and determine the response to expect in the 3-D simulations. The 2-D results were later used to create the 3-D transient simulation in Chapter 5. Table 1, in Chapter 1, contains the reference conditions used in the 2-D simulations. The Table 1 values are the same ones entered into the VULCAN input file.

For the boundary conditions, the sides of the isolator were set as adiabatic walls (no heat transfer) since the simulation is based on a cold flow experiment. For surface roughness, the Wilcox wall matching function was set for smooth walls, and was used to reduce the need for grid clustering in the boundary layers (Wilcox, 1989). Information on the inflow boundary layer thickness from the AFIT experiments was unavailable, so the nozzle itself was simulated, attached to the isolator, and two simulations were executed. The first simulation (using 50,000 time steps) was used to develop a boundary layer profile in the isolator based on the reference conditions in Table 1. The second simulation (another 50,000 time steps) represented the AFIT experiment with the boundary layer profile from the first simulation applied to the isolator inflow as a fixed boundary condition. The back pressure used in the simulations was as shown in Table 1, and was

applied as a subsonic outflow boundary condition. For a transient simulation, a Runge-Kutta time-stepping scheme was used with a specified time step of 1.0×10^{-7} seconds, based on the results of the temporal resolution study.

Transient 2-D Simulation

The results for the transient 2-D simulation are shown below and divided into six sections. The first three sections deal with grid convergence, temporal resolution, and the turbulence model used. The fourth section shows the results when the back pressure is applied instantaneously, and the fifth section has the results for a gradient back pressure applied over a finite time interval. The final section is a summary of the 2-D results.

Grid Convergence Study

Figure 9 has the boundary layer profiles at the exit of the nozzle/isolator for the coarse, medium, and fine grids with a backpressure of 89.6 kPa instantaneously applied at the exit, a condition that causes a PCST and subsequent subsonic flow. For the coarse grid, almost all the grid points (except one) have a Mach number greater than one. Without enough subsonic grid points, the coarse grid cannot resolve the subsonic portion of the boundary layer, and therefore cannot propagate the backpressure upstream in the isolator to create the shock train and subsequent subsonic outflow. The coarse grid was determined unacceptable and was omitted from the research. The medium and fine grids both resolved the subsonic portion of the boundary layer, and therefore could propagate the backpressure upstream, creating the desired shock train and subsequent subsonic outflow. The asymmetry shown in the medium and fine grid's profiles is the result of the unusual shape of the nozzle. Figure 10 shows the pressure contours for a steady-state

comparison of the three grids, each tested with a back pressure of 89.6 kPa. The coarse grid does not form a shock train, confirming again that it is unacceptable. Both the medium and fine grids show similar results, with the shock train clearly identified at the same location on both grids. To save computer time, the medium grid was used for the remainder of the simulations.

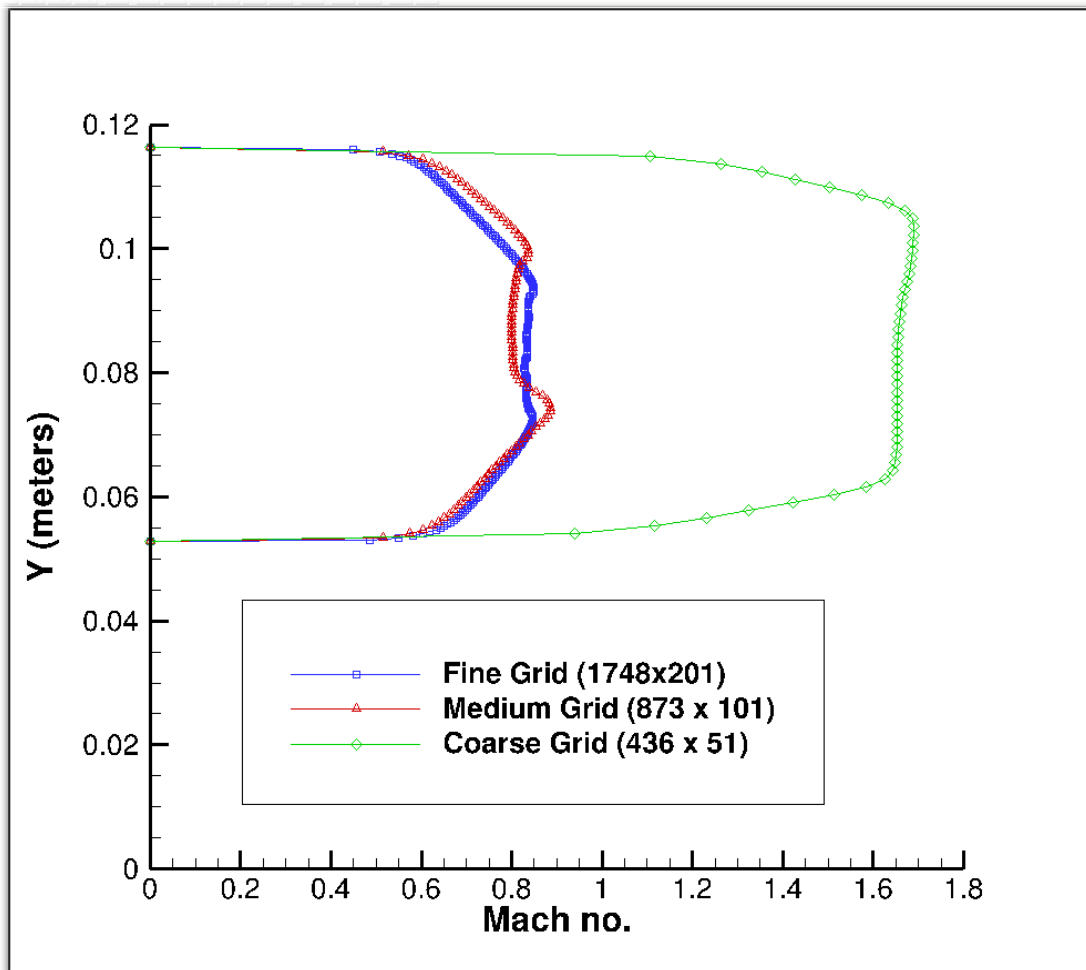


Figure 9. Boundary layer profile for Mach 1.8 nozzle/isolator

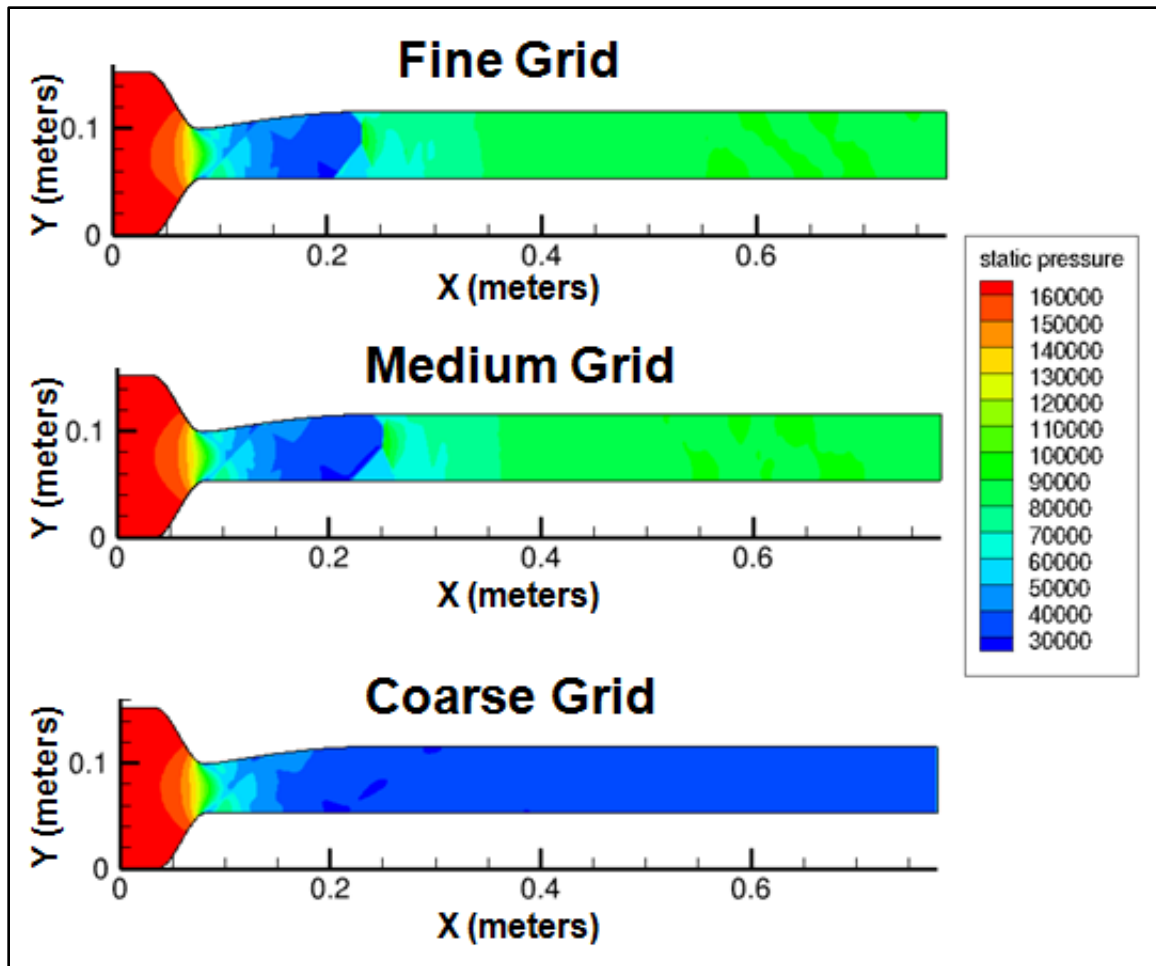


Figure 10. Grid comparison for nozzle/isolator (89.6 kPa back pressure)

Temporal Resolution Study

For a transient simulation, a temporal resolution study must be accomplished. Just as a grid independence study verifies a converged solution is independent of the grid, a temporal resolution study verifies the solution is independent of the time step. In the grid convergence study there were three grids of different densities to determine grid independence. Similarly, three different time steps were used to determine whether using a different time step would affect the results. Using time steps of 1.0×10^{-6} , 1.0×10^{-7} , and 1.0×10^{-8} seconds, a study was done where the back pressure of 89.6 kPa was applied instantaneously for 1 millisecond. For the 1.0×10^{-6} time step, the simulation diverged

after it started. The results of the other two time steps are shown in Figure 11. The results in Figure 11 are practically the same regardless of the time step. The difference in the leading edge at 1 millisecond (at approximately 0.45 meters on the x-axis) is just barely 1 millimeter. Since there is no significant difference between the two time steps, the time step of 1.0×10^{-7} seconds was used to save computer time.

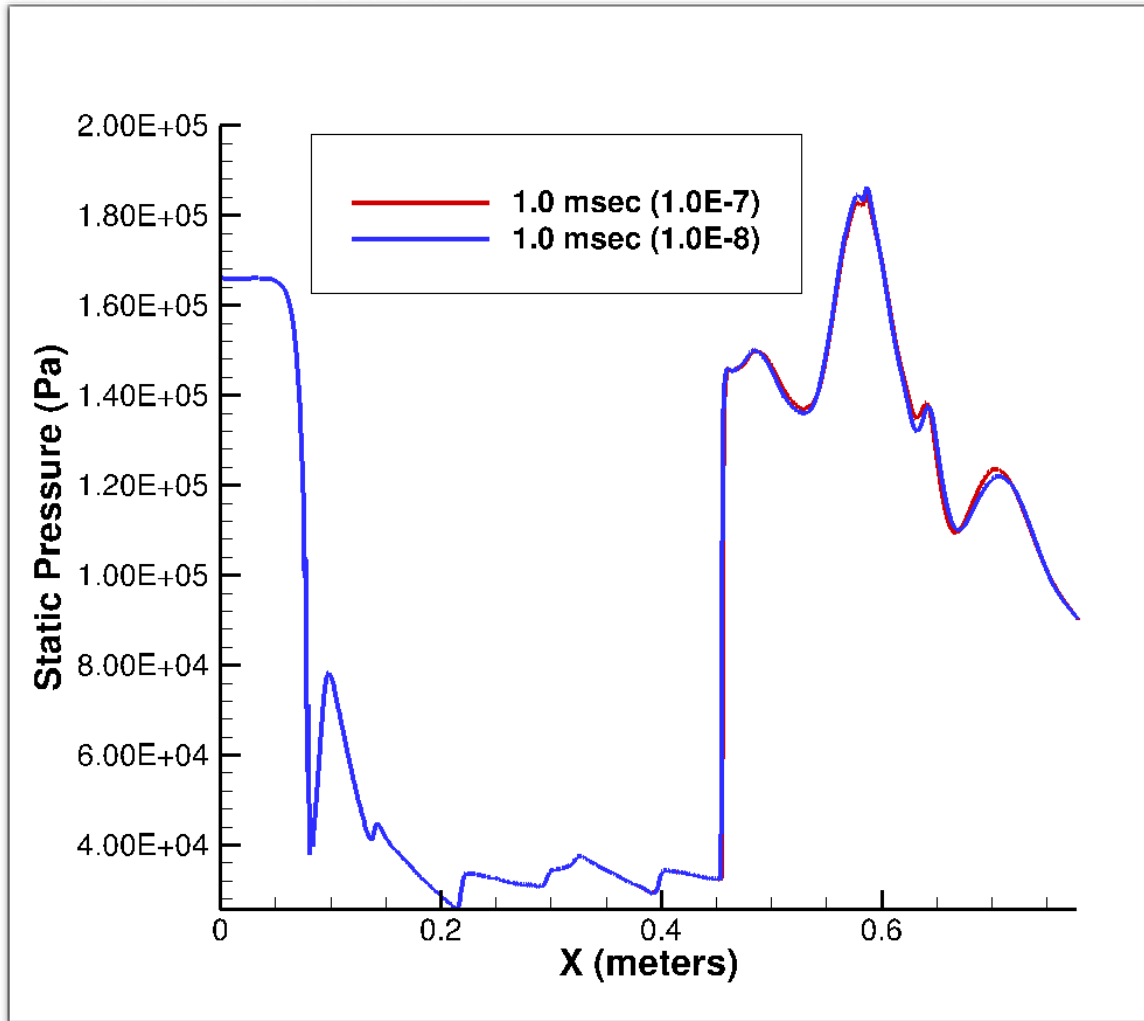


Figure 11. 2-D Temporal Resolution Results

Turbulence Model Comparison

As stated previously in the Governing Equations section, the choice of turbulence model affects the location of the shock train in the 2-D simulations. In Figure 12, a

comparison was done of the final locations of the leading edge of the shock train using the three turbulence models available in VULCAN at a back pressure of 89.6 kPa for an inflow pressure of 168.2 kPa. The Menter-SST model had the shock train furthest upstream in the isolator, followed by $k-\omega$ and Menter. As mentioned in the Literature Review section, the $k-\omega$ turbulence model works well for a turbulent boundary layer interacting with a shock wave, and the Menter-SST model combines the best features of both the $k-\omega$ and $k-\epsilon$ turbulence models for regions both close to and far away from the wall, respectively. In addition, the purpose of running these simulations is to determine how far the leading edge travels upstream in an isolator. Menter-SST would provide results using both the $k-\omega$ and $k-\epsilon$ models, and provide the most conservative results of how far the shock train went upstream in the isolator. Menter-SST was the best model to use in the 2-D simulations.

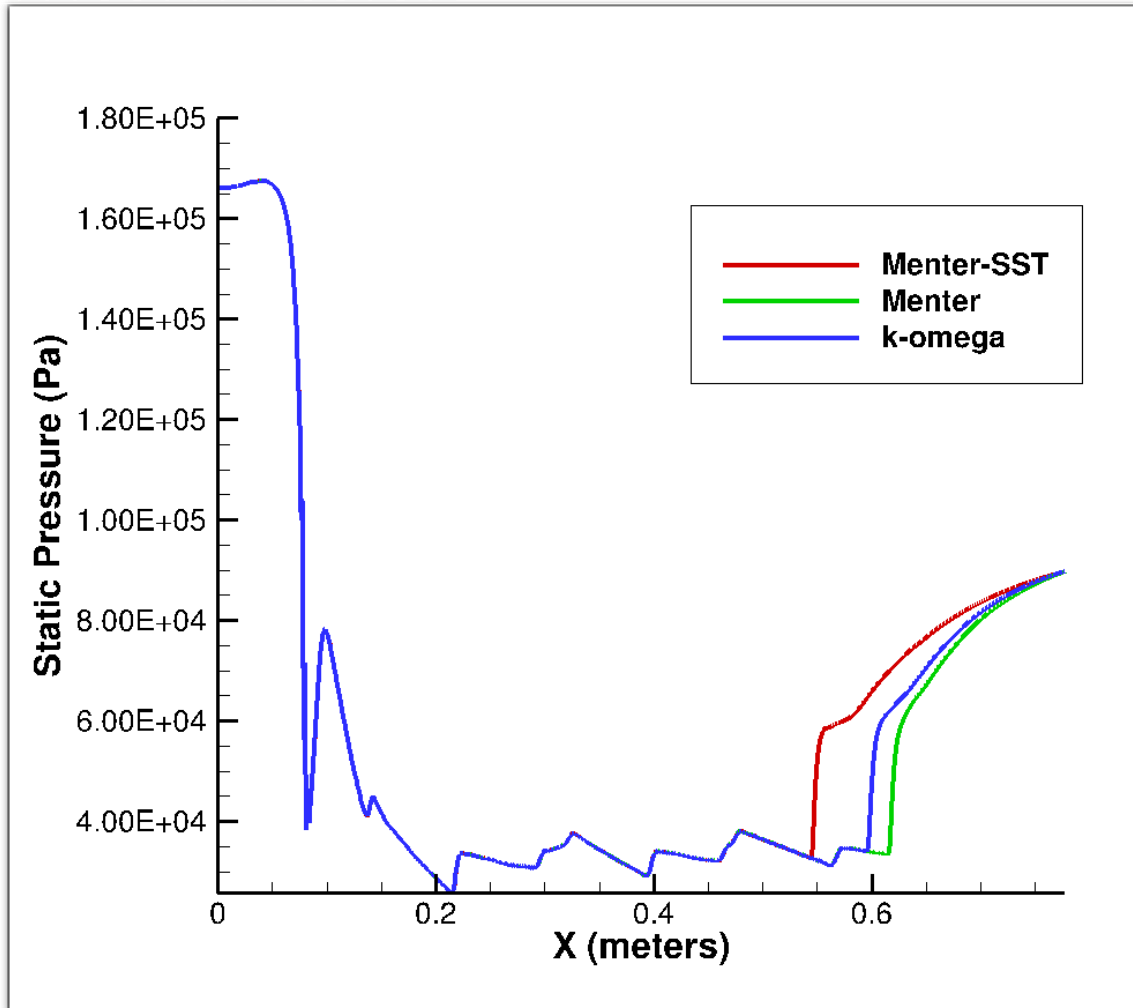


Figure 12. Comparison of Turbulence Models in 2-D

Instantaneous application of backpressure

Figure 13 shows the formation of a PCST and movement of the shock train at Mach 1.8 inlet flow for a back pressure of 89.6 kPa. The results in Figure 13 are shown after running the simulation for 10 milliseconds of steady flow, at which time a back pressure is instantaneously applied to the exit plane. After the back pressure is applied for 1 millisecond, the top panel in Figure 13 has the leading edge of the shock train at approximately 44 cm on the x-axis traveling upstream in the isolator. At 2.5 milliseconds (the second panel), the shock train is in the nozzle at 13 cm. The third panel, at 5

milliseconds, has the shock train at approximately the same location as at 2.5 milliseconds. In the next panel (7.5 milliseconds) the leading edge is further downstream at 20 cm in the isolator than its previous location at 5 milliseconds. The final panel has the leading edge location even further downstream at 10 milliseconds. These panels show that the shock train formed and traveled upstream to a location between 2.5 and 5 milliseconds, and then reversed direction and began moving downstream in the isolator. After the 10 milliseconds, the simulation continued with the results in Figure 14. The shock train continued moving downstream until 27 milliseconds, where the mass imbalance was now at -0.80%, below the 1% for stopping criteria. The simulation was then continued for another millisecond to confirm that the shock train location had not changed and that the mass imbalance was still less than 1% (-0.59% at 28 milliseconds). At 28 milliseconds, the simulation was terminated.

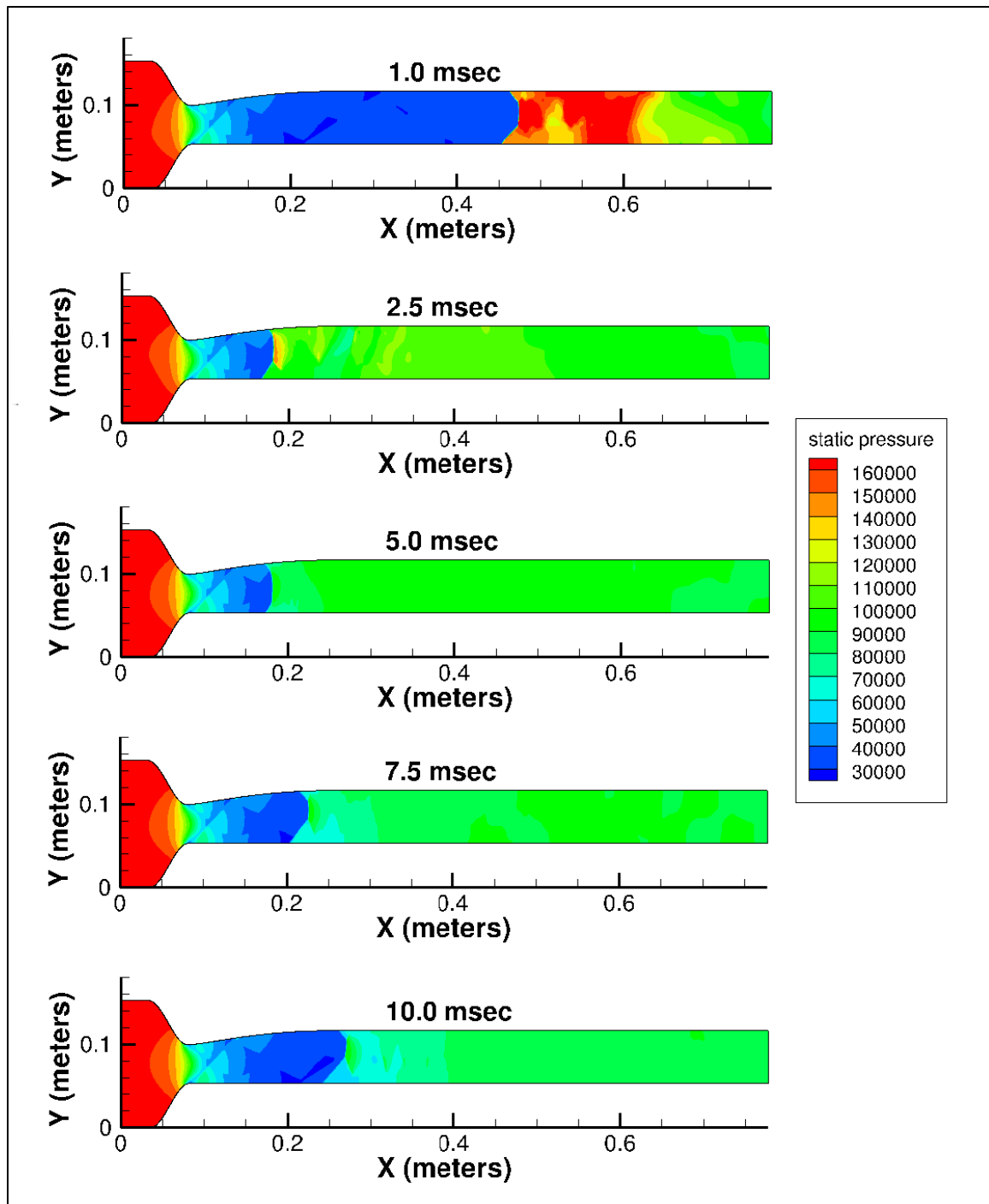


Figure 13. Evolution of PCST solution for instant 89.6 kPa back pressure

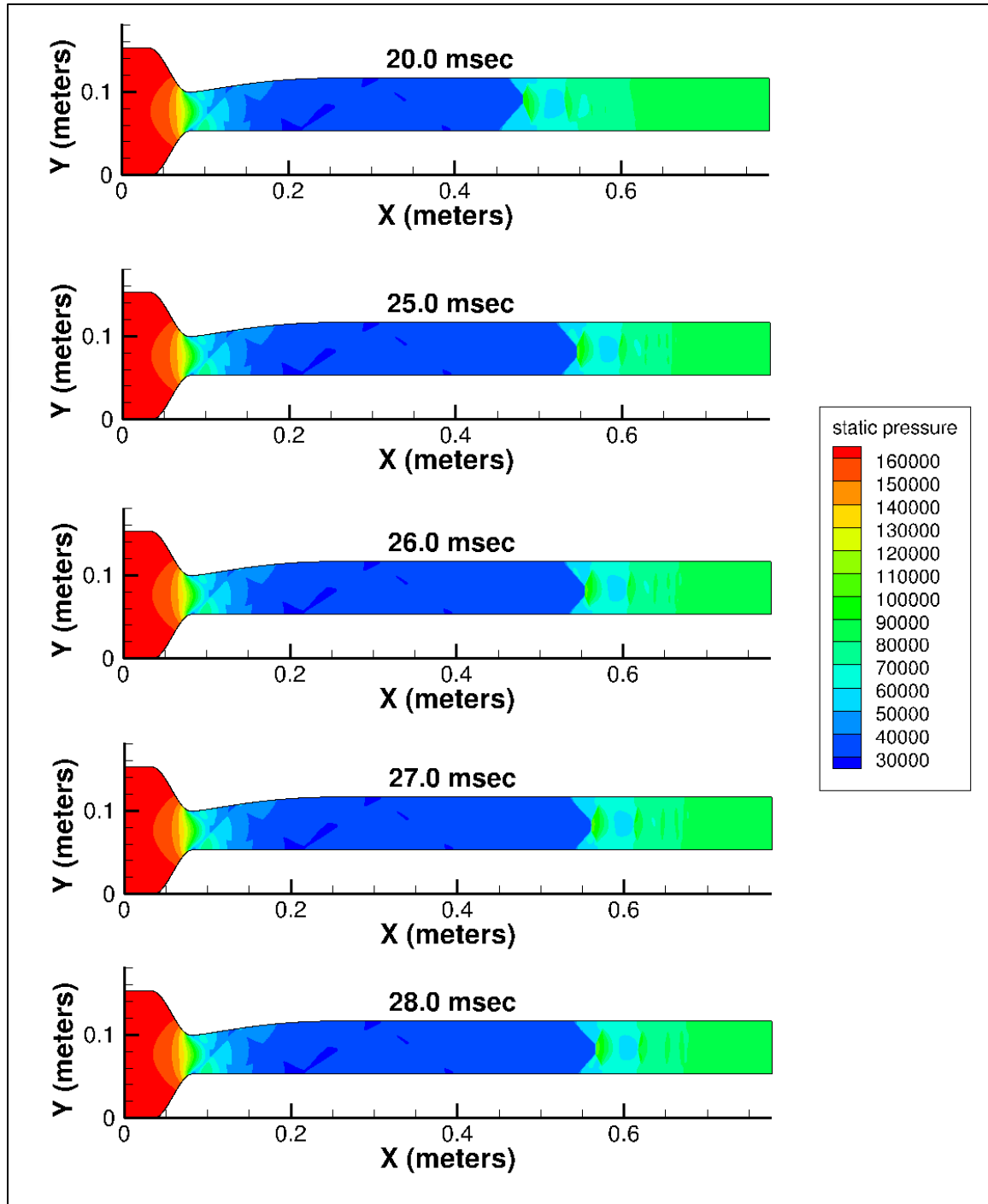


Figure 14. Evolution of PCST solution for instant 89.6 kPa back pressure continued

To examine the movement of the leading edge more closely, the time history of the simulation was analyzed. A baseline of the static pressure before application of the back pressure was needed to be established first so that the leading edge could be identified

and tracked through the simulation. Figure 15 shows the baseline static pressure distribution computed along the bottom of the isolator wall before the back pressure is applied. As corroborated in Figures 13 and 14, the pressure starts at approximately the same value as the inflow (168.2 kPa) and decreases through the nozzle and downstream through the isolator. There is a sharp pressure spike near the nozzle throat at 10 cm on the x-axis due to the geometry of the nozzle, and nothing can be done about neutralizing or removing the spike. This baseline will be used to identify the location of the leading edge of the shock train after the backpressure is applied.

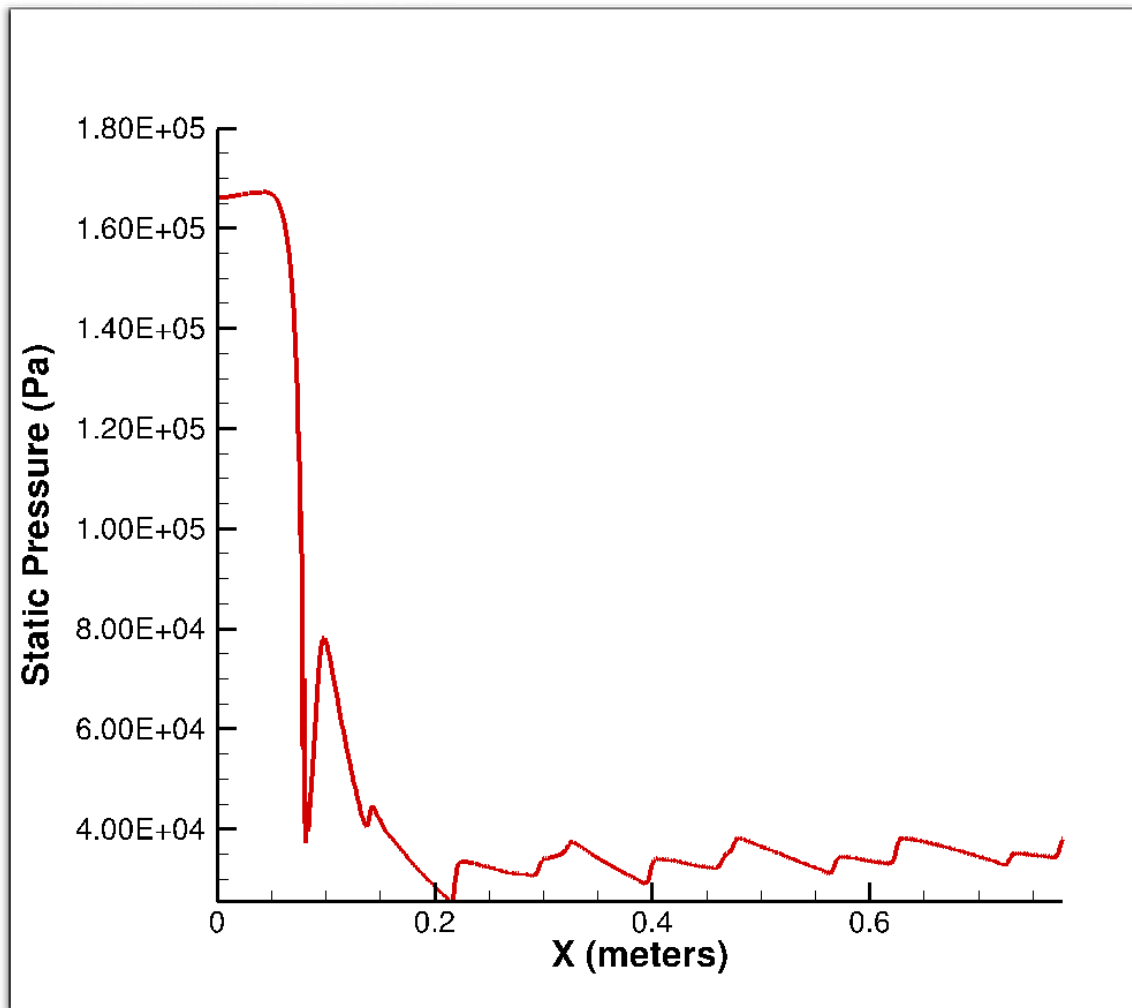


Figure 15. CFD static pressures along floor of nozzle/isolator

Figure 16 shows the static pressure time history after application of an instantaneous back pressure. The baseline static pressure profile from Figure 15 can be seen along the bottom of the graph. The time after application of the back pressure is shown starting at 0.1 milliseconds and going up to 1 millisecond. When the back pressure is applied, the PCST forms and starts moving upstream (to the left) in the isolator (indicated by the solid lines in this and subsequent graphs). The location of the leading edge of the shock train is where the line deviates (shown as a vertical line) from the baseline profile, indicating a sudden increase in pressure. At 0.1 milliseconds, the solid red line indicates a deviation at 77 cm on the x-axis. At 0.2 milliseconds, the solid orange line shows a deviation at 75 cm on the x-axis. The deviations continue every 0.1 milliseconds, where the leading edge and its location can be identified, until 1 millisecond, where the solid black line indicates a deviation at 46 cm on the x-axis. The results in Figure 16 show that the leading edge can be identified and tracked at specific times as it travels upstream through the isolator. Figure 16 shows the leading edge of the shock train forming at the downstream end of the isolator and starting to move upstream. Figure 17 is a close-up of Figure 16, focusing on the last 37 cm of the isolator. Using the information from these figures, the leading edge of the shock train has traveled 31 cm in 0.9 millisecond (from 77 cm at 0.1 milliseconds to 46 cm at 1 millisecond) the velocity of the shock train can be calculated. In this simulation, it was initially traveling at a speed of ~344 m/s.

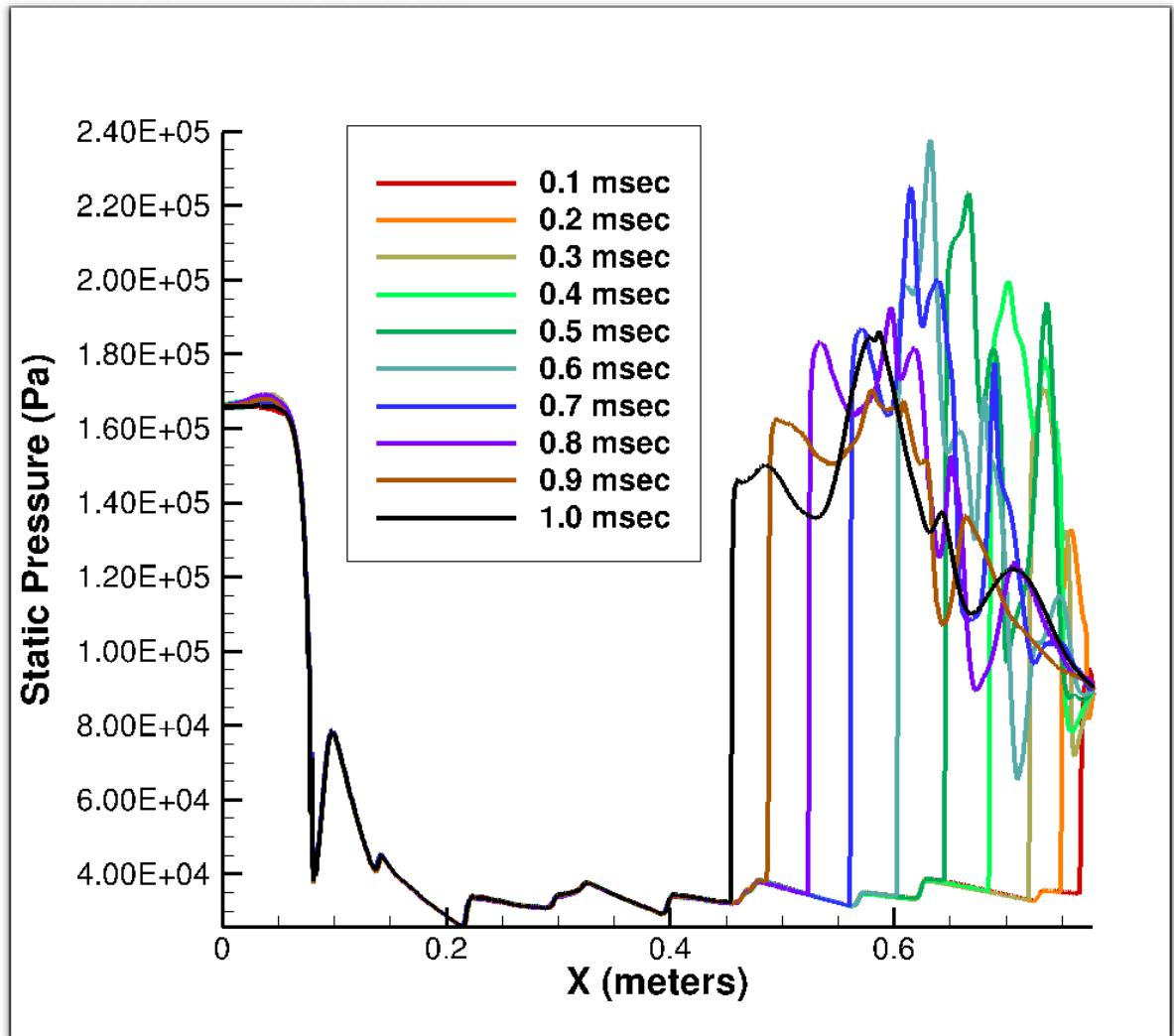


Figure 16. Time history of static pressures after 89.6 kPa back pressure applied

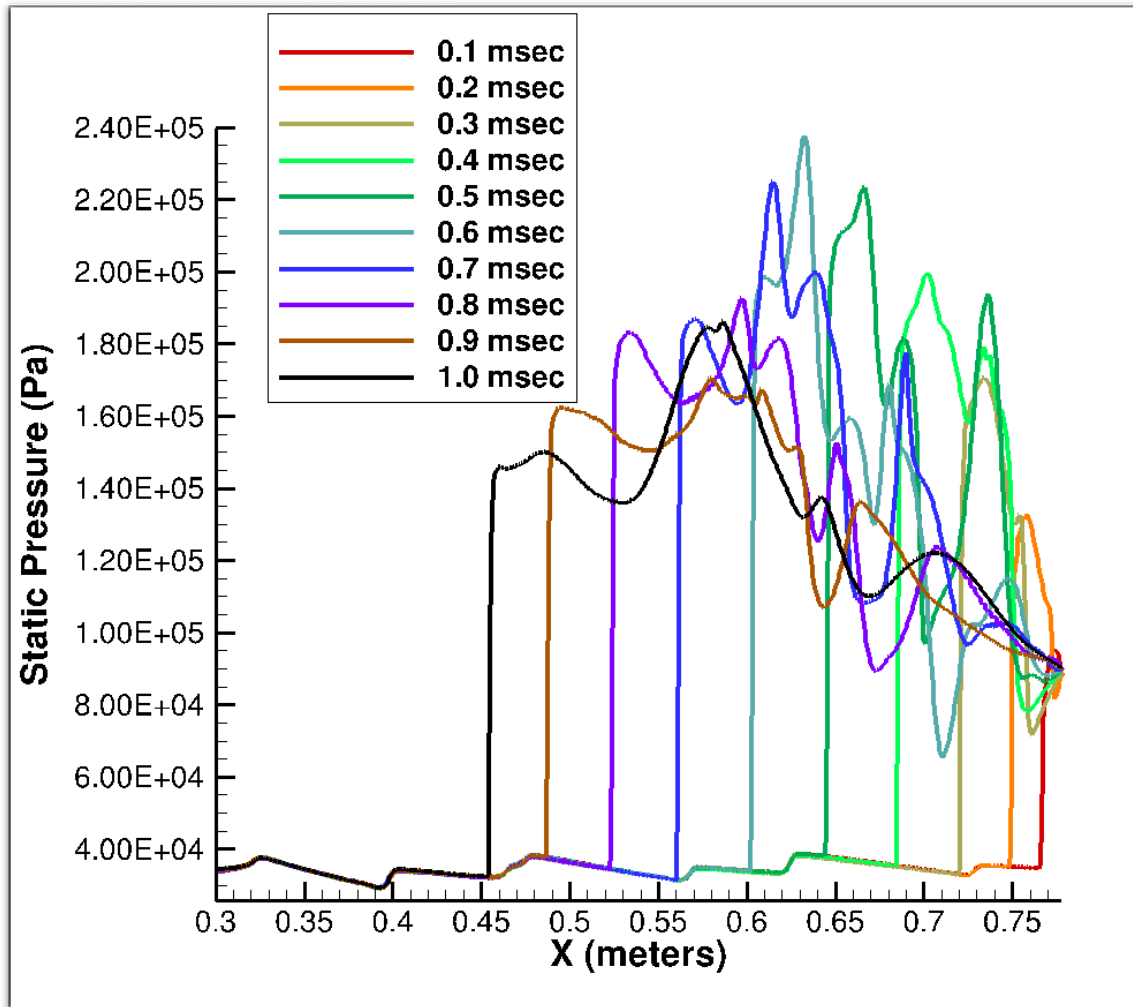


Figure 17. Close-up view of static pressures after 89.6 kPa back pressure applied

Figure 18 shows the shock train movement from 1 to 3 milliseconds. In Figures 16 and 17, the solid black line indicates the location of the leading edge after instantaneous application of the back pressure at 1 millisecond. In Figure 18, the solid red line is that same line. Figure 18 displays the continuing upstream movement of shock train, ending at 3.2 milliseconds (15.2 cm). Analysis of the time history showed this is the farthest upstream location the shock train traveled before reversing direction and beginning its downstream movement. Figure 19 continues the time history showing the shock train moving downstream (to the right, indicated by the dash-dot lines in this and subsequent

graphs) in the isolator until 28 milliseconds, where it meets the stopping criteria identified previously in Fig 14. To summarize the results of Figures 16-19, after instantaneous application of the 89.6 kPa back pressure, the shock train traveled upstream in the isolator, then reversed direction and traveled back downstream to its final location. The location of the shock train can be identified at any point during the simulation, and the velocity can be calculated based on that information. The initial movement upstream was the response for an instantaneously applied back pressure as the shock train formed, adjusted, and eventually reached its final location and met the stopping criteria.

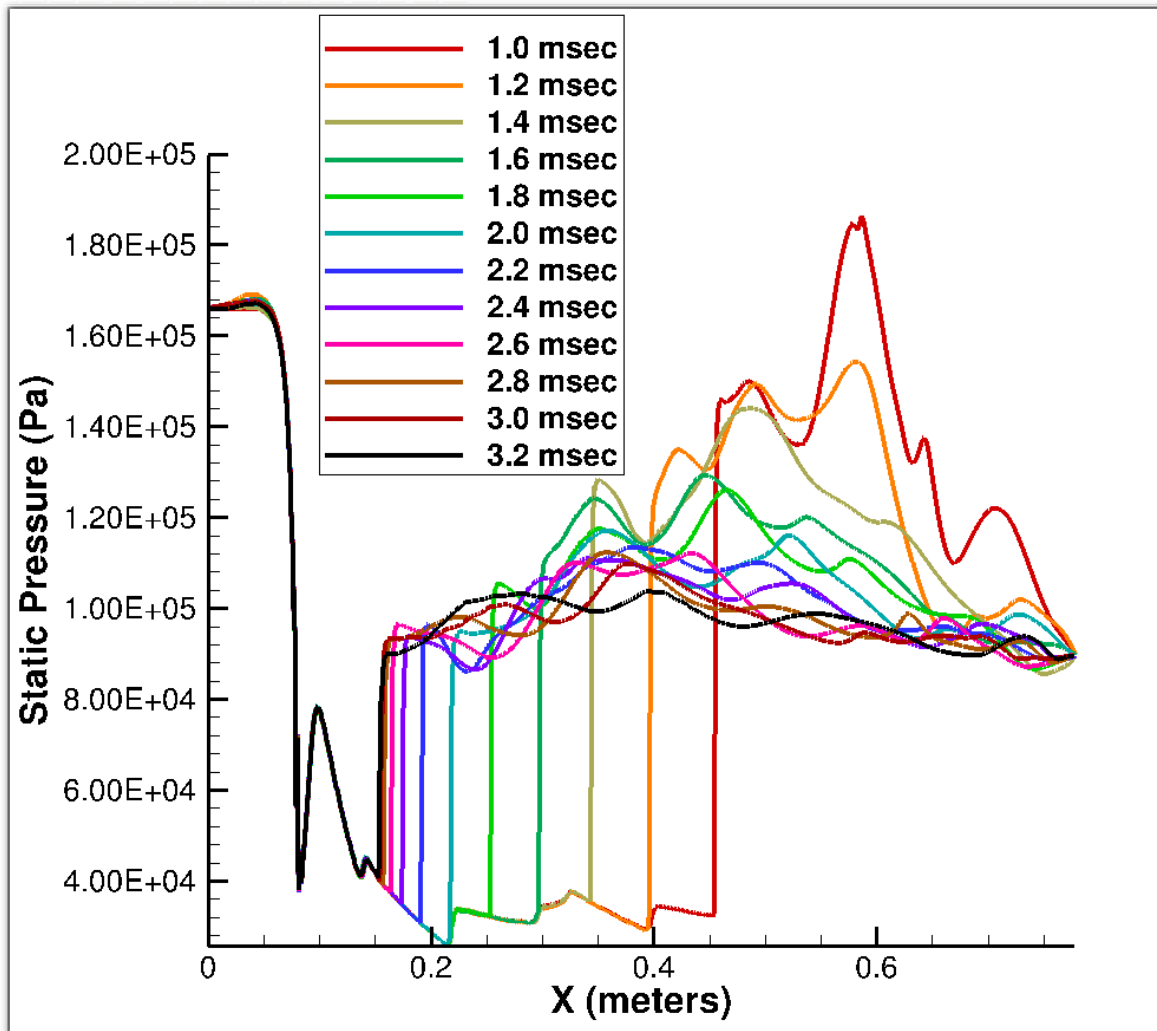


Figure 18. Time history of static pressure after 89.6 kPa back pressure applied

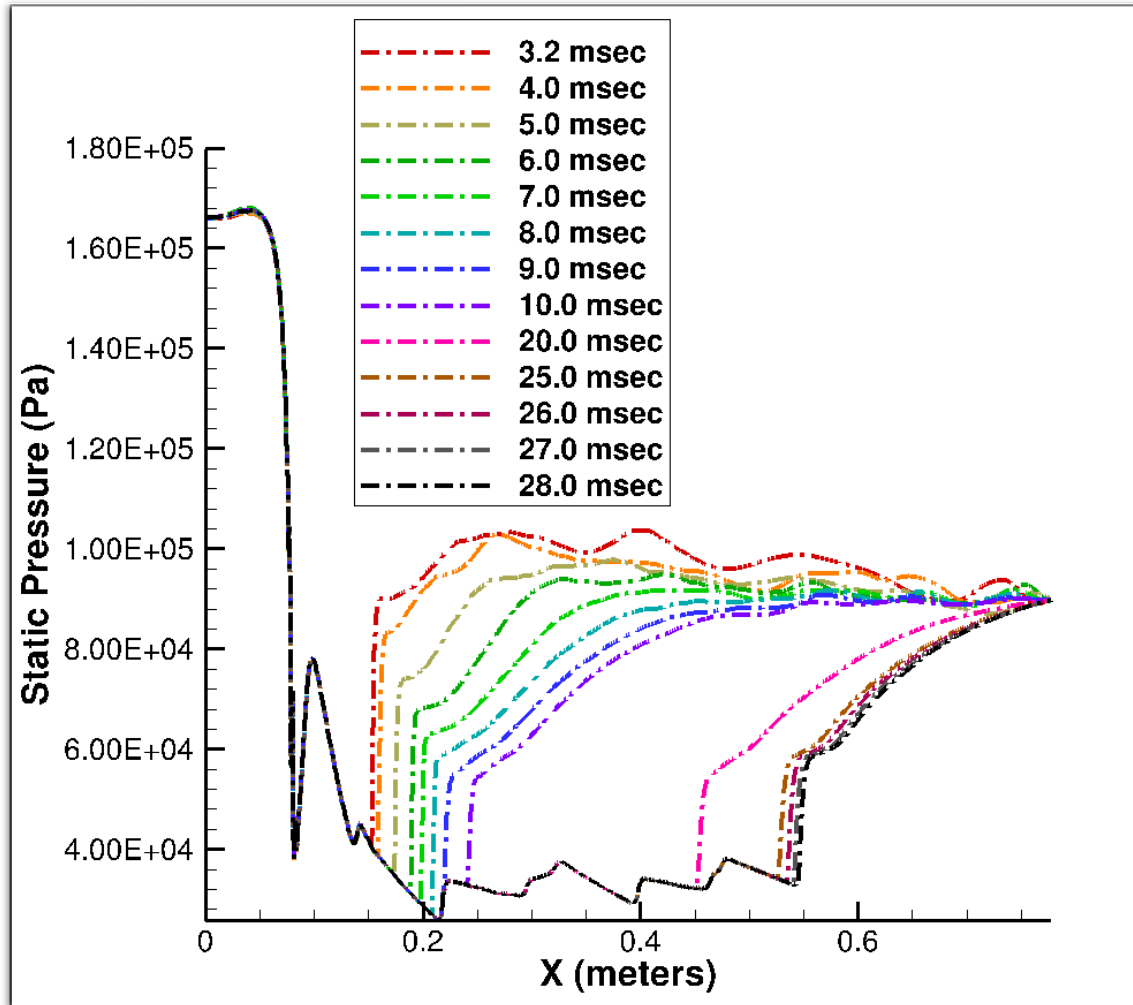


Figure 19. Solution evolution to shock stability for 89.6 kPa back pressure applied

The simulation with 168.2 kPa inflow pressure was run for two other instantaneously applied back pressures. Figure 20 displays the formation and movement of a PCST resulting from the instantaneous application of a back pressure of 85.0 kPa, for a back to inflow pressure ratio of 0.506 (smaller than the 89.6 kPa case, which had a ratio of 0.533). The panels show the same pattern as with the 89.6 kPa simulation of the shock wave traveling upstream in the isolator after the back pressure is applied, reaching the location furthest upstream sometime between 2.5 and 5 milliseconds before reversing

direction and moving downstream. Figure 21 displays the continuation of the simulation until the stopping criteria is met at 23 milliseconds.

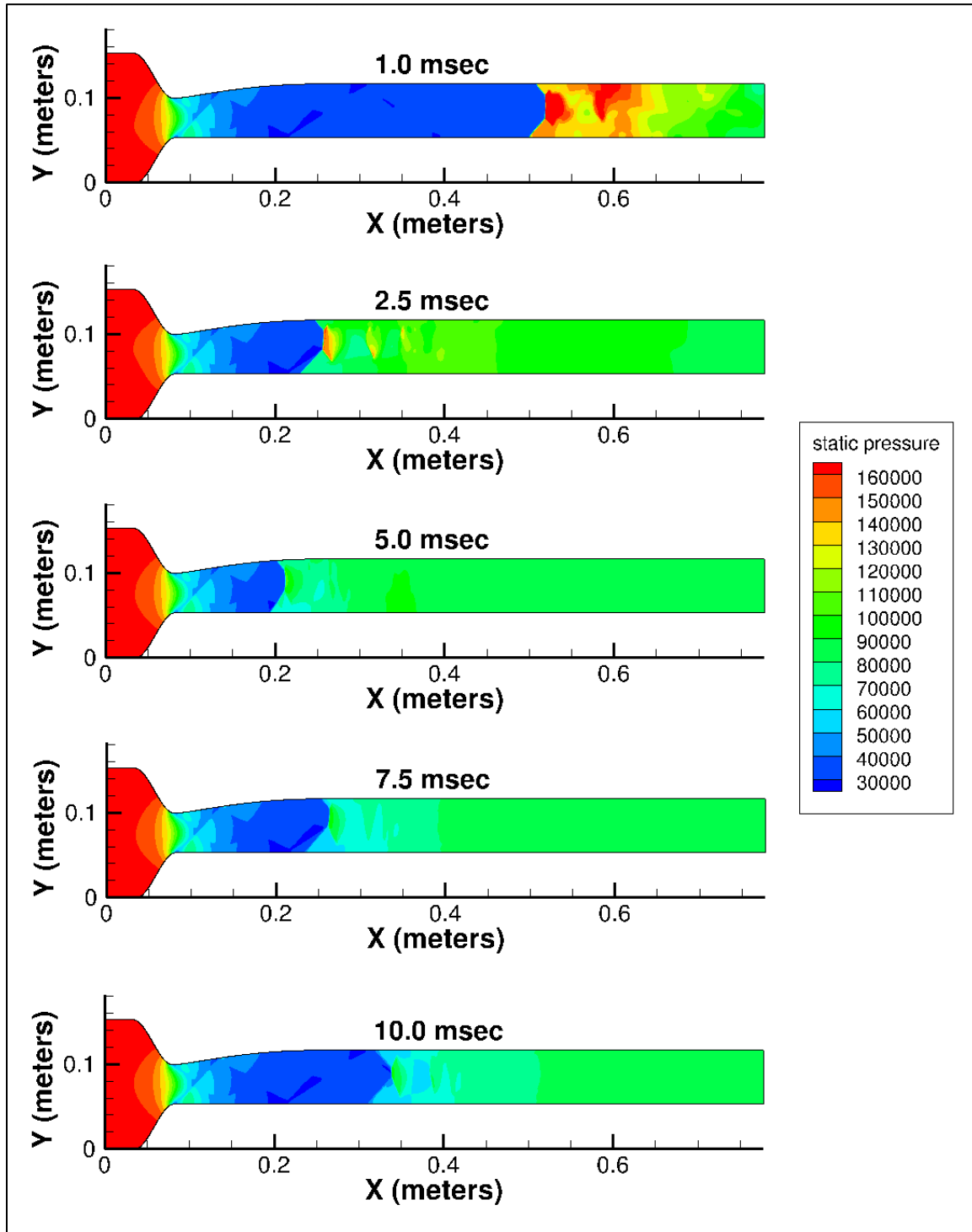


Figure 20. Evolution of PCST solution for instant 85.0 kPa back pressure

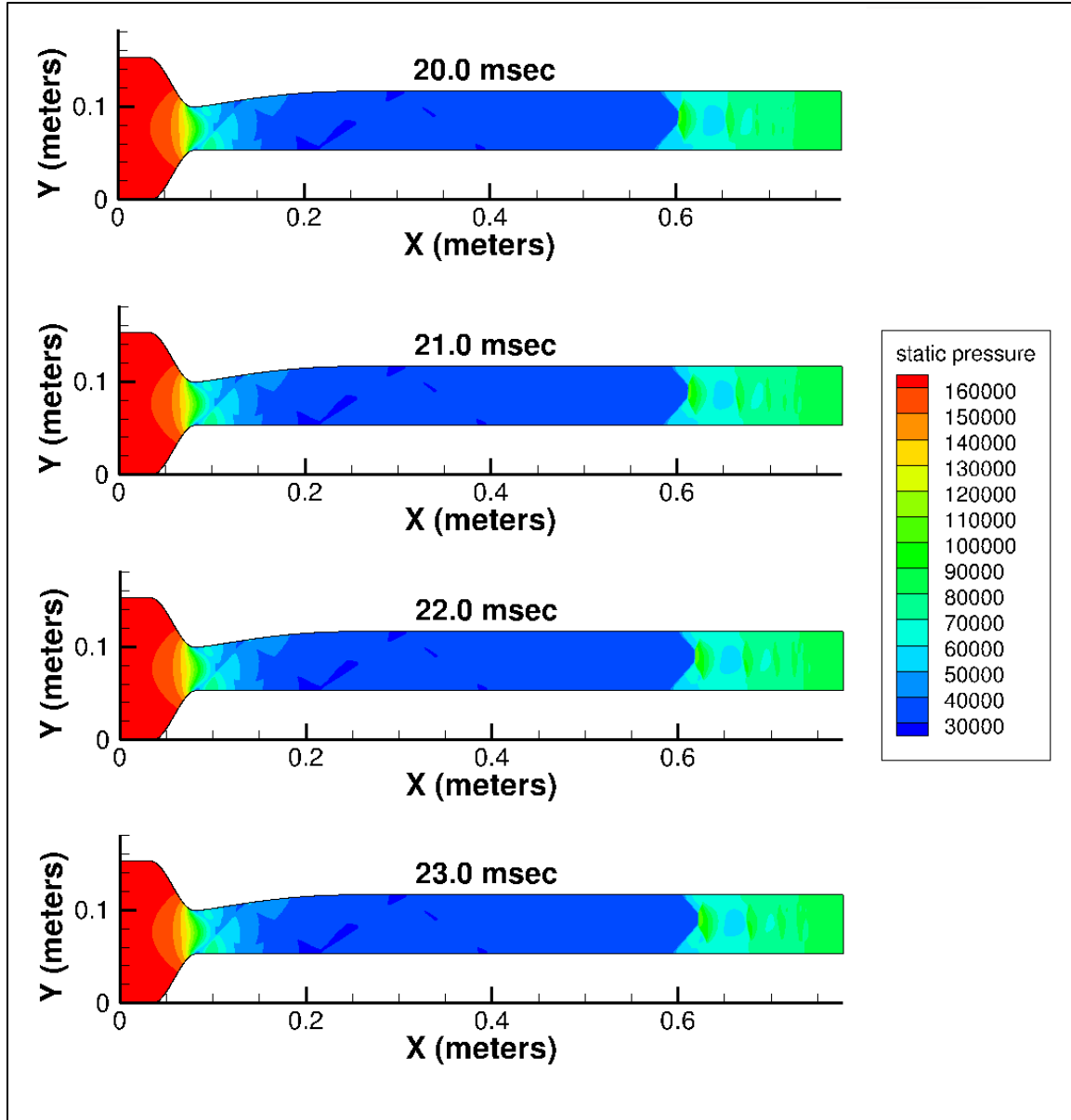


Figure 21. Evolution of PCST solution for instant 85.0 kPa back pressure continued

Figure 22 presents the static pressure time history along the bottom of the isolator after application of the 85.0 kPa back pressure. The bottom of the isolator was used since the leading edge of the shock train in Figures 20 and 21 was farther upstream than the isolator top. The same baseline static pressure profile from Figure 15 is seen again. The time history is shown from 1 to 23 milliseconds after application of the back pressure at different time intervals to identify both the furthest location upstream and the final

location. The shock train formed and moved upstream (the solid lines) until 3.8 milliseconds (the furthest identified location upstream at 18.1 cm) before reversing direction. It then traveled back downstream (dash-dot lines) until 23 milliseconds where it reached the stopping criteria.

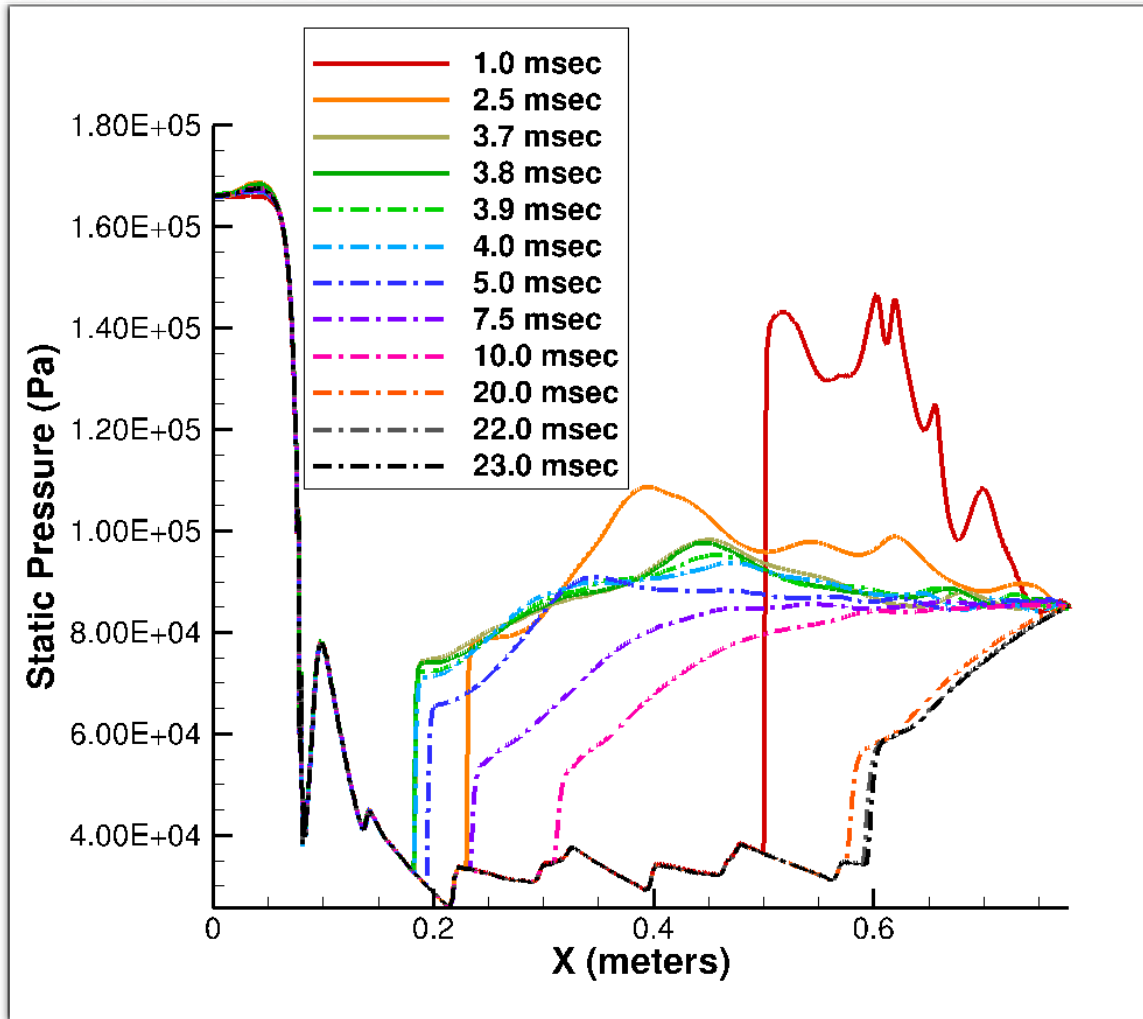


Figure 22. Time history of static pressure after 85.0 kPa back pressure applied

Figures 23 and 24 show the movement of the PCST for a back pressure of 75.0 kPa. Figure 23 has the shock wave traveling upstream in the isolator through 2.5 milliseconds. At 5 milliseconds the leading edge is already moving back downstream, indicating the furthest point upstream occurred sometime between 2.5 and 5 milliseconds. Figure 24

continues the simulation, with the shock train moving downstream until reaching the stopping criteria at 13.0 milliseconds.

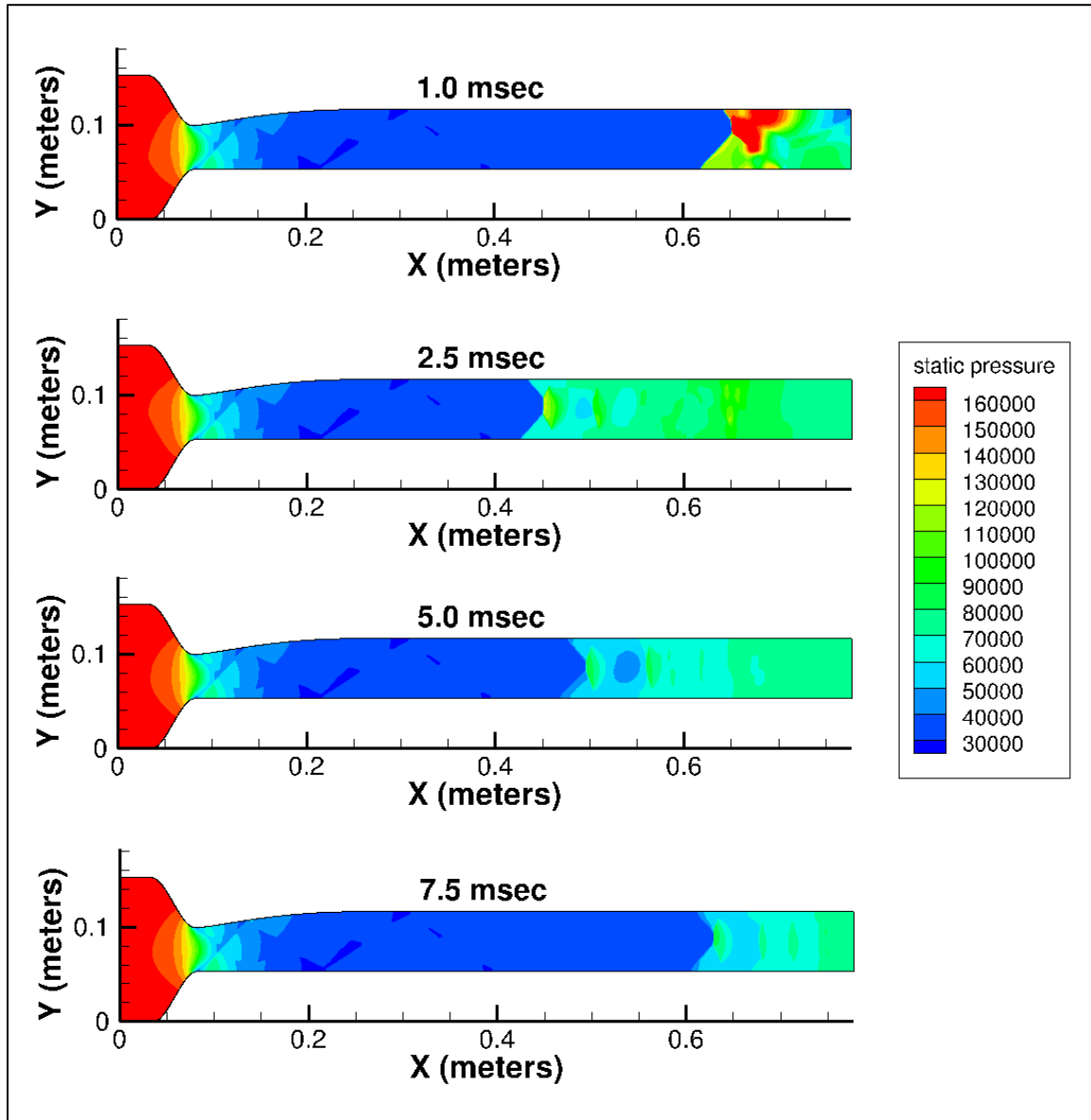


Figure 23. Evolution of PCST solution for instant 75.0 kPa back pressure

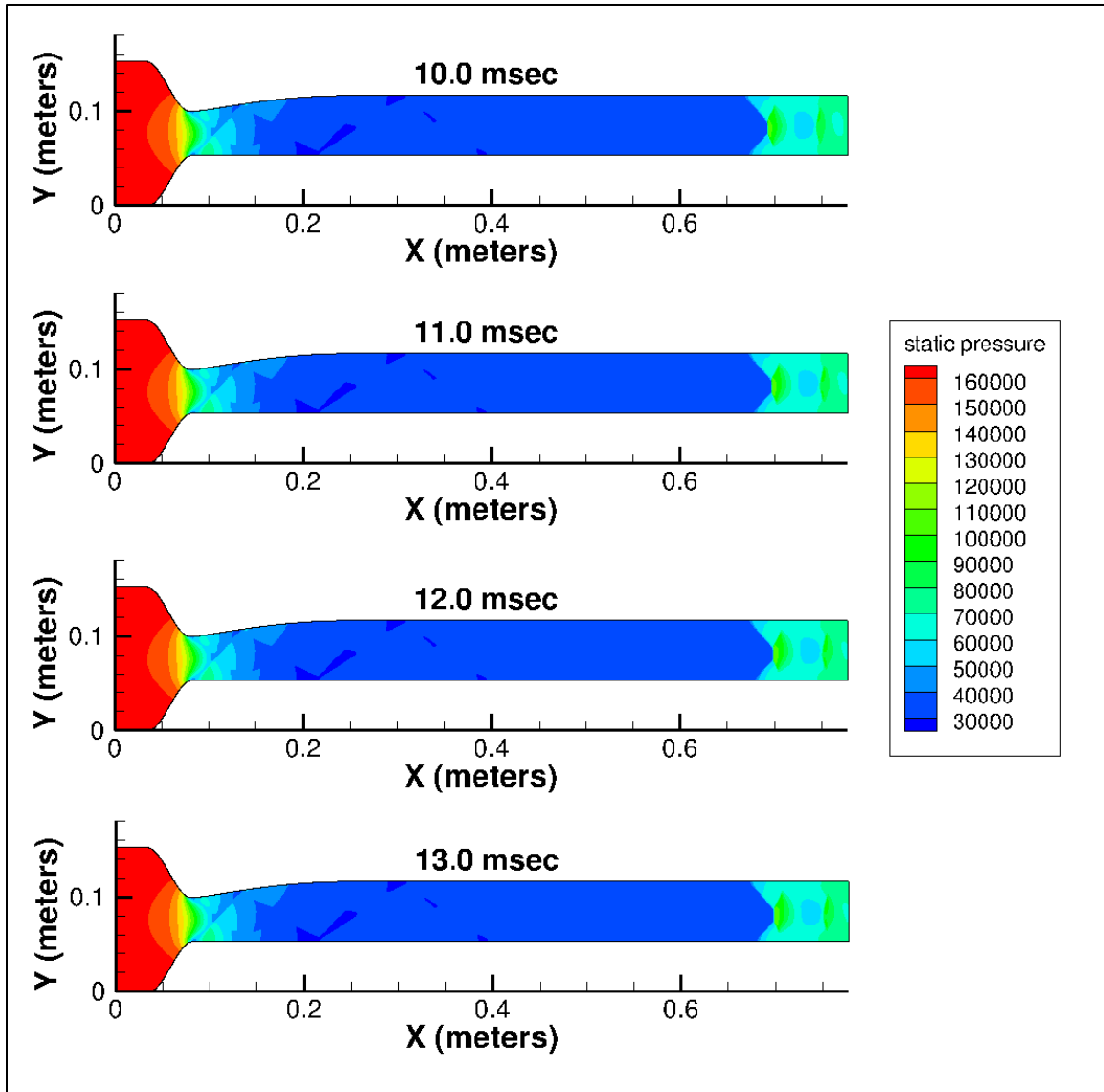


Figure 24. Evolution of PCST solution for instant 75.0 kPa back pressure continued

Figure 25 shows static pressure time history after application of the 75.0 kPa back pressure. The time history is shown from 1-13 milliseconds in varying time intervals to identify both the furthest location upstream and the final location. Figure 25 shows the shock train moving upstream until 2.9 milliseconds, and then traveling back downstream until 13 milliseconds.

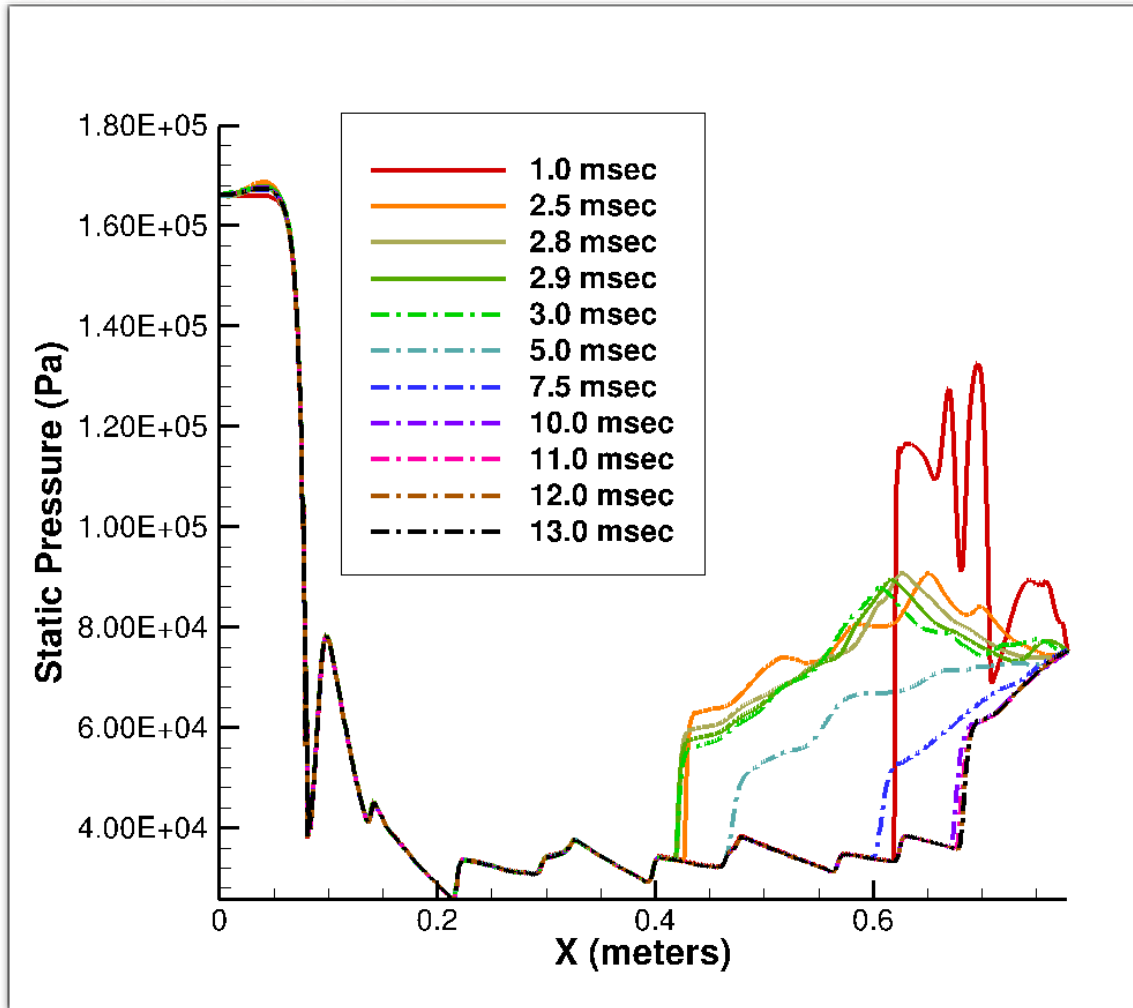


Figure 25. Time history of static pressure after 75.0 kPa back pressure applied

In all 3 cases with different back pressures (89.6 kPa, 85.0 kPa, and 75.0 kPa) and respective back pressure to inflow pressure ratios (0.533, 0.506, and 0.466), the shock train formed, traveled upstream and then reversed direction and traveled back downstream to a final location. In the simulation with the 89.6 kPa back pressure (a 0.533 ratio), the shock train traveled upstream to 15.2 cm and then traveled back downstream and ended at its final location at 54.3 cm. In the 85.0 kPa simulation (0.506 ratio), the shock train traveled upstream to 18.1 cm and then downstream to 59.2 cm while in the 75 kPa simulation (0.446 ratio), the shock traveled upstream to 41.7 cm and then

downstream to 67.8 cm. In summary, as the back to inflow pressure ratio decreases, the shock train reversal and final locations were farther downstream.

Three more simulations were performed for an inflow total pressure of 140.6 kPa while the back pressures of 75.0, 71.1 and 62.78 kPa were applied instantaneously. The ratios of back pressure to total inflow pressure in these next three cases were the same as the previous three cases just presented for the inflow pressure of 168.2 kPa, as shown in Table 1.

The formation of a PCST and movement of the shock train for an inflow total pressure of 140.6 kPa and back pressure of 75.0 kPa are shown in Figures 26 and 27. Figure 26 displays the shock wave traveling upstream in the isolator through five milliseconds. At 7.5 milliseconds, the leading edge is further downstream from where it was at five milliseconds, indicating the furthest point upstream occurred sometime between 2.5 and 5 milliseconds. Figure 27 continues the simulation, with the shock train moving downstream until reaching the stopping criteria at 31 milliseconds. The pattern and profile of Figures 26 and 27 is similar in terms of movement and time as the ones seen in Figures 13 and 14. The reason for these movement and time similarities is because the ratio of back to total inflow pressure (0.533) was the same as the simulation presented in Figures 13 and 14.

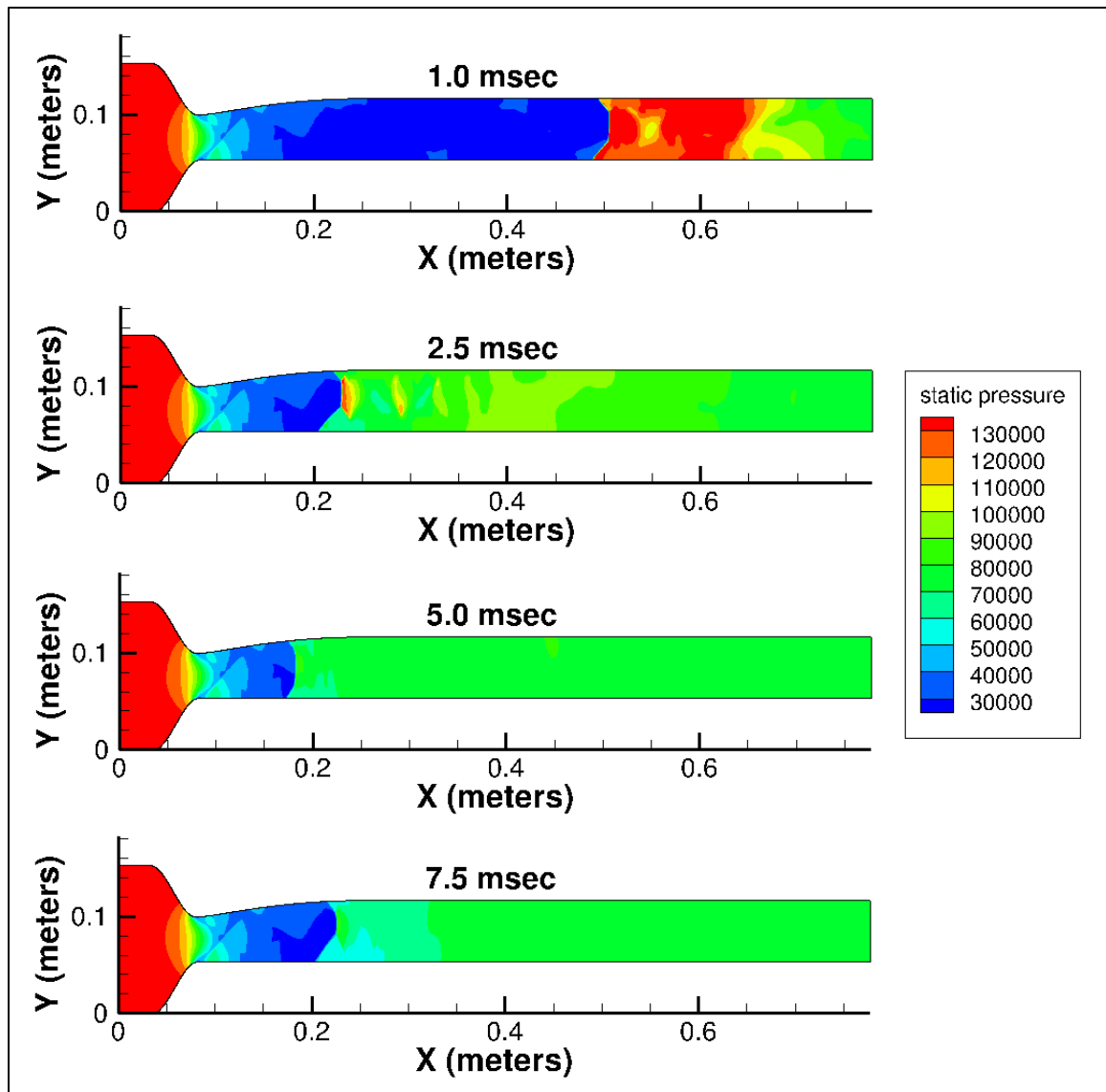


Figure 26. Evolution of PCST solution for instant 75.0 kPa back pressure (140.6 kPa inflow)

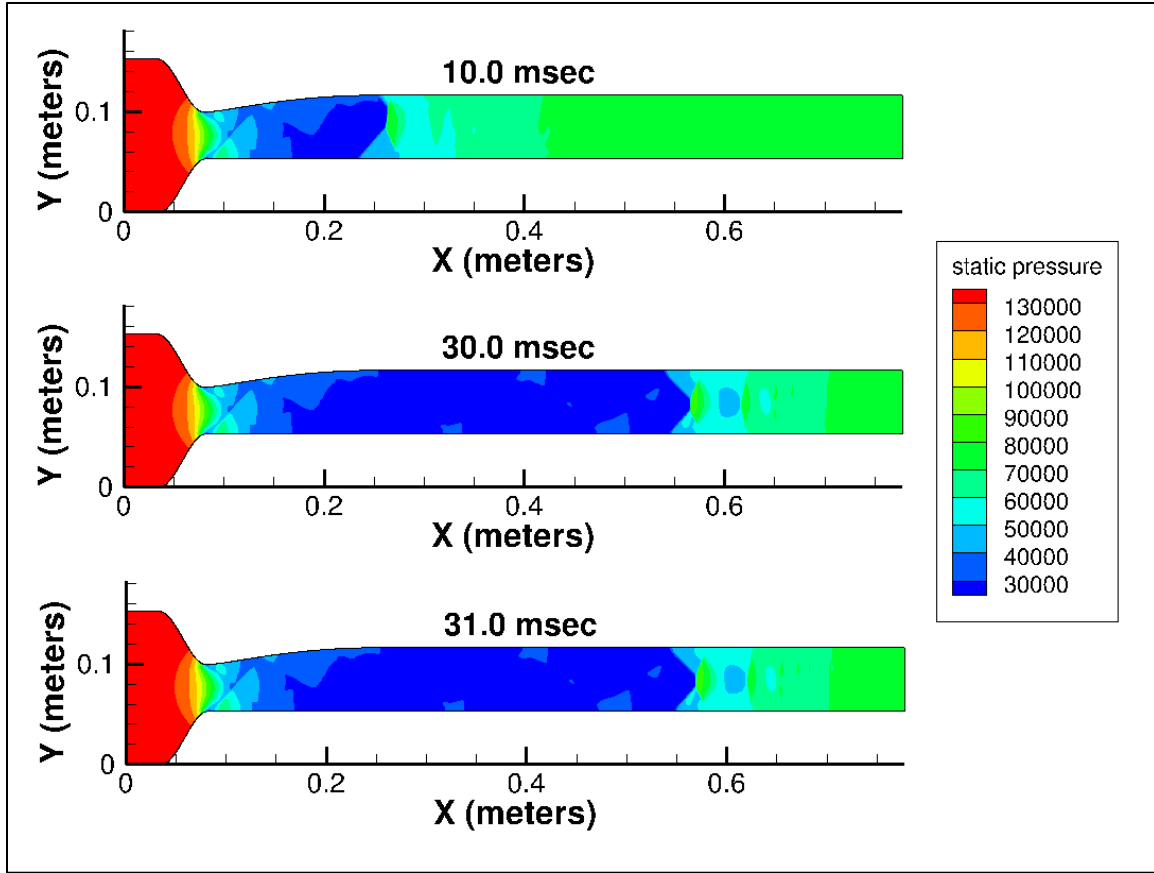


Figure 27. Evolution of PCST solution for instant 75.0 kPa back pressure continued (140.6 kPa inflow)

Figure 28 shows static pressure time history after instantaneous application of 75.0 kPa back pressure. The same baseline profile from Figure 15 is clearly visible again along the bottom of the graph. The time history is shown from 1 to 31 milliseconds after the back pressure is applied. Figure 28 shows the shock train forming and moving upstream (solid lines), to its furthest location upstream (16.5 cm at 4.1 milliseconds) and then moving downstream (dash-dot lines) until it reaches the stopping criteria (54.6 cm at 31 milliseconds). A comparison of these results with the ones for an inflow pressure of 168.2 kPa and a back pressure of 89.6 kPa in Figures 16-19 has different pressure values, but the same pattern and profile for PCST movement. In the 89.6 kPa case, the farthest upstream the leading edge reaches is 15.2 cm, while here it is 16.5 cm (a 1.3 cm

difference). The final location for the 89.6 kPa simulation was 54.3 cm while here it is 54.6 cm (a 0.3 cm difference).

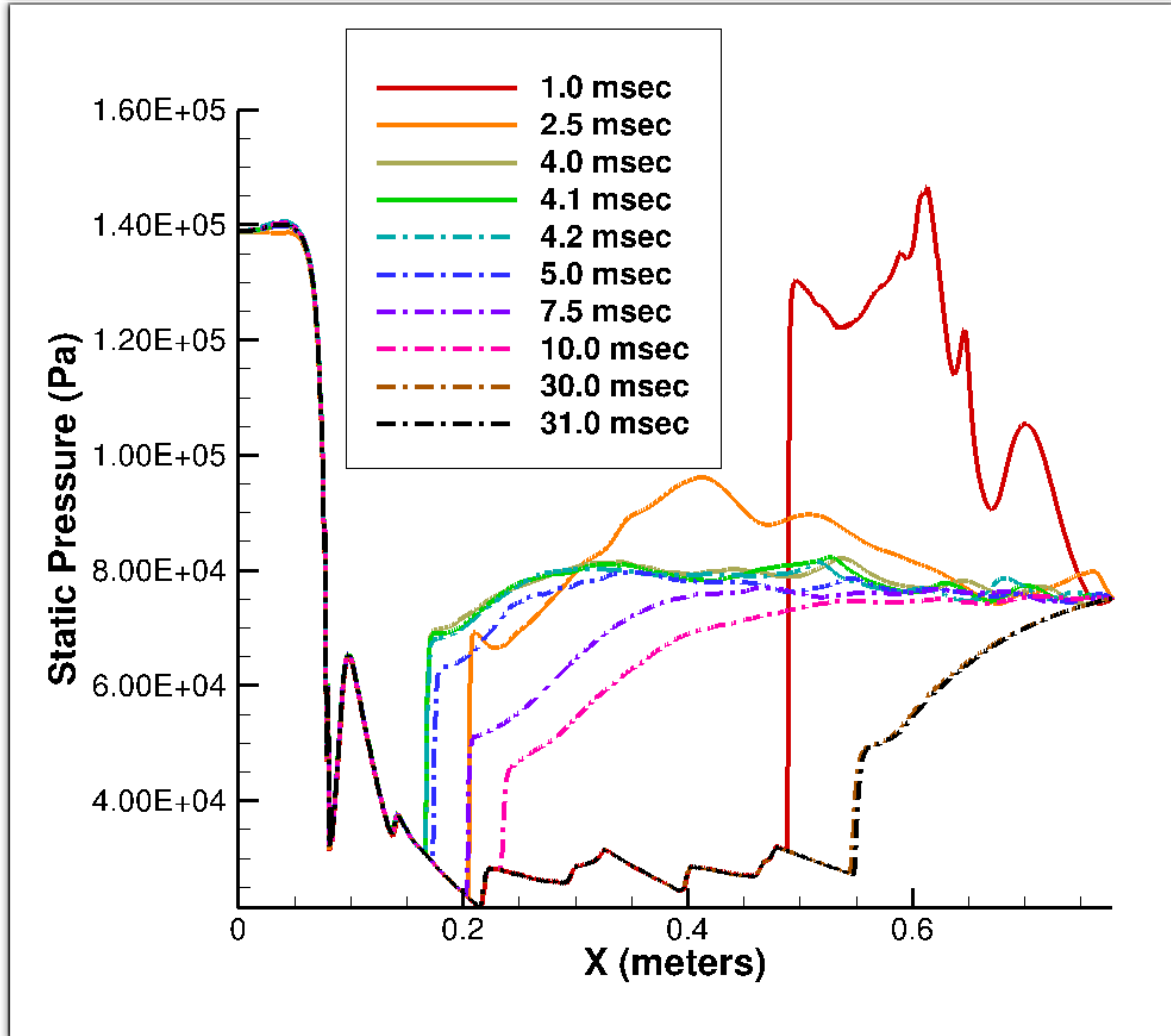


Figure 28. Time history of static pressure after 75.0 kPa back pressure applied (140.6 kPa inflow)

Figures 29 and 30 have the formation and movement of a PCST with a back pressure of 71.1 kPa for an inflow of 140.6 kPa, resulting in a back to inflow pressure ratio of 0.506 (the same as a back pressure of 85.0 kPa for an inflow of 168.2 kPa). Figure 29 shows the shock wave traveling upstream, again indicating the furthest point upstream occurred sometime between 2.5 and 5 milliseconds. Figure 30 continues the simulation,

with the shock train moving downstream until reaching the stopping criteria at 24 milliseconds.

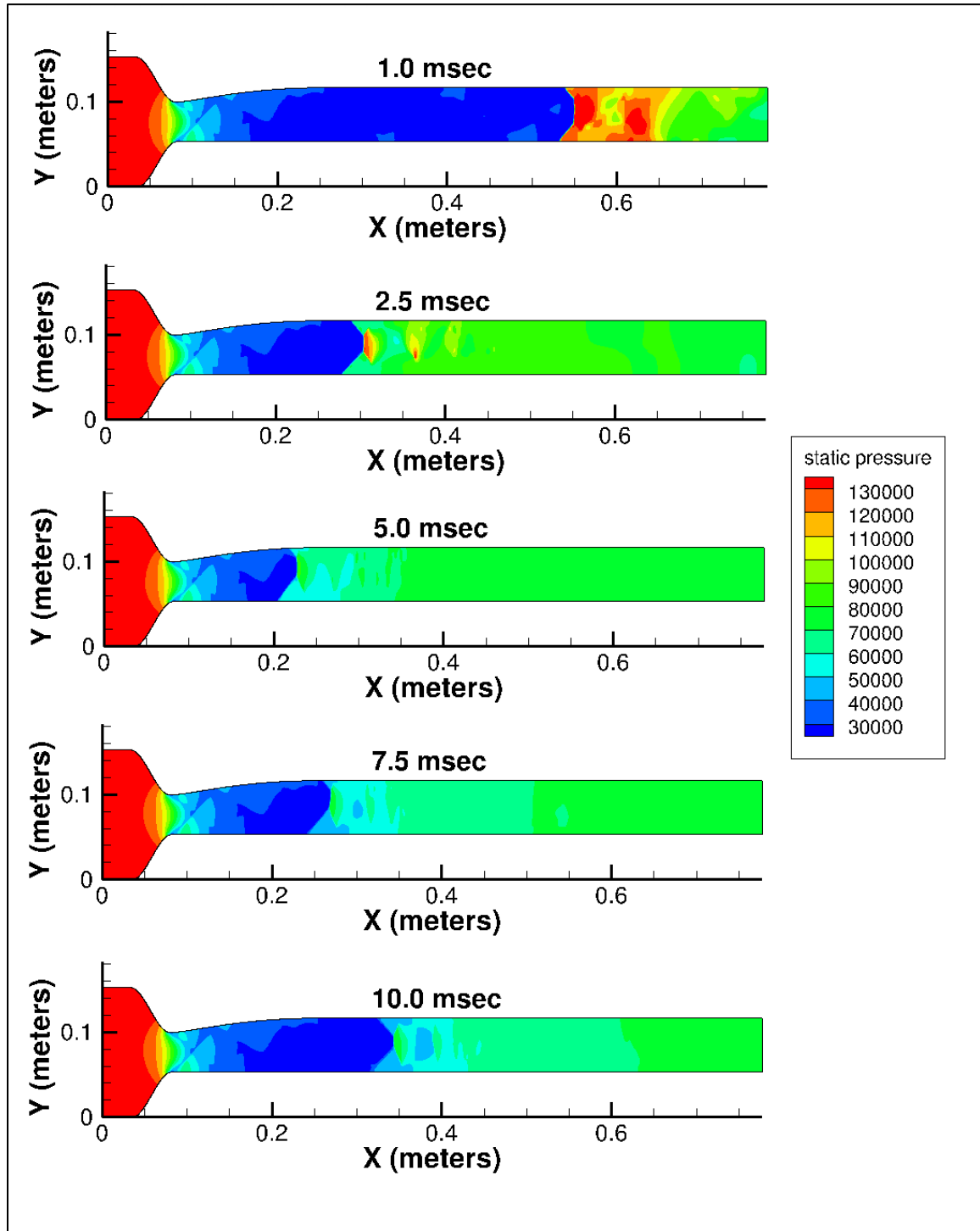


Figure 29. Evolution of PCST solution for instant 71.1 kPa back pressure

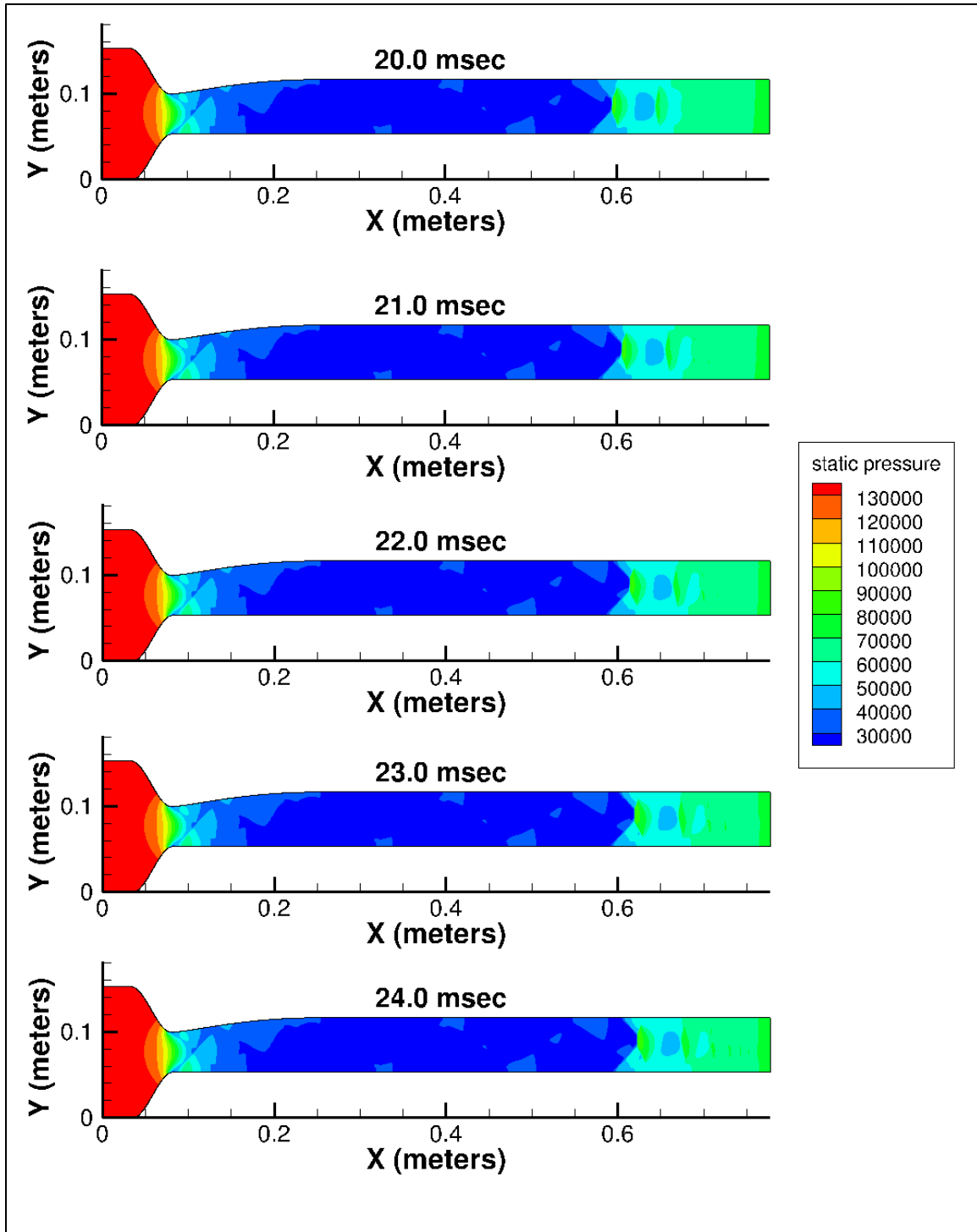


Figure 30. Evolution of PCST solution for instant 71.1 kPa back pressure continued

Figure 31 displays the static pressure time history for the 71.1 kPa back pressure simulation. The time history is shown from 1 to 24 milliseconds after the back pressure

is applied. It shows the shock train moving upstream to its furthest location upstream (20.0 cm at 4.4 milliseconds) and then moving downstream until it reaches the stopping criteria (59.3 cm at 24 milliseconds). A comparison of these results with Figure 22 for the back pressure simulation of 85.0 kPa shows a 1.9 cm difference between the farthest upstream locations of the leading edge, and a 0.1 cm difference in its final location.

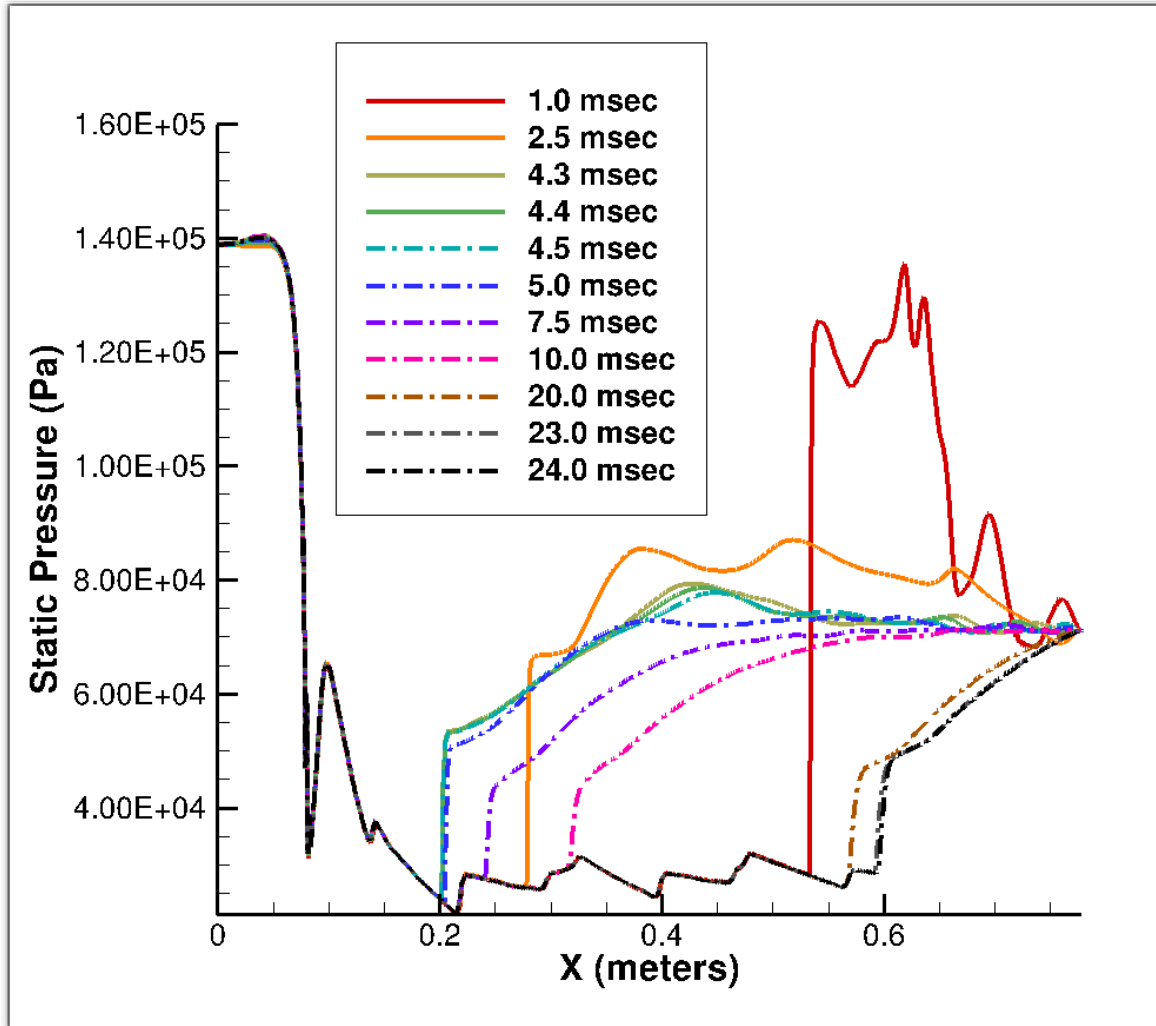


Figure 31. Time history of static pressure after 71.1 kPa back pressure applied

The final simulation for a back pressure of 62.78 kPa is shown in Figures 32 and 33. Figure 32 shows the shock wave traveling upstream in the first and second panels. The second and third panels indicate that the location where the shock train reversed direction

occurred sometime between 2.5 and 5 milliseconds. Figure 33 continues the simulation, with the shock train moving downstream until reaching the stopping criteria at 14 milliseconds.

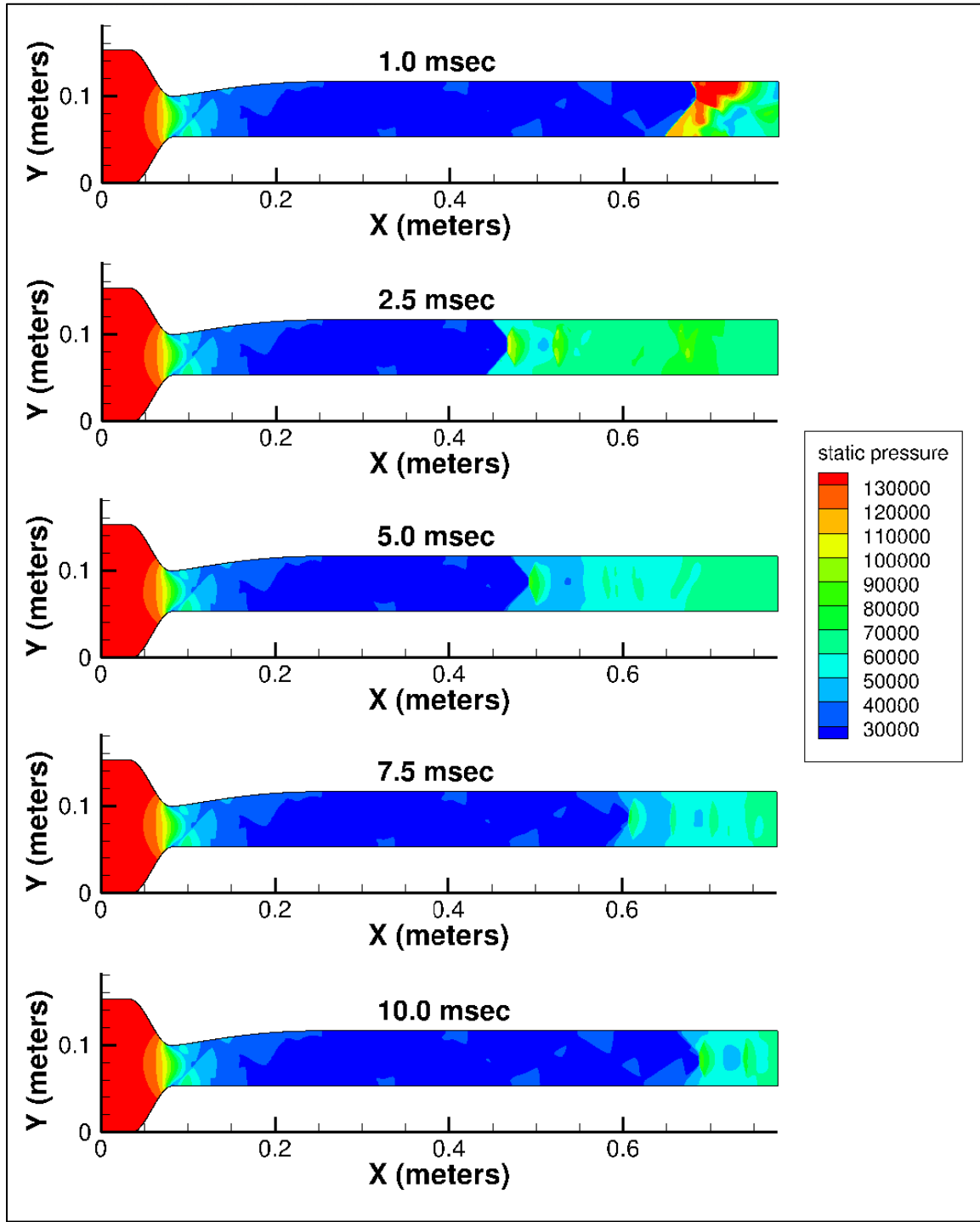


Figure 32. Evolution of PCST solution for instant 62.78 kPa back pressure

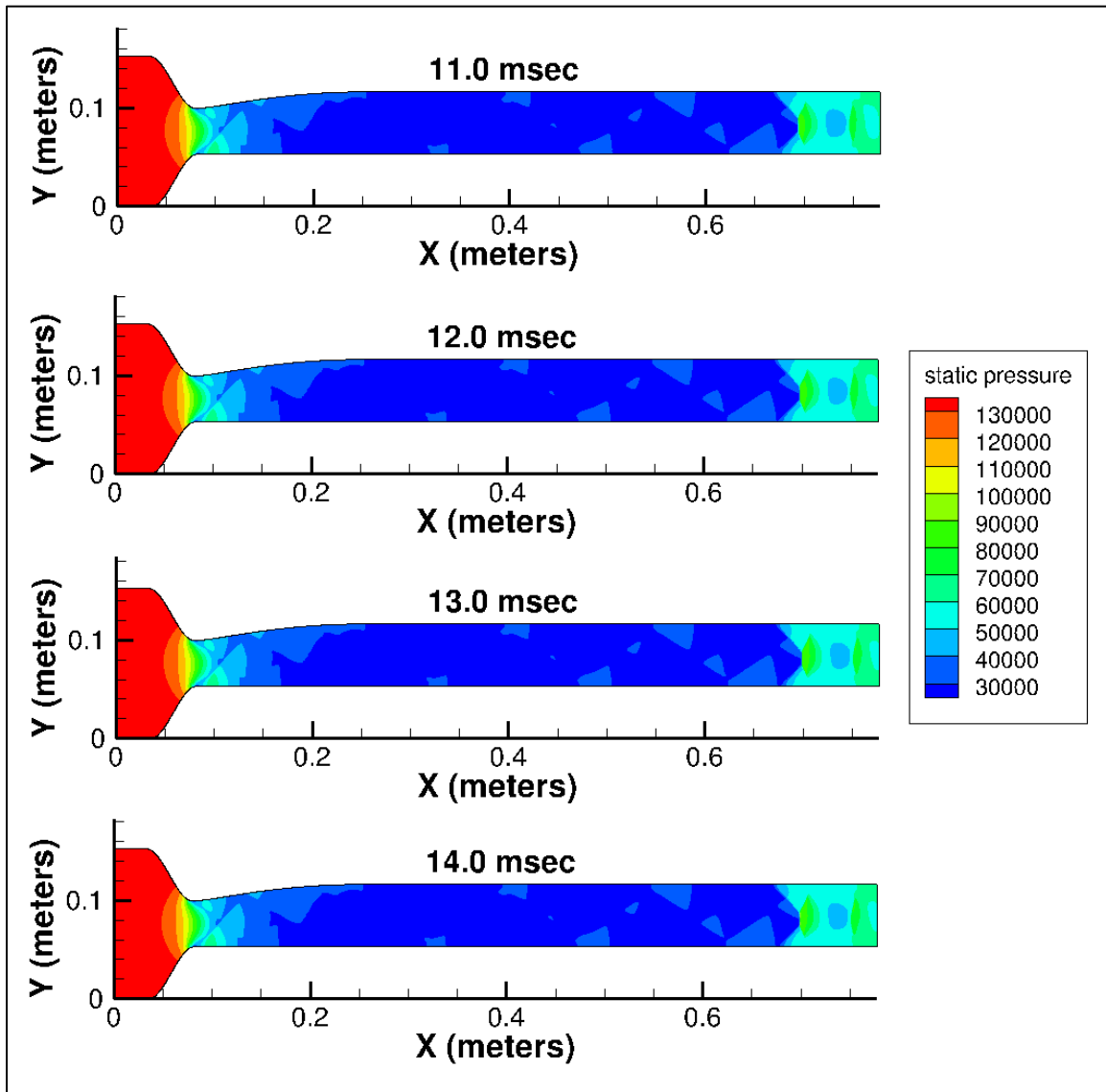


Figure 33. Evolution of PCST solution for instant 62.78 kPa back pressure continued

Figure 34 has the static pressure time history for the 62.78 kPa back pressure simulation. The time history is shown from 1 to 14 milliseconds after the back pressure is applied. Figure 34 shows the shock train moving upstream to its furthest location upstream (42.7 cm at 3.2 milliseconds) and then moving downstream until it reaches the stopping criteria (67.8 cm at 14 milliseconds). A comparison of these results with the results for the back pressure simulation of 75.0 kPa (with 168.2 kPa inflow) shows a 1.0

cm difference between the farthest upstream locations of the leading edge. The final locations are the same (67.8 cm).

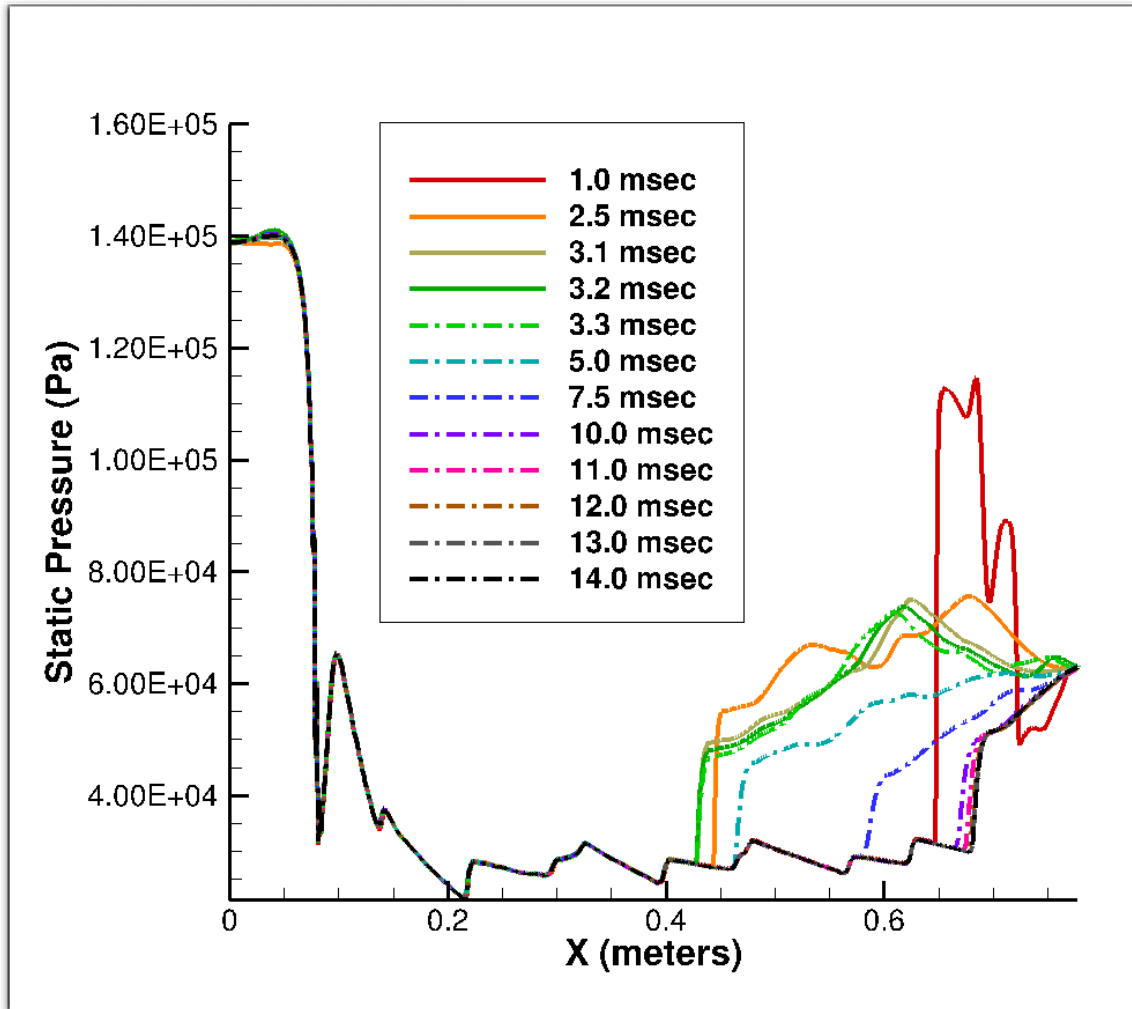


Figure 34. Time history of static pressure after 62.78 kPa back pressure applied

Gradual application of backpressure

The shocks in the preceding discussions were all observed to overshoot their final isolator position, moving upstream beyond the equilibrium position and then gradually back downstream to a stable location. The observed overshoot traveled farther upstream at higher backpressures. This overshoot did not occur in the AFIT experiment. One possible reason for this overshoot is the manner in which the experimental backpressure

is applied. The CFD simulations shown in Figures 13-34 had the back pressure applied instantaneously as a subsonic outflow boundary condition. In the experiment, the ramp took approximately 10 milliseconds to raise and create the back pressure needed, and an additional one to two milliseconds for the flow to adjust. The set of results presented next will use a gradually applied back pressure to determine if an overshoot occurs. Figure 35 shows the time history of the experimentally applied back pressure (red line) for the 85.0 kPa case. To replicate this with the CFD simulation, the 89.6 kPa back pressure simulation was repeated, with the back pressure gradually applied at an increment of 8.96 kPa per 1 millisecond intervals (with 10,000 time steps at 1.0×10^{-7} sec each) up to 89.6 kPa over a total 10 millisecond period (blue line). Similarly, the stepping up to any other required backpressure was done in 10% increments over ten 1 millisecond intervals.

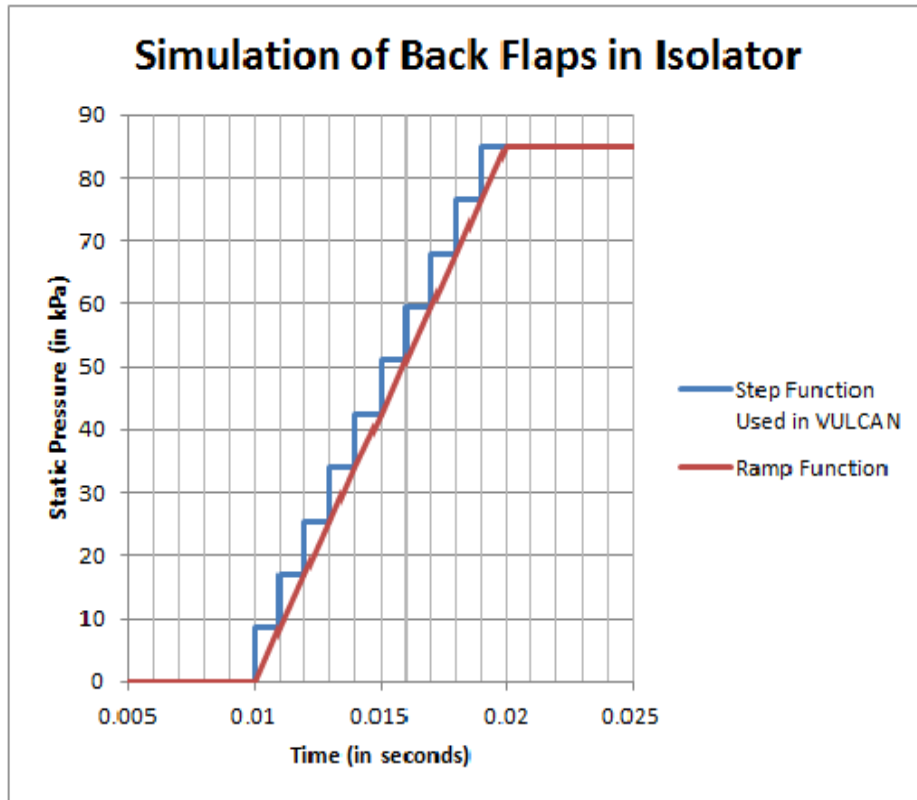


Figure 35. Simulation of back flap in isolator for 85.0 kPa case

The results of the 89.6 kPa applied gradient (stepped) back pressure are shown in Figures 36 and 37. The first seven milliseconds showed no shock train after the initial change (first step) in back pressure. At eight milliseconds, the shock train appears, moving upstream in the isolator. The shock train continues traveling upstream through 11 milliseconds, indicating the furthest point upstream occurred sometime between 11 and 12 milliseconds. Figure 37 continues the simulation, with the shock train moving downstream until reaching the stopping criteria at 23.0 milliseconds.

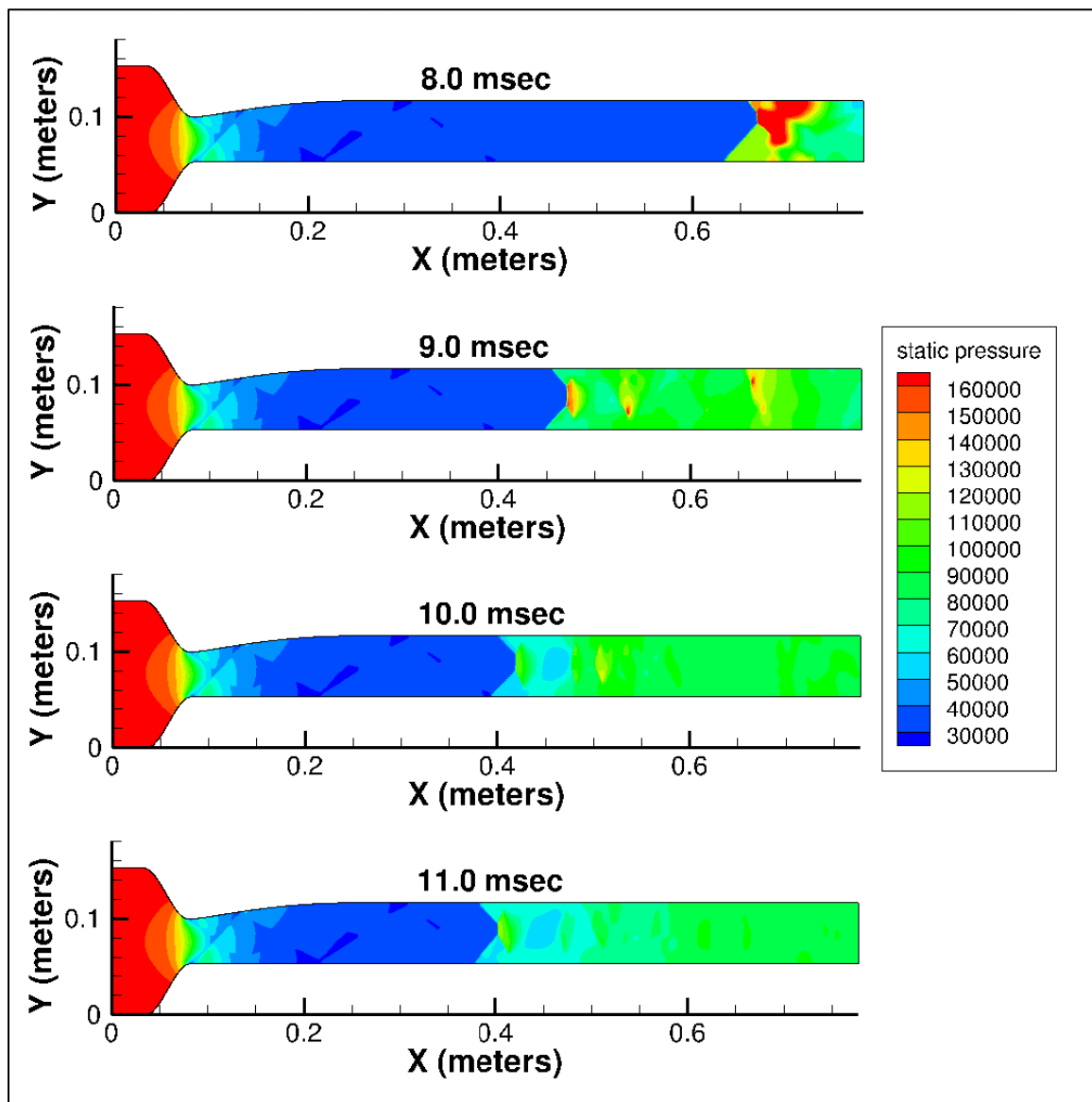


Figure 36. Evolution of PCST solution with back pressure stepped to 89.6 kPa

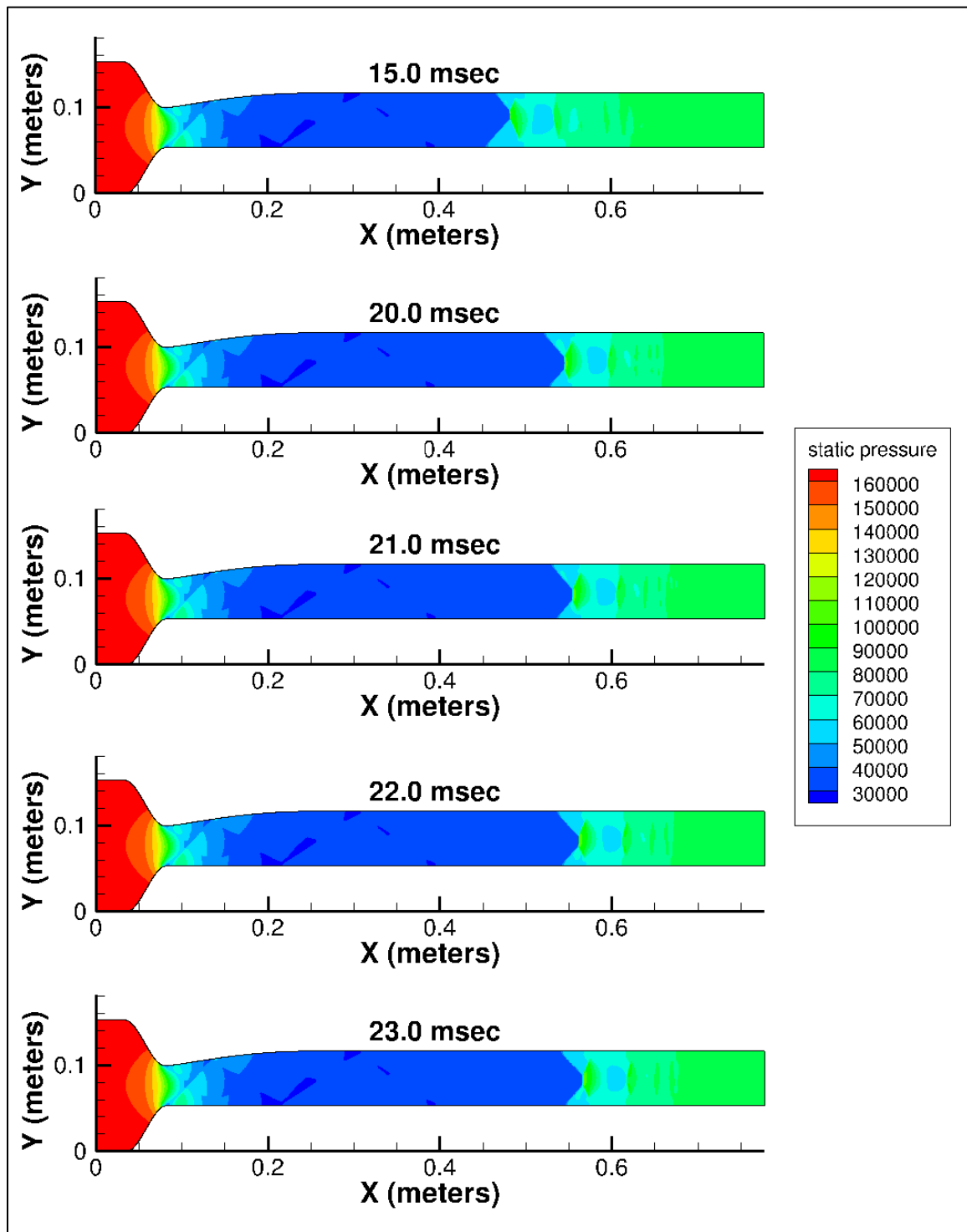


Figure 37. Evolution of PCST solution with back pressure stepped to 89.6 kPa

Figure 38 shows the time history of wall static pressures for the 89.6 kPa back pressure gradually applied over the same time period shown in Figure 35. As seen in

Figure 36, the leading edge of the shock train is first detected at 0.008 seconds. The time is shown from 8 to 23 milliseconds after the back pressure is applied. Figure 38 has the shock train moving upstream to its furthest location upstream (37.5 cm at 11.2 milliseconds) and then moving downstream until it reaches the stopping criteria (54.3 cm at 23 milliseconds). A comparison of these results with those for the instantaneous back pressure simulation of 89.6 kPa shows a significant difference between the farthest upstream locations of the leading edge (37.5 cm vs. 15.2 cm), but the final locations are the same (54.3 cm).

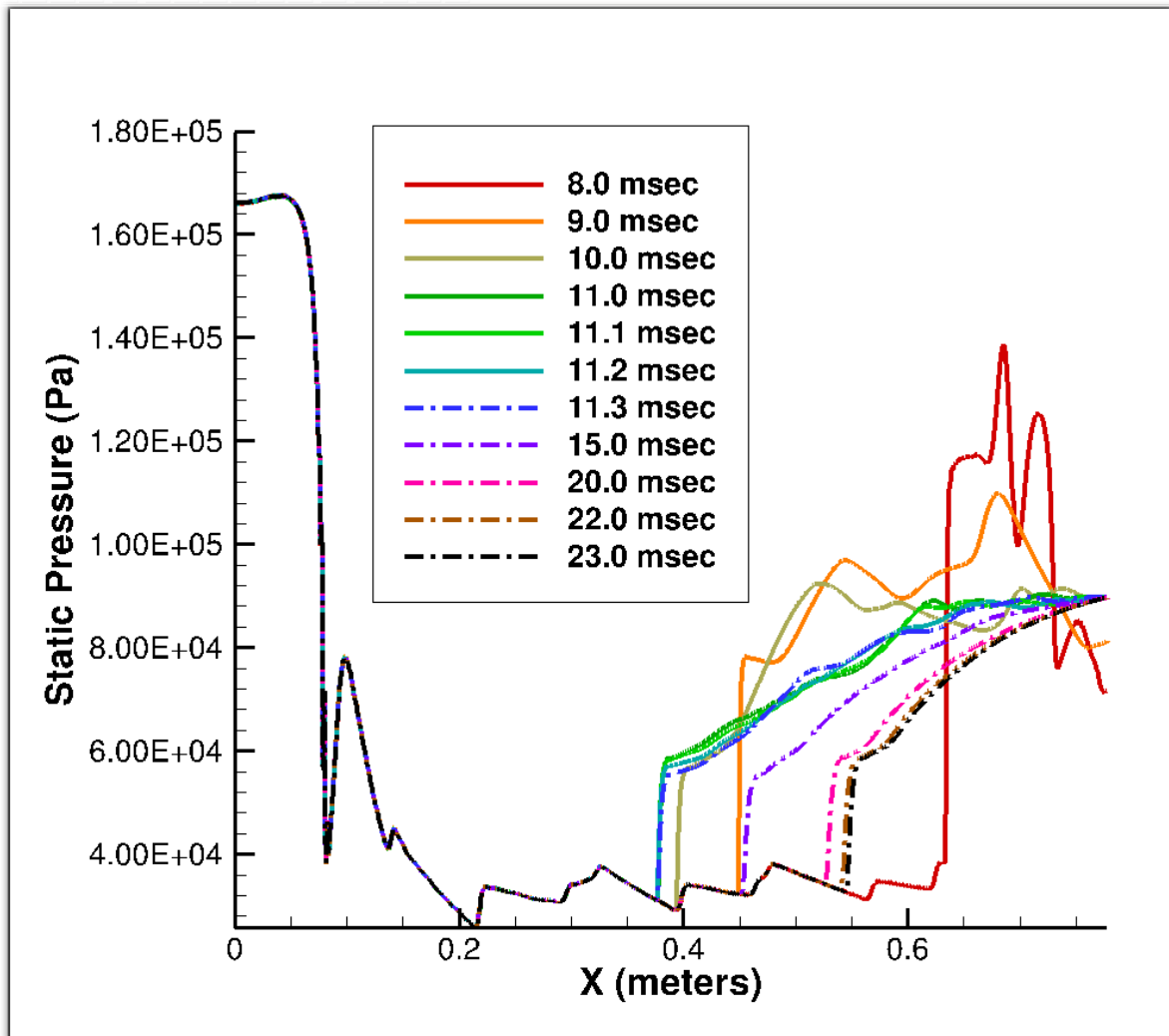


Figure 38. Time history of static pressure for stepped 89.6 kPa back pressure

Figure 39 shows the simulation of the applied gradient (stepped) back pressure for 85.0 kPa back pressure. In this simulation, the shock train does not appear until eight milliseconds. The shock train continues traveling upstream through 10 milliseconds. In Figure 39, the total distance from where the shock train reverses direction, moves downstream, and reaches the final location starts is much smaller than in previous simulations. The time history of the bottom static pressures for the 85.0 kPa stepped back pressure is shown in Figure 40. The shock train appears at 8 milliseconds and moves upstream. The leading edge reaches 59.6 cm as its furthest point upstream at 10.8 milliseconds. The shock train then moves downstream and reaches the final location of 59.8 cm, reaching the stopping criteria at 13.0 milliseconds. Figure 41 is a close up of the last 23 cm of the isolator during the stepped 85.0 back pressure simulation from 8 to 13 milliseconds. Close analysis of Figure 41 indicates there is some minor movement of the leading edge upstream and downstream before reaching the stopping criteria at 13 milliseconds. When the gradual back pressure simulation of 85.0 kPa is compared to the instantaneous back pressure simulation of 85.0 kPa, the difference between the farthest upstream locations of the leading edge is 41.5 cm, while the difference of the final locations is just 0.6 cm.

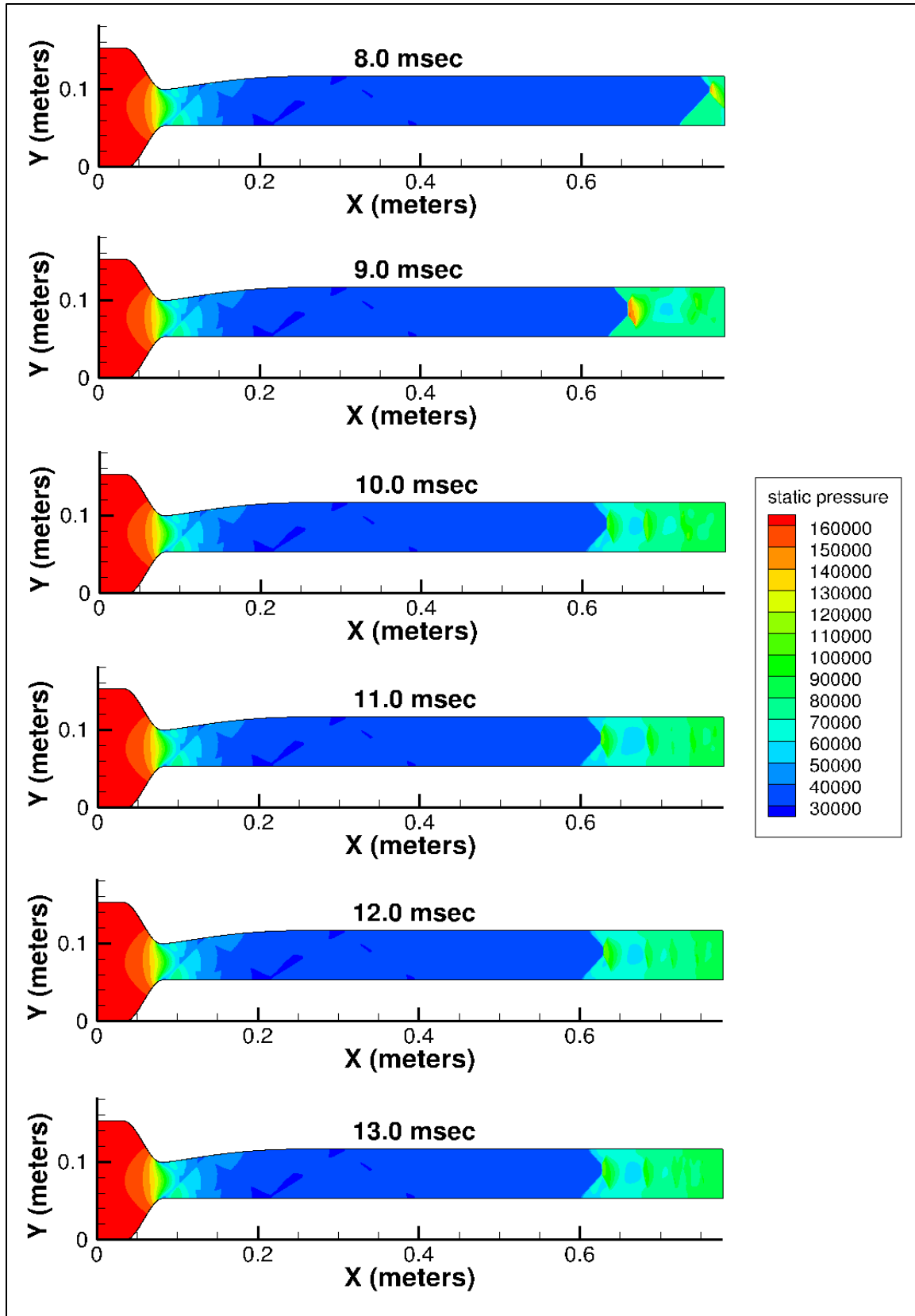


Figure 39. Evolution of PCST solution with back pressure stepped to 85.0 kPa

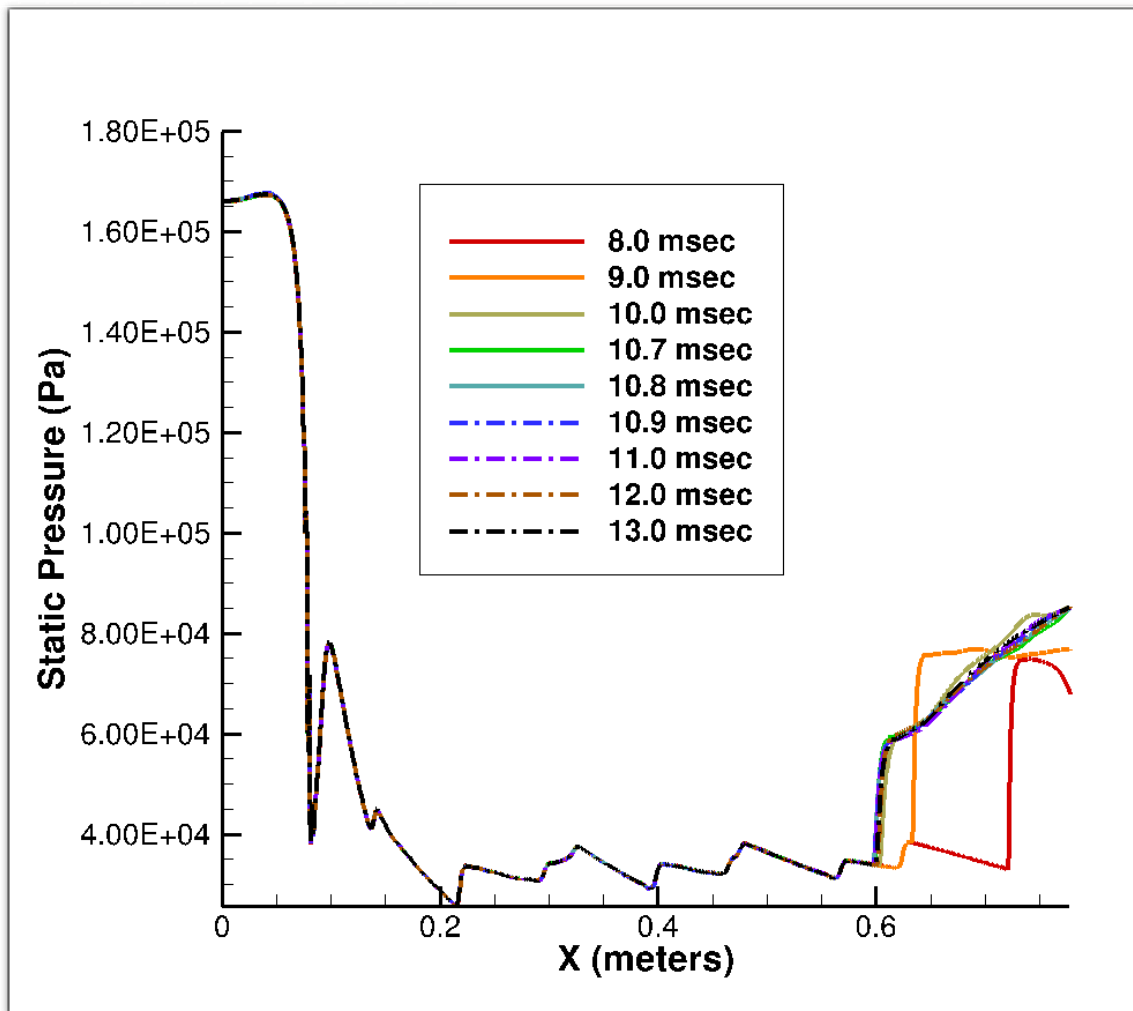


Figure 40. Time history of static pressure for stepped 85.0 kPa back pressure

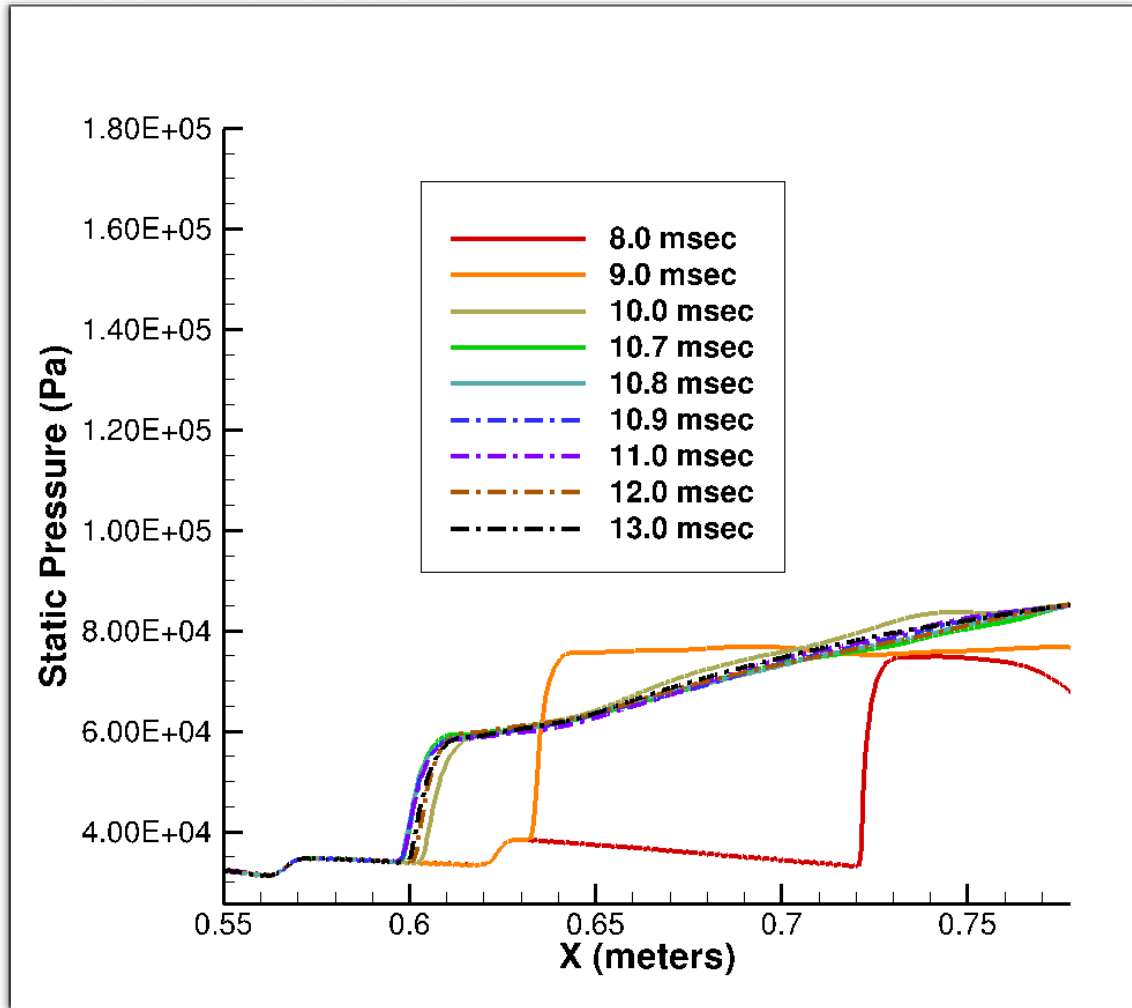


Figure 41. Time history of static pressure from 0.008 to 0.012 seconds

Figures 42 and 43 display the simulation results of 75.0 kPa stepped back pressure. The shock train appears at 9 milliseconds and moves upstream until 11 milliseconds. At 12 milliseconds, the shock train has reversed direction and traveled downstream, indicating the reversal point occurs between 10 and 12 milliseconds. The simulation continues with the shock train moving downstream to the final location of 67.8 cm, meeting the stopping criteria at 16 milliseconds.

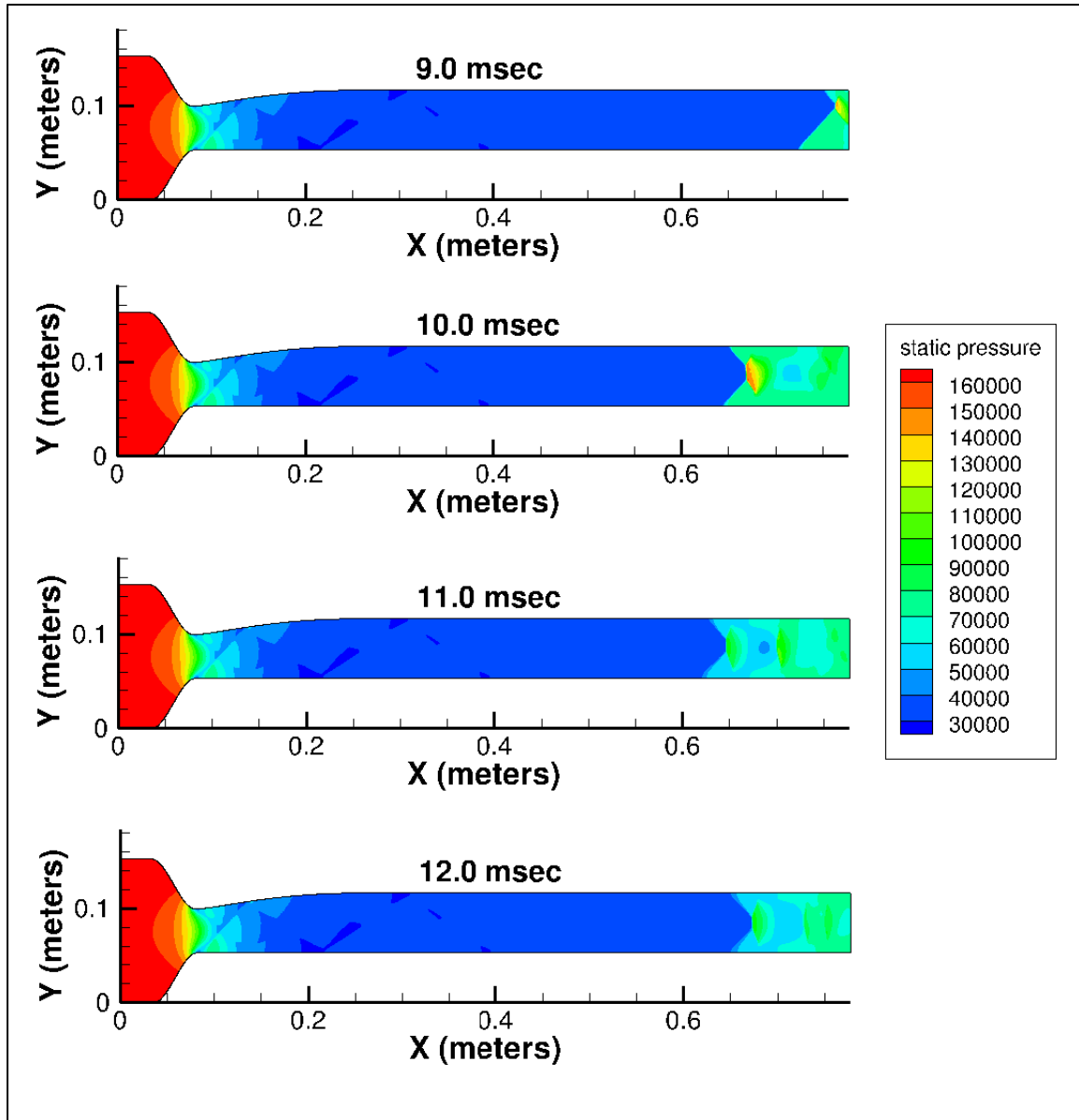


Figure 42. Evolution of PCST solution with back pressure stepped to 75.0 kPa

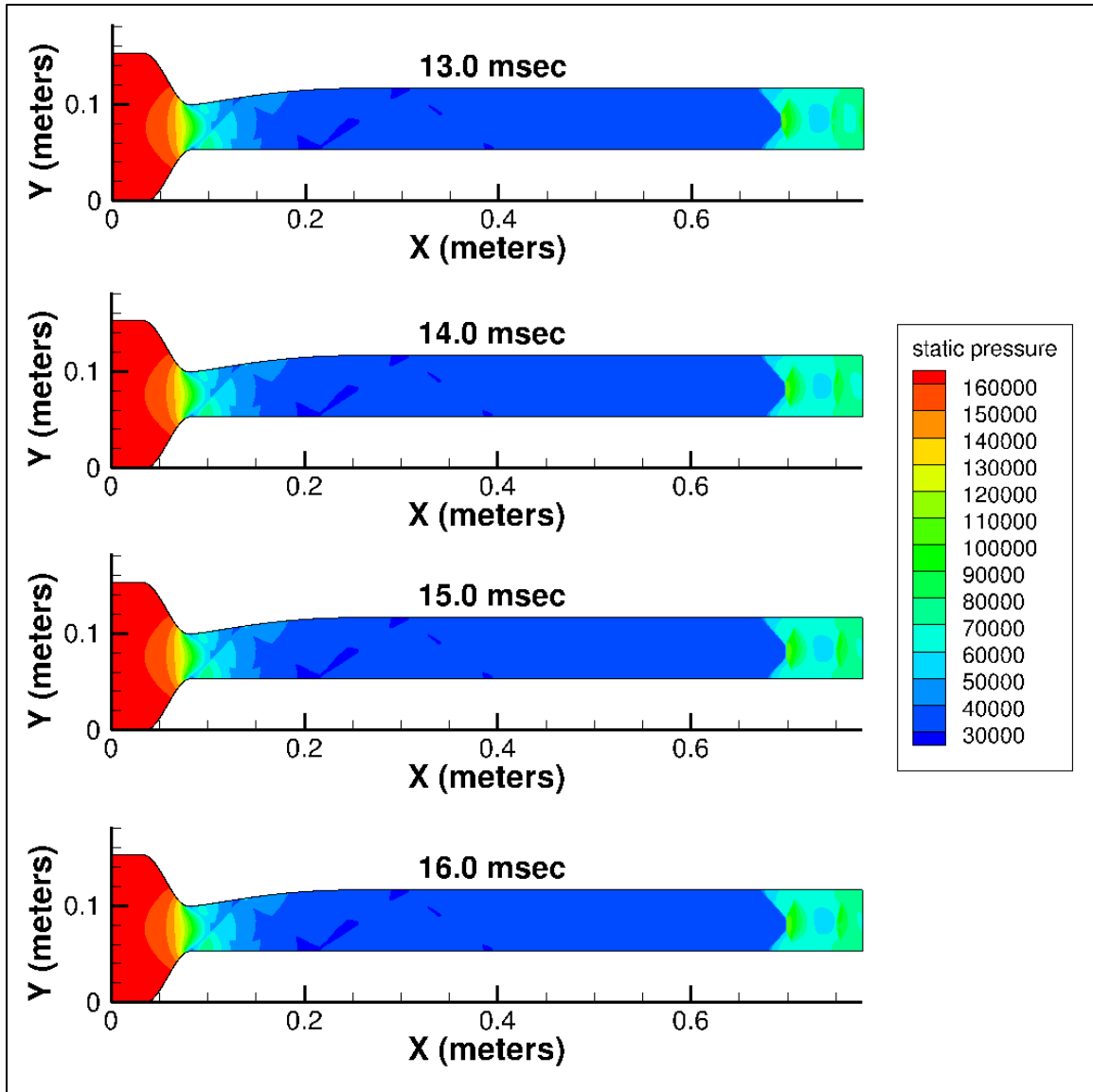


Figure 43. Evolution of PCST solution with back pressure stepped to 75.0 kPa continued

Figure 44 shows the time history of wall static pressures for the stepped 75.0 kPa back pressure. The time history is shown from nine milliseconds (where the leading edge is first detected) to 16 milliseconds after the back pressure is applied. The shock train traveled to its furthest upstream location (61.4 cm at 10.7 milliseconds) before reversing direction and moving downstream until the shock train reached the stopping criteria (67.8 cm at 16 milliseconds). A comparison of these results with the 75.0 kPa instantaneous

back pressure simulation shows (just like in the other stepped simulations) a significant difference between the farthest upstream locations of the leading edge is (19.7 cm), while the final locations are still the same (67.8 cm).

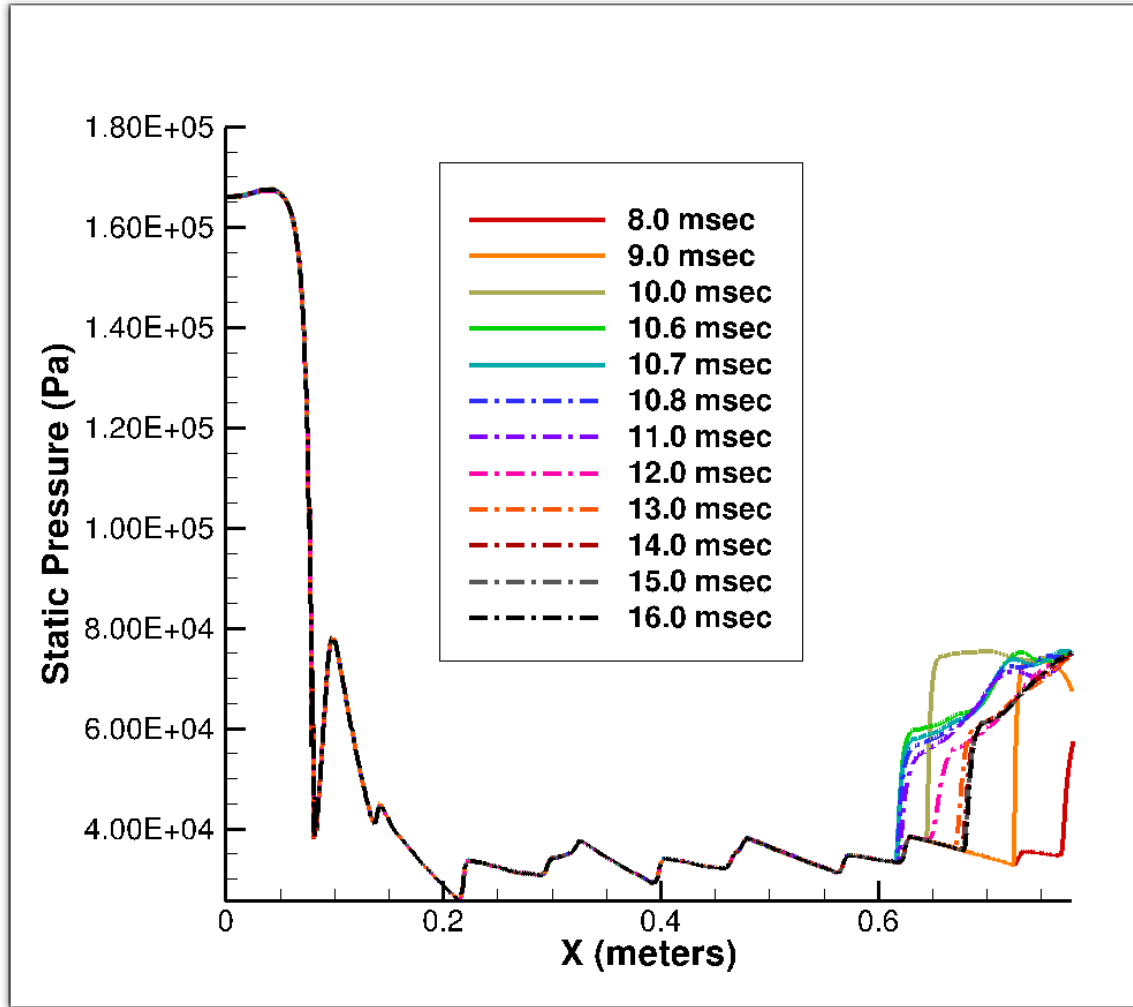


Figure 44. Time history of static pressure for stepped 75.0 kPa back pressure

A second set of simulations were performed for an inflow total pressure of 140.6 kPa with the applied gradient (stepped) back pressures of 75.0, 71.1 and 62.78 kPa. AS with the instantaneous application of back pressure section, the ratios of back pressure to total inflow pressure in this set are the same as the previous set for the inflow pressure of 168.2 kPa. Figures 45 and 46 display the movement of the PCST for an inflow pressure

of 140.6 kPa and a stepped back pressure of 75.0 kPa. The shock train appears at 8 milliseconds and moves upstream until 11 milliseconds, indicating the reversal point occurs between 10 and 12 milliseconds. The simulation continues with the shock train moving downstream to the final location of 54.4 cm, meeting the stopping criteria at 32 milliseconds.

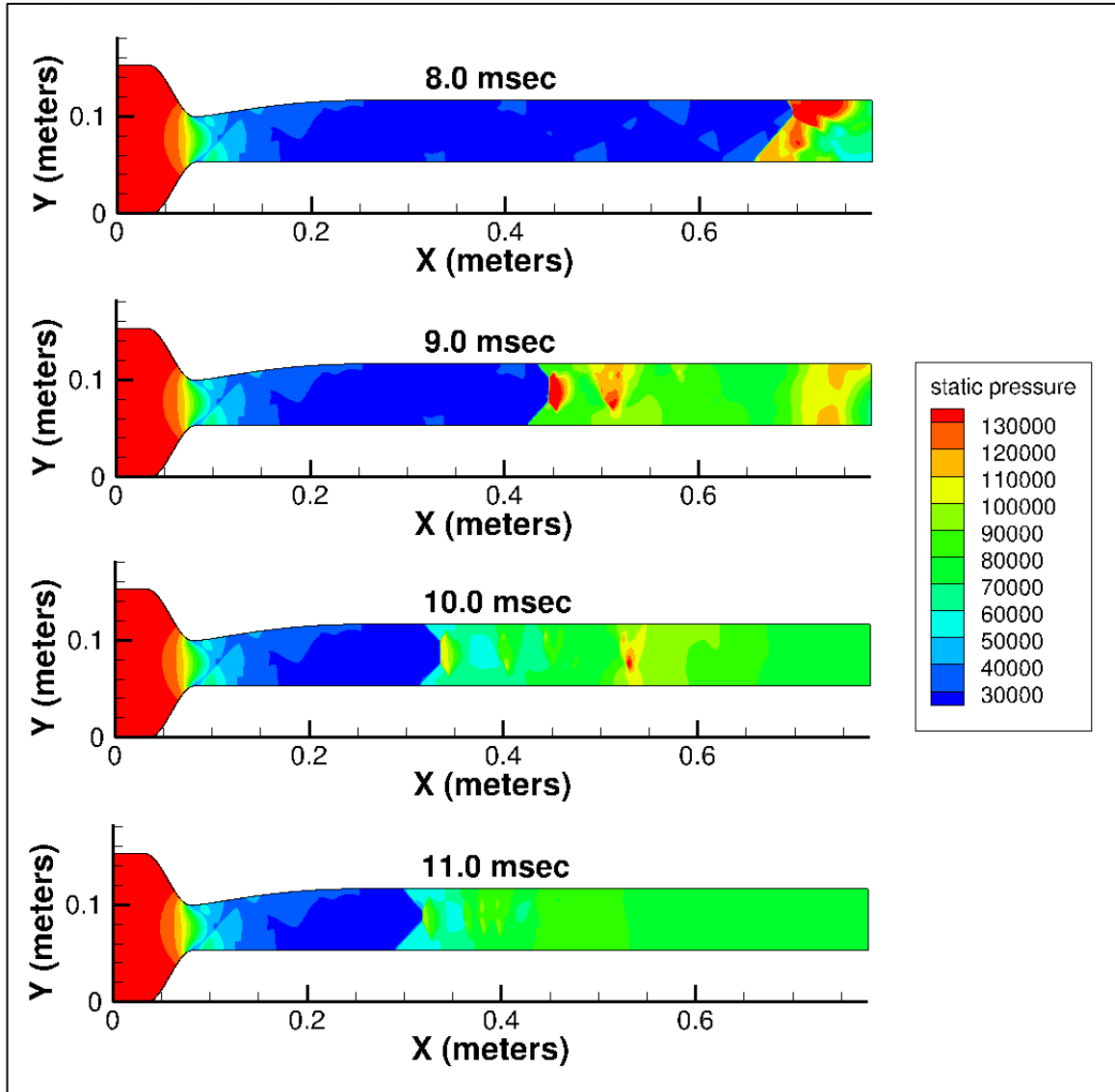


Figure 45. Evolution of PCST solution with back pressure stepped to 75.0 kPa (140.6 kPa inflow)

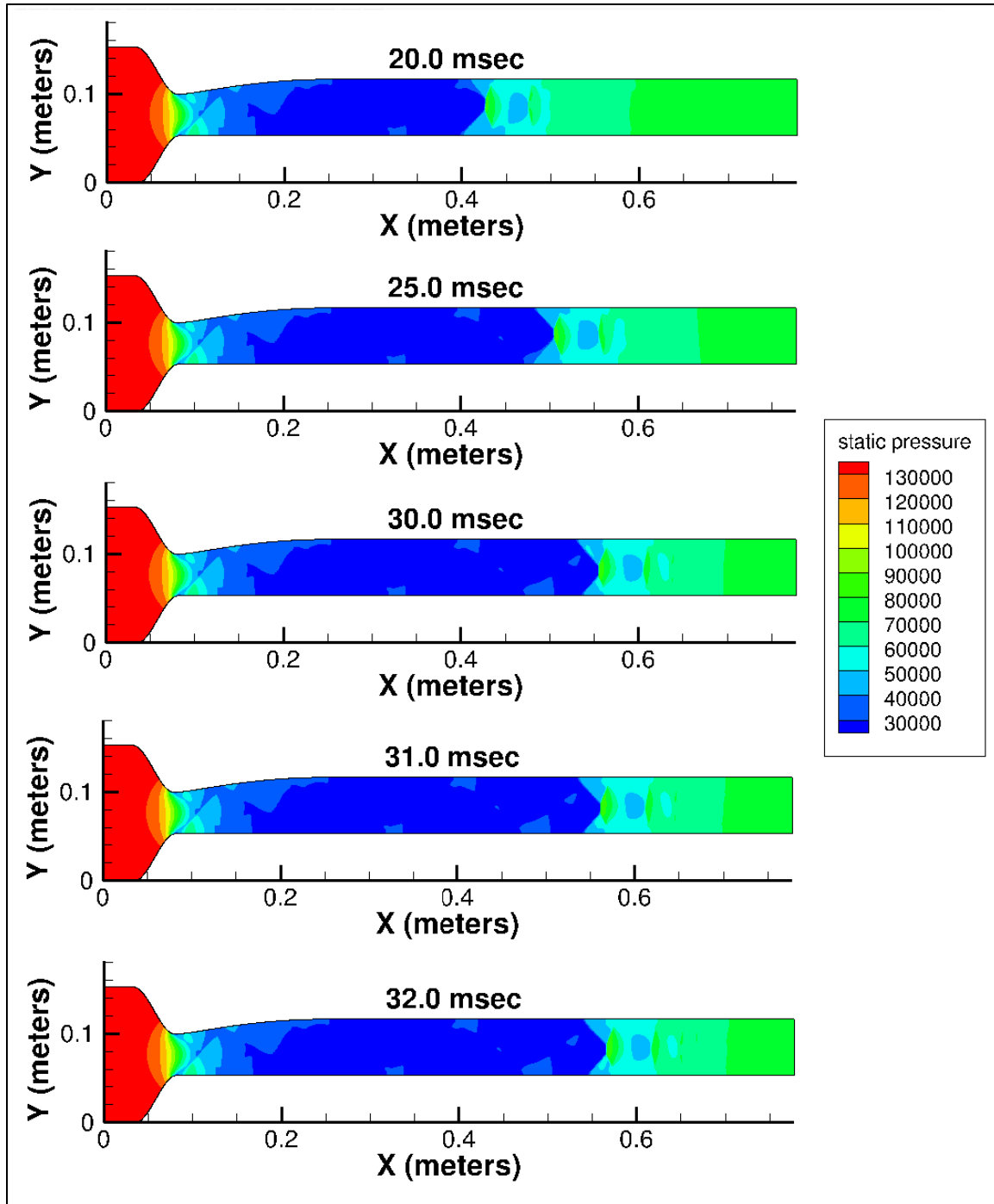


Figure 46. Evolution of PCST solution with back pressure stepped to 75.0 kPa continued (140.6 kPa inflow)

Figure 47 has the time history of the static wall pressures for the 75.0 kPa stepped back pressure. There is no sign of a shock train until 8 milliseconds. The shock train traveled upstream until 11.0 milliseconds (at 28.9 cm), and then moved downstream until

it reaches its final location (at 54.4 cm) and the stopping criteria at 32 milliseconds. A comparison of this simulation with the instantaneous back pressure of 75.0 kPa (with 140.6 kPa inflow) shows the difference between the furthest upstream locations is 12.4 cm while the final location difference is just 0.2 cm. When compared to the stepped 89.6 kPa back pressure simulation (which has the same back to inflow pressure ratio of 0.533), the difference between the furthest upstream locations is 8.6 cm while the final location difference is just 0.1 cm.

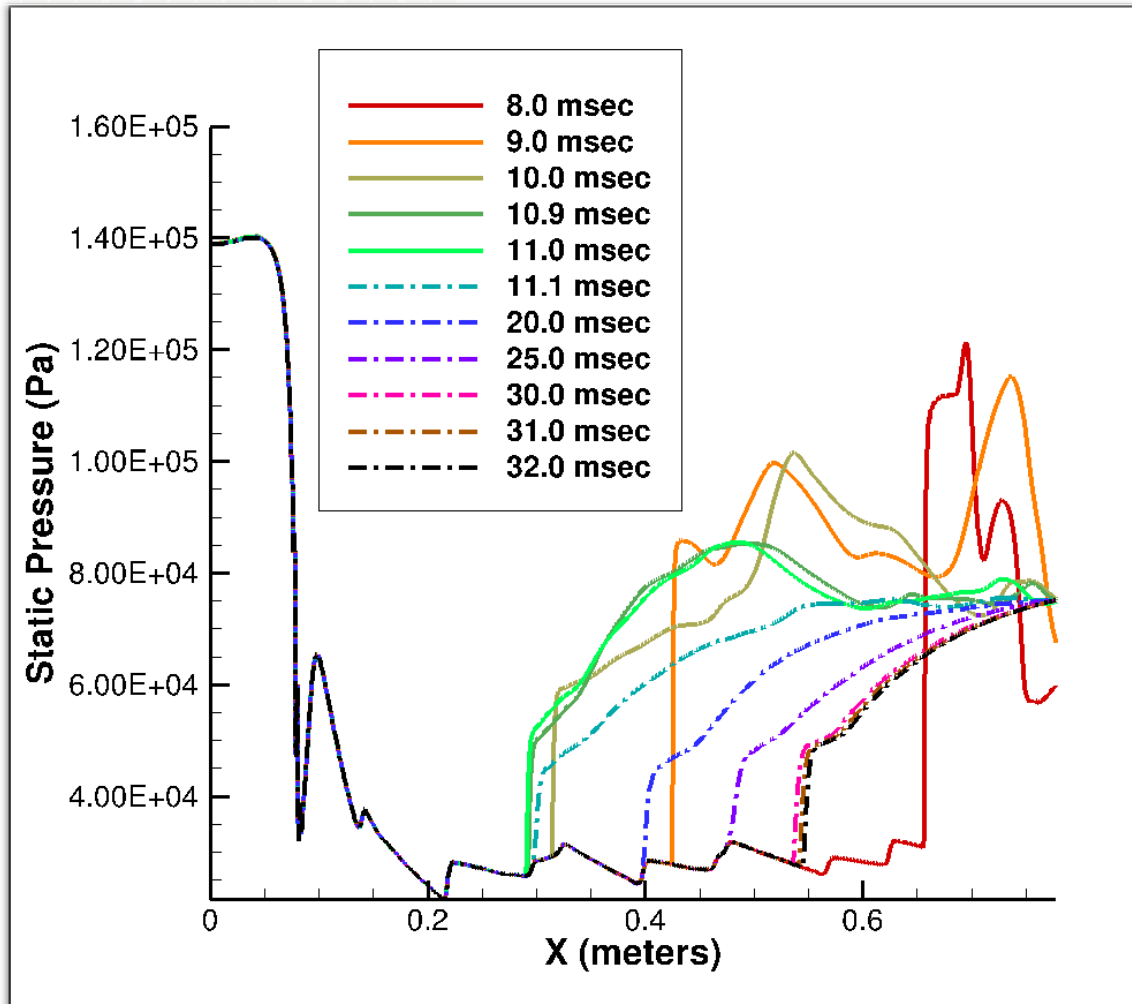


Figure 47. Time history of static pressure for stepped 75.0 kPa back pressure (140.6 kPa inflow)

Figure 48 shows the simulation for a stepped back pressure of 71.1 kPa. In this simulation, the shock train does not appear until eight milliseconds, and traveled upstream through 11 milliseconds. In the stepped 85.0 kPa simulation (Figures 40 and 41) with the same back to inflow pressure ratio, the distance from reversal location to final location is smaller than simulations with different back to inflow pressure ratios. Here, the leading edge reached 57.5 cm as its furthest point upstream at 10.2 milliseconds. The shock train then moved downstream and reached the final location of 59.0 cm, reaching the stopping criteria at 32.0 milliseconds. The time history of the static pressures for the stepped 71.1 kPa back pressure is in Figure 49. The shock train appears at 8 milliseconds, and moves upstream through 10 milliseconds. The furthest the shock train traveled upstream is identified at 10.2 milliseconds. After 10.2 milliseconds, the shock train has reversed direction and started moving downstream until reaching the final location of 59.0 cm and the stopping criteria at 13 milliseconds. When this simulation is compared to the instantaneous 71.1 kPa back pressure simulation, the difference between the farthest upstream locations of the leading edge is 37.5 cm, while the difference of the final locations is just 0.3 cm. When compared to the stepped 85.0 kPa back pressure (which has the same back to inflow pressure ratio of 0.506), the difference between the farthest upstream locations of the leading edge is 2.1 cm, while the difference of the final locations is just 0.2 cm.

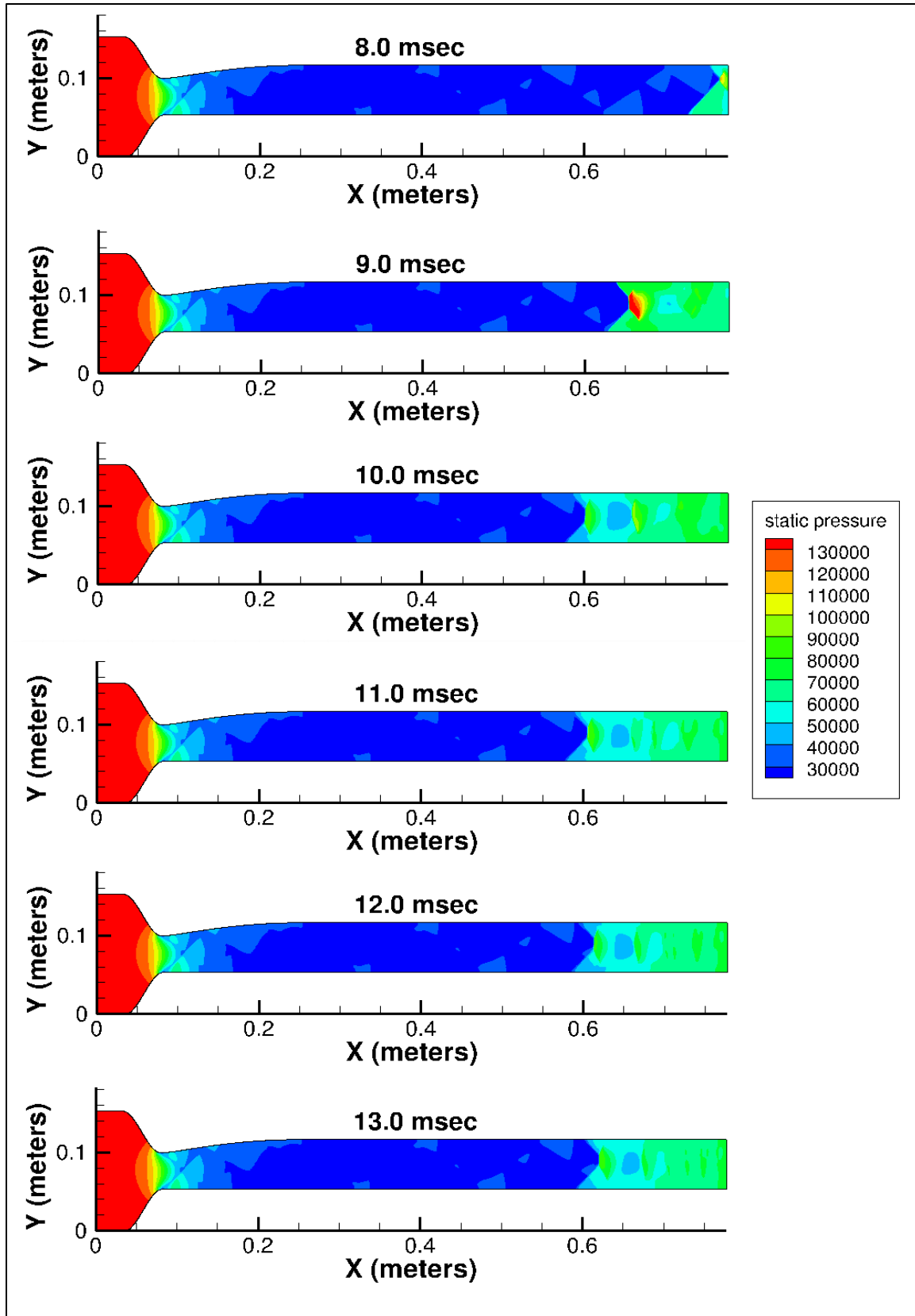


Figure 48. Evolution of PCST solution with back pressure stepped to 71.1 kPa

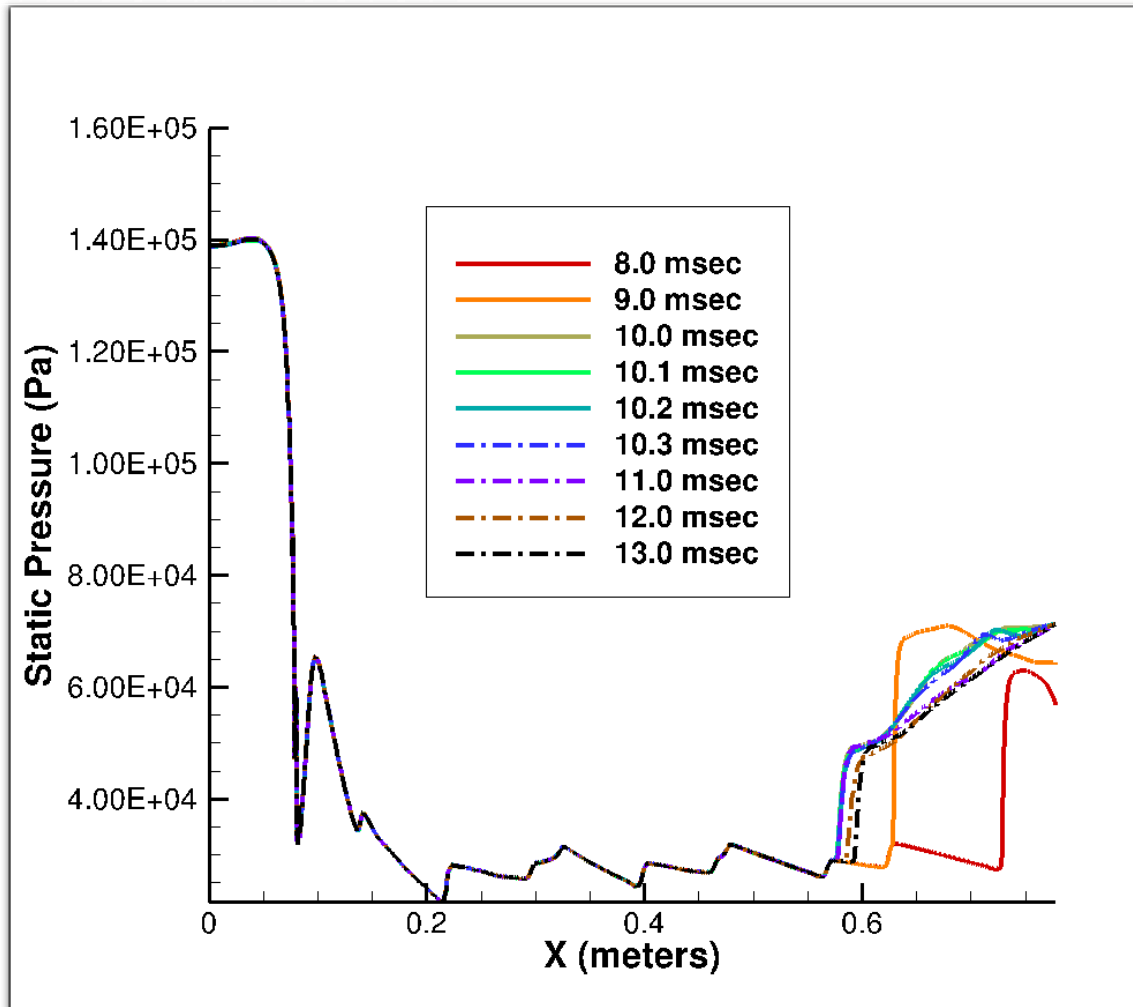


Figure 49. Time history of static pressure for stepped 71.1 kPa back pressure

Figures 50 and 51 display the final CFD simulation for a stepped 62.78 kPa back pressure. In this simulation, there is no shock train until 9 milliseconds. Figure 50 has the shock wave traveling upstream in the isolator through 11 milliseconds, indicating the furthest point upstream occurred sometime between 10 and 12 milliseconds. Figure 51 continues the simulation, with the shock train moving downstream until reaching the stopping criteria at 32 milliseconds.

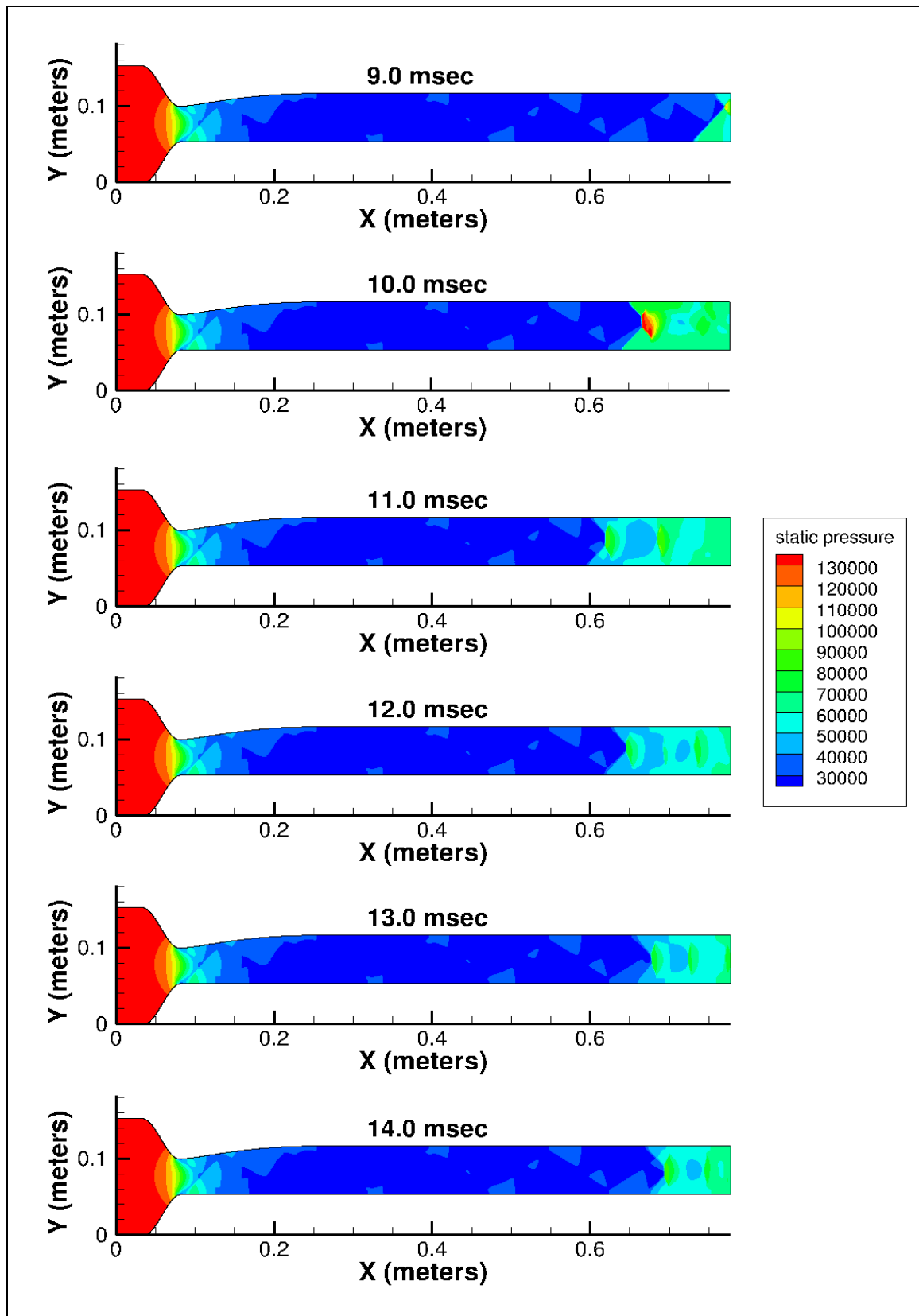
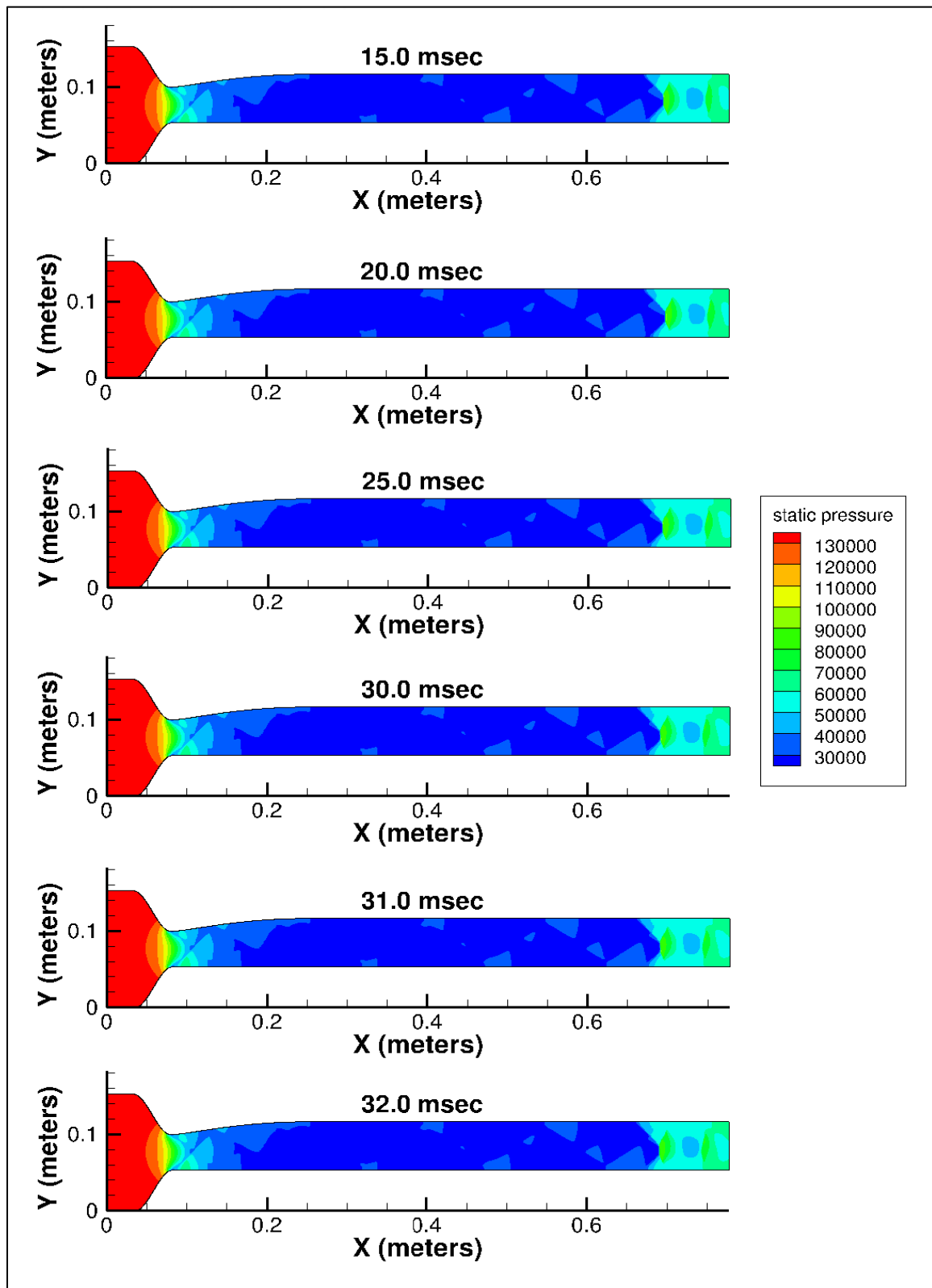


Figure 50. Evolution of PCST solution with back pressure stepped to 62.78 kPa



**Figure 51. Evolution of PCST solution with back pressure stepped to 62.78 kPa
continued**

Figure 52 shows the time history of the static pressures for the stepped 62.78 kPa back pressure. The shock train traveled to its furthest upstream location (59.3 cm at 11.0 milliseconds) before reversing direction and moving downstream until it reached the stopping criteria (67.2 cm at 32 milliseconds). A comparison of this simulation with Figure 34 shows a 16.6 cm difference between the farthest upstream locations, while the difference between the final locations is just 0.6 cm. A comparison with Figure 44 (with the same back to inlet pressure ratio of 0.446) shows a 2.1 cm difference between the farthest upstream locations, while the difference between the final locations is also 0.6 cm.

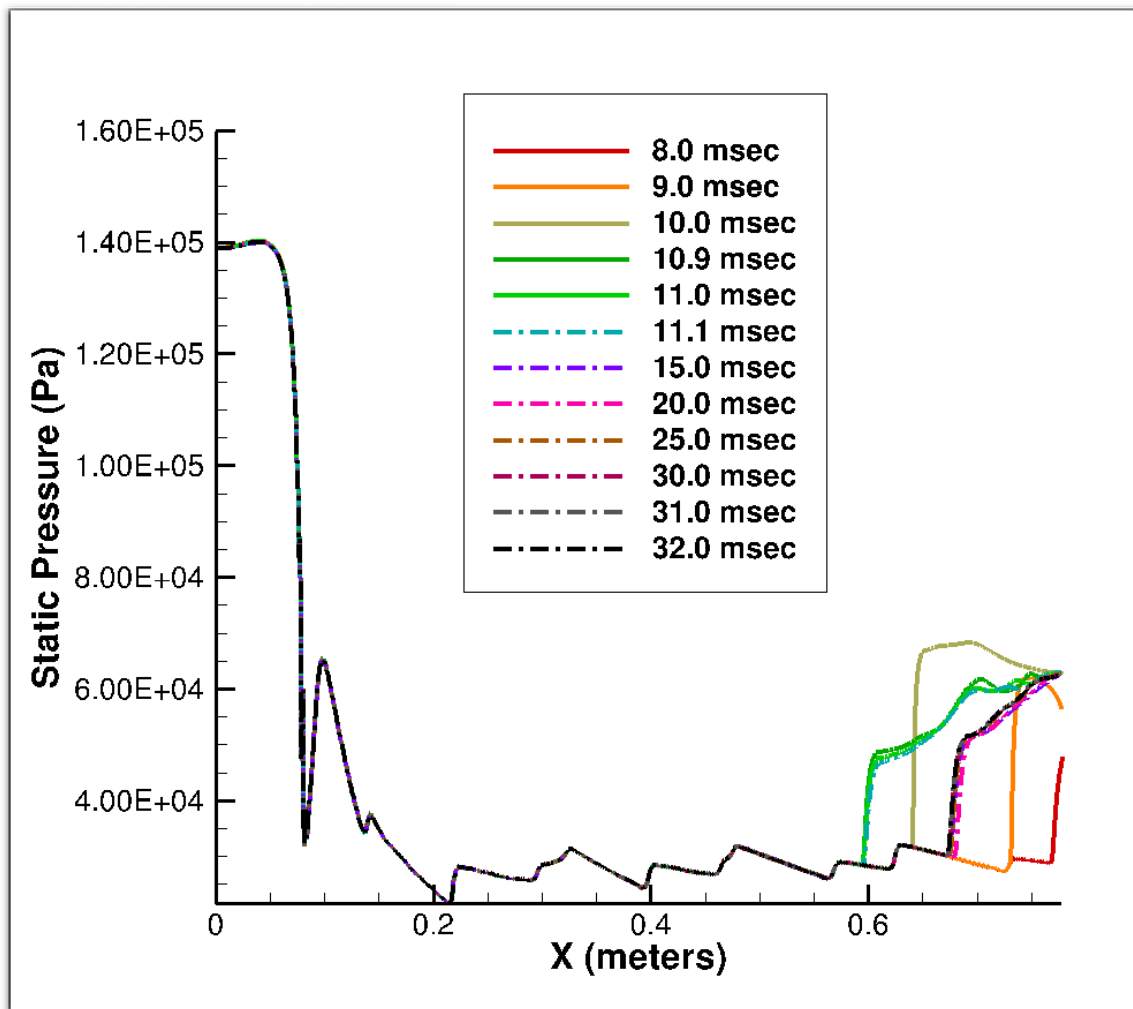


Figure 52. Time history of static pressure for stepped 62.78 kPa back pressure

The final results of the two back pressure methods for all six back pressure cases are shown in Tables 3 and 4 for comparison. As can be seen, final locations of the shock train are independent of the method of back pressure (instantaneous or stepped), but strongly correlated with the back pressure ratio. In general, the gradual application (stepped) causes the shock train to travel less far upstream and thus stabilize at the final location more quickly. In all cases, higher back pressure ratios result in further upstream reversal locations and further upstream final locations. In all cases with a gradually applied (stepped) back pressure, the shock train formed at 8-9 milliseconds after the stepped back pressure started and at locations farther upstream for higher back pressure ratios. The PCST traveled upstream as did the instantaneous back pressure cases, but with much less upstream travel before reversal. The reason the reversal locations are further downstream is that in the instantaneous cases, the back pressures are already at their maximum values when the shock train forms and starts moving upstream. In the gradual cases, they are not at their maximum back pressure values. At 8-9 milliseconds, the back pressure values of the gradual cases are only at 80-90% of the maximum back pressure values. Thus, the shock train in the gradual cases will not travel as far upstream since the back pressure at the moment the shock train forms and begins its movement upstream in the gradual cases as it will in the instantaneous cases.

Table 3. 2-D Results of instantaneous back pressure method

Inflow Pressure (kPa)	Back Pressure (kPa)	Back to Inflow Pressure Ratio	Instantaneous			
			Time to Reverse (msec)	Reversal Location (cm)	Time to Final (msec)	Final Location (cm)
168.2	89.6	0.533	3.2	15.2	28.0	54.3
140.6	75.0	0.533	4.1	16.5	31.0	54.6
168.2	85.0	0.506	3.8	18.1	23.0	59.2
140.6	71.1	0.506	4.4	20.0	24.0	59.3
168.2	75.0	0.446	2.9	41.7	13.0	67.8
140.6	62.78	0.446	3.2	42.7	14.0	67.8

Table 4. 2-D Results of gradual (stepped) back pressure method

Inflow Pressure (kPa)	Back Pressure (kPa)	Back to Inflow Pressure Ratio	Gradual application					
			Time Initial Shock Detected (msec)	Location of Initial Shock (cm)	Time to Reverse (msec)	Reversal Location (cm)	Time to Final (msec)	Final Location (cm)
168.2	89.6	0.533	8.0	63.1	11.2	37.5	23.0	54.3
140.6	75.0	0.533	8.0	65.6	11.0	28.9	32.0	54.4
168.2	85.0	0.506	8.0	72.1	10.8	59.6	13.0	59.8
140.6	71.1	0.506	8.0	72.5	10.2	57.5	13.0	59.0
168.2	75.0	0.446	9.0	72.3	10.7	61.4	16.0	67.8
140.6	62.78	0.446	9.0	72.6	11.0	59.3	32.0	67.2

Summary of 2-D Results

For 2-D transient simulations, the grid independence study showed the medium grid was acceptable, and the temporal resolution study showed the time step of 1.0×10^{-7} seconds was acceptable. The final location of the leading edge of the shock train was able to be determined in 2-D by observing vertical spikes in pressure. Both the instantaneous and gradual application of back pressure contained an overshoot where the shock train traveled upstream before reversing direction and traveling to its final location. The final location in both application methods were roughly the same (within 0.6 cm of each

other). The overshoot in the gradual application was significantly less than the instantaneous. The reason for this difference is that when the PCST forms, the back pressure in the gradual application is not at the maximum back pressure value, while it is in the instantaneous application. The higher back pressure in the instantaneous cases pushes the overshoot farther upstream. The gradually applied back pressure cases with a pressure ratio of 0.506 had the shortest final times compared to the other gradually applied back pressure cases. The reason for this difference is that the cases with a 0.506 pressure ratio had their reversal and final locations the closest to each other, needing less time than other gradually applied cases to reach their final locations. When the same back to inflow pressure ratio is used, regardless of whether the back pressure was applied instantaneously or gradually, the final locations were within 0.6 cm of each other.

The results of both grid independence study and the temporal resolution study in 2-D will be also done in 3-D using the 2-D results as a starting point to see if the 3-D studies have the same results. The vertical spikes in pressure used to identify the leading edge of the shock train should also be present in 3-D. In 2-D, the final locations were further upstream in the isolator for higher back to inflow pressure ratios. The same characteristic should occur in 3-D too. Another characteristic that should be observed in 3-D and compared to 2-D results is the overshoot. If the overshoot occurs in 3-D, it should also be measured in terms of how far it travels and where it reverses. Finally, the final locations in 2-D were approximately the same for the same back to inflow pressure ratio. The 3-D results will need to be analyzed to see if the same results occur too.

V. Three-Dimensional CFD Results

Introduction

This section presents the 3-D, time-accurate, CFD results. The reference conditions used in these simulations are the same as those in Table 1 (Chapter 1) are entered into the VULCAN input file. As in the 2-D results, the four walls of the isolator were set as adiabatic walls with Wilcox wall matching functions, and a 3-stage Runge-Kutta time-stepping scheme was used with a specified time step of 1.0×10^{-7} seconds. A simulation was executed first without a back pressure (for 10 milliseconds) to develop a boundary layer profile in the isolator based on the reference conditions in Table 1. An attempt was made to apply the backpressure instantaneously, as had been done in the 2-D results, but the simulation diverged while it was running. Since the back pressure cannot be applied instantaneously in a 3-D case (as in a realistic, experimental case), the back pressure was applied gradually over a finite time interval as a subsonic outflow boundary condition, as presented in Figure 35. Two additional simulations were done for a back pressure applied in the same manner as in the AFIT experiment with the back flaps.

Transient 3-D Simulation

The results for the transient 3-D simulation are divided into six sections. Just like with the 2-D results, the first three sections deal with grid convergence, temporal resolution, and the choice of turbulence models. The fourth section shows the results for a gradually applied back pressure, and the fifth section shows the results for a gradient back pressure applied in the same way as the ramp deployed in the AFIT experiment. The sixth section is a summary of the 3-D results.

Grid Convergence Study

Like the 2-D grid, a 3-D grid convergence study was conducted to determine if the converged solution is independent of the grid density. The 2-D grids used were extended to 3-D, with the medium grid having 873 cells in the x-direction, 101 cells in the y-direction, and 101 cells in the z-direction (8,905,473 total cells). The spacing and grid stretching for the z-direction were the same as in 2-D (a hyperbolic tangent distribution function giving the spacing in the nozzle a Δz of 0.4913 mm and in the isolator a Δz of 0.3175 mm). The coarse grid was 435 x 51 x 51 (1,131,435 total cells) and the fine grid was 1747 x 201 x 201 (70,580,547 total cells). Figure 53 shows boundary layer profiles from top to bottom (y-axis), along the center (z-axis) at the end of the isolator stream wise (x-axis) for the 3-D coarse, medium, and fine grids with a backpressure of 89.6 kPa applied gradually for 10 milliseconds, causing a PCST. For all 3 grids, the profiles resolve the subsonic portion and propagate the backpressure upstream, creating the desired shock train. The coarse grid is not as detailed as the medium and fine grids with the leading edge of the PCST not as far out as the medium and fine grids. The leading edges of the medium and fine grids were both at the same general location, with the medium grid's further out on top and bottom while the fine grid is further out in the middle. Figure 54 displays the pressure contours for a comparison of the three grids, each tested with a stepped back pressure of 89.6 kPa. The steps were done the same way as the 2-D cases, in 10% increments every 1 millisecond until it reached 89.6 kPa back pressure. The coarse grid does not have enough cells to provide more detail than the medium grid, and the fine grid required more time steps at a smaller time scale to reach the same time period as the medium grid, and did not have the same shock location as the medium grid. Since both the medium and fine grids give approximately the same results

and the medium grid requires fewer time steps, the medium grid was used for the remainder of the simulations to save computer time.

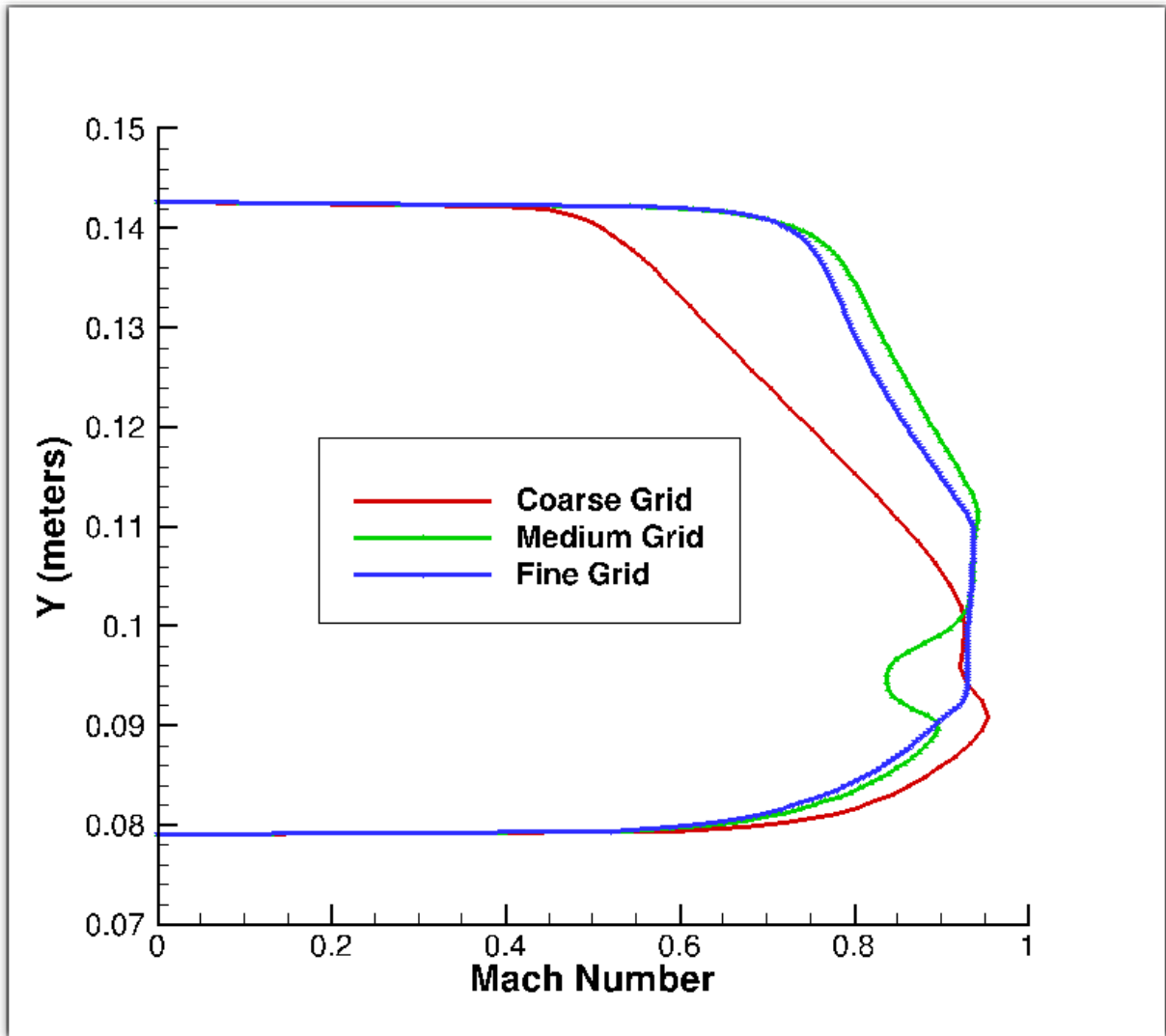


Figure 53. Boundary layer profile for 3-D Mach 1.8 nozzle/isolator

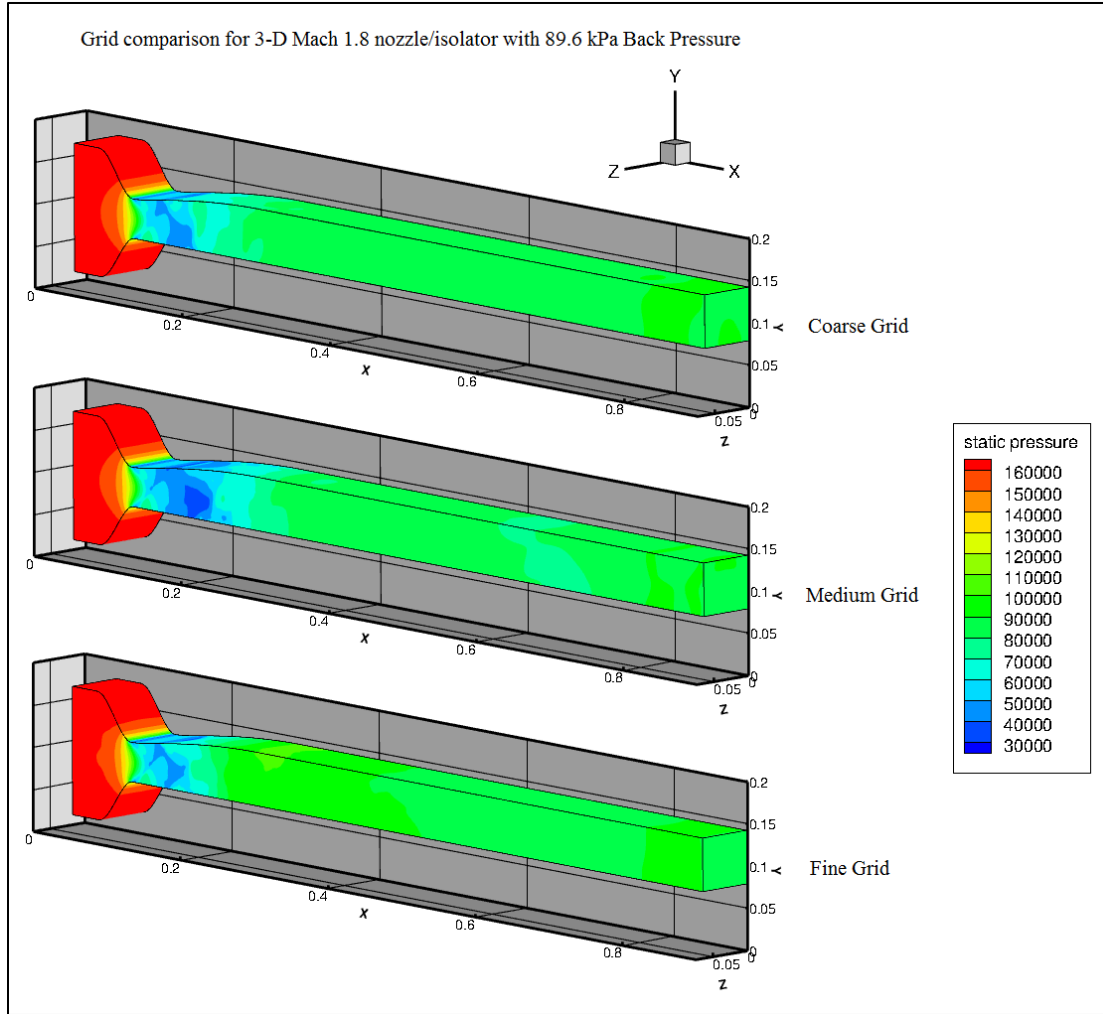


Figure 54. Grid comparison for 3-D nozzle/isolator for 89.6 kPa back pressure

Temporal Resolution Study

Like the 2-D section, a temporal resolution study was accomplished for 3-D to check that the solution is independent of the time step. Three time steps (1.0×10^{-6} , 1.0×10^{-7} , and 1.0×10^{-8}) were used to determine the effect on results. The stepped back pressure of 89.6 kPa was applied from 1 to 6 milliseconds using the time steps above. The simulation with the 1.0×10^{-6} time step diverged when started. Figure 55 presents the results of the other two time steps. Like the 2-D temporal resolution study, the difference in the leading edge

here (at 0.52 meters on the x-axis) is also just barely 1 millimeter. As with the 2-D, the time step of 1.0×10^{-7} was used to save computer time and resources.

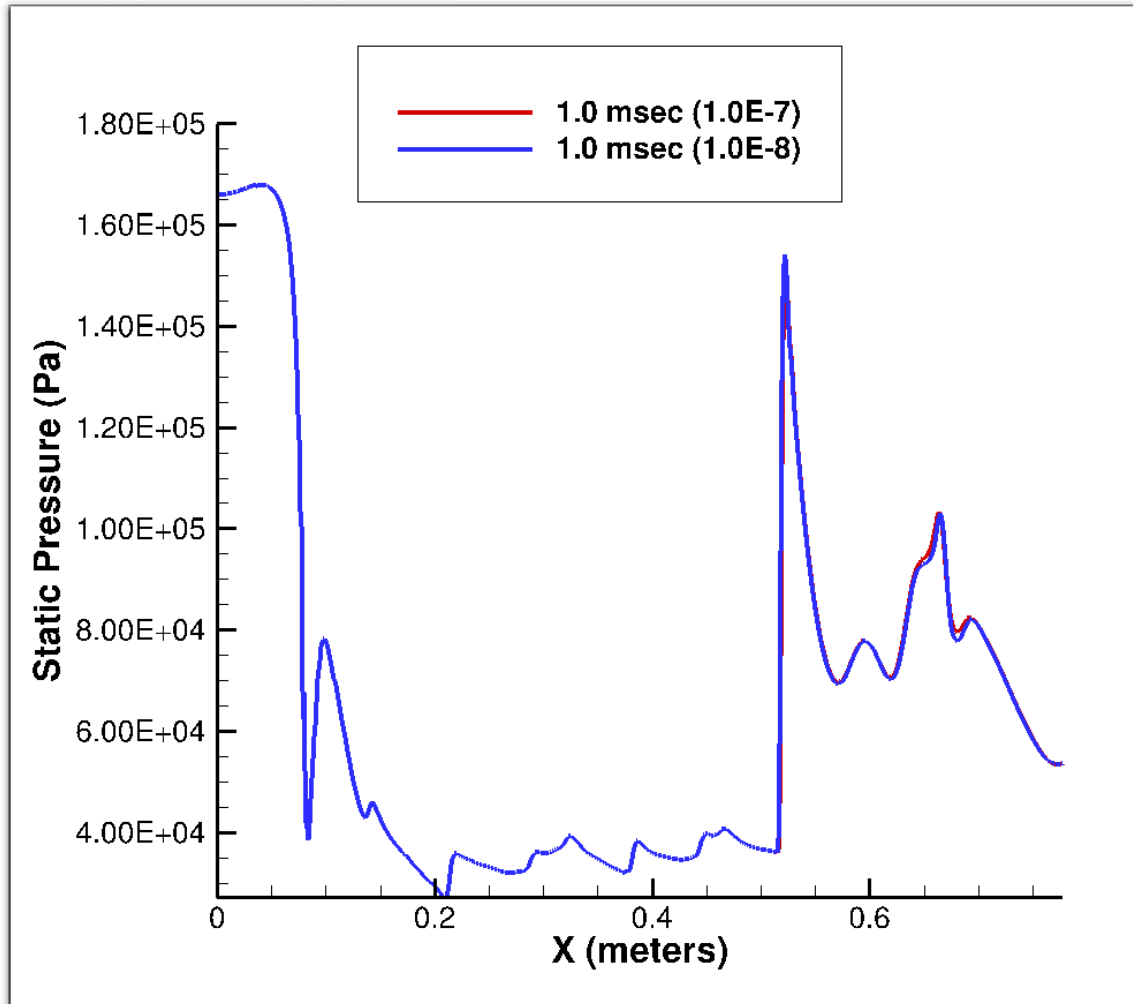


Figure 55. 3-D Temporal Resolution Results

Turbulence Model Comparison

As done previously in the 2-D section, a comparison was done of the final locations of the leading edge of the shock train using the three turbulence models available in VULCAN at a back pressure of 89.6 kPa for an inflow pressure of 168.2 kPa. Figure 56 has the results. The Menter-SST model had the shock train furthest upstream in the isolator, followed by Menter and $k-\omega$. For the 3-D simulations, the turbulence model

used was $k-\omega$, since $k-\omega$ was closest to the AFIT experimental runs for the final location (which is presented in the Analysis section).

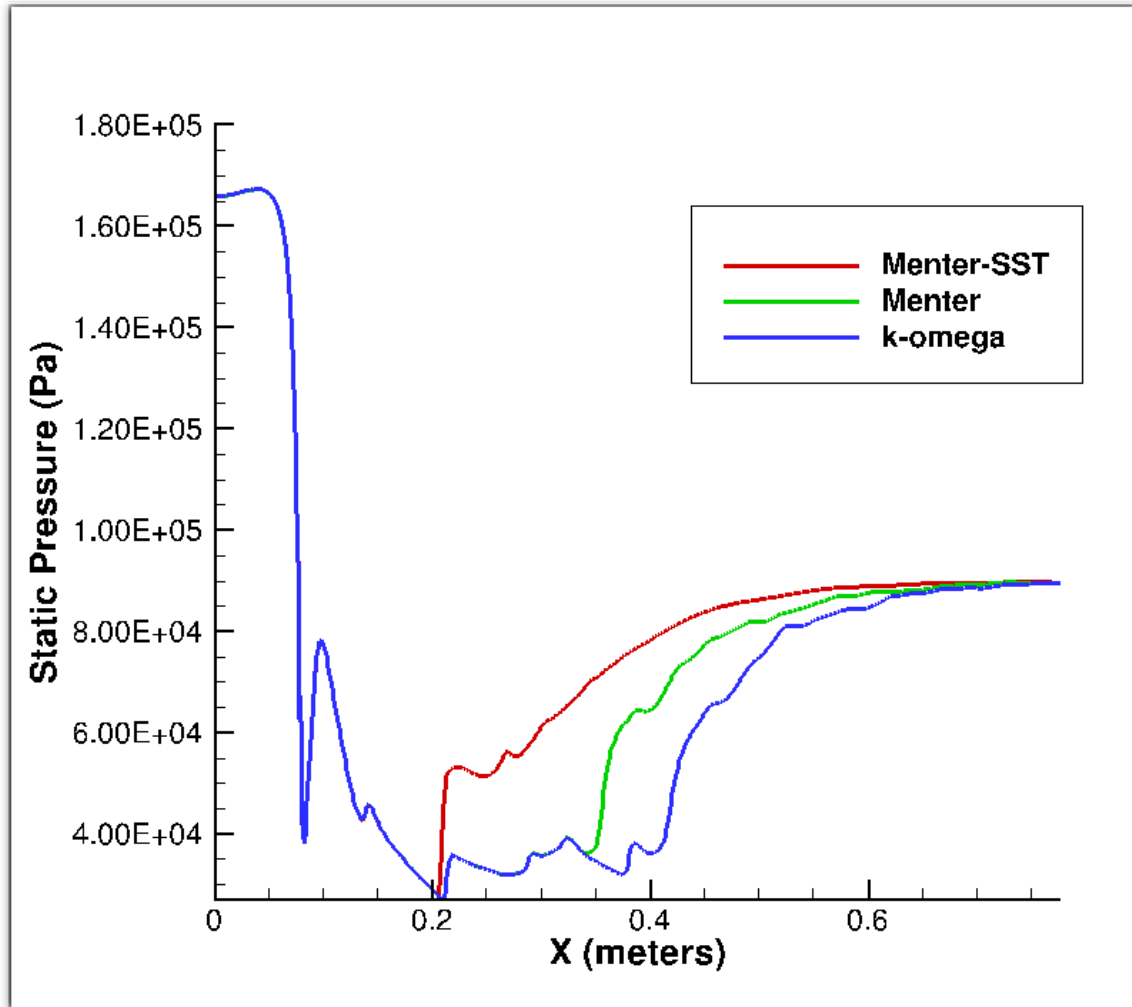


Figure 56. Comparison of Turbulence Models in 3-D

Gradual application of backpressure

Figures 57 and 58 show the evolution of the PCST in the 3-D nozzle/isolator when 89.6 kPa back pressure was applied gradually (stepped) in the same manner as the 2-D simulation (Figure 35). The PCST appeared at six milliseconds after the gradual application of the back pressure started. At seven milliseconds, the shock train was further upstream. At eight milliseconds, the shock train is at a location further downstream than where it was at seven milliseconds. The shock train location at eight

milliseconds indicates the shock train traveled upstream and reversed direction back downstream sometime between seven and eight milliseconds. The simulation continued until the stopping criteria was met at 14 milliseconds, when the leading edge stopped moving and the mass imbalance was less than 1% (-0.59%).

The results in Figures 57 and 58 showed that the leading edge of the shock train (identified as the diagonal line between blue and green in the top panel of Figure 57) along the bottom wall at 6 and 7 milliseconds was further upstream than at the top or side walls. The differences in the leading edge indicate the time history needs to be analyzed along all four walls of the isolator for 3-D. Figure 59 shows the locations of where the time histories in the 3-D simulation were examined. The bottom of the isolator wall in the stream wise direction is identified on Figure 59 as line S1 and was used to track and graph the leading edge of the shock train in 3-D. The time history of the top (S2), left (S3), and right (S4) walls of the isolator walls were also tracked and graphed. Figures 60, 61, 62, and 63 show time histories along these four lines, respectively. In Figure 60, the shock train at the bottom of the isolator appears at 6 milliseconds. It traveled upstream until 7.7 milliseconds (at 25.4 cm), reversed direction, and then moved downstream until reaching a final location (at 39.7 cm) and the stopping criteria at 14 milliseconds. A comparison of Figures 60 and 61 showed that the bottom (S1) was further upstream for both reversal and final locations than the top (S2). The reason for this difference between the top and bottom walls is the asymmetric shape (geometry) of the nozzle, already seen and identified in the 2-D results. The left and right sides (Figures 62 and 63) are almost identical with no major differences in location. The remaining back pressure cases show similar results for the differences in the walls in the next several pages of this chapter.

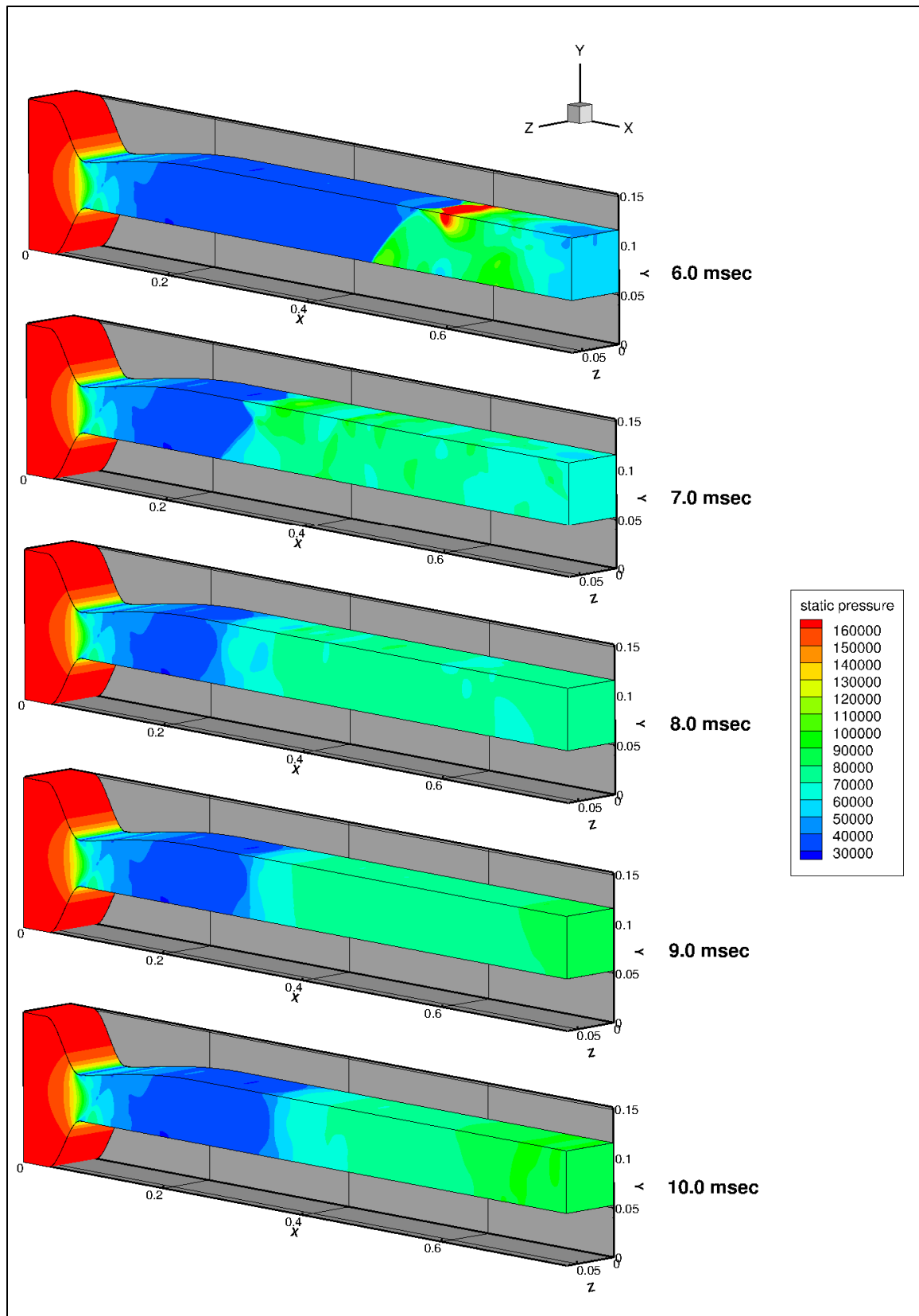


Figure 57. Evolution of PCST solution for 89.6 kPa back pressure

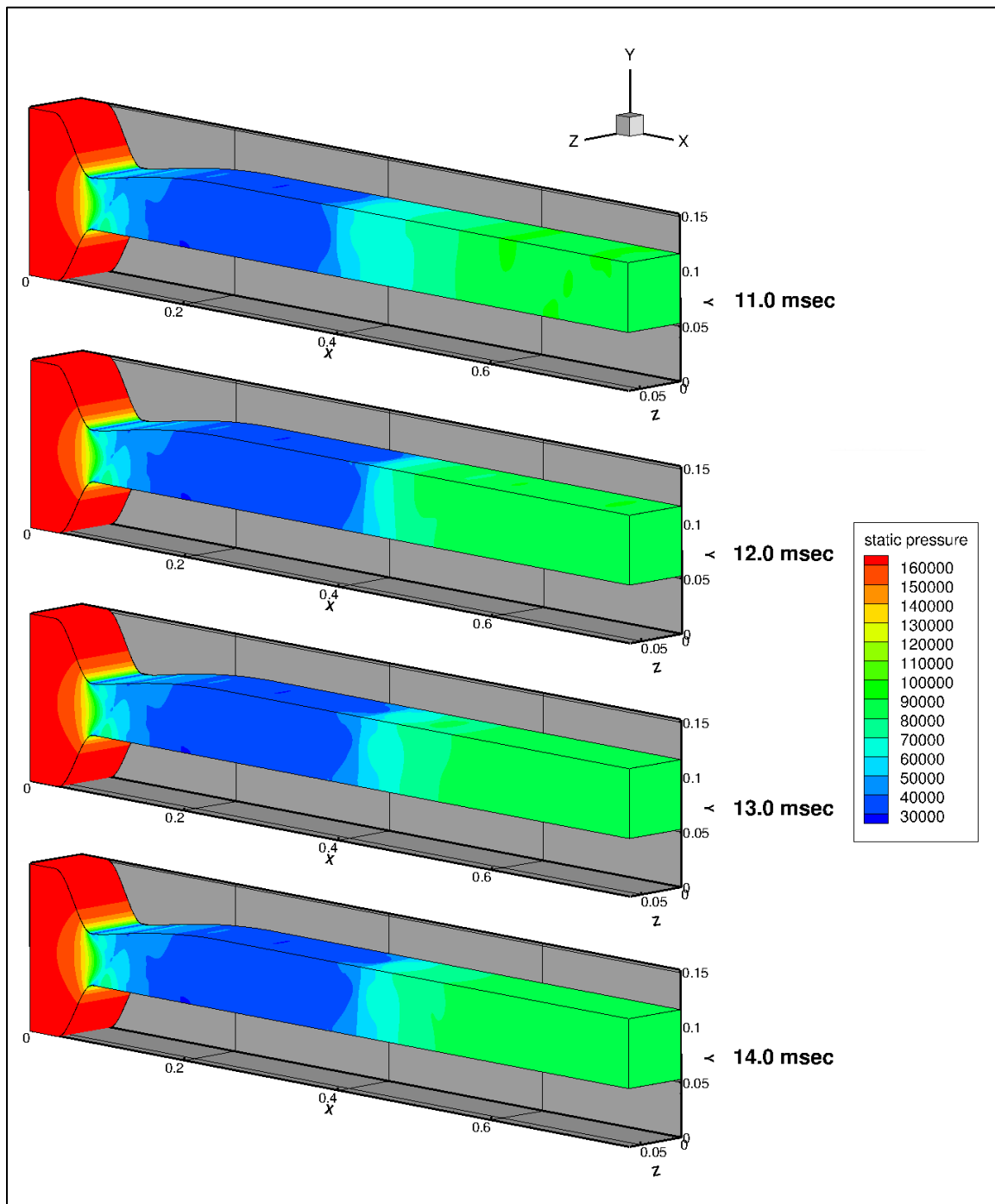


Figure 58. Evolution of PCST for 89.6 kPa back pressure continued

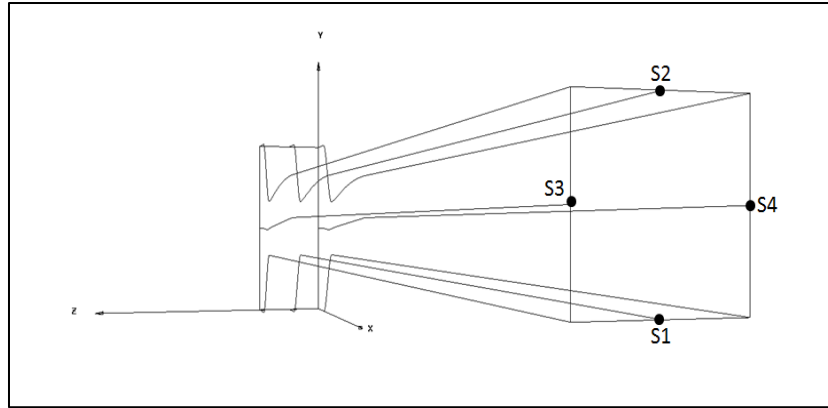


Figure 59. Lines of time history read for back pressure

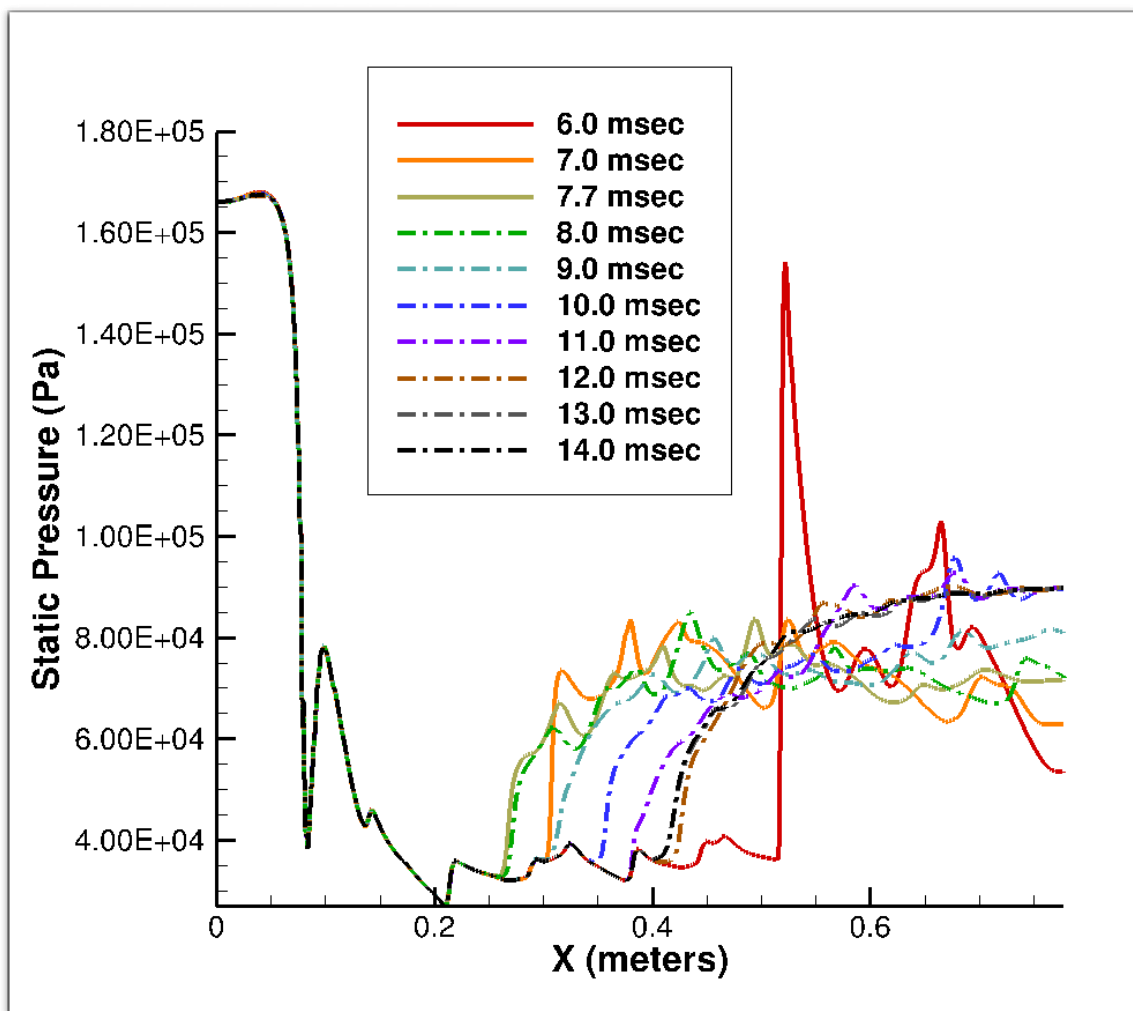


Figure 60. Time history for 89.6 kPa back pressure along line S1 (bottom) in the nozzle/isolator.

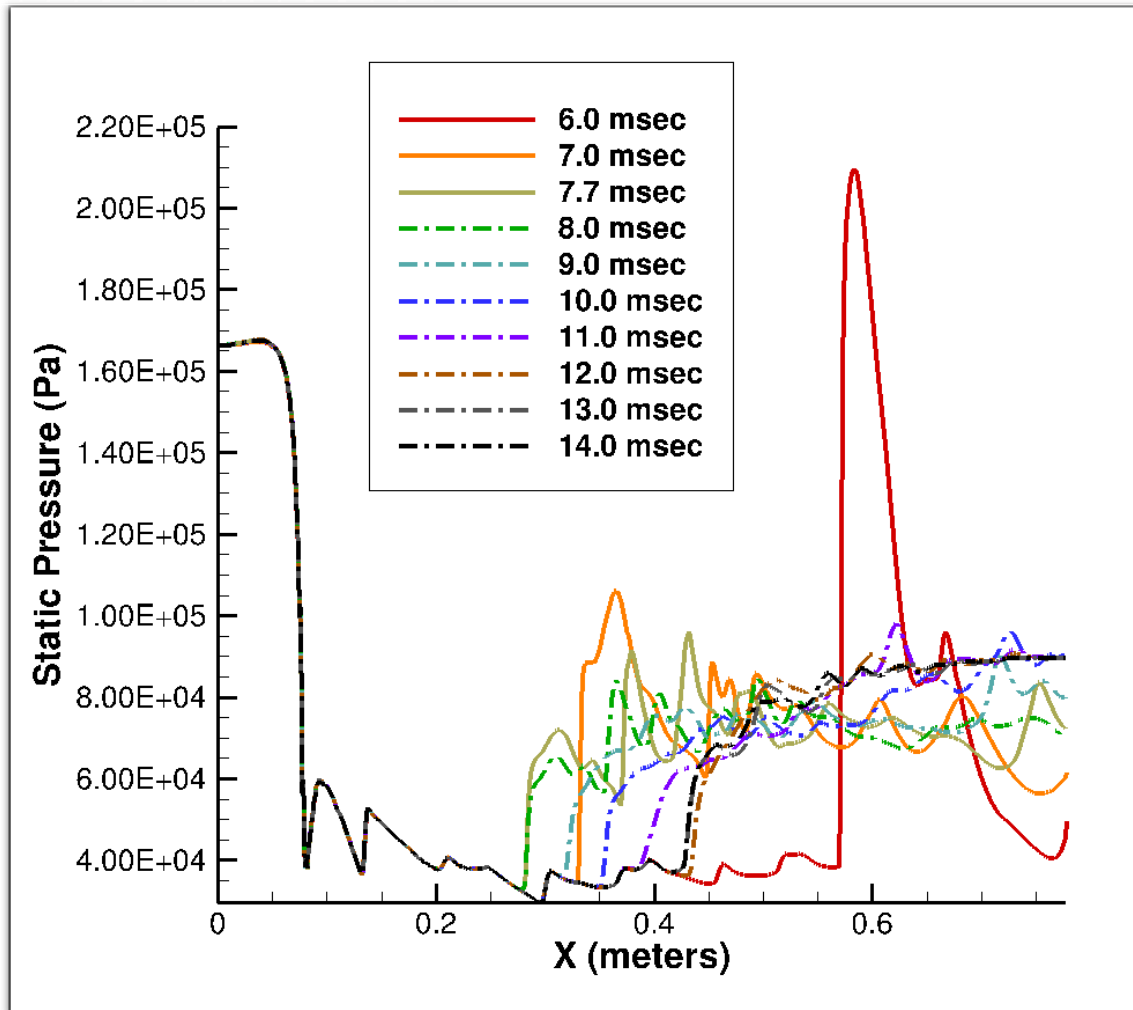


Figure 61. Time history for 89.6 kPa back pressure along line S2 (top) in the nozzle/isolator

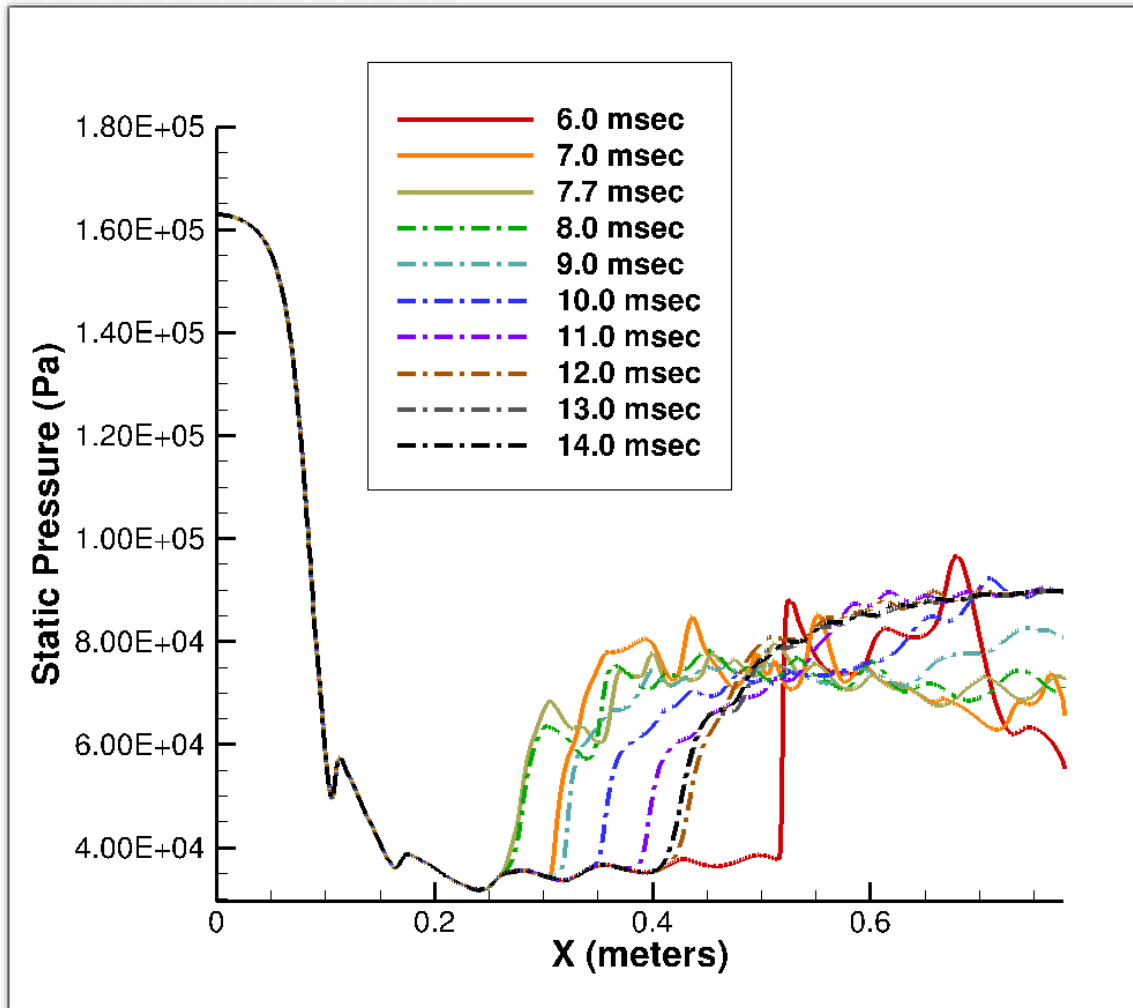


Figure 62. Time history for 89.6 kPa back pressure along line S3 (left) in the nozzle/isolator

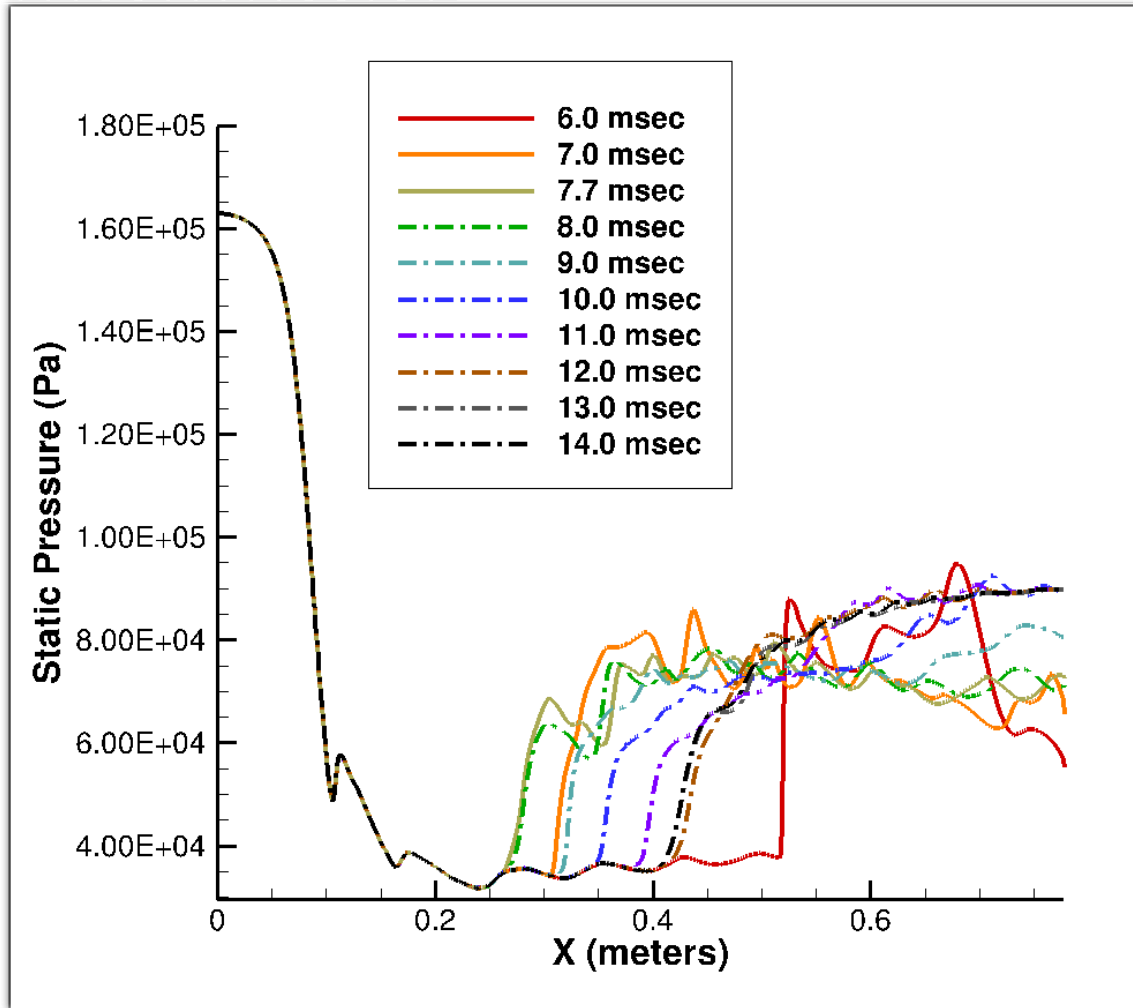


Figure 63. Time history for 89.6 kPa back pressure along line S4 (right) in the nozzle/isolator

Figures 64 and 65 show the evolution of the PCST in the 3-D nozzle/isolator for an 85.0 kPa back pressure. The PCST appeared at seven milliseconds after the back pressure gradual application started. At eight and again at nine milliseconds, the shock train is further upstream. At 10 milliseconds, the shock train is at a location further downstream than at 9 milliseconds, indicating the shock train traveled upstream and reversed direction back downstream sometime between 9 and 10 milliseconds. The simulation continued until 36 milliseconds, when the stopping criteria were reached.

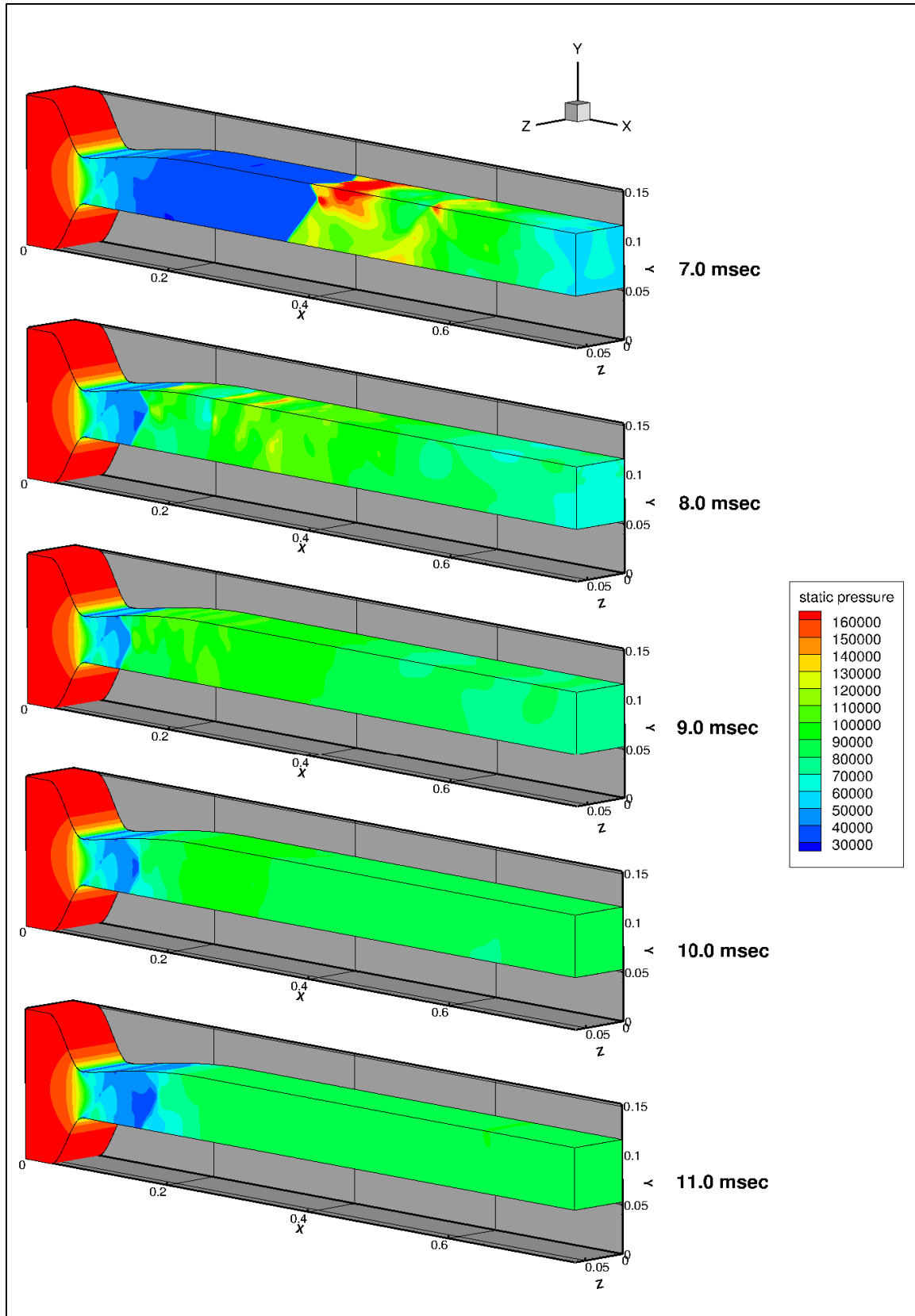


Figure 64. Evolution of PCST solution for 85.0 kPa back pressure

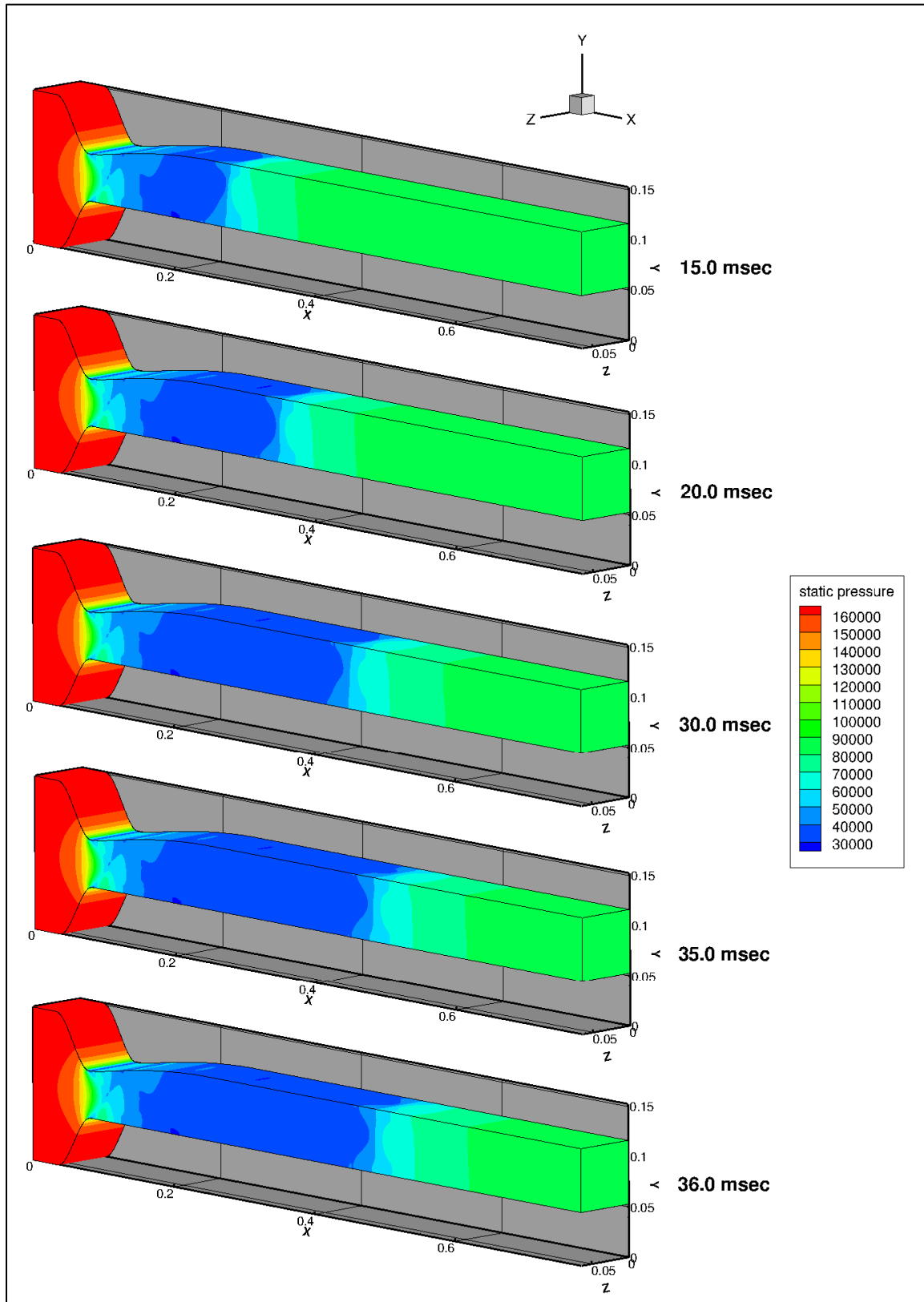


Figure 65. Evolution of PCST solution for 85.0 kPa back pressure continued

Figures 66 and 67 show the time histories of the top and bottom walls, respectively, for the 85.0 kPa simulation. In Figure 66, the shock train at the bottom of the isolator appears at seven milliseconds. The shock train then traveled upstream until 7.7 milliseconds (at 25.4 cm), and then moved downstream until reaches its final location (at 39.7 cm) and the stopping criteria at 14 milliseconds. A comparison of Figures 66 and 67 shows the bottom went further upstream and downstream compared to the top, just like the comparison in the 89.6 kPa simulation.

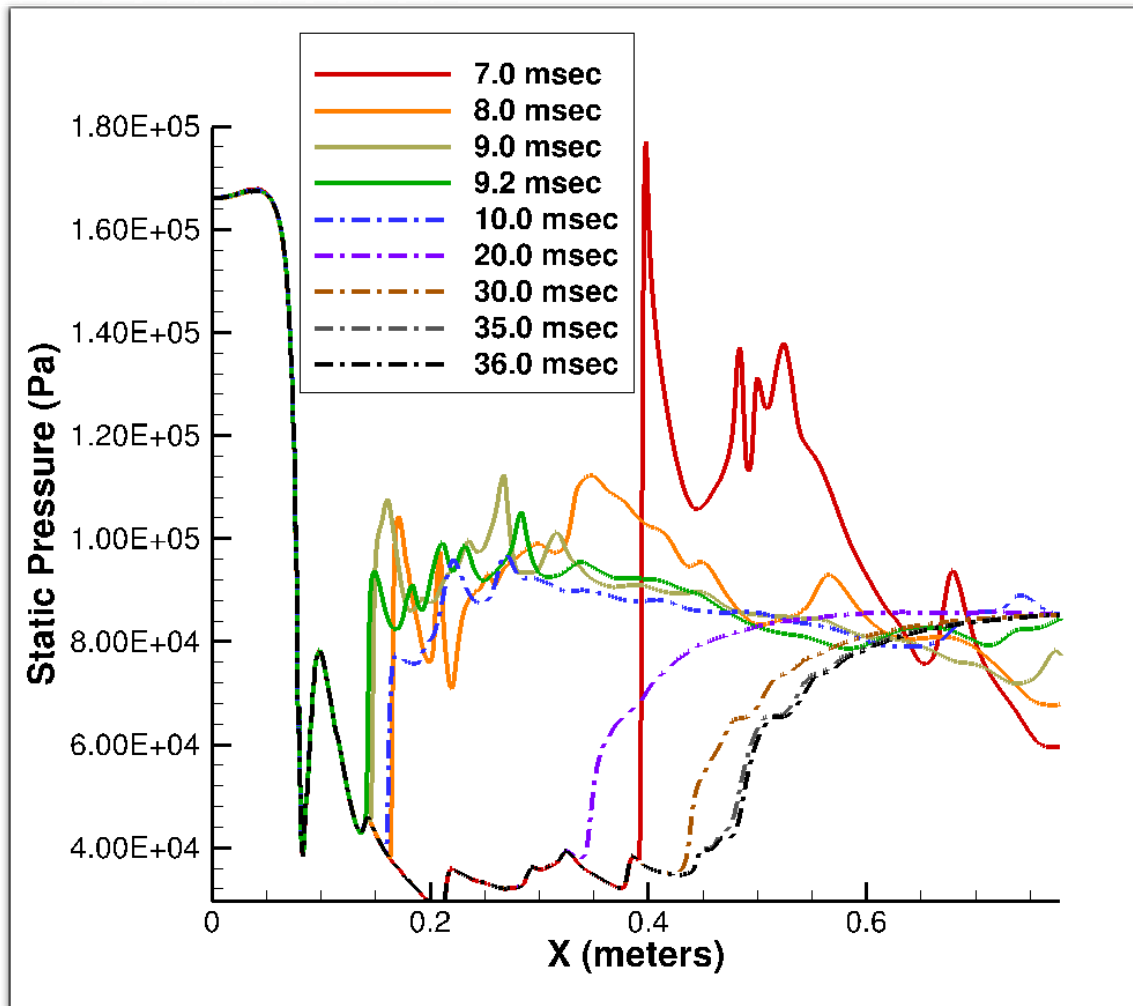


Figure 66. Time history for 85.0 kPa back pressure along line S1 (bottom) in the nozzle/isolator

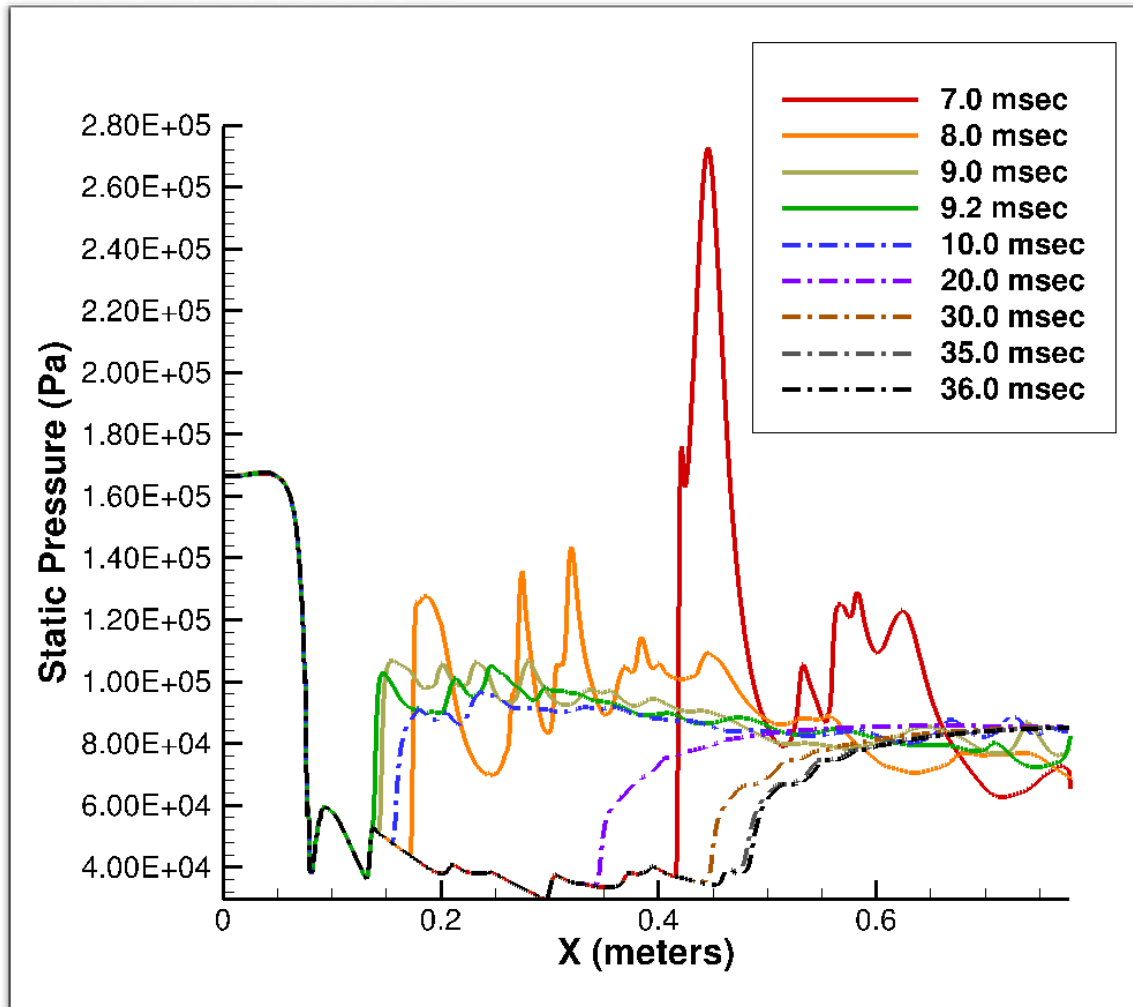


Figure 67. Time history for 85.0 kPa back pressure along line S2 (top) in the nozzle/isolator

The S3 and S4 lines (Figures 68 and 69) of the 85.0 kPa simulation are almost identical. The comparison between the left and right sides of the 85.0 kPa case is similar to the results seen in the S3 and S4 lines of the 89.6 kPa simulation, which were also almost identical.

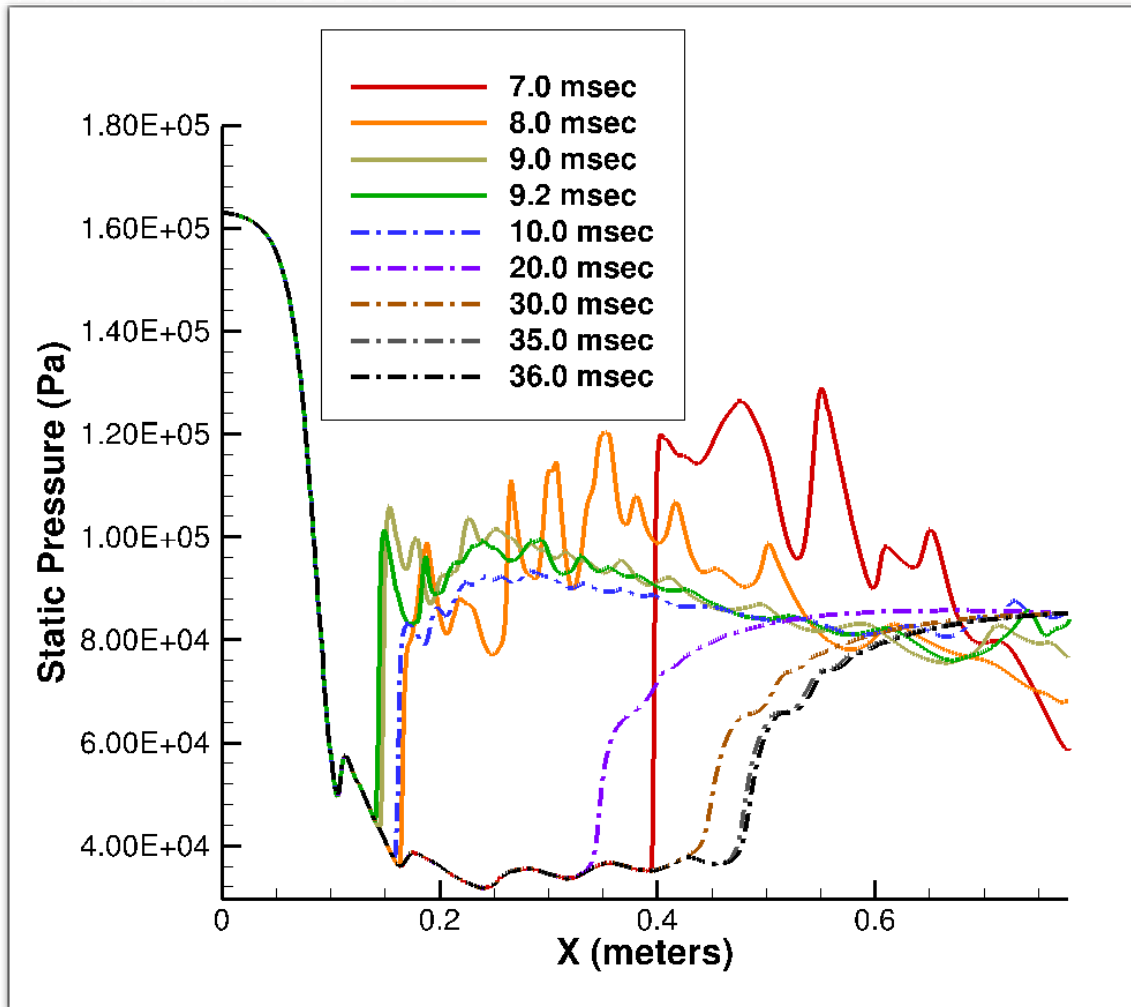


Figure 68. Time history for 85.0 kPa back pressure along line S3 (left) in the nozzle/isolator

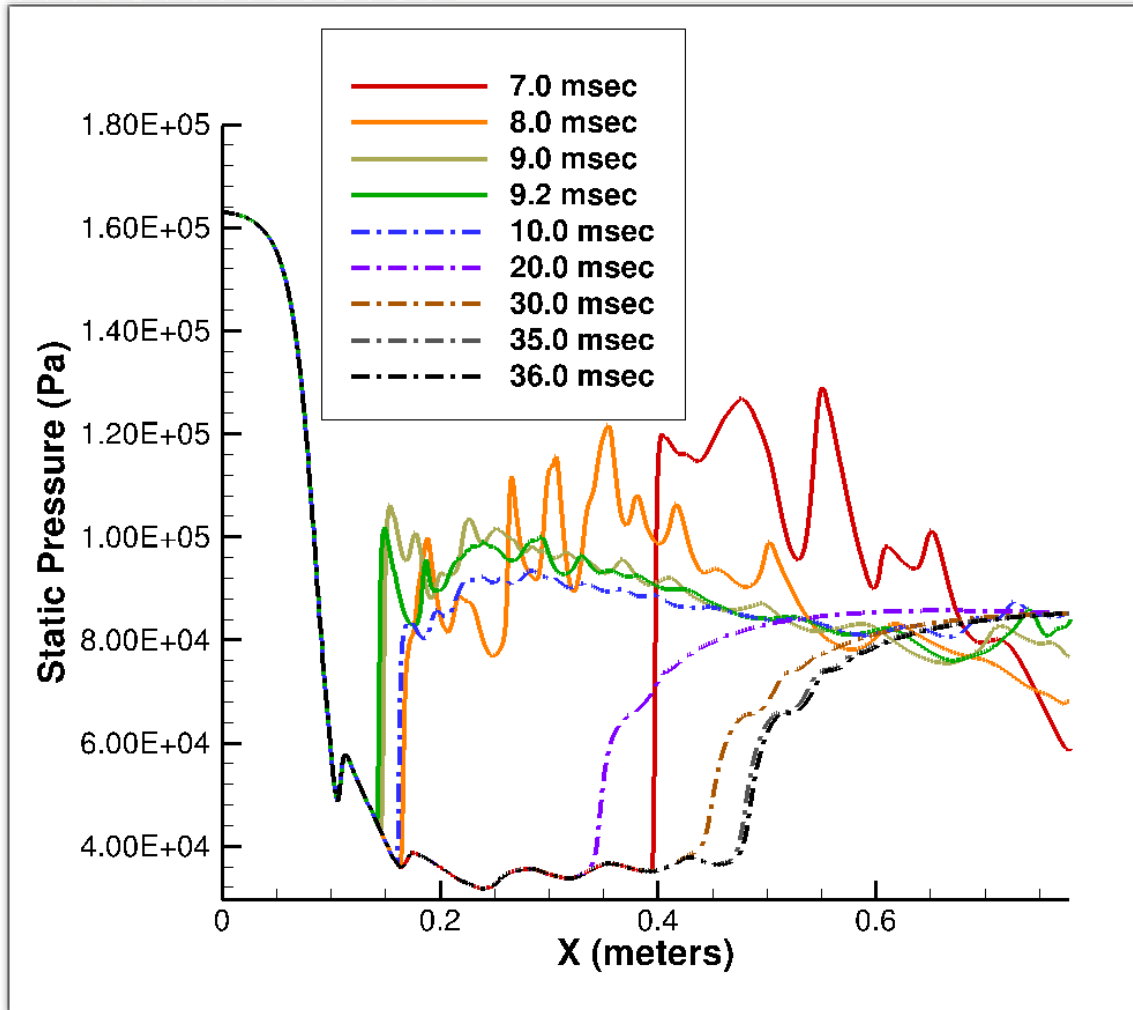


Figure 69. Time history for 85.0 kPa back pressure along line S4 (right) in the nozzle/isolator

Figures 70 and 71 show the evolution of the PCST in the 3-D nozzle/isolator for a 75.0 kPa back pressure. The PCST appeared at 7 milliseconds. At eight milliseconds, it was further upstream while at nine milliseconds, it was further downstream. The difference in location between eight and nine milliseconds means the shock train reversed direction sometime during that one millisecond time interval. The simulation continued until the stopping criteria were met at 26 milliseconds.

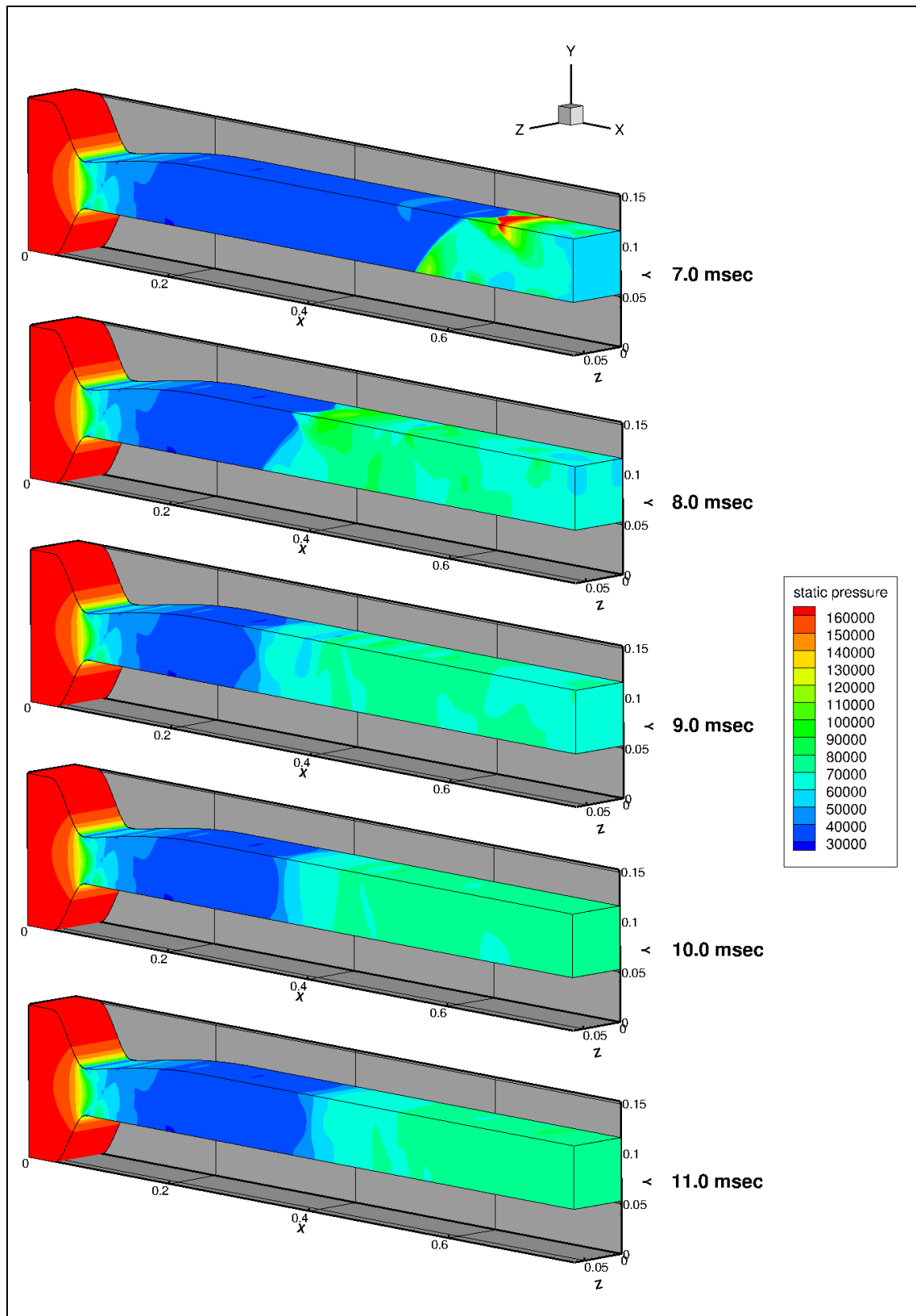


Figure 70. Evolution of PCST solution for 75.0 kPa back pressure

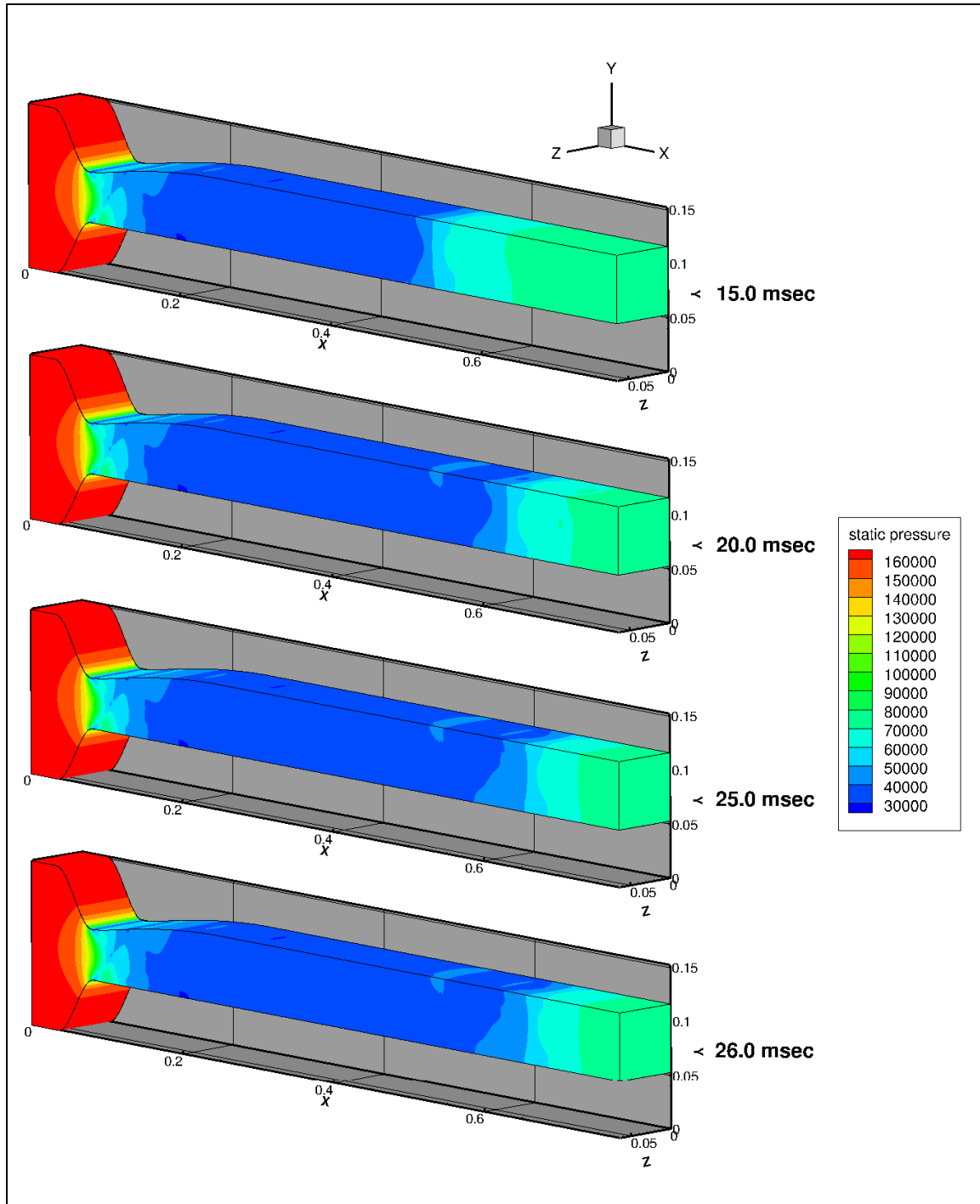


Figure 71. Evolution of PCST solution for 75.0 kPa back pressure continued

Figures 72 and 73 show the time histories of the top and bottom walls, respectively, for the 75.0 kPa simulation. In Figure 72, the shock train appears at seven milliseconds. It traveled upstream until 8.9 milliseconds (at 29.3 cm), then reversed direction and moved downstream until it reaching a final location (at 62.9 cm) and the stopping criteria at 26 milliseconds. A comparison of Figures 72 and 73 with the Figures 60-61 and 66-67 show the same differences between top and bottom.

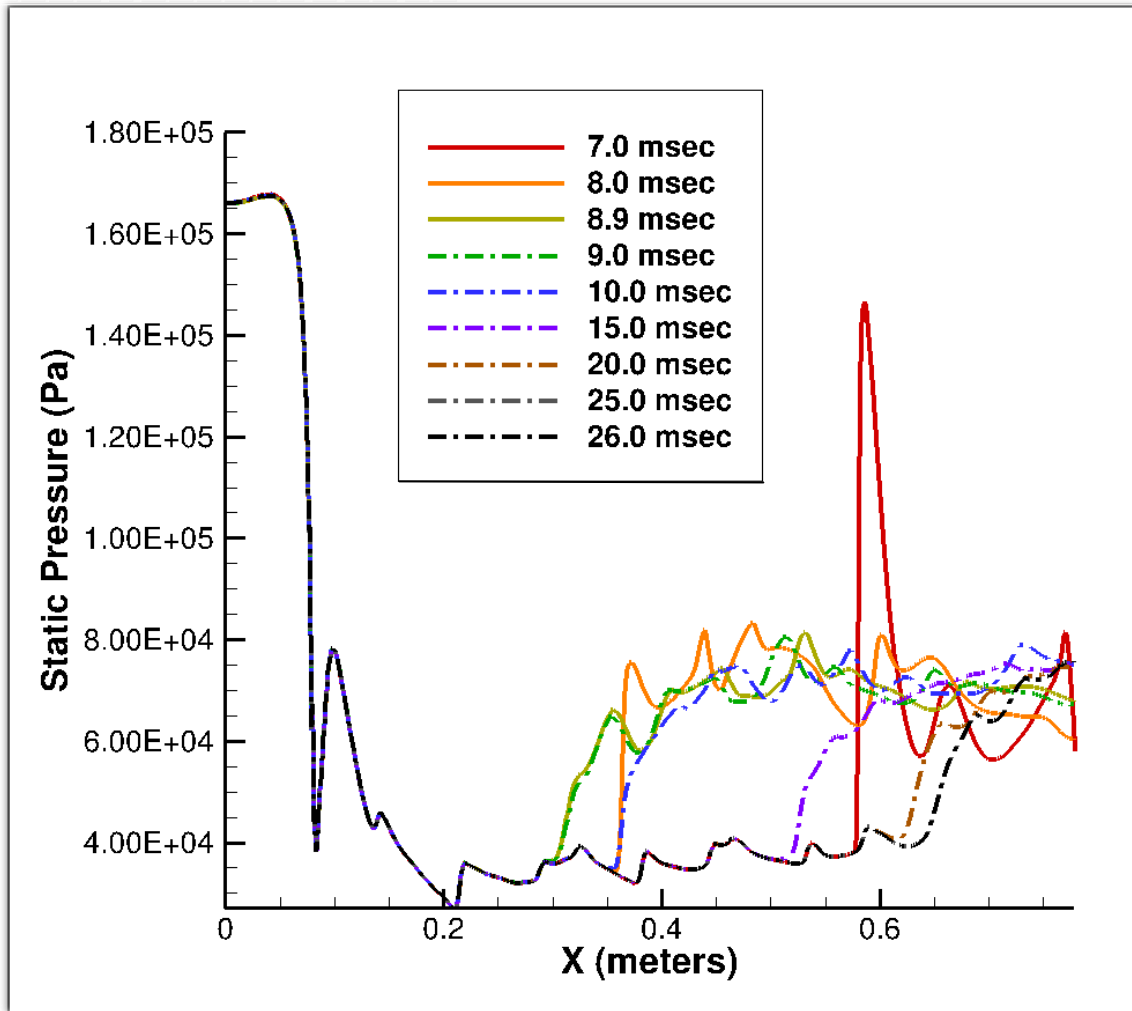


Figure 72. Time history for 75.0 kPa back pressure along line S1 (bottom) in the nozzle/isolator

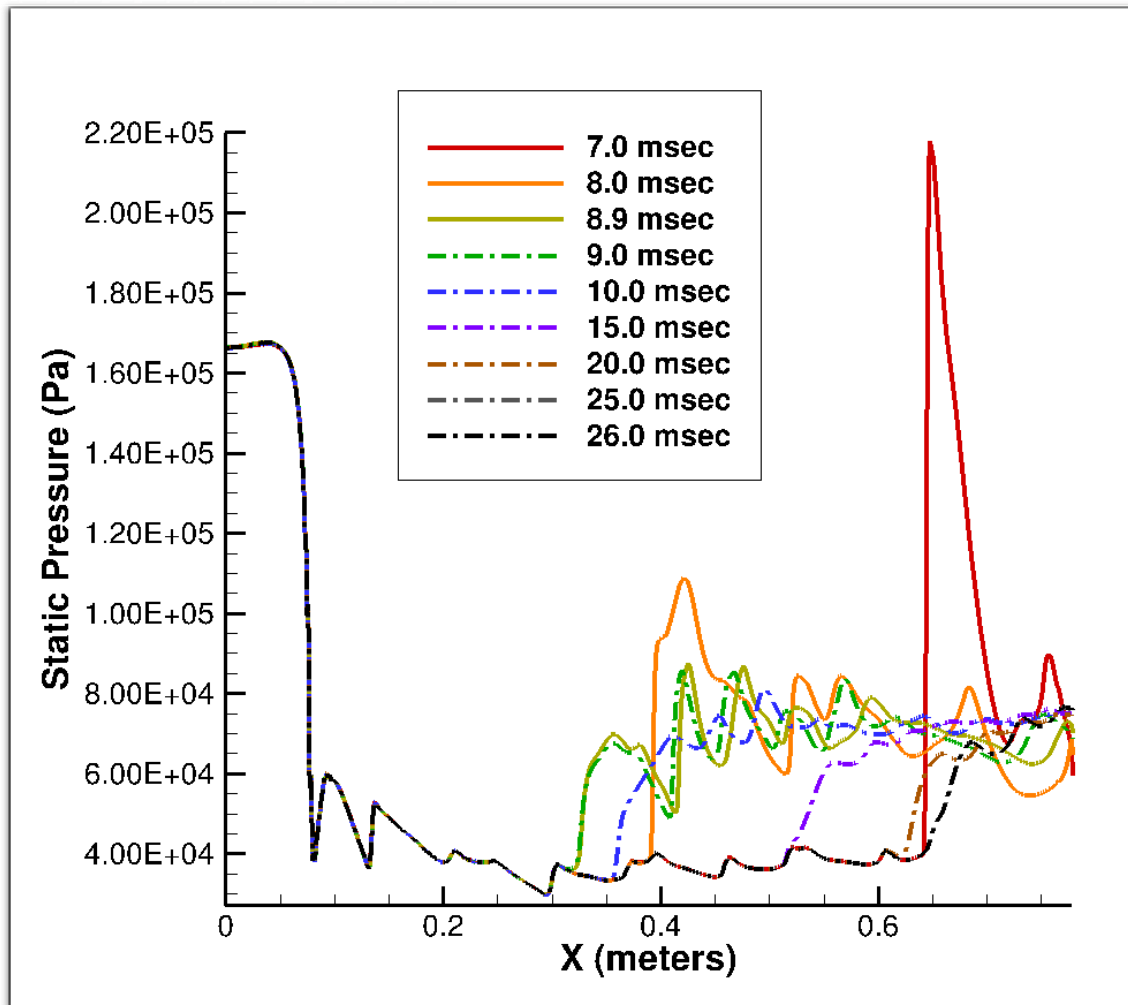


Figure 73. Time history for 75.0 kPa back pressure along line S2 (top) in the nozzle/isolator

The left and right sides (Figures 74 and 75) of the 75.0 kPa simulation are almost identical. The identical S3 and S4 lines are, again, the same characteristic that was also seen in both the 89.6 kPa and 85.0 kPa simulations.

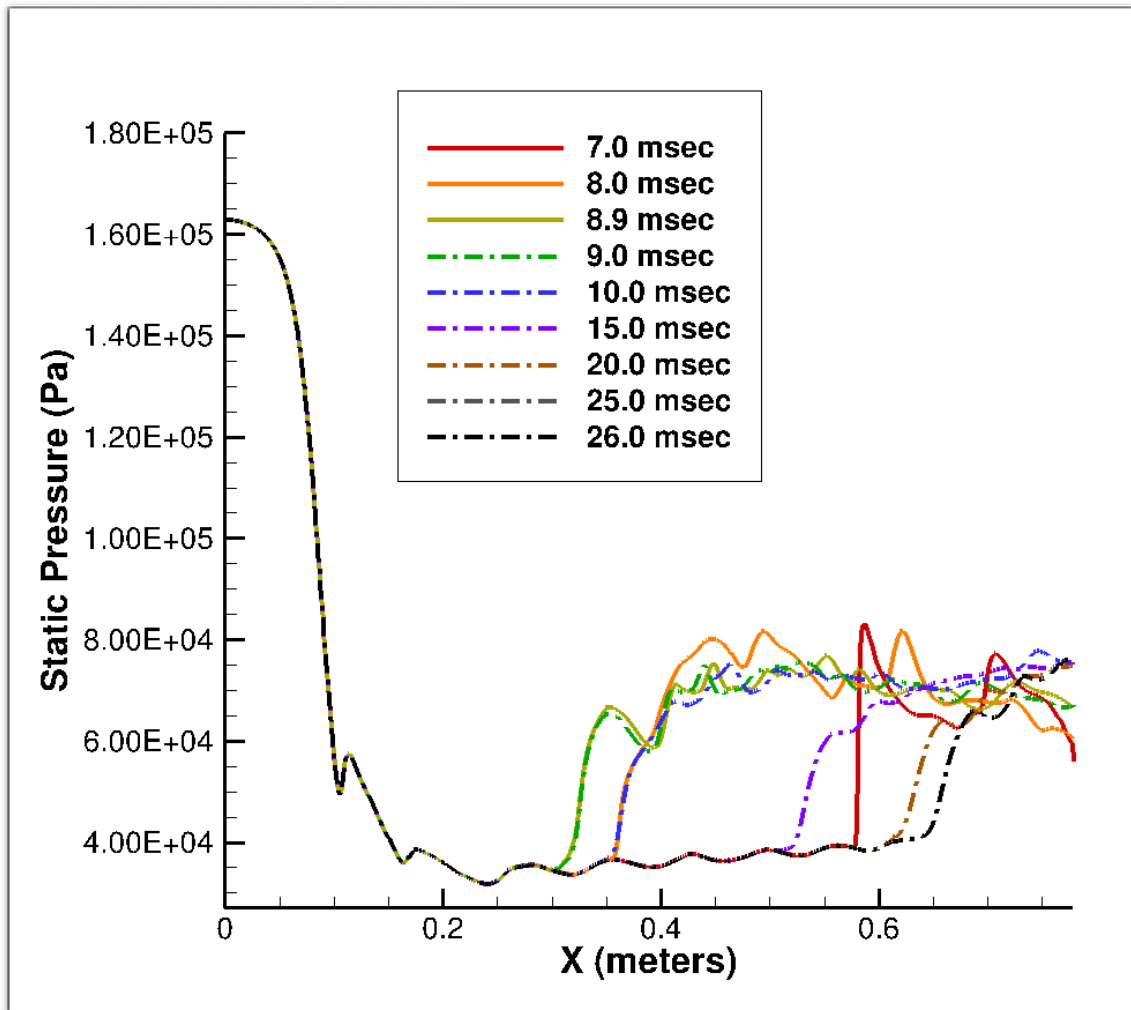


Figure 74. Time history for 75.0 kPa back pressure along line S3 (left) in the nozzle/isolator

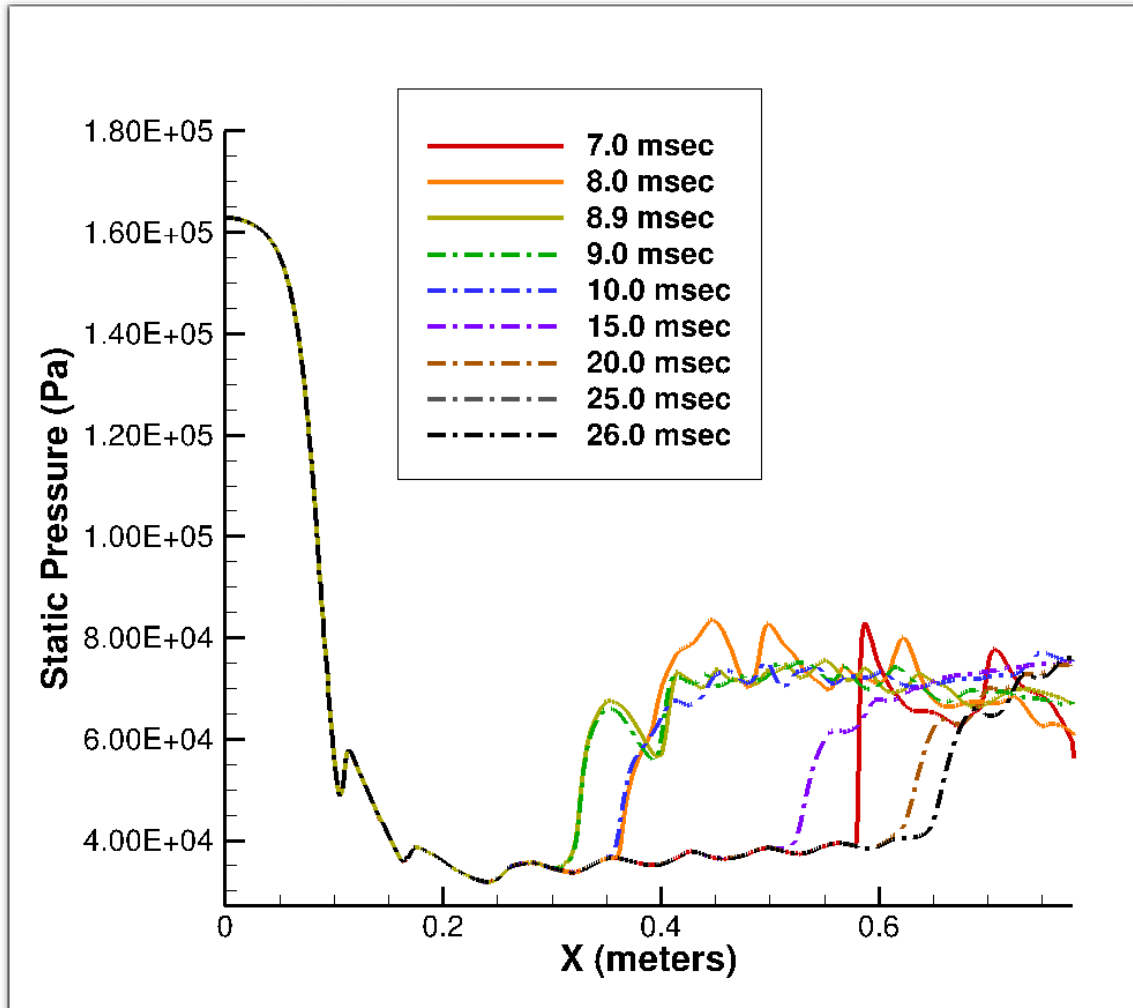


Figure 75. Time history for 75.0 kPa back pressure along line S4 (right) in the nozzle/isolator

The next three 3-D simulations were with an inflow pressure of 140.6 kPa for ramped back pressures of 75.0, 71.1 and 62.78 kPa. The ratios of back to total inflow pressure in these three cases were the same as the previous 89.6, 85.0 and 75.0 kPa cases. Figures 76 and 77 are the results of 75.0 kPa back pressure with 140.6 kPa inflow. The PCST appeared at six milliseconds and was further upstream at seven and eight milliseconds while at nine milliseconds, it was further downstream. The locations at eight and nine milliseconds indicate the PCST reversed direction sometime between them. The simulation continued until 15 milliseconds when the stopping criteria were met.

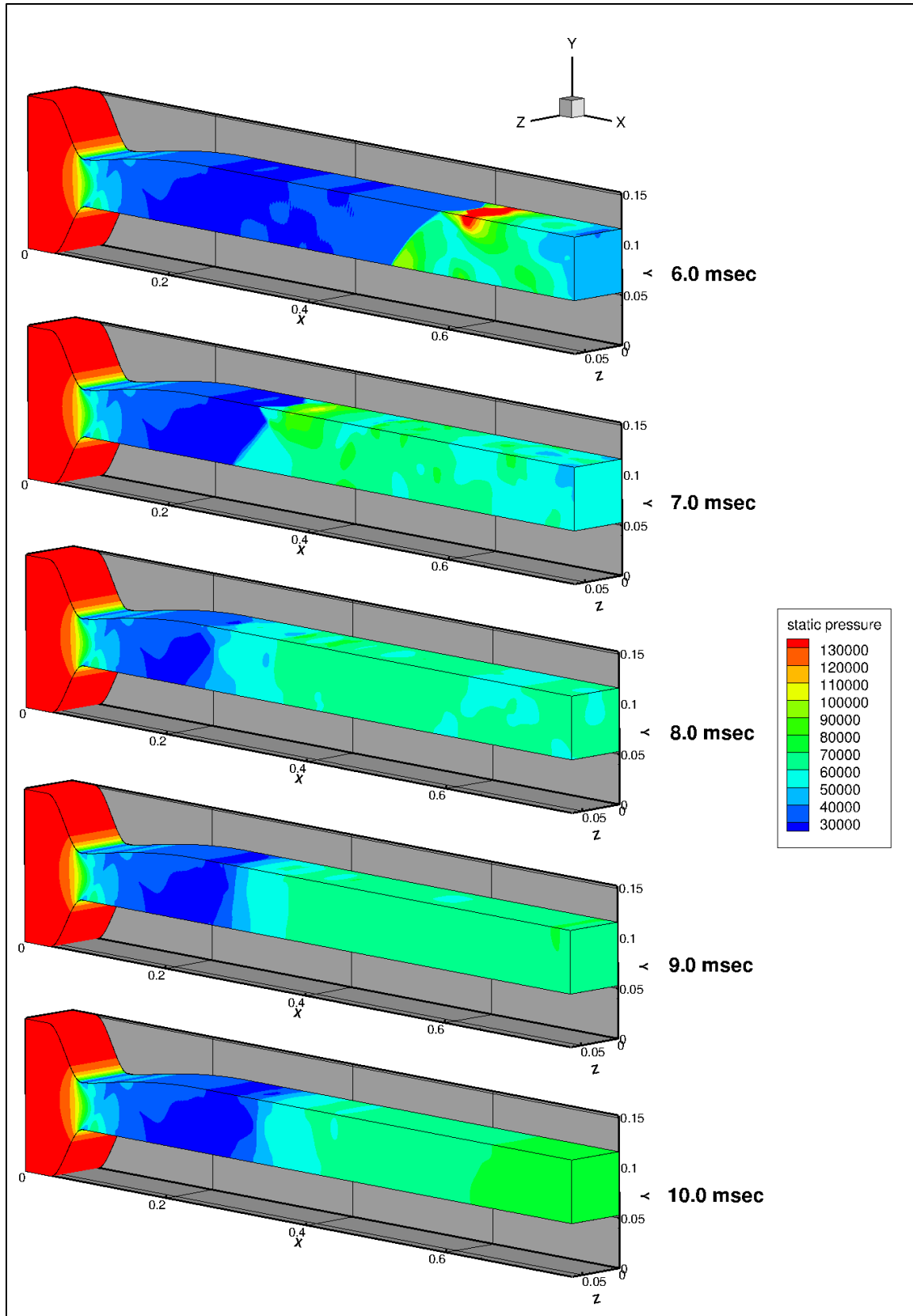
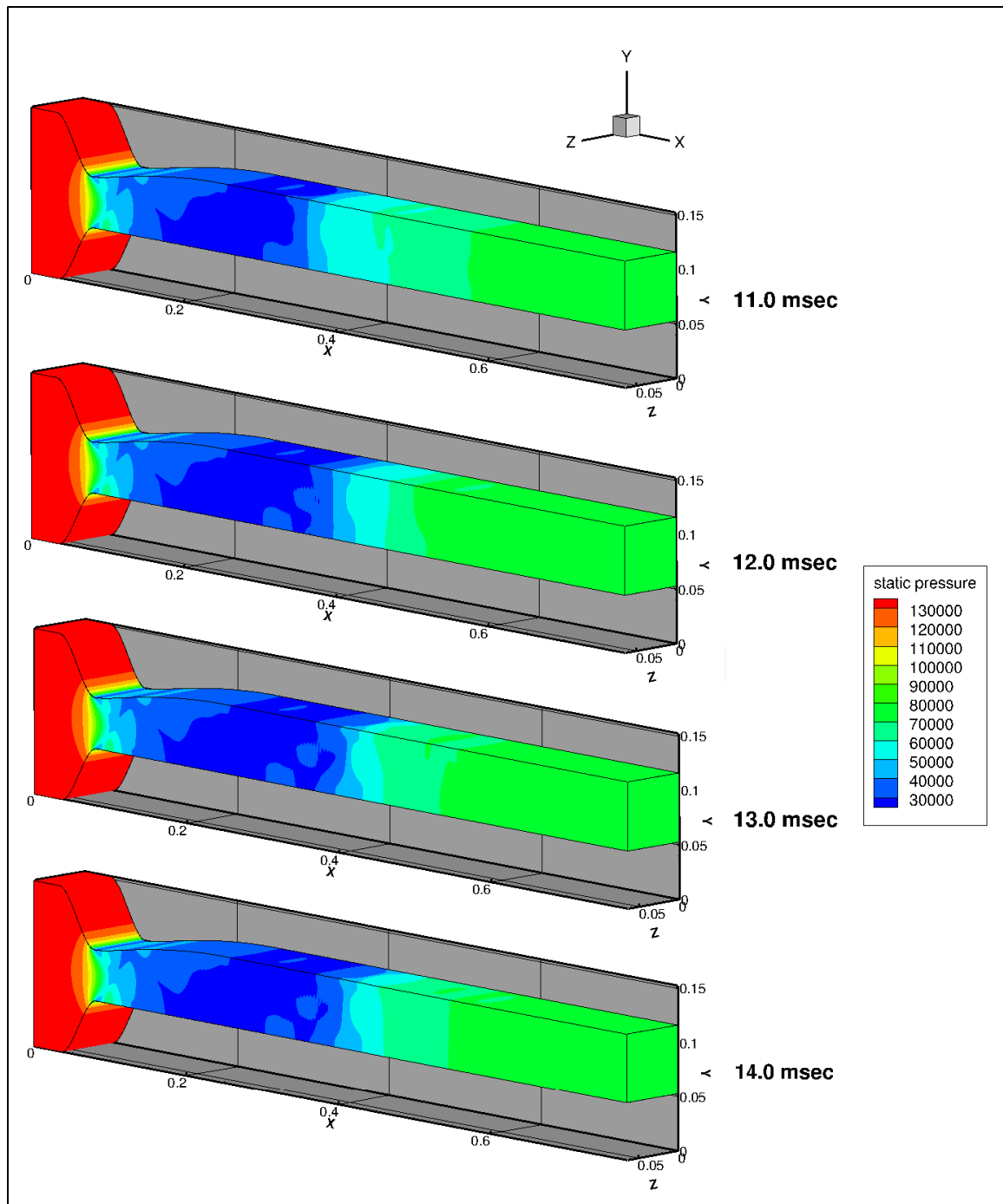


Figure 76. Evolution of PCST solution for 75.0 kPa back pressure (140.6 kPa inflow)



**Figure 77. Evolution of PCST solution for 75.0 kPa back pressure (140.6 kPa inflow)
continued**

Figures 78 and 79 show time histories of the top and bottom wall pressures, respectively, for the 75.0 kPa simulation. In Figure 78, the shock train appeared at six milliseconds, traveled upstream to 24.6 cm (at eight milliseconds), then reversed direction and moved downstream to a final location of 38.2 cm (at 26 milliseconds). Comparison of Figures 78 and 79 showed that both the reversal and final locations of the bottom are farther upstream than the top. Comparison of the simulation with the 89.6 kPa simulation (with the same back to inlet pressure ratio) shows only a 0.3 cm difference between the reverse locations, while the difference between the final locations is 1.5 cm.

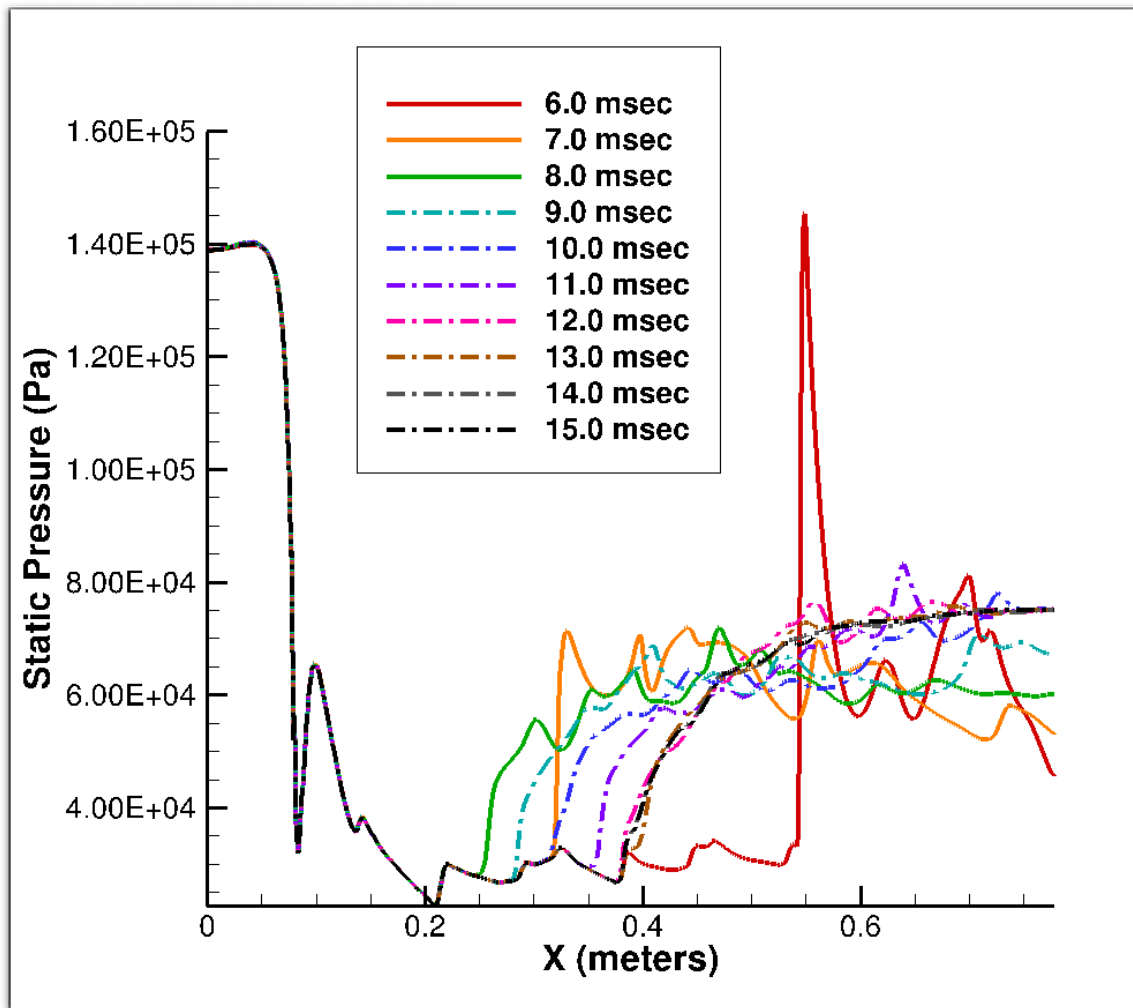


Figure 78. Time history for 75.0 kPa back pressure (140.6 kPa inflow) along line S1 (bottom) in the nozzle/isolator

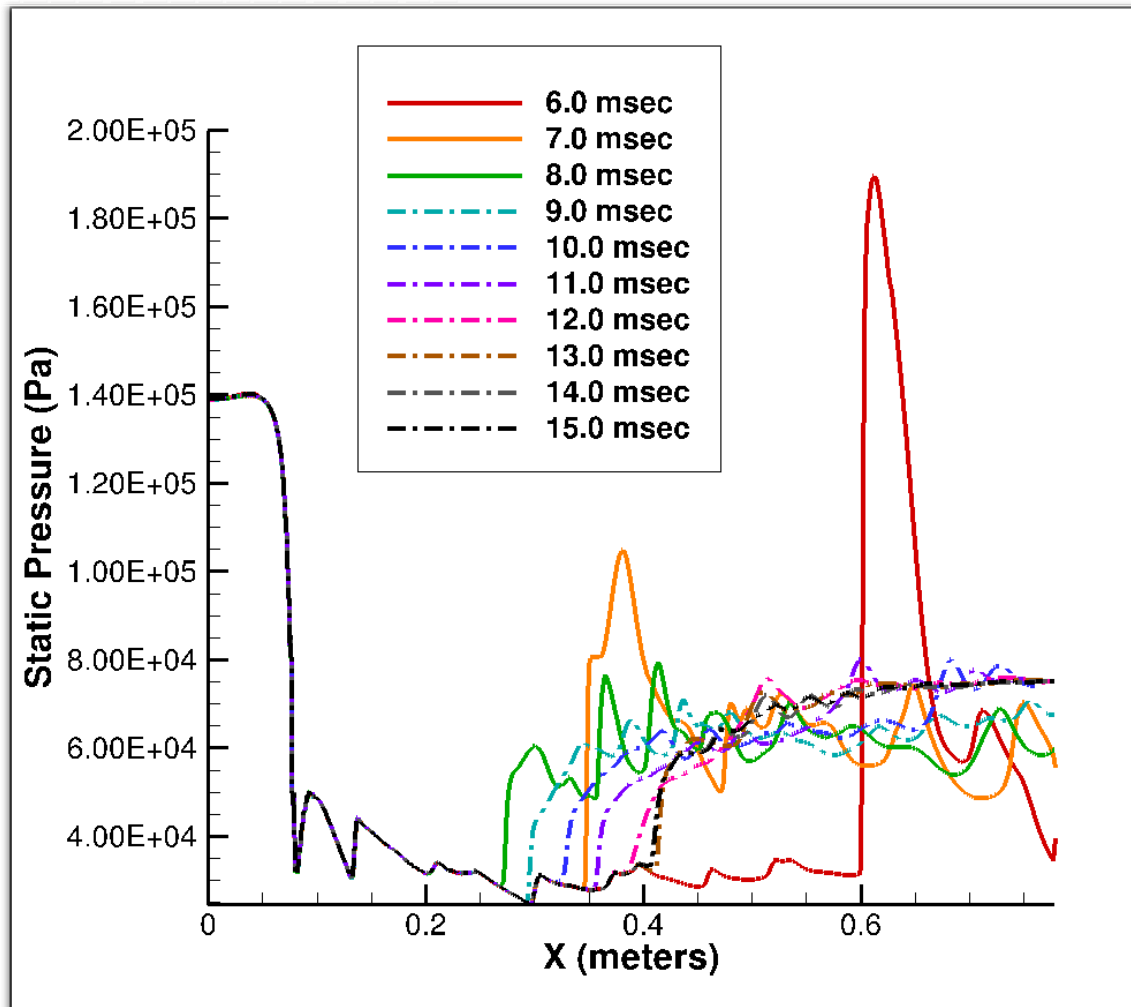


Figure 79. Time history for 75.0 kPa back pressure (140.6 kPa inflow) along line S2 (top) in the nozzle/isolator

Figures 80 and 81 represent the left and right sides of the 75.0 kPa simulation. Comparison of the two figures showed the S3 and S4 lines are almost identical, indicating the results seen for the left and right sides in the simulations with 168.2 kPa inflow pressure are still happening for different back and inflow pressure values.

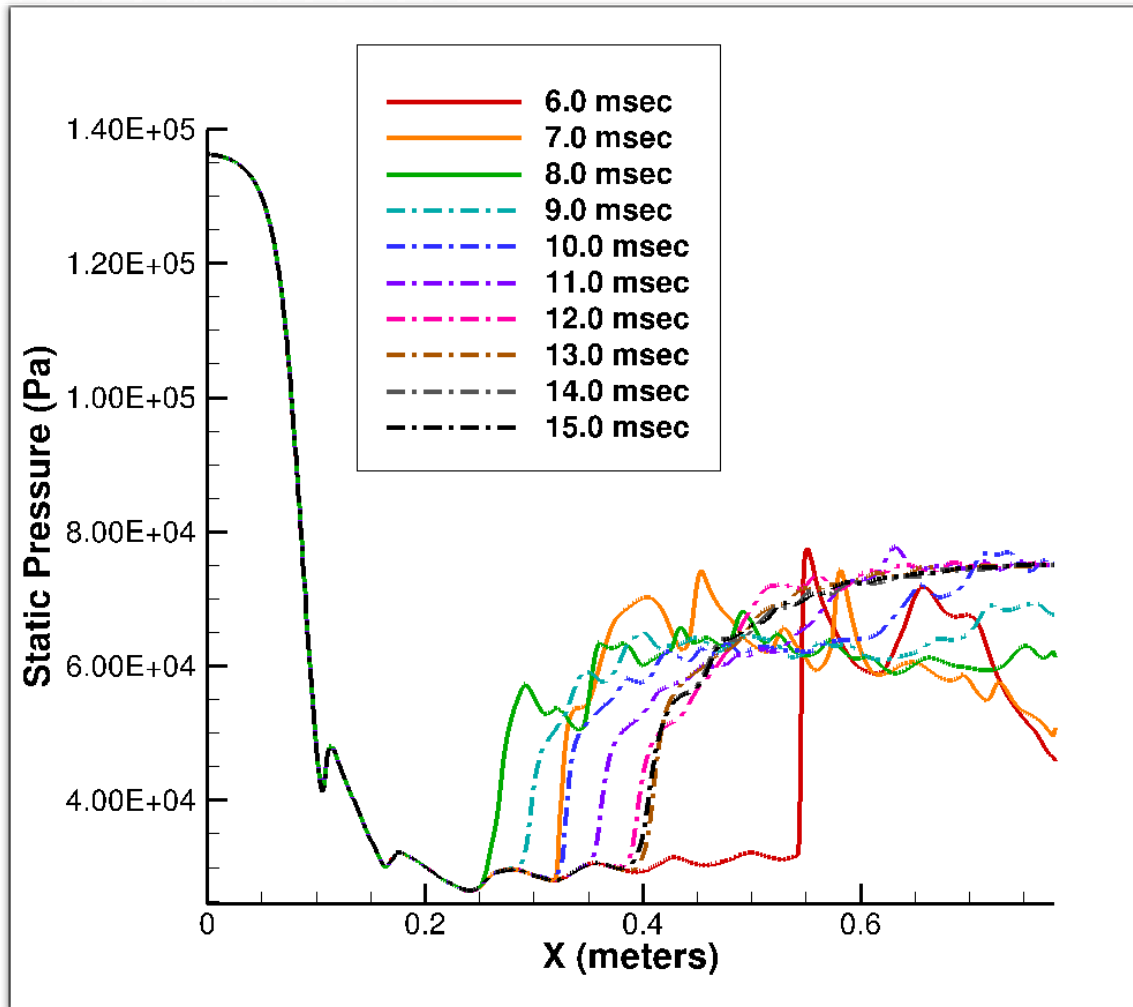


Figure 80. Time history for 75.0 kPa back pressure (140.6 kPa inflow) along line S3 (left) in the nozzle/isolator

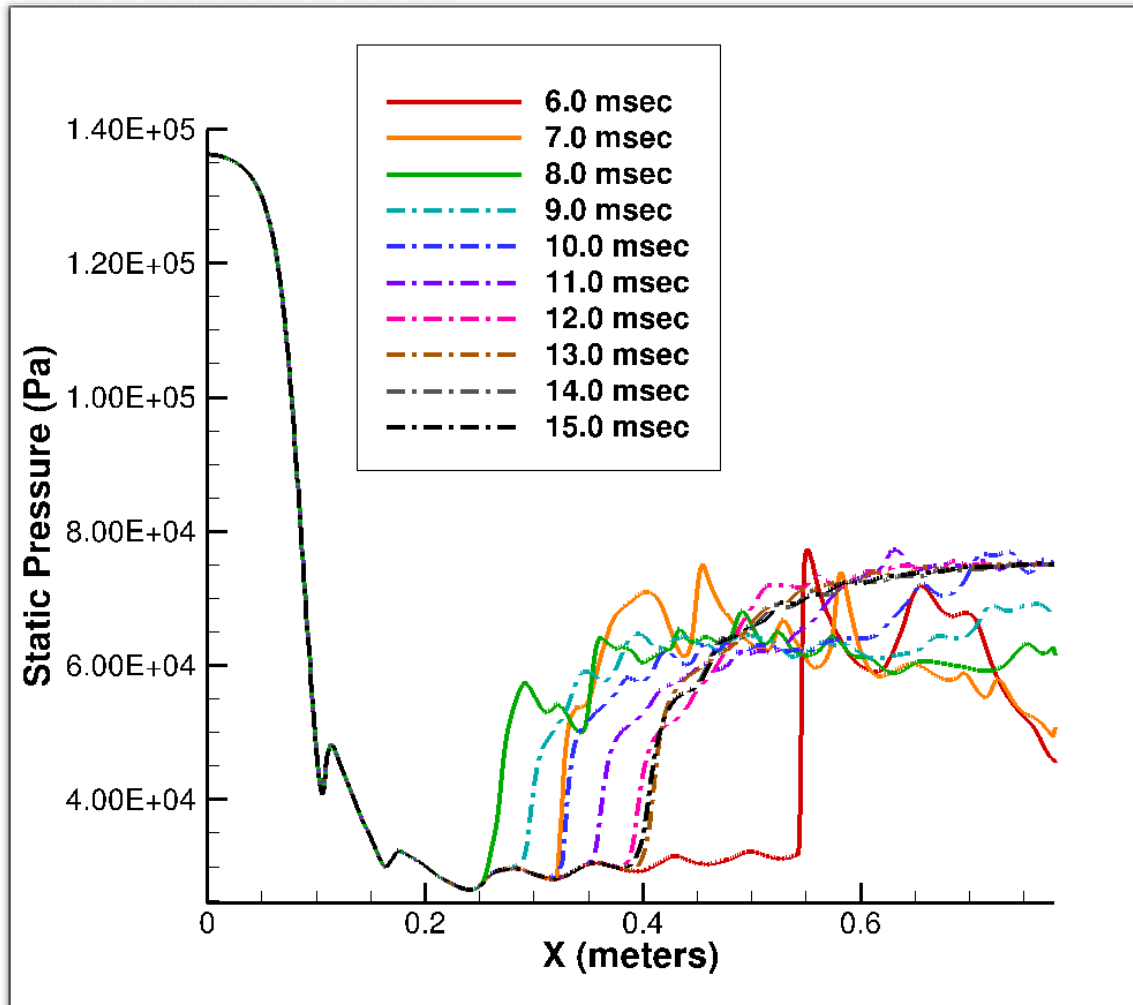


Figure 81. Time history for 75.0 kPa back pressure (140.6 kPa inflow) along line S4 (right) in the nozzle/isolator

Figures 82 and 83 show the results of the 71.1 kPa back pressure simulation with 140.6 kPa inflow. The PCST appeared at seven milliseconds. At both eight and nine milliseconds, the shock train was further upstream. At 10 milliseconds, the shock train was further downstream indicating reversal occurred between 9 and 10 milliseconds (the same pattern as in the other 3-D simulations to find the reversal time). The simulation continued until reaching the stopping criteria at 37 milliseconds.

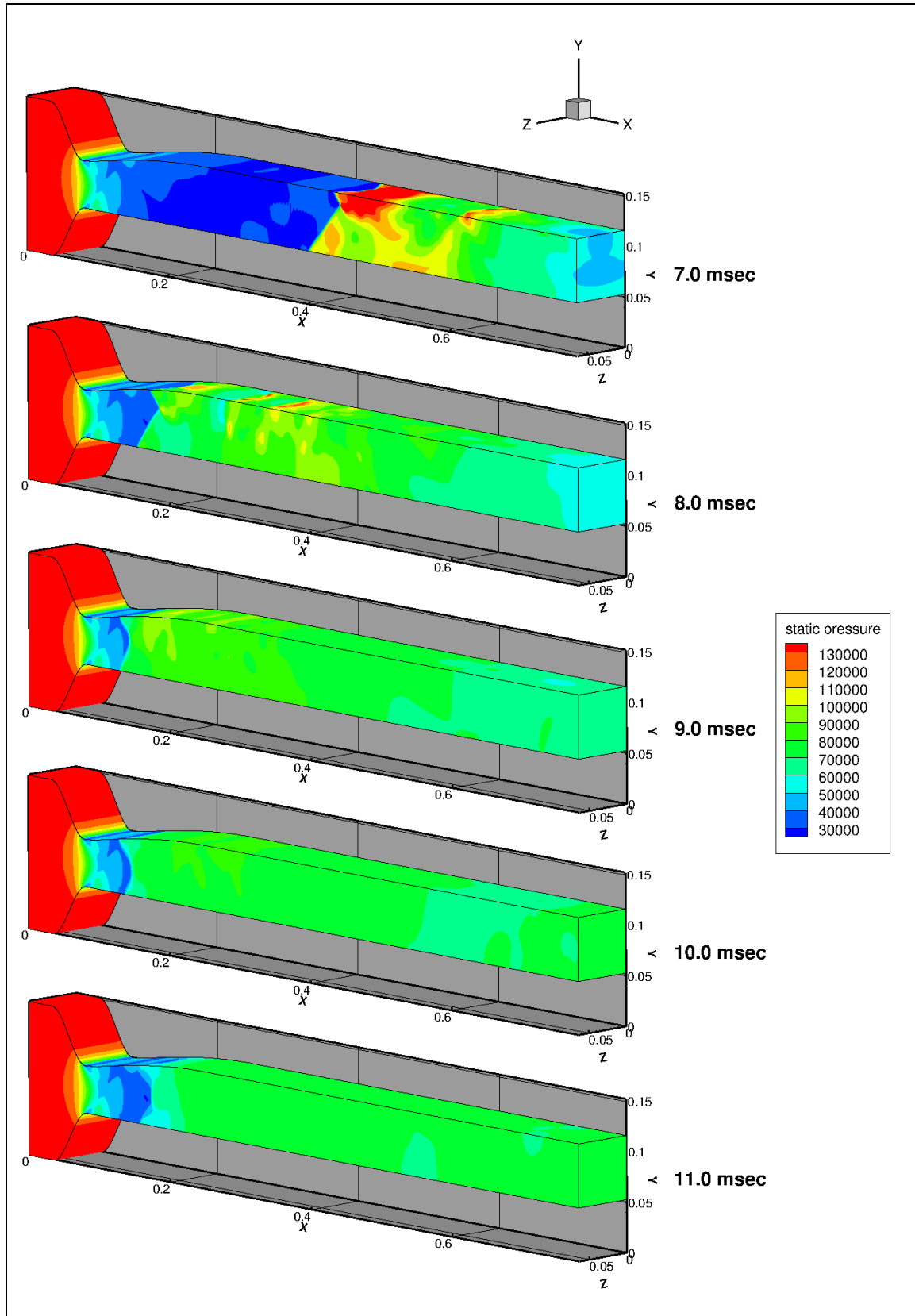


Figure 82. Evolution of PCST solution for 71.1 kPa back pressure

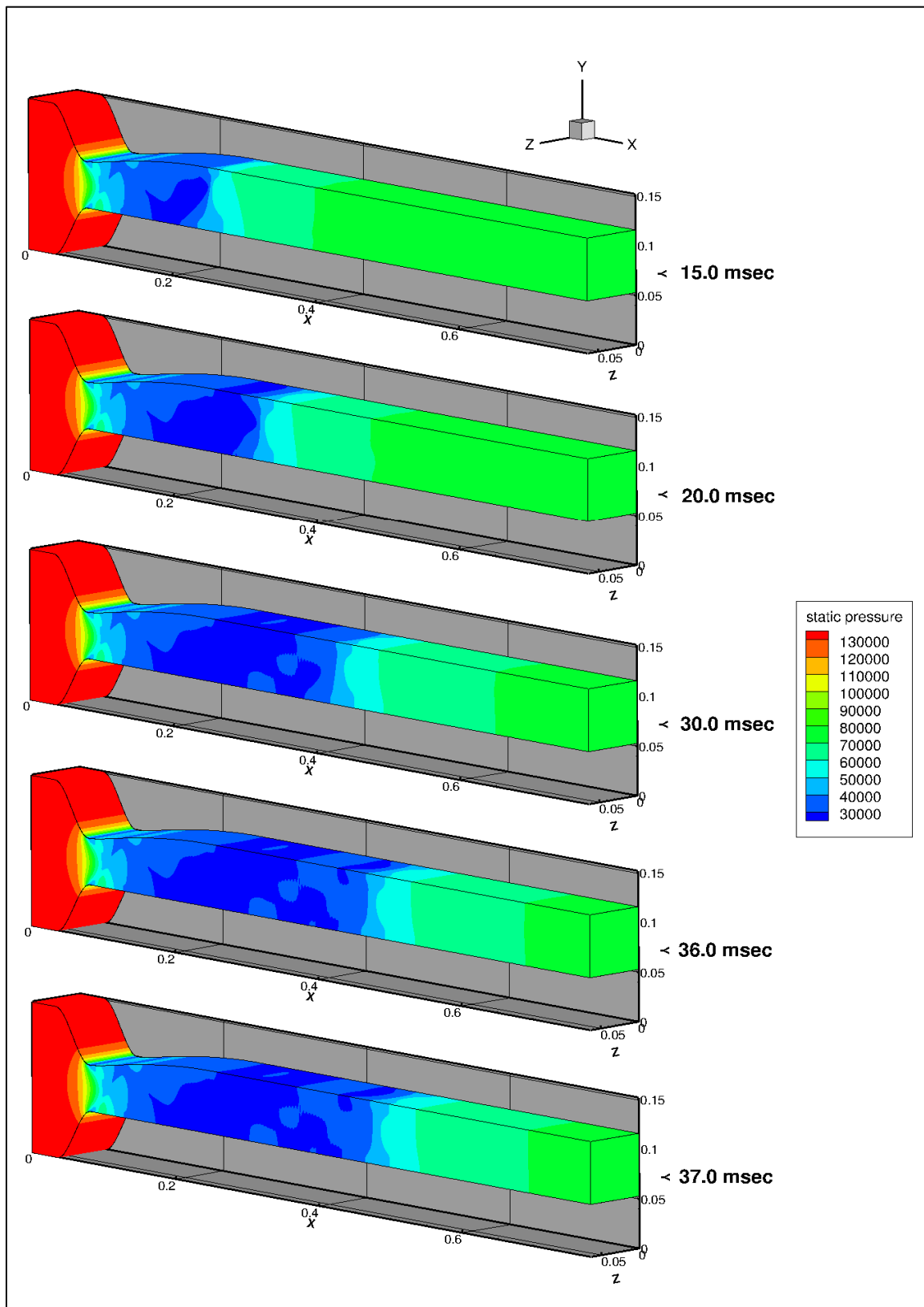


Figure 83. Evolution of PCST solution for 71.1 kPa back pressure continued

Figures 84 and 85 show time histories of the top and bottom walls for the 71.1 kPa simulation. In Figure 84, the shock train appeared at seven milliseconds and traveled upstream to 13.2 cm at 9.4 milliseconds. The shock train then reversed direction and moved downstream to its final location of 45.3 cm at 37 milliseconds. A comparison of Figures 84 and 85 indicate, again, the same difference as in previous simulations between reversal locations and final locations. Comparison of the simulation with the 85.0 kPa simulation (with the same back to inlet pressure ratio) shows only a 0.8 cm difference between the reverse locations, while the difference between the final locations is 1.3 cm.

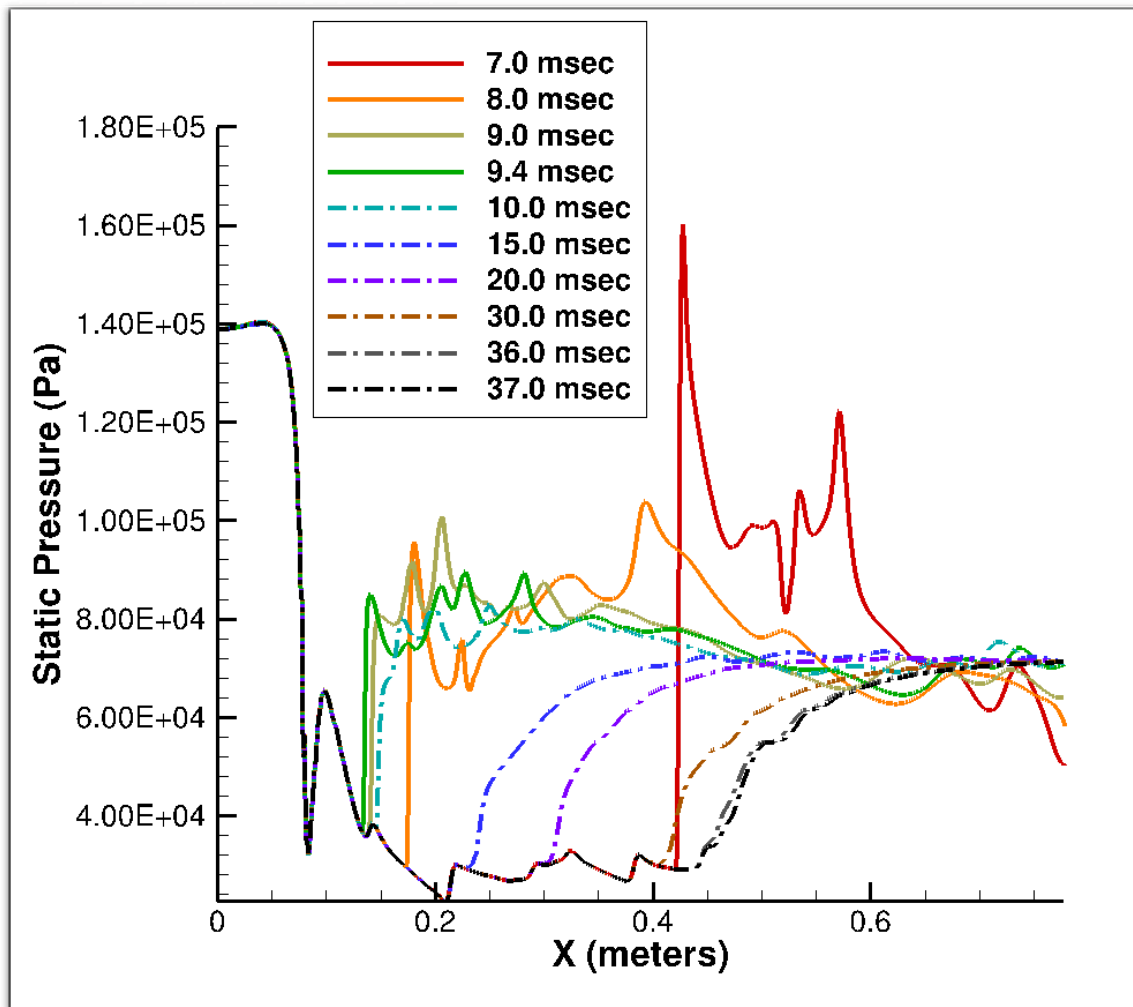


Figure 84. Time history for 71.1 kPa back pressure along line S1 (bottom) in the nozzle/isolator

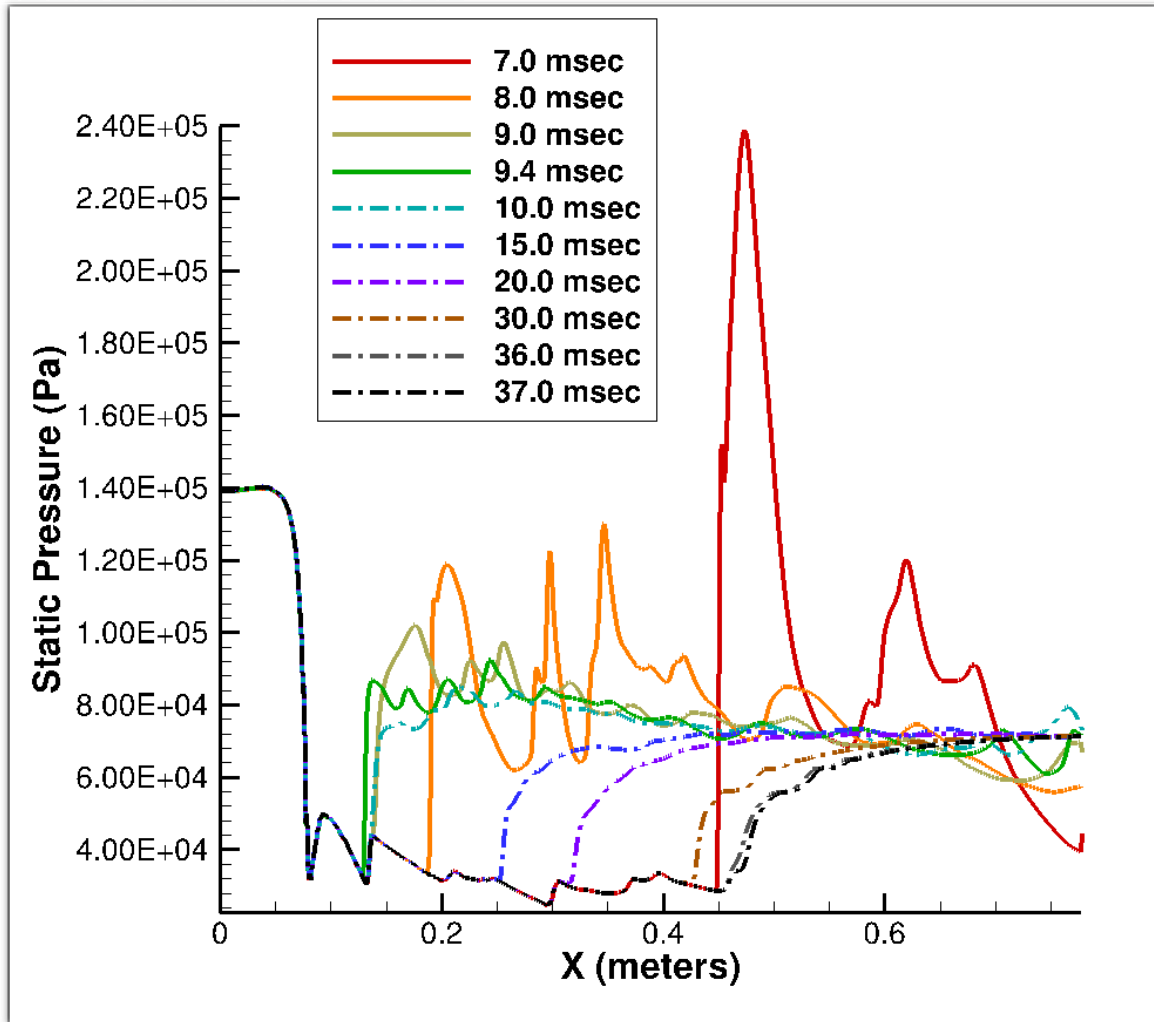


Figure 85. Time history for 71.1 kPa back pressure along line S2 (top) in the nozzle/isolator

Figures 86 and 87 show the left and right sides of the 71.1 kPa simulation. When comparing the two sides in these figures, they are almost identical. Again, the identical S3 and S4 lines are similar to the results seen in the previous 3-D simulations where the S3 and S4 lines are almost the same.

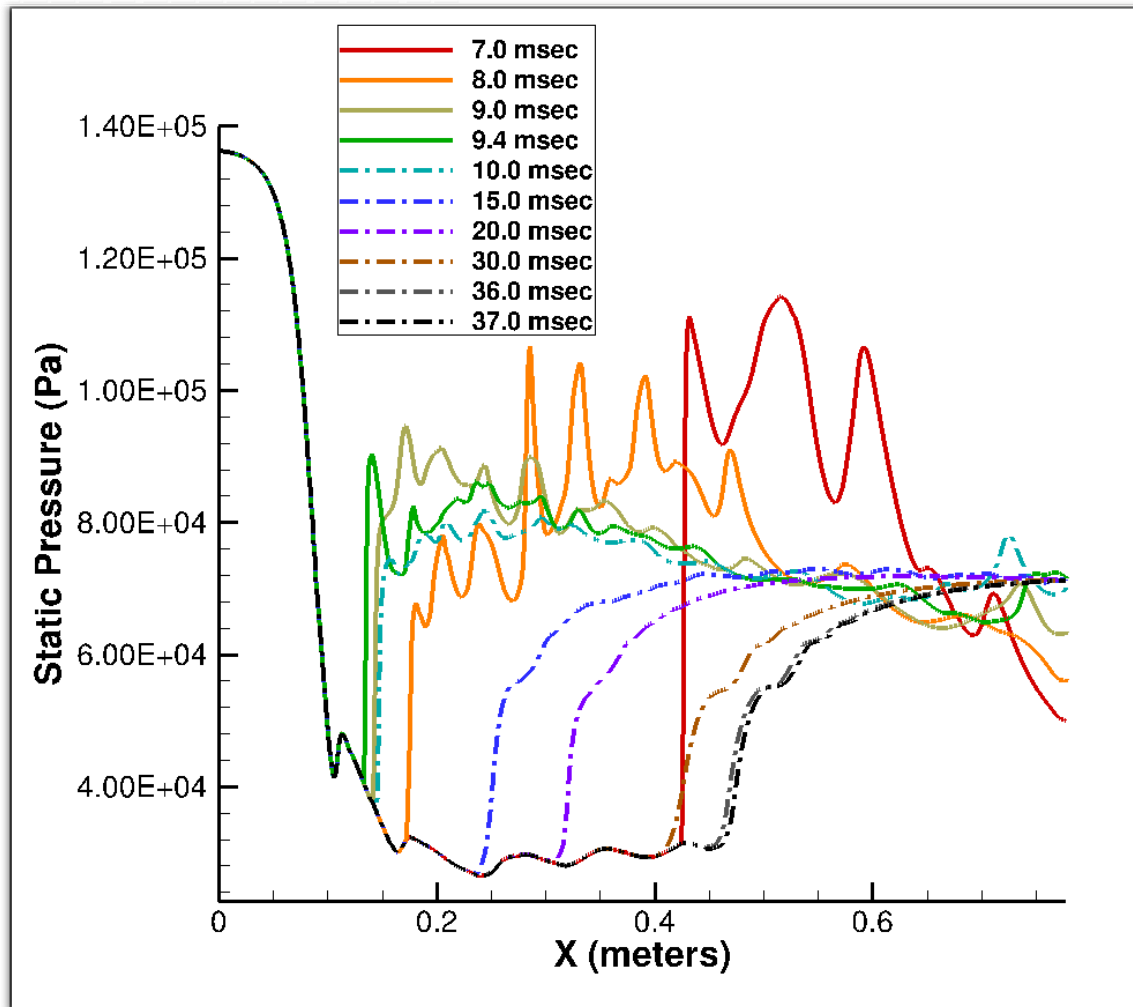


Figure 86. Time history for 71.1 kPa back pressure along line S3 (left) in the nozzle/isolator

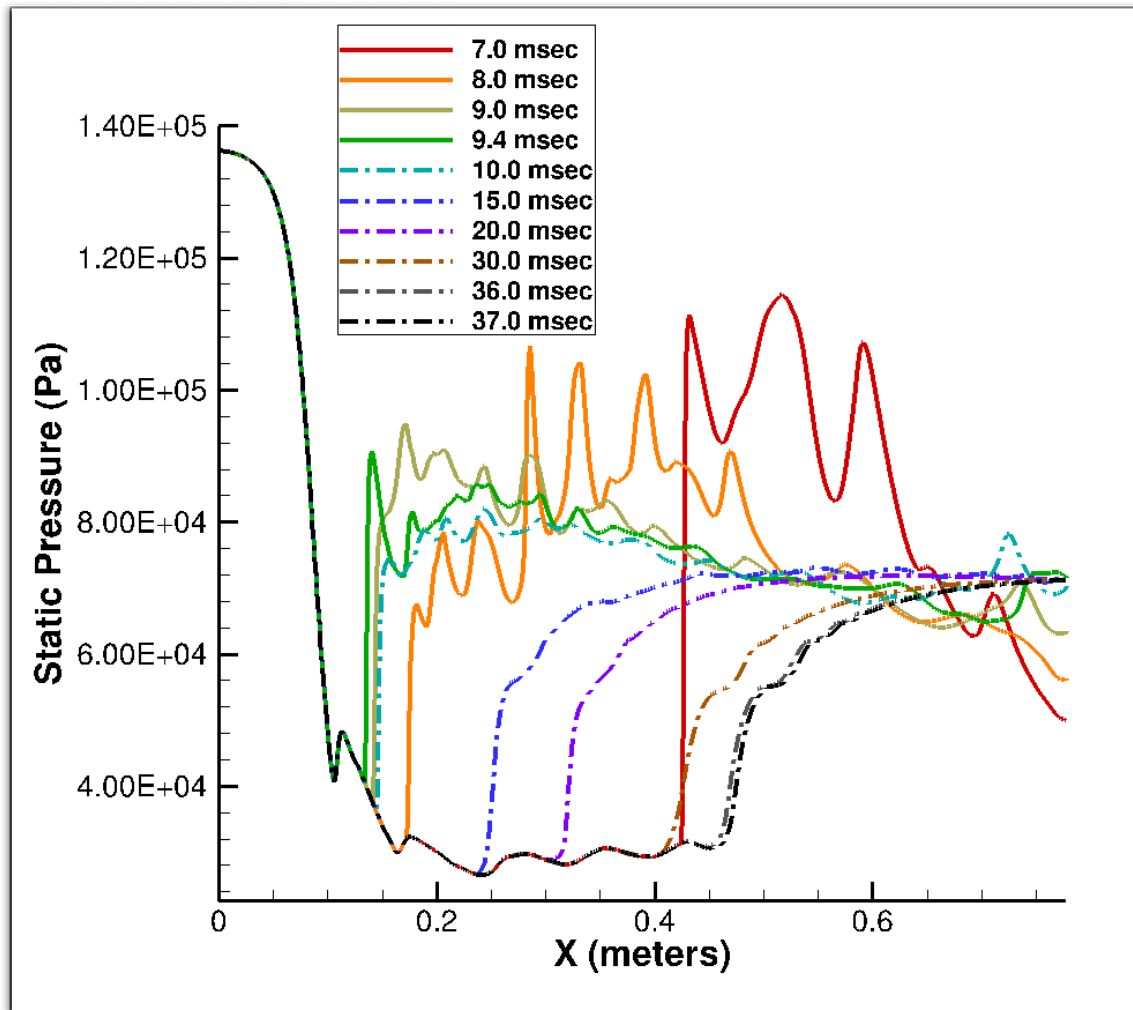


Figure 87. Time history for 71.1 kPa back pressure along line S4 (right) in the nozzle/isolator

Figures 88 and 89 display the results of the last simulation: 62.78 kPa backpressure with 140.6 kPa inflow pressure. The PCST appeared at seven milliseconds and moved upstream at eight and nine milliseconds. At 10 milliseconds, the shock train is further downstream, meaning the shock train reversed direction sometime between 9 and 10 milliseconds. The simulation continued until reaching the stopping criteria at 29 milliseconds.

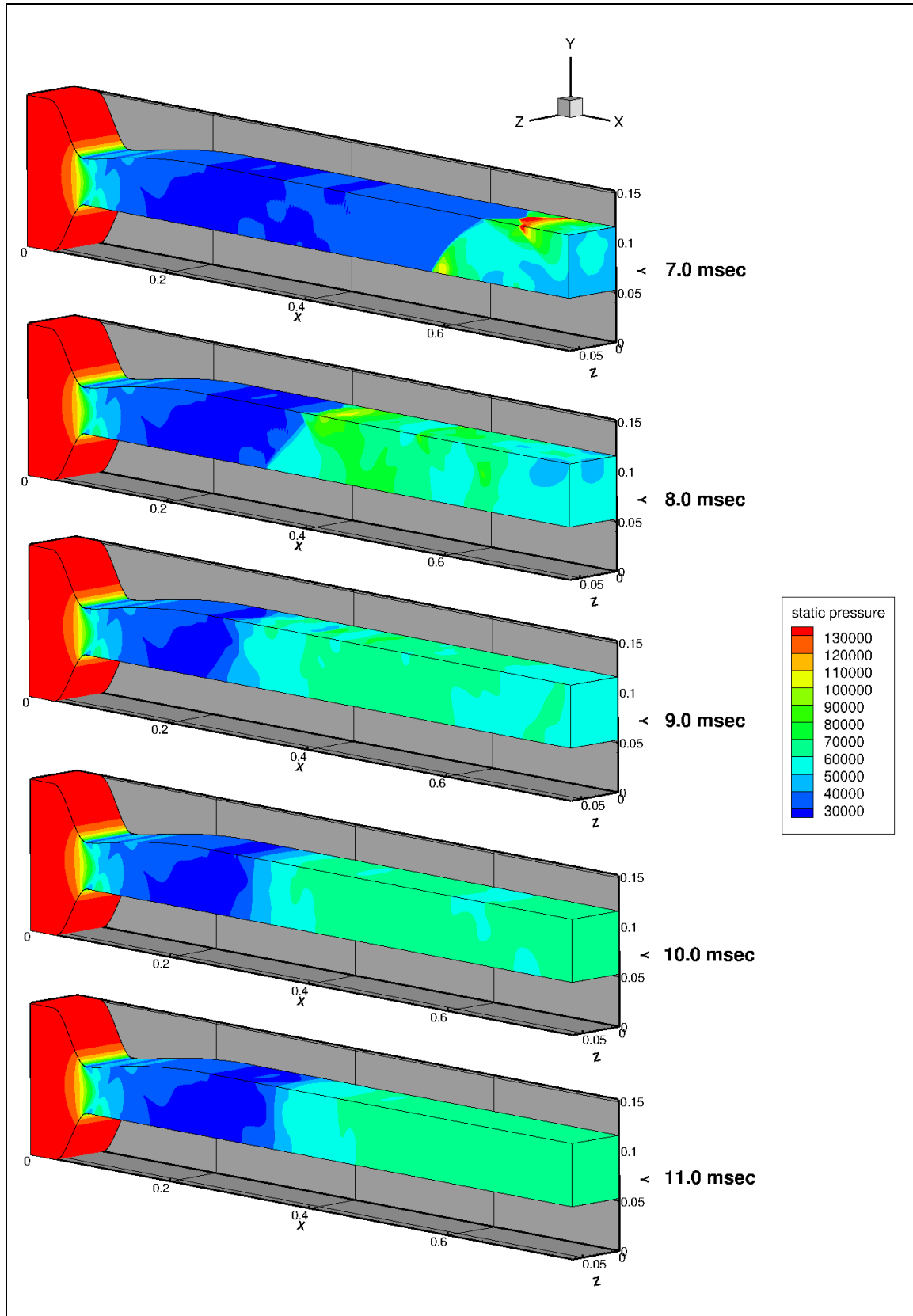


Figure 88. Evolution of PCST solution for 62.78 kPa back pressure

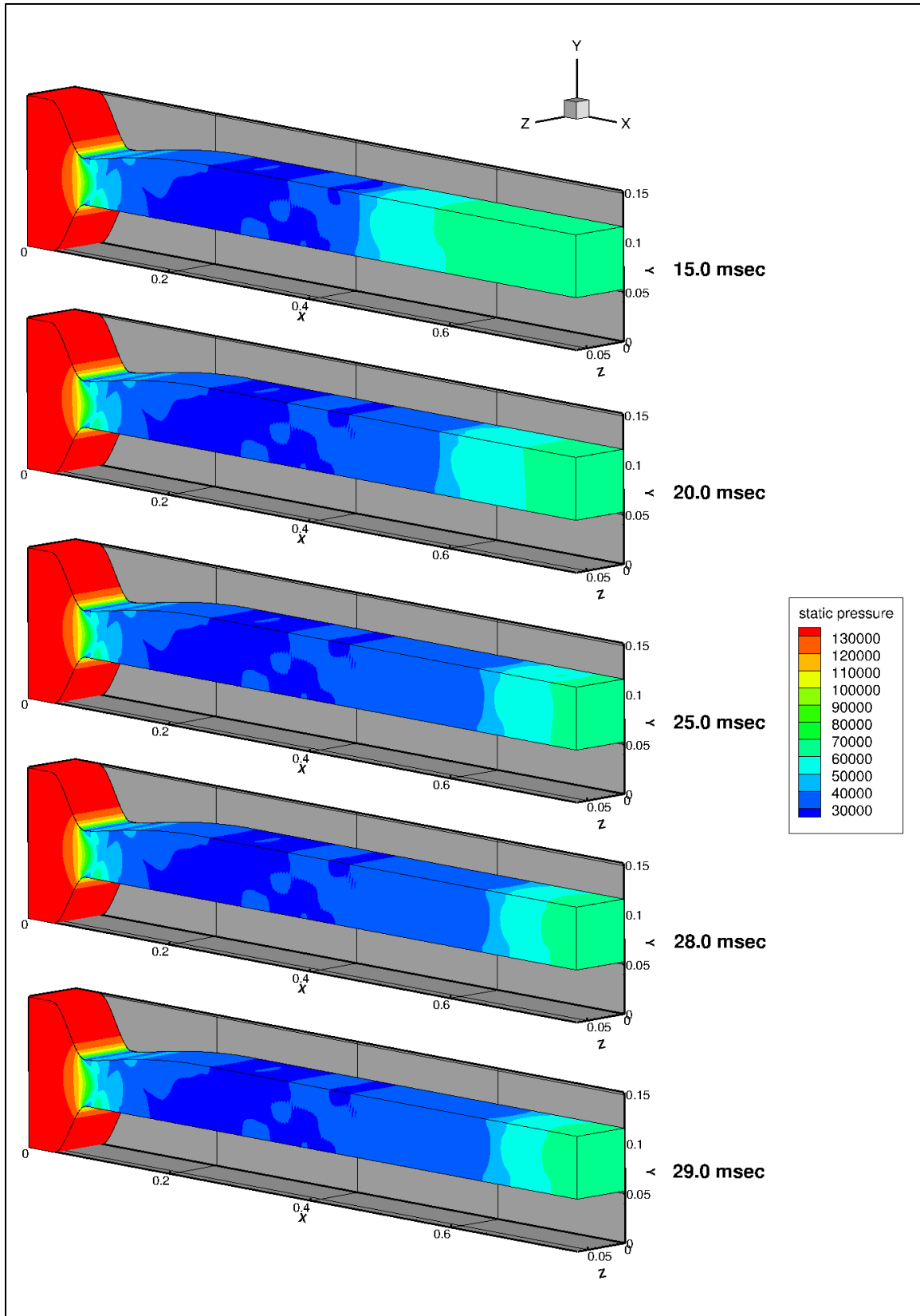


Figure 89. Evolution of PCST solution for 62.78 kPa back pressure continued

Figures 90 and 91 show time histories of the top and bottom walls for the 62.78 kPa simulation. In Figure 90, the shock train appeared at 7 milliseconds and traveled upstream to 27.2 cm at 9.2 milliseconds, then reversed direction and moved downstream to its final location of 62.8 cm at 29 milliseconds. A comparison of Figures 90 and 91 proves, again, the same difference between reversal locations and final locations as in previous simulations. Comparison of this simulation with the 75.0 kPa simulation (again, with the same back to inlet pressure ratio) shows a 2.1 cm difference between the reverse locations, while the difference between the final locations is only 0.1 cm.

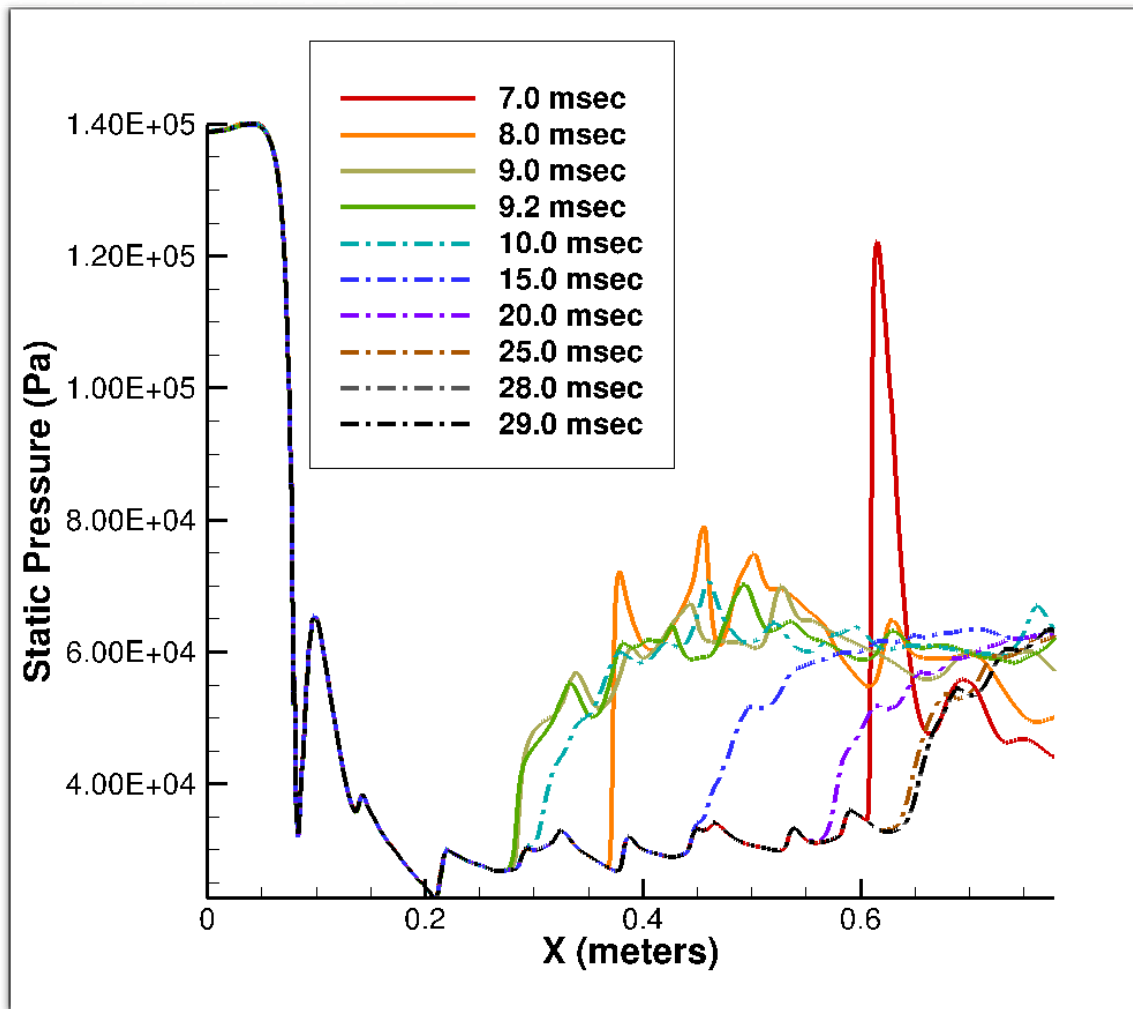


Figure 90. Time history for 62.78 kPa back pressure along line S1 (bottom) in the nozzle/isolator

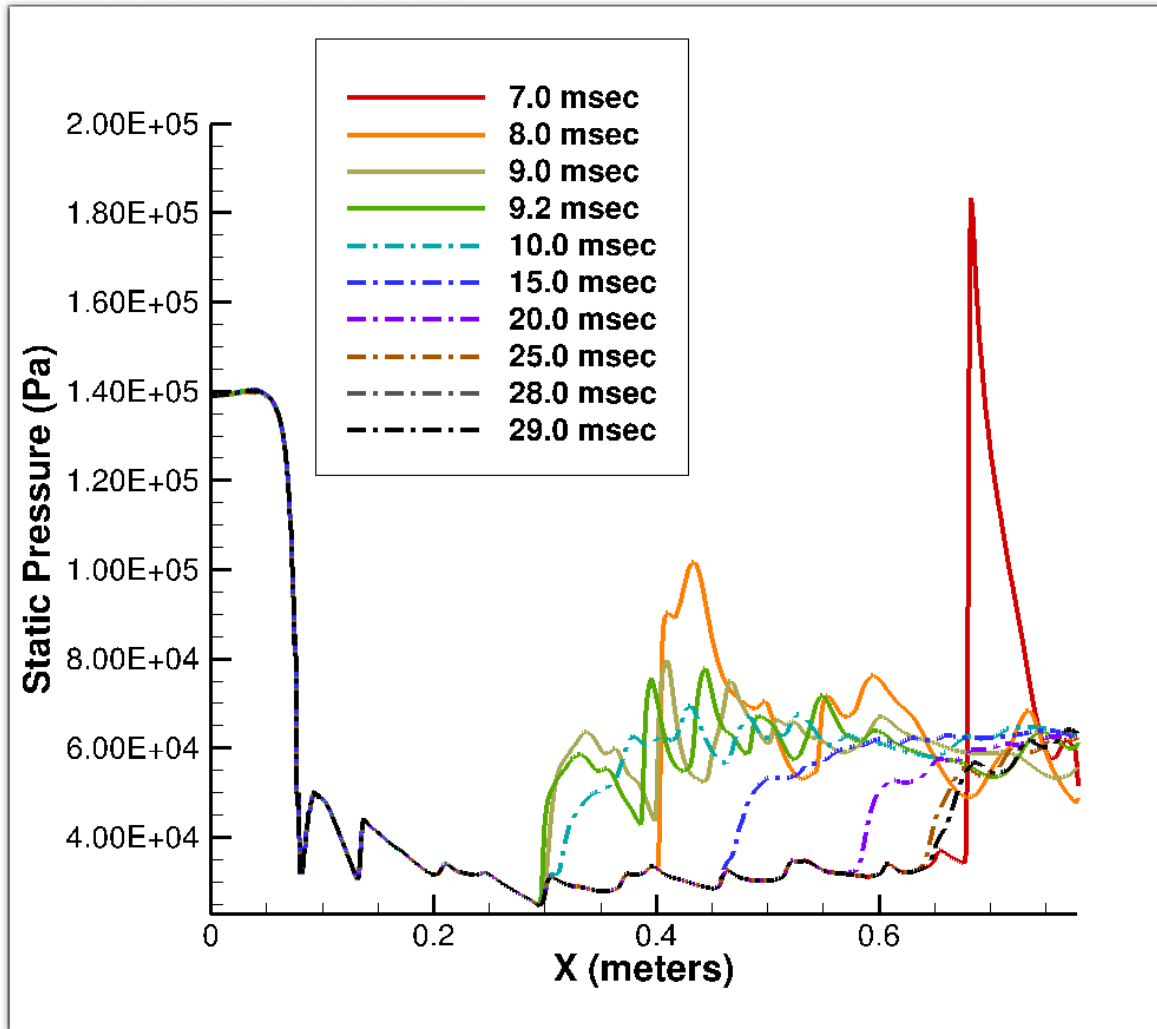


Figure 91. Time history for 62.78 kPa back pressure along line S2 (top) in the nozzle/isolator

Figures 92 and 93 represent the left and right sides of the 62.78 kPa simulation. Again, as seen in all the other 3-D simulations, a comparison of the S3 and S4 lines show the S3 and S4 lines are almost identical.

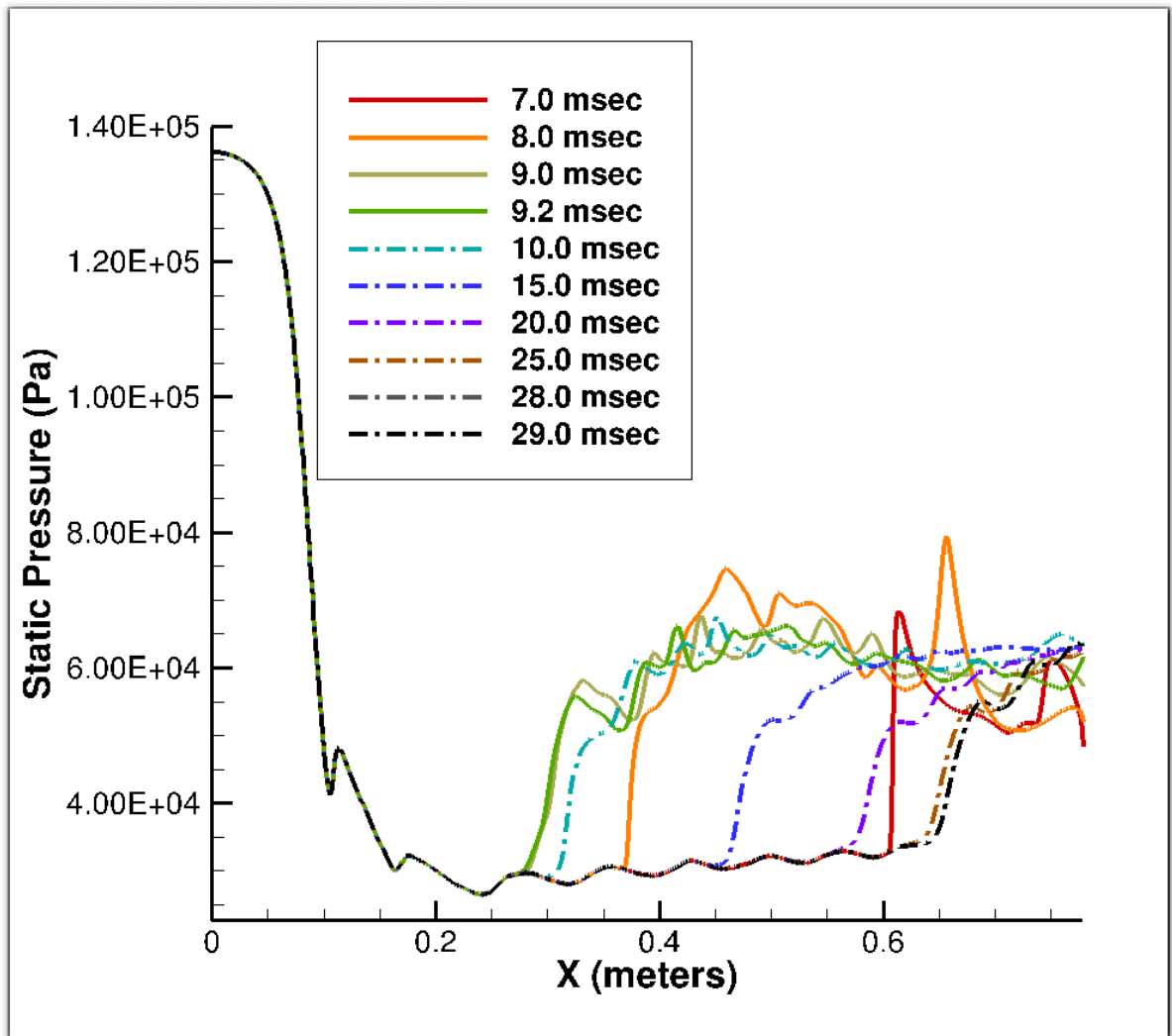


Figure 92. Time history for 62.78 kPa back pressure along line S3 (left) in the nozzle/isolator

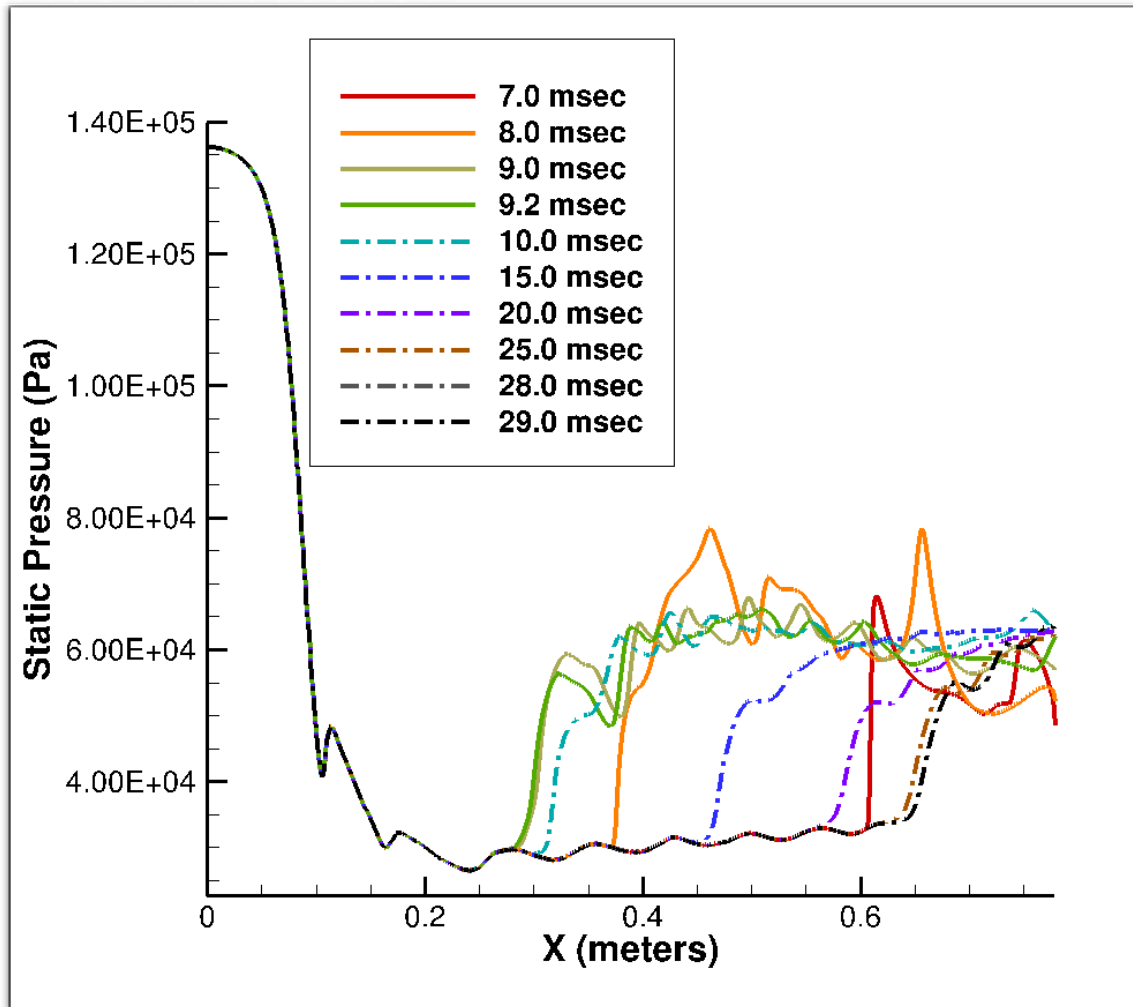


Figure 93. Time history for 62.78 kPa back pressure along line S4 (right) in the nozzle/isolator

Table 5 is a summary of the six 3-D cases. The locations shown are based on measurements of the bottom centerline (S1), which had the furthest upstream reversal location in all cases. The shock train movement where the shock train travels upstream, then reverses direction and travels downstream to the final location is present in all six cases. Again, as seen in the 2-D cases, the final shock location is strongly correlated with the back pressure ratio. As the back pressure decreases, the final location is further downstream in the isolator. A comparison of the cases with the same ratios (for example, 168.2/89.6 and 140.6/75.0 which both have a ratio of 0.533), shows that both the reverse

locations and final locations are the same within 2 cm, while the reversal times and times to reaching the stopping criteria were also the same within 3 milliseconds. Table 5 also shows that the 0.506 ratio results have reverse locations further upstream than the 0.533 ratio results. The 0.506 ratio reverse locations are unusual since the reverse and final locations are normally further upstream for higher ratios. The reason for this difference is that the shock train forms earlier for 0.533 ratios at 6 milliseconds further downstream (see Figures 57 and 76) in the isolator while at 0.506 ratios, it forms at seven milliseconds further upstream (see Figures 64 and 82). This extra millisecond of time and extra distance in the isolator for the 0.533 ratio as the PCST slows down traveling upstream in the isolator leads to a reversal location further downstream than at the 0.506 ratio.

Table 5. Results of the six 3-D back pressure cases

Inflow Pressure (kPa)	Back Pressure (kPa)	Back to Inflow Pressure Ratio	Time Initial Shock Detected (msec)	Location of Initial Shock along S1 (cm)	Time to Reverse (msec)	Reverse Location (cm)	Time to Final (msec)	Final Location (cm)
168.2	89.6	0.533	6.0	51.4	7.7	25.4	14.0	39.7
140.6	75.0	0.533	6.0	54.1	8.0	24.6	15.0	38.2
168.2	85.0	0.506	7.0	39.1	9.2	14.0	36.0	46.6
140.6	71.1	0.506	7.0	42.0	9.4	13.2	37.0	45.3
168.2	75.0	0.446	7.0	57.7	8.9	29.3	26.0	62.9
140.6	62.78	0.446	7.0	60.6	9.2	27.2	29.0	62.8

Figure 94 displays a partial time plot of the shock train leading edge (from the end of the 78.2 cm isolator) from the time PCSTs forms until 15 msec. The 168.2 kPa inflow pressure corresponds to a Reynolds/meter number of 2.3×10^7 and is identified in Figure 94 as Re_1 while the 140.6 kPa inflow pressure corresponds to a Reynolds/meter number of 1.9×10^7 and identified as Re_2 . Figure 94 shows similar back pressure ratios follow the same profiles, with approximately the same reversal and final locations and times.

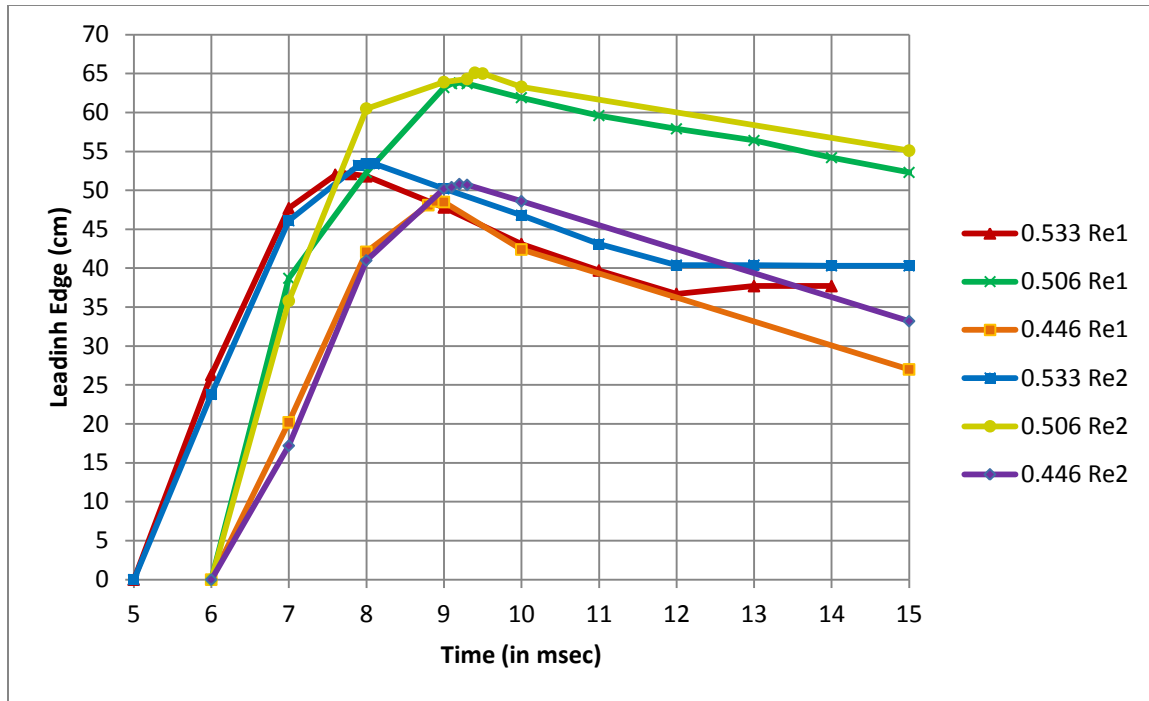


Figure 94. Plot of the location of the leading edge of PCST vs. time

Ramped application of backpressure

While the previous cases shown above were more realistic in terms of a gradually applied (stepped) back pressure as opposed to an instantaneous change, the rise in back pressure in the AFIT experiment was slightly different. Figure 95 shows the back pressure rise as the ramp is deployed in the AFIT experiment for an inflow pressure of 167.91 kPa. In Figure 95, a sudden jump in pressure occurs from 41.0 kPa to 62.5 kPa in 2.5 milliseconds, followed by a gradual rise (not as fast as the rise in the 3-D stepped simulations) to the final back pressure of 85.0 kPa. To simulate the AFIT experiment, two additional back pressure cases were done with a stepped back pressure profile which more closely matched that of the AFIT experiment. The profile used first is shown in Figure 95 as a black line for comparison. There are other back pressure profiles that could be used here which would alter the results before the shock train shown is formed and identifiable, but the shock train itself and its final location would be the same.

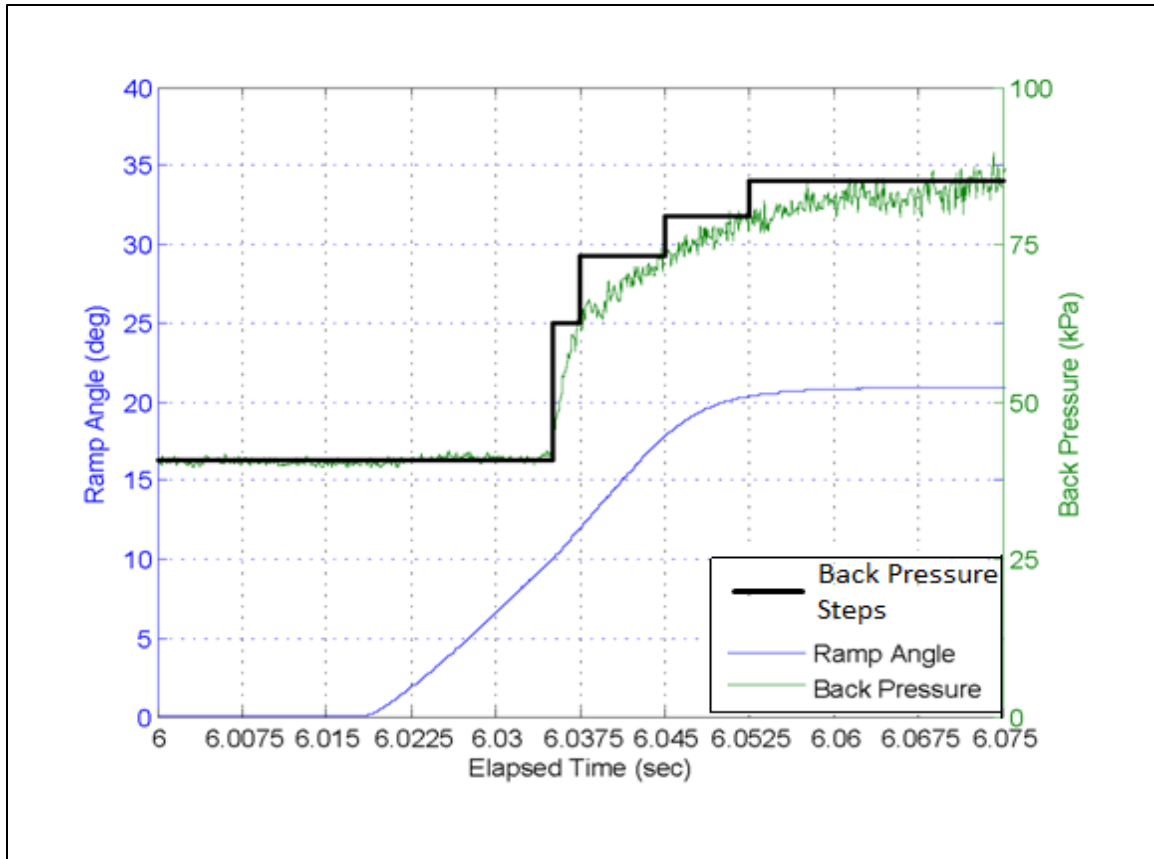


Figure 95. Rise in back pressure and ramp angle during the AFIT experiment for 85.0 kPa back pressure (Hutzel, 2011)

Figure 96 shows the results for the “ramped” back pressure. In the first 10 milliseconds, 41.0 kPa back pressure was applied at the isolator exit, but was not high enough to form a PCST. At 12.5 milliseconds in Figure 96, the back pressure is 62.5 kPa, causing the increase shown throughout the entire nozzle. At 20 milliseconds, the back pressure is 73.0 kPa with a shock train formed and at 27.5 milliseconds, the back pressure is 79.0 kPa with the shock train moving downstream. At 30.0 milliseconds, the back pressure has reached 85.0 kPa and its final location of 49.2 cm, a 2.6 cm difference compared to the gradually applied (stepped) 85.0 kPa simulation in Figure 65.

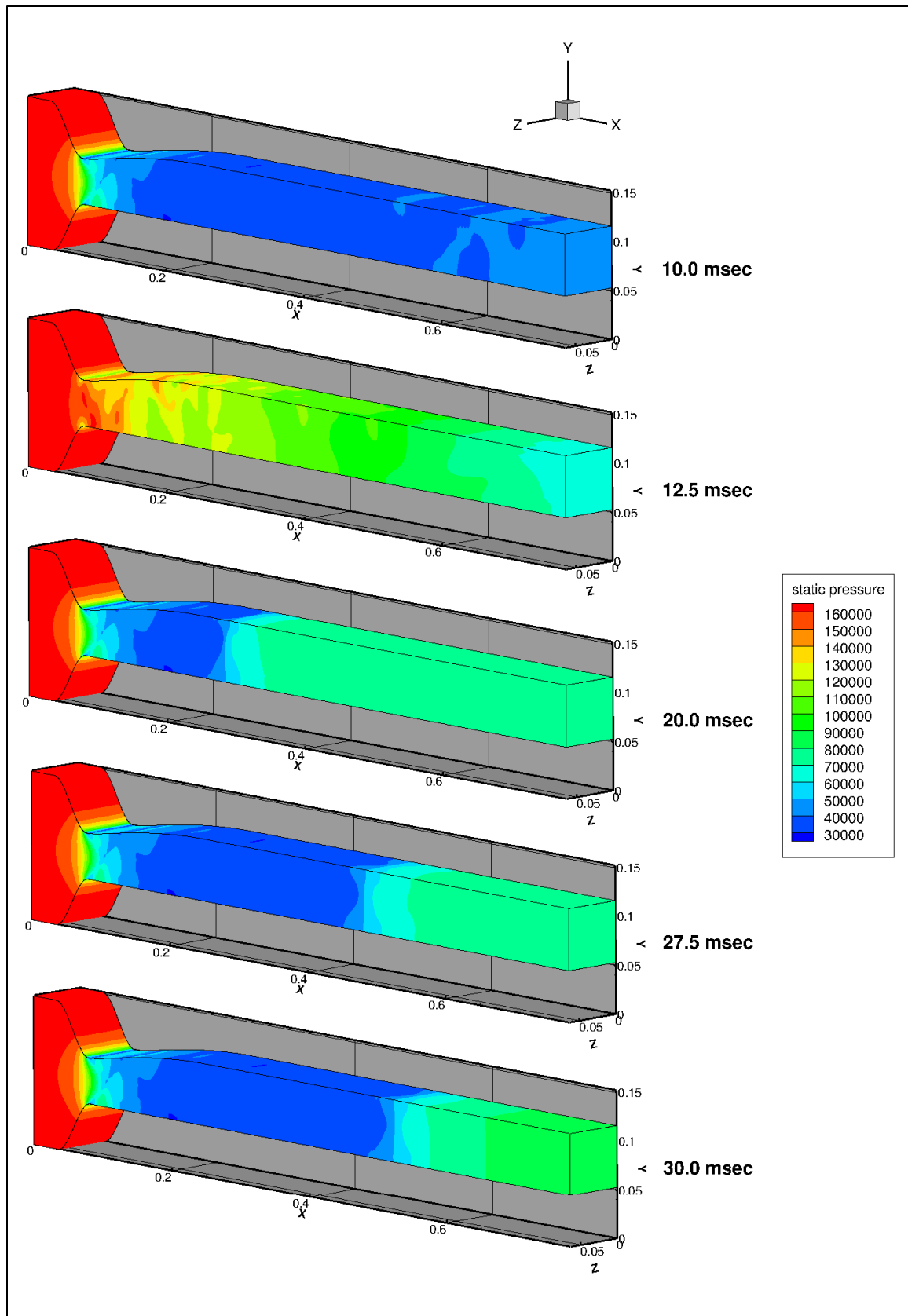


Figure 96. Evolution of PCST solution for 85.0 kPa back pressure ramp case

Figures 97 and 98 show the time histories for the bottom and top wall pressures of the isolator, respectively. In both figures, when the pressure jumps at 12.5 milliseconds, the pressure increases through the isolator into the nozzle until 20.0 milliseconds, where the shock train has stabilized and resumed its more expected pattern. The leading edge of the PCST can now be identified and tracked as it moved downstream to its final location in the isolator.

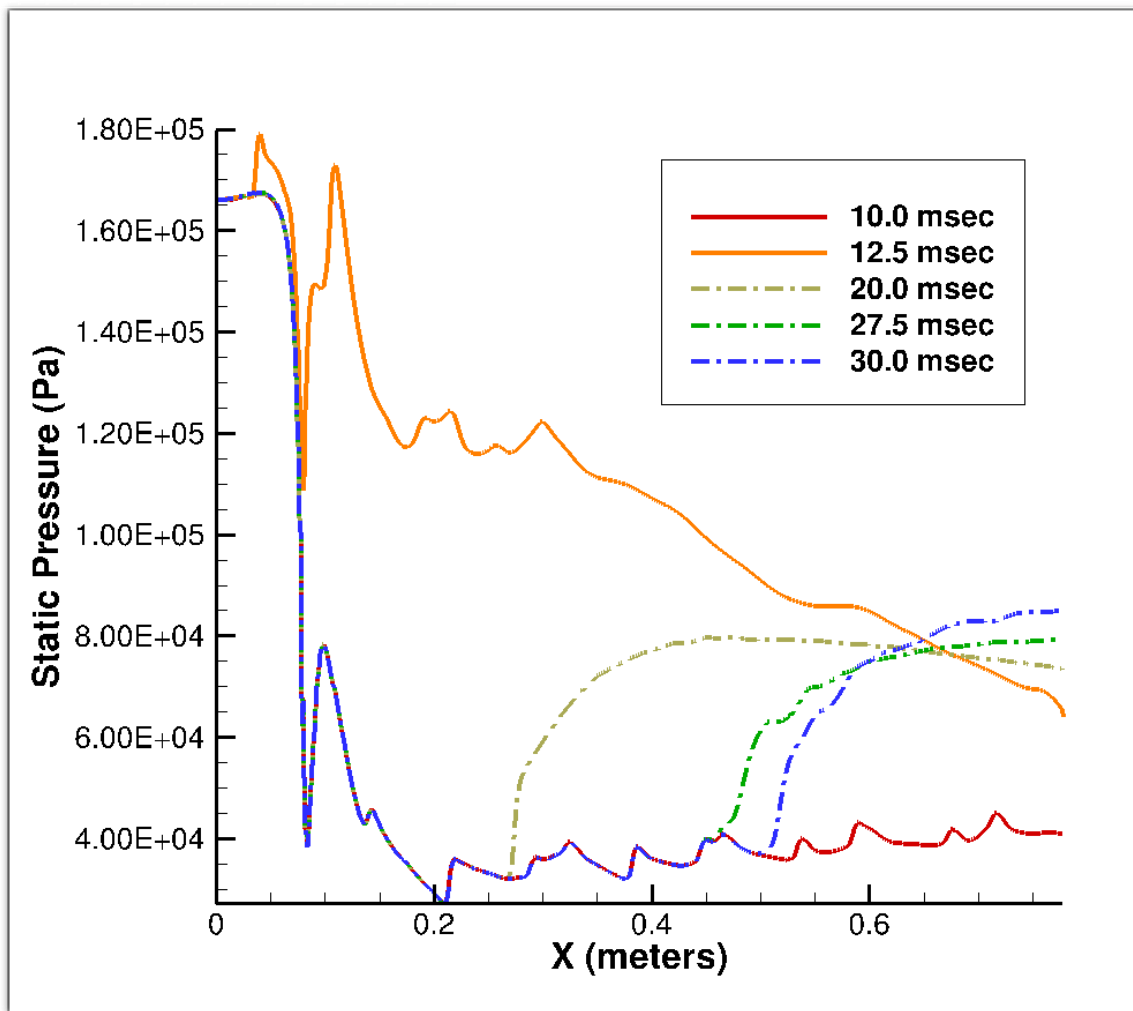


Figure 97. Time history for 85.0 kPa back pressure ramp case along line S1 (bottom) in the nozzle/isolator

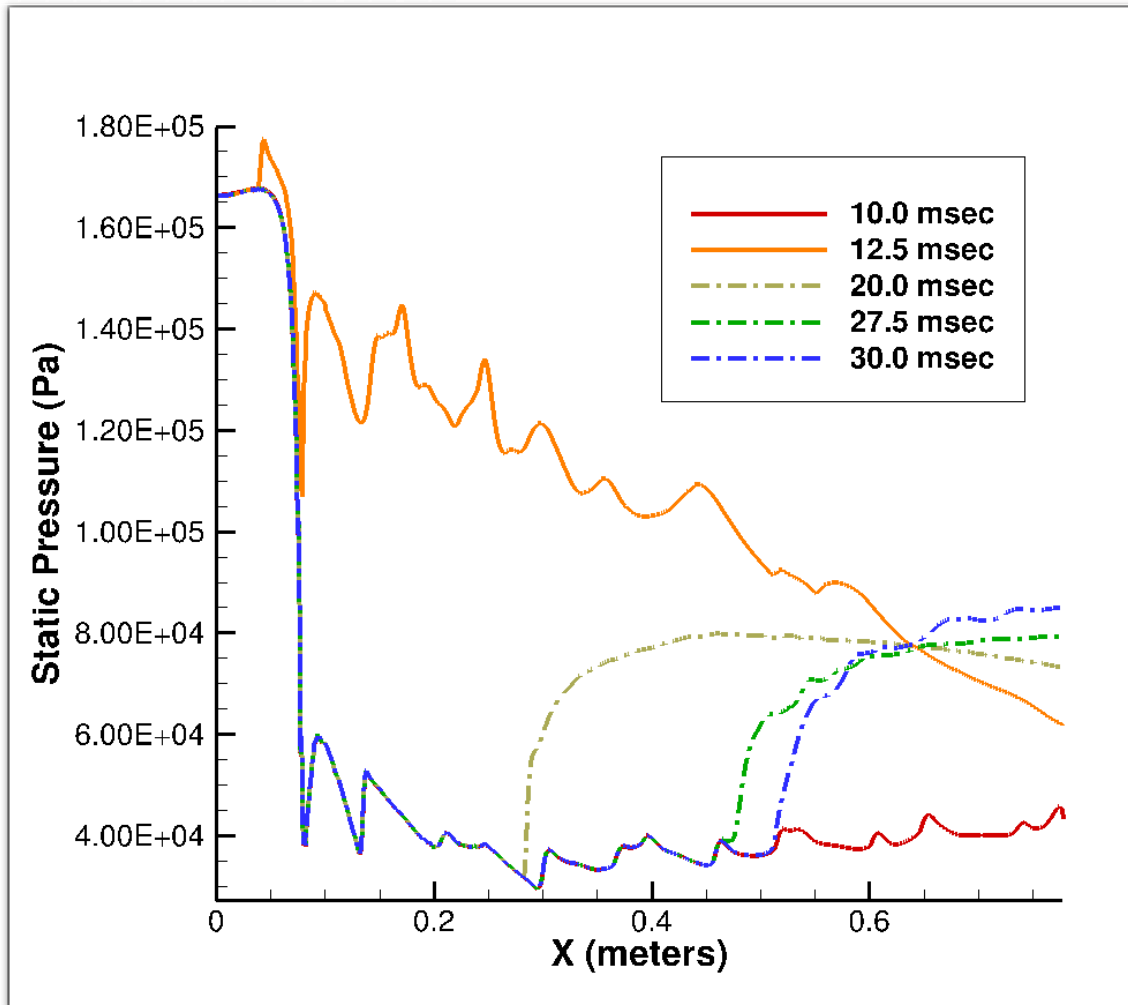


Figure 98. Time history for 85.0 kPa back pressure ramp case along line S2 (top) in the nozzle/isolator

Figures 99 and 100 show the time histories for the left and right walls of the isolator. In both of these figures, the same pressure jump at 12.5 milliseconds seen in Figures 97 and 98 is also present here before settling back down and the leading edge identified and tracked as it moved downstream to its final location.

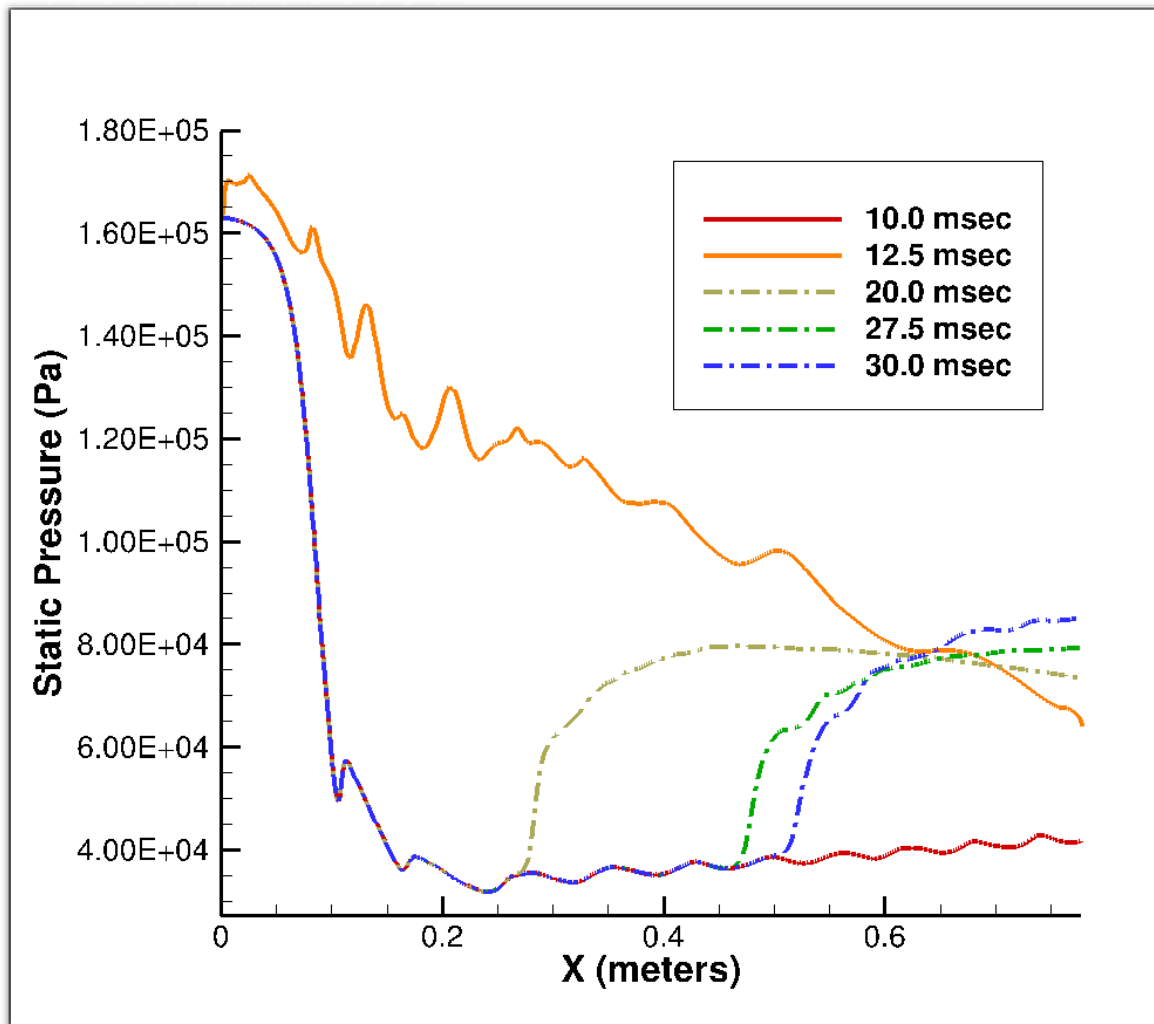


Figure 99. Time history for 85.0 kPa back pressure ramp case along line S3 (left) in the nozzle/isolator

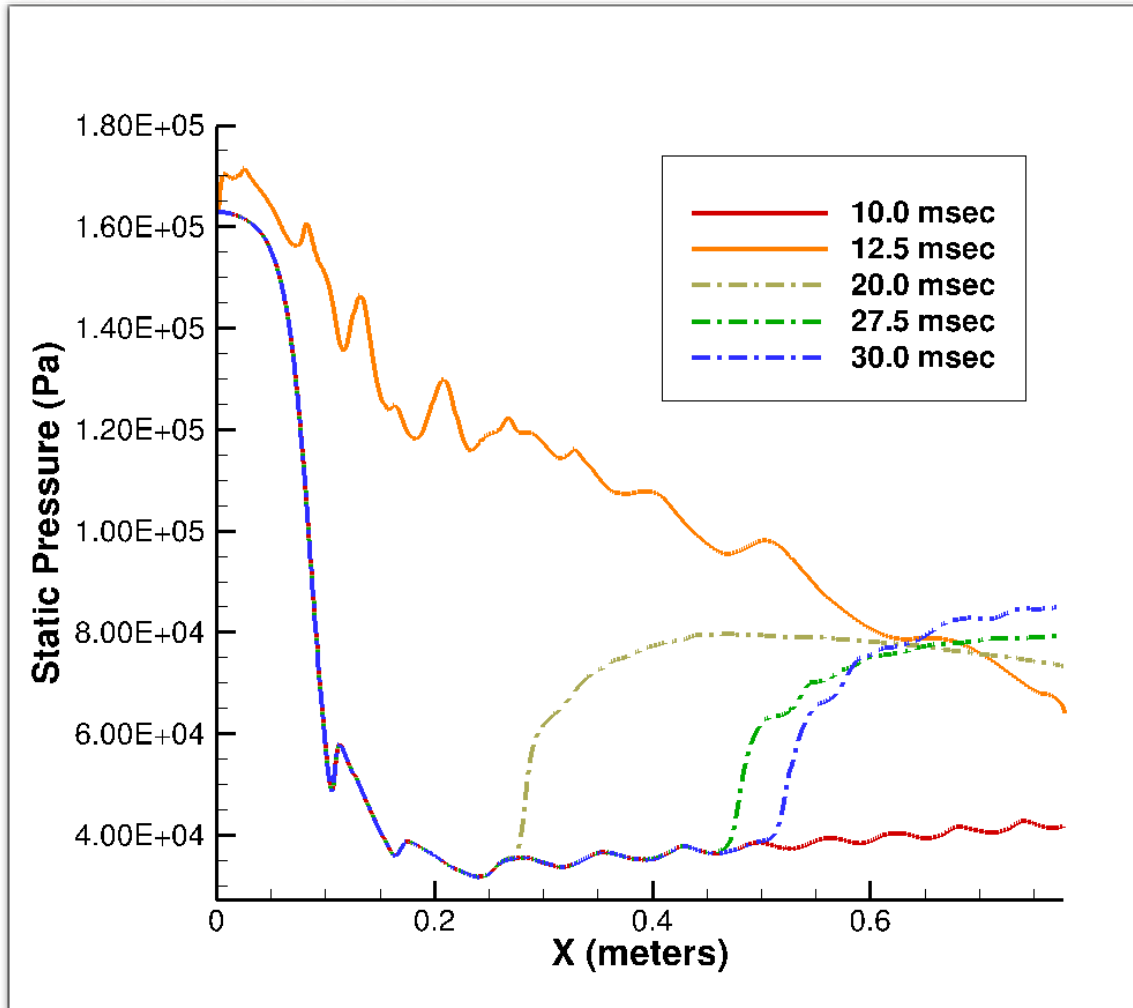


Figure 100. Time history for 85.0 kPa back pressure ramp case along line S4 (right) in the nozzle/isolator

A second ramp case was simulated, based on an inflow pressure of 112.9 kPa, and a back pressure of 56.5 kPa. Figure 101 presents the results of the back pressure rise as the ramp is deployed in this experiment. In Figure 101, there is a steep rise in pressure from 28.3 kPa to 44.8 kPa, followed by a gradual rise (as in the previous ramped case) to the final back pressure of 56.5 kPa. As in the previous ramped case, the back pressure shown in Figure 101 was applied in steps (shown as the blue line in Figure 101) as it had been done for the previous ramped case. Figure 102 shows the results for the ramped back pressure of 56.5 kPa. For the first 10 milliseconds, a back pressure of 28.3 kPa was

applied at the isolator exit. The 28.3 kPa back pressure is high enough to create a weak normal shock train approximately halfway in the isolator. At 13.0 milliseconds in Figure 102, the back pressure jumped to 44.8 kPa, and the PCST has traveled downstream. At 19.0 milliseconds, the back pressure is at 49.6 kPa and the shock train has moved further downstream. For the remaining 25 milliseconds, the back pressure increased to 56.5 kPa and the shock train traveled back upstream in the isolator until it reached the final location of 53.1 cm.

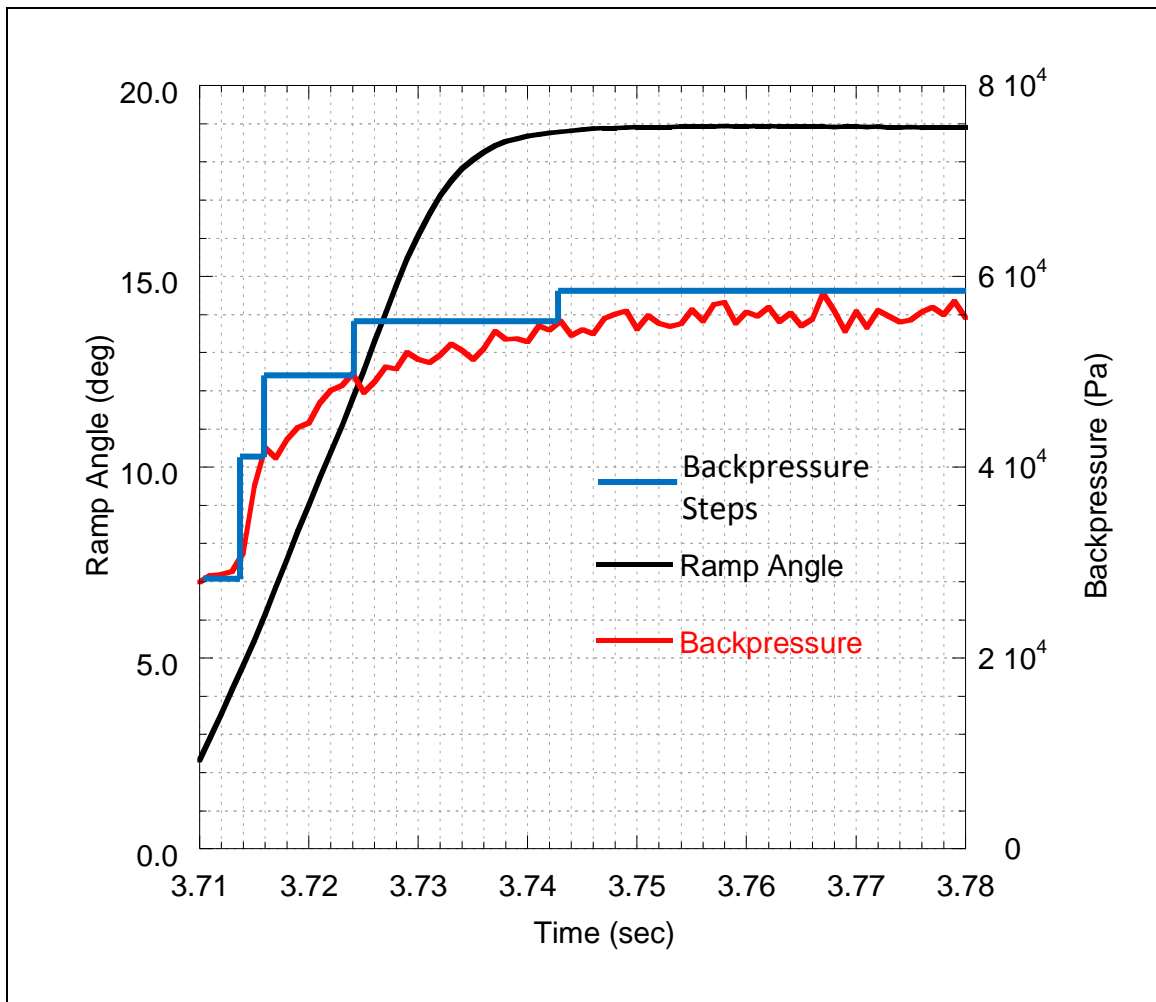


Figure 101. Rise in back pressure and ramp angle during the AFIT experiment for 56.5 kPa back pressure (Hutzel, 2011)

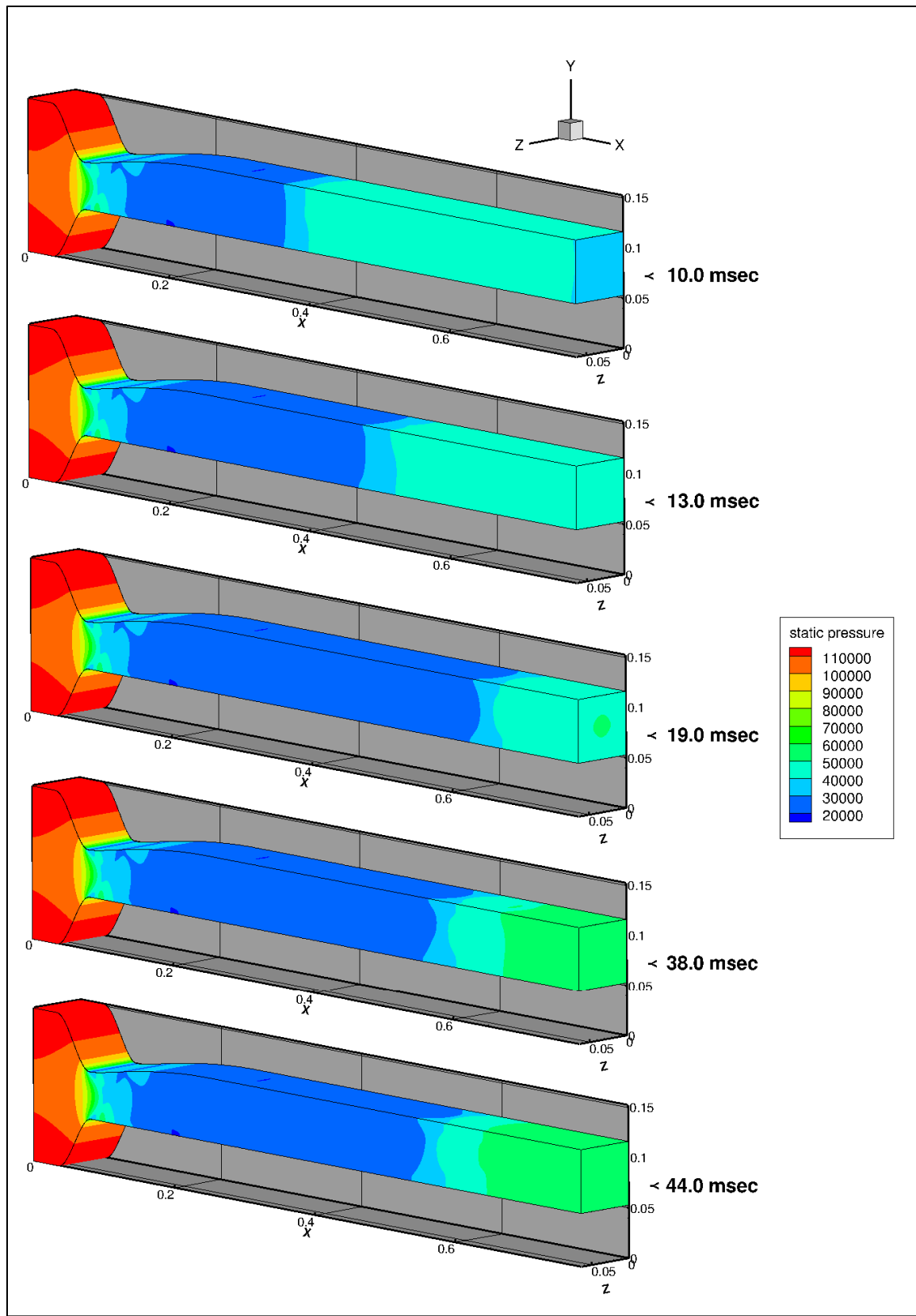


Figure 102. Evolution of PCST solution for 56.5 kPa back pressure ramp case

Figures 103 and 104 show the time histories for the top and bottom, respectively, for the ramped case of 56.5 kPa. Initially, the PCST at 10 milliseconds is located at 35.9 cm on the x-axis for both the top and bottom walls. After the pressure changed and the shock train settled at 44 milliseconds, the leading edge of the bottom wall is at 53.6 cm while the top is at 54.7 cm. Figures 103 and 104 indicate an asymmetry that formed from the increase in back pressure.

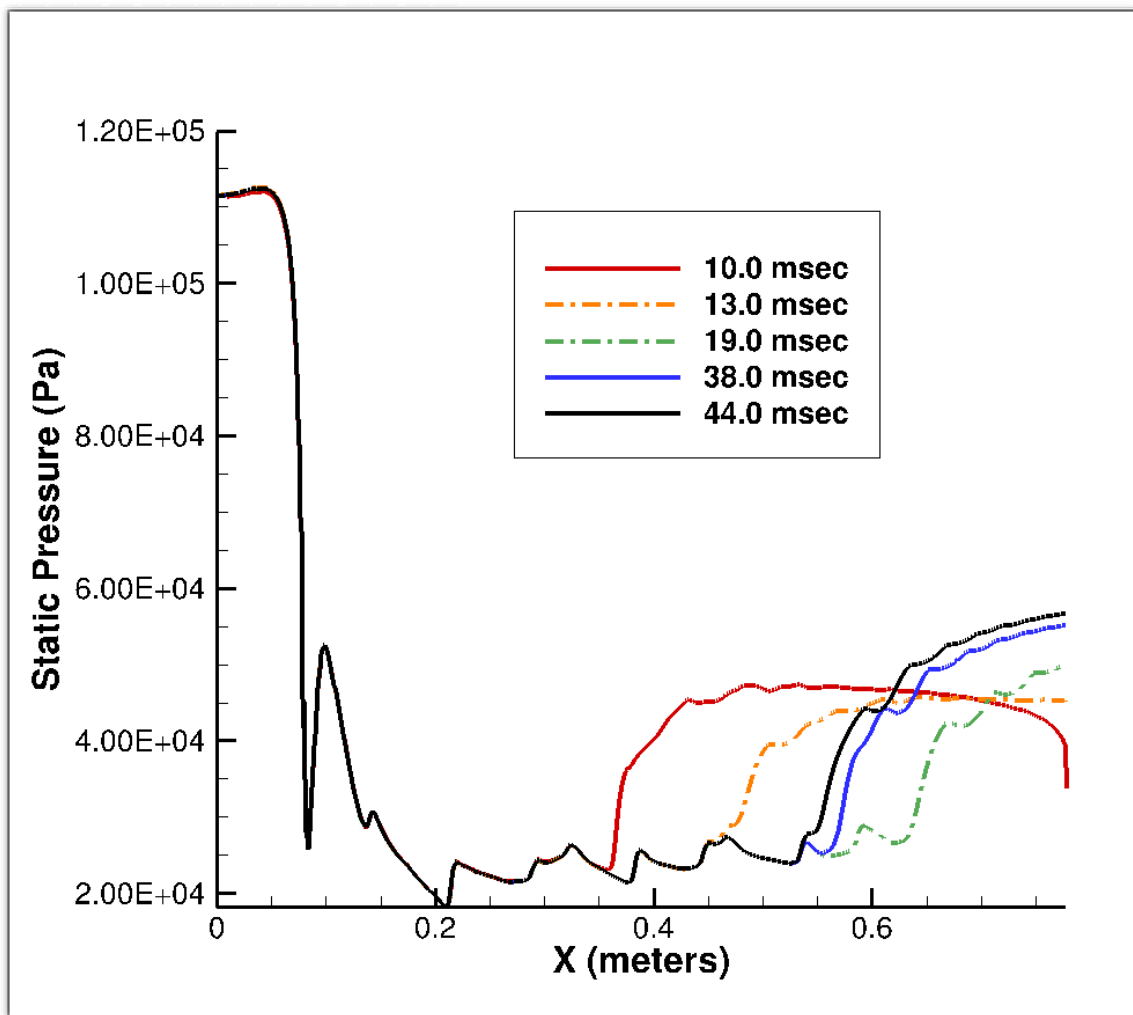


Figure 103. Time history for 56.5 kPa back pressure ramp case along line S1 (bottom) in the nozzle/isolator

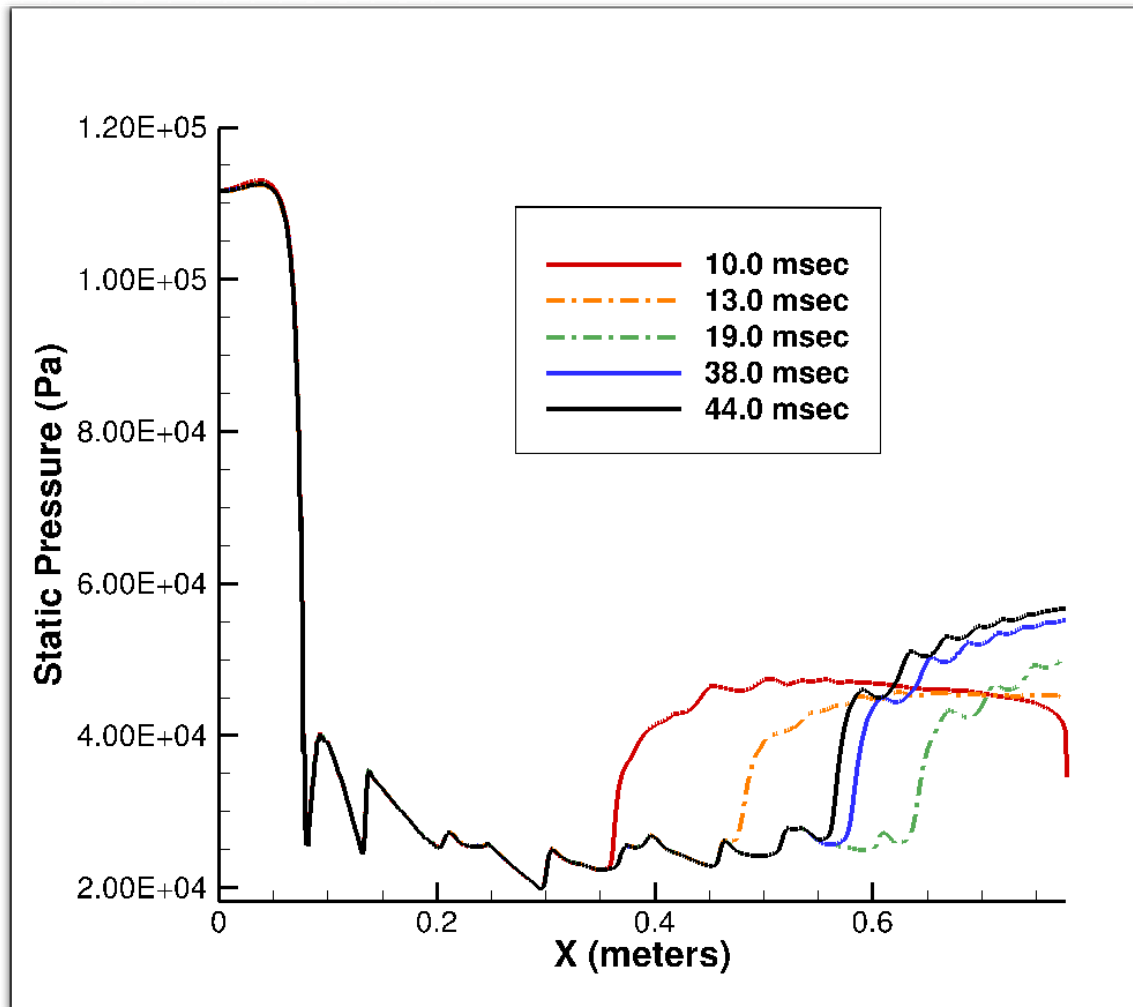


Figure 104. Time history for 56.5 kPa back pressure ramp case along line S2 (top) in the nozzle/isolator

Figures 105 and 106 show the time histories for the left and right sides, respectively, for the ramped case of 56.5 kPa. A comparison of these two figures indicates they are almost identical, indicating symmetry on both the left and right walls of the isolator.

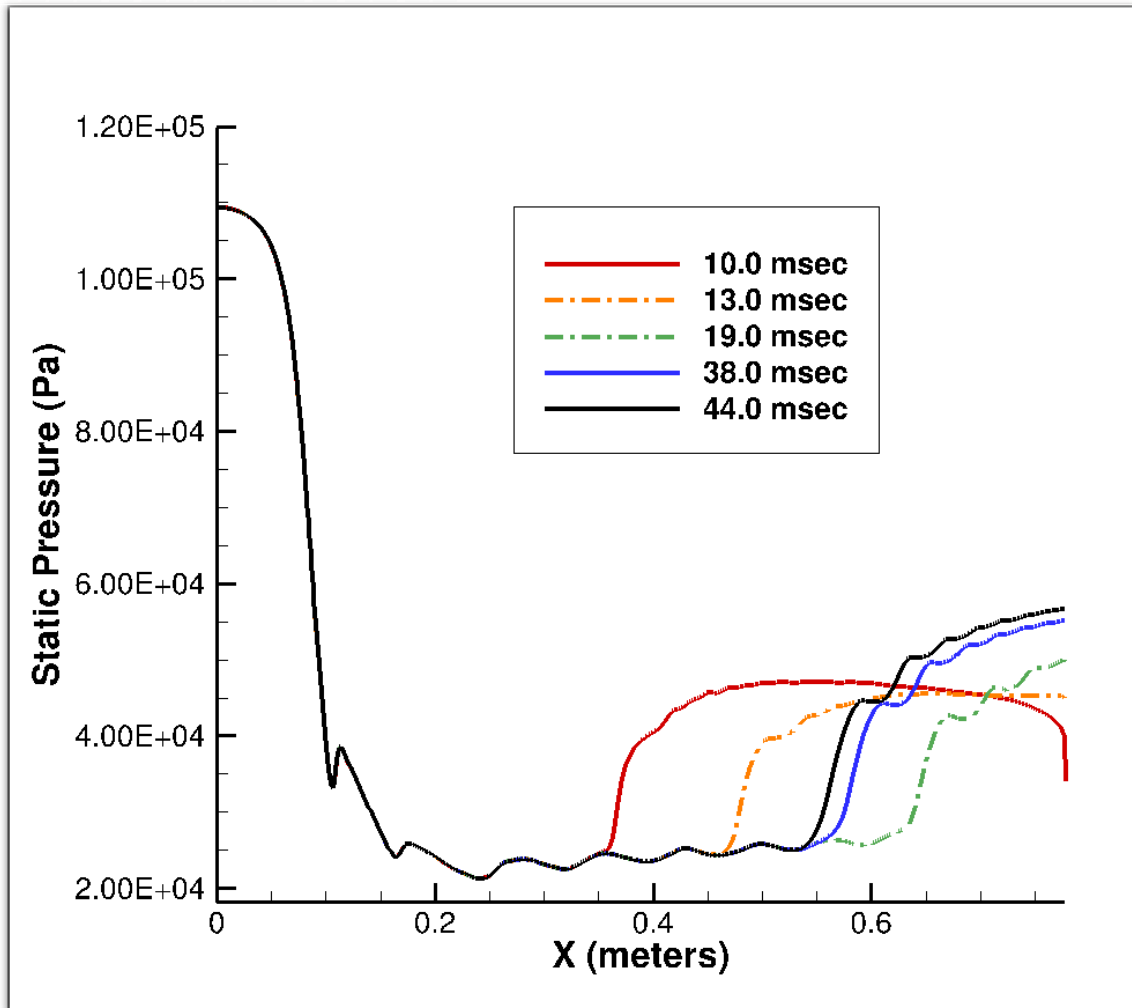


Figure 105. Time history for 56.5 kPa back pressure ramp case along line S3 (left) in the nozzle/isolator

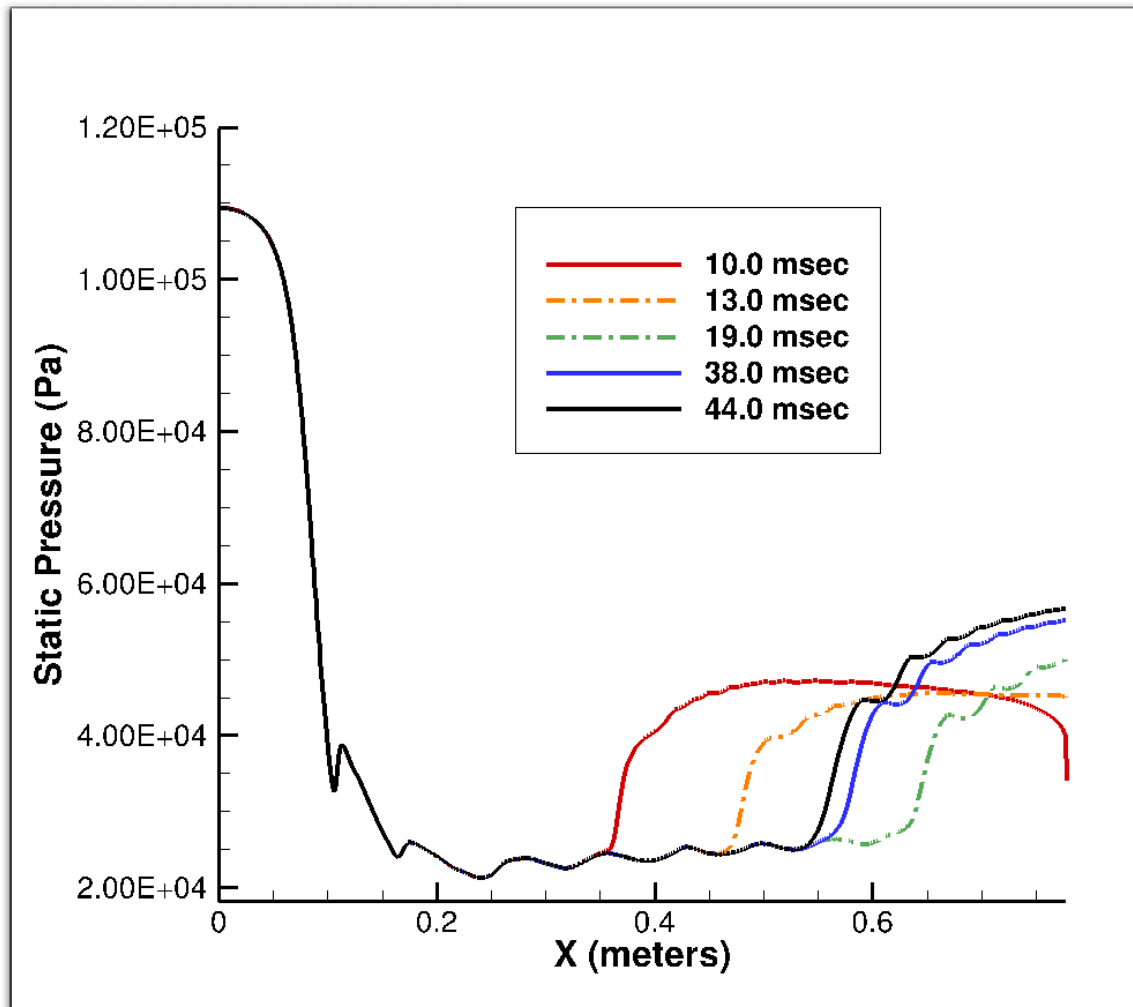


Figure 106. Time history for 56.5 kPa back pressure ramp case along line S4 (right) in the nozzle/isolator

VI. Analysis

Billig's Correlation

Figure 107 presents a comparison of the 2-D and 3-D CFD final position results with the Billig correlation (Billig, 1993). As explained in the Literature Review section, this experimental correlation defines the relationship of the pressure ratio to the length of the PCST. In Figure 107, the x-axis has Billig's correlation formula, where S_t is the measured shock train length (from the leading edge to the end of the isolator), M_4 is the Mach number at the leading edge of the PCST, θ is the calculated momentum thickness of the boundary layer, and h is the isolator height. On the y-axis, P_s is the static pressure measured at locations along the shock train from the leading edge and P_4 is the pressure at the leading edge. The 2-D data points are generally above the correlation line, but follow the same profile and direction of the line. This difference is expected since the correlation was developed based on 3-D experiments. In 3-D, there are four walls with boundary layers forcing the shock train upstream while in 2-D, there is just the top and bottom of the isolator. The 2-D shock is able to sustain a higher pressure ratio than the 3-D, which is why the 2-D points are above the correlation line. The 3-D data points follow the same profile and direction below the correlation line but generally fall within the scatter of the data upon which the correlation is based, shown in Figure 108 (Billig, 1993). In Figure 108, the majority of data shown between values 0 and 1 on the x-axis and between values 1 and 3 on the y-axis is also below the correlation line. The distance between the points and the correlation line in Figure 107 is not greater than the distance between the points and correlation line in Figure 108. Overall, both the 2-D and 3-D

points in Figure 107 are within the scatter range expected for this correlation. Both the 2-D and 3-D points follow the Billig correlation.

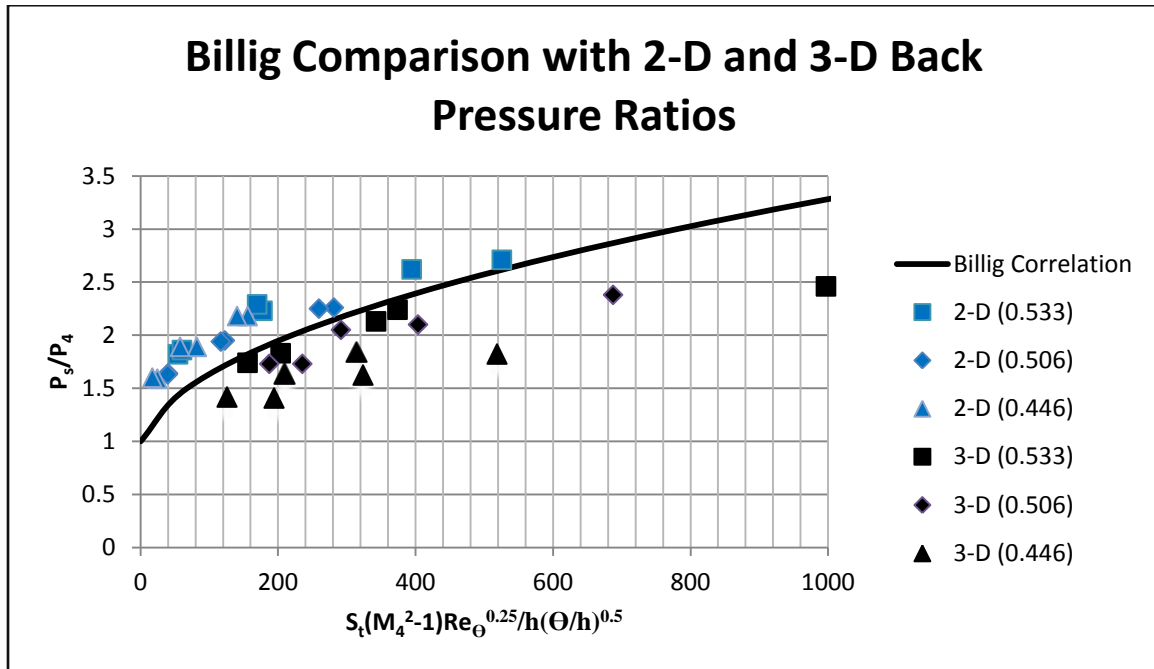


Figure 107. Billig comparison with 2-D and 3-D back pressure ratios

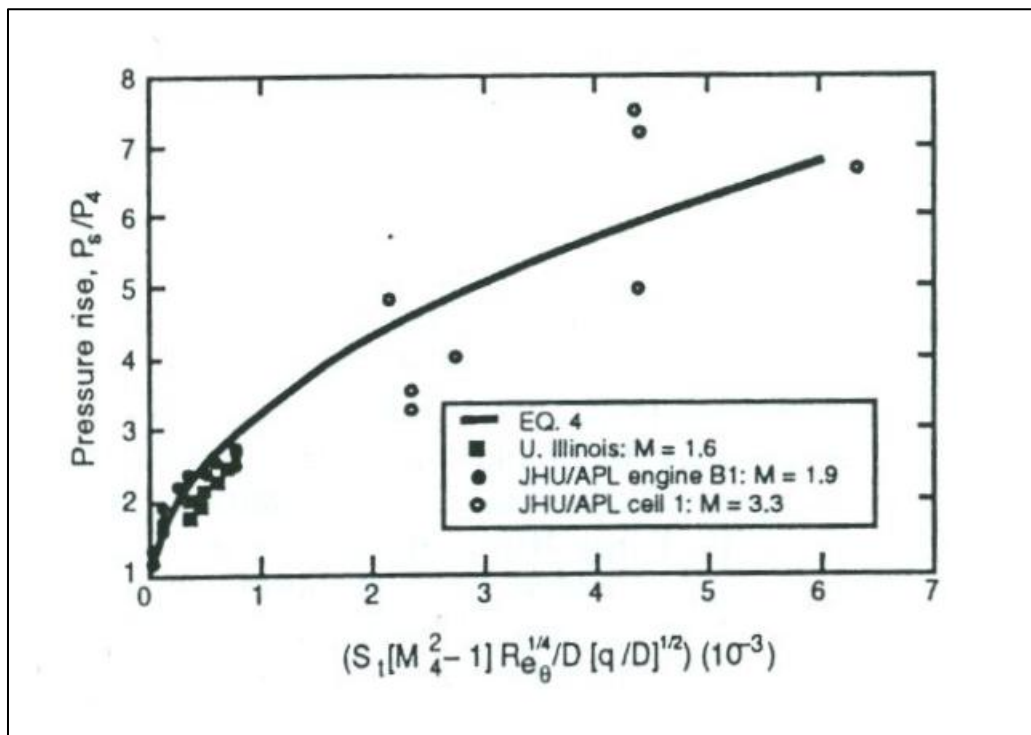


Figure 108. Pressure rise correlation for rectangular ducts (Billig, 1993)

Shock Speed

Figure 109 displays the shock speed (extracted from the simulations) of all four centerlines of each wall in the isolator for the two back pressure cases (89.6 kPa and 75.0 kPa for 140.6 kPa inflow) with the same back to inflow pressure ratio (0.533). Movement in an upstream direction is a positive shock speed value while movement downstream is indicated negative. In both back pressure cases, the shock train appears at 6 milliseconds after the first back pressure step started and begins moving upstream at an initial speed between 300 and 350 m/s. At seven milliseconds (one millisecond after the shock train has appeared) the shock train speed begins decreasing and slows to zero within the next two milliseconds. The shock train reverses direction and travels downstream at a speed between 0 and 40 m/s to its final location. At six milliseconds in both cases, the shock speed along the top (S1) is slower than the other sides initially. The slower S1 speed is most likely due to the geometry of nozzle, where the curvature is on the top wall, while the other 3 walls are flat plates. The curvature retards the motion of the shock speed as it adjusts to the geometry in the top wall. The difference in the location of the leading edge between the top and the other 3 walls is seen at 6 milliseconds in both Figure 57 for the 89.6 kPa simulation and Figure 76 for the 75.0 kPa simulation (with 140.6 kPa inflow). The S2 line increases and then decreases and joins the other lines at 7.5 milliseconds. Both back pressure cases show similar shock speed profiles from the formation of the shock train to the point where both shock trains reverse direction. After the shock trains reverse direction, they both travel back downstream, with the S1 through S4 centerlines in each back pressure case fluctuating after 9 seconds until the simulations reach the stopping criteria.

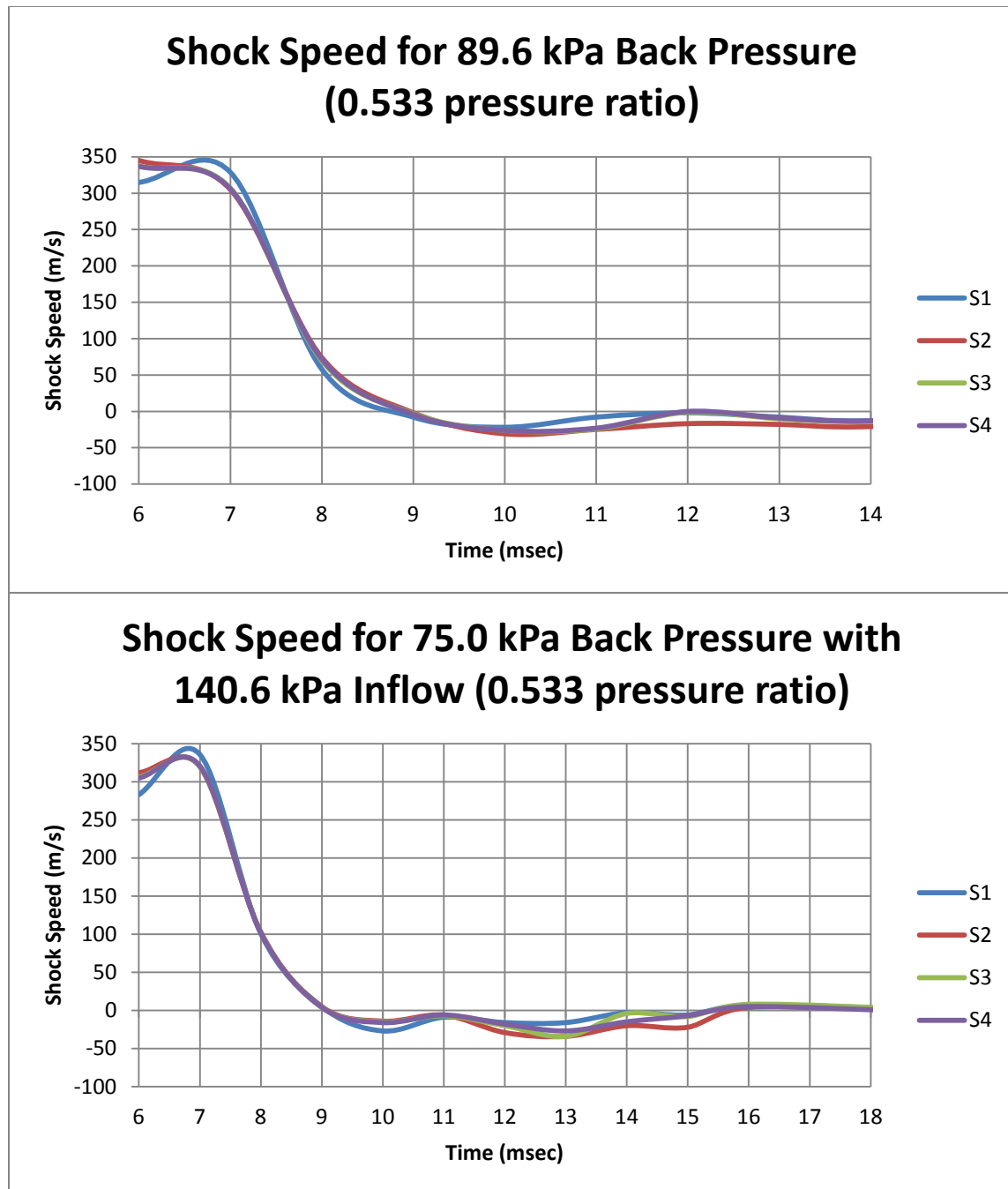


Figure 109. Shock speed for 0.533 ratios

Figure 110 contains the shock speed of all four isolator walls for the back to inflow pressure ratio of 0.506 (the 85.0 kPa and 71.1 kPa cases). The shock train in both the 85.0 kPa case and the 71.1 kPa case begins at 6 milliseconds moving upstream initially in the range of 200 to 300 m/s. By 7 milliseconds, the shock train has started

slowing until the shock speed reaches zero within the next 2 milliseconds and reverses direction, traveling downstream at a speed between 0 and 50 m/s to its final location. To summarize the pattern of the shock speeds in Figure 110, an initial “bump” in speed within the first millisecond of shock train formation followed by a decrease in speed to zero within two milliseconds followed by a downstream movement with a shock speed no greater than 50 m/s. This same summary could also be used to describe the back pressure cases in Figure 109. Another similarity Figure 110 has with Figure 109 is at six milliseconds, again, the shock speed along the top (S1) is not as fast as the other sides initially. The difference in S1 speed, again, appears to be the result of the geometry in the nozzle and confirms that seen in both Figures 62 and 80 for these two simulations. In comparing Figures 109 and 110, both sets of results for the 0.533 and 0.506 pressure ratios show that in the first three milliseconds after the shock train is formed and detected, the shock train initially travels upstream. As the shock train stabilizes, the shock train slows down, stops its movement and reverses direction. The shock train then travels downstream until reaching the stopping criteria at specific locations, based on the back to inflow pressure ratio. The same pattern of upstream, reversal, and downstream movement is also shown in Figure 111 for a back to inflow pressure ratio of 0.446 (the 75.0 kPa and 62.78 kPa cases). The pattern of upstream, reversal, and downstream shock train movement (now starting at seven milliseconds) is present again as in Figures 109 and 110, with the same initial shock speed difference along S1, seen in both Figures 70 and 88 for these two simulations.

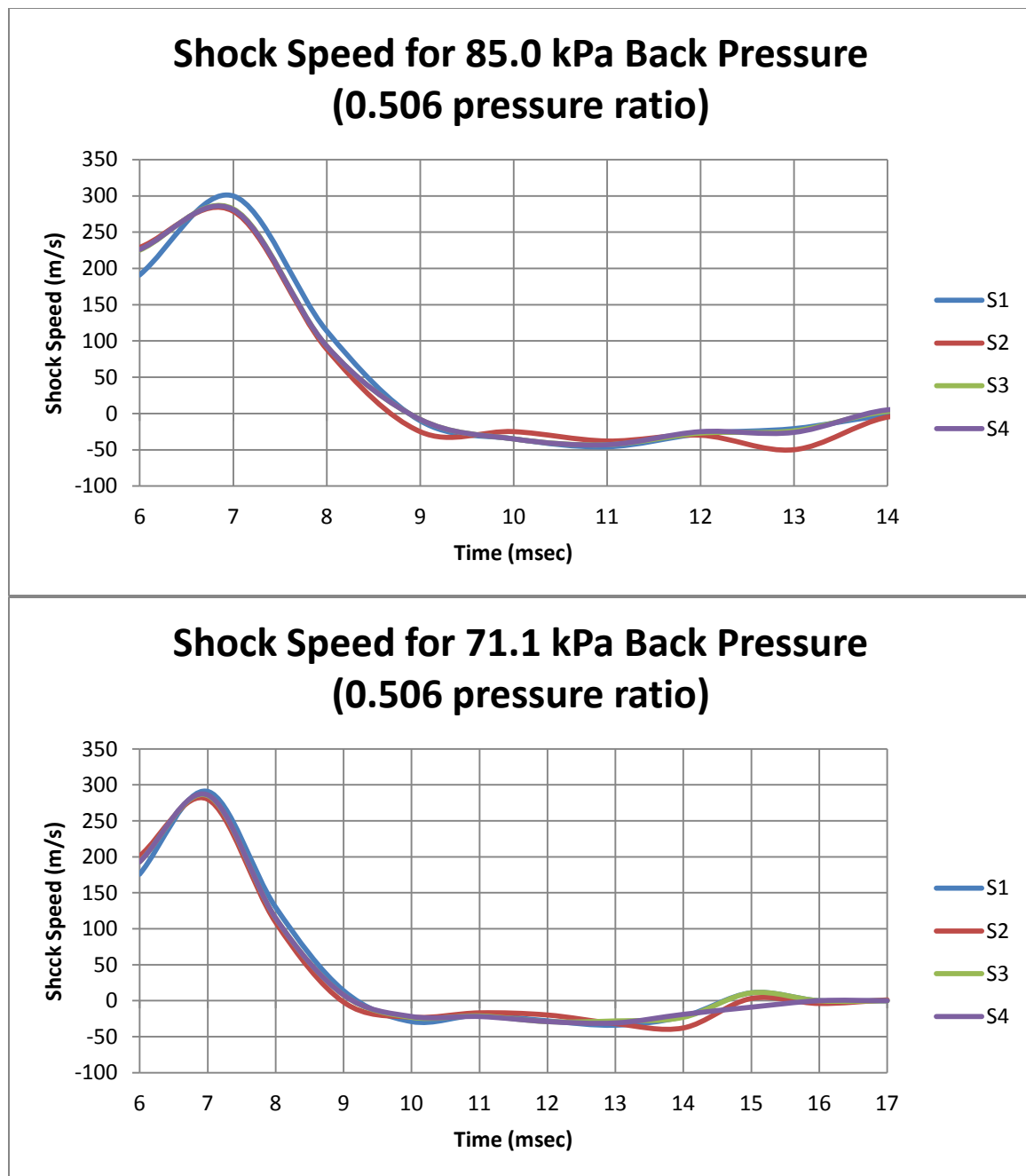


Figure 110. Shock speed for 0.506 ratios

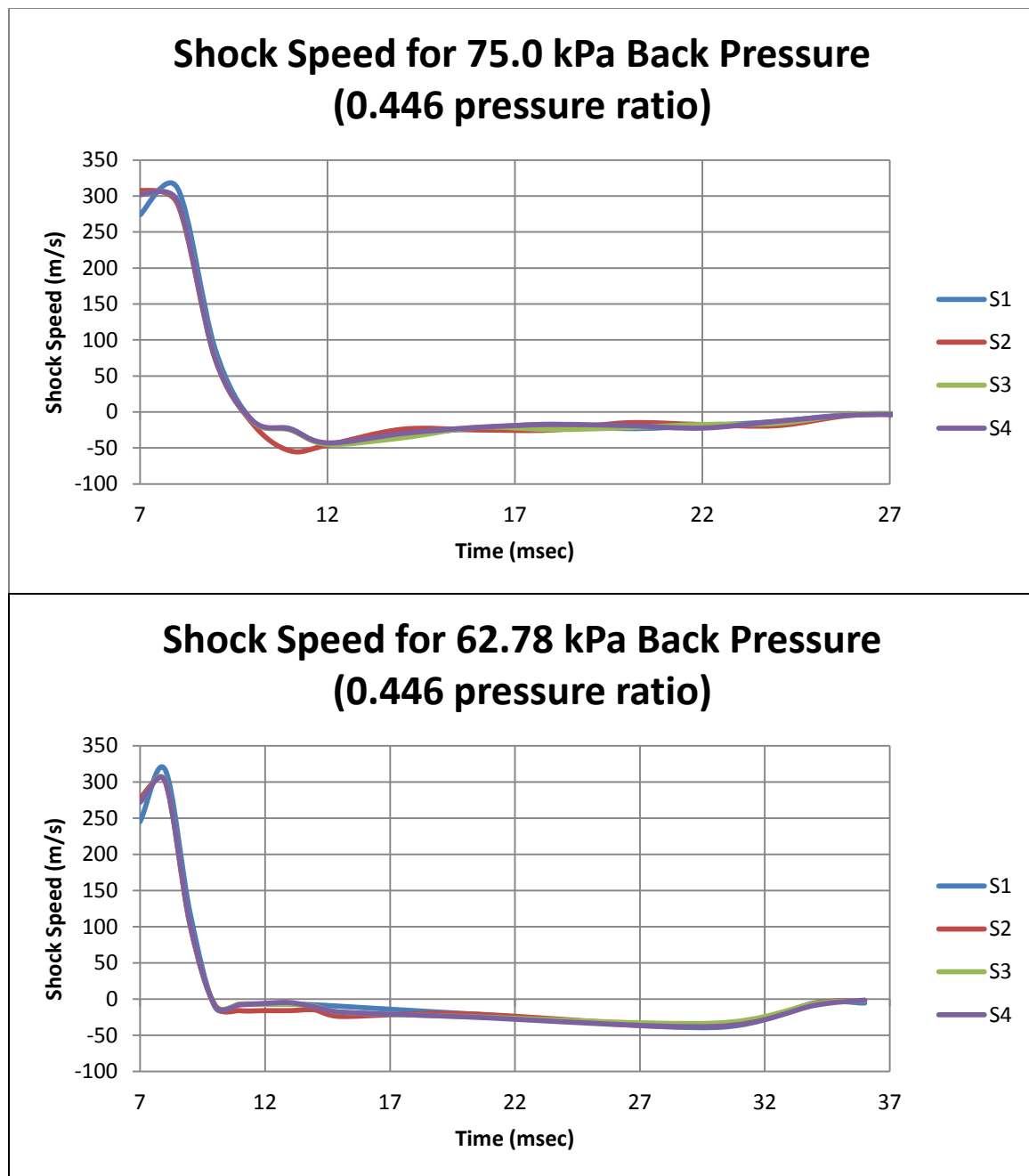


Figure 111. Shock speed for 0.446 ratios

Off-Centerline Analysis

The time histories in the 3-D cases were all measured at the centerlines of the walls of the isolator. An off-centerline analysis was done along the bottom wall at distances of 0.635 cm (0.25 inches), 1.27 cm (0.5 inches), and 2.54 cm (1 inch) from the corner between lines S1 and S4 (see Figure 59) to determine if there was any difference between the centerline and other locations along the walls. These results are shown below in Figures 112-114.

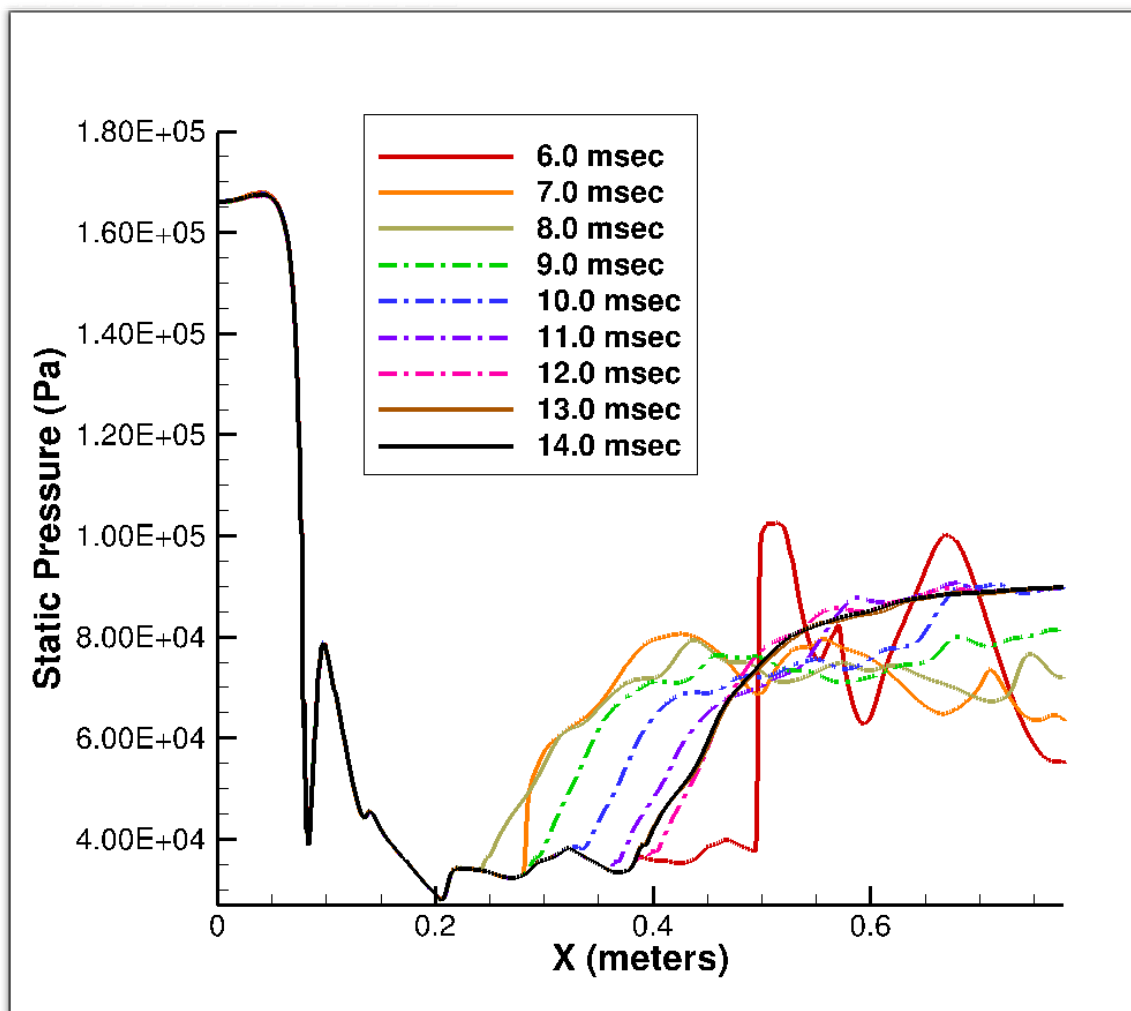


Figure 112. Time history for 89.6 kPa back pressure 0.25 inches from the S1 / S4 corner

When Figures 112-114 are compared to Figure 60 (which measured the bottom centerline for 89.6 kPa) and each other, the locations of the leading edge at the times specified are generally the same. The big difference among traces is the magnitude of the spikes of pressure as the shock train travels upstream and then downstream in the isolator. The spikes get larger and sharper at 1.27 cm (0.5 inches) compared to 0.635 cm (0.25 inches) and sharper yet at 2.54 cm (1 inch) from the wall. The change in spikes is the result of moving further away from the corner. The corners contain boundary layer separation bubbles that lower the magnitude of the pressures. Without a boundary layer in the corners, no information can be propagated upstream so no shock train can form there. The same change in pressure magnitude is seen in the other five back pressure cases as well. In the AFIT experiment, pressure transducers were located along the center of the bottom wall (S1) of the isolator. For future experiments, transducers should be placed closer to the corner of the isolator to measure the pressures from the corner to the centerline. The pressure measurements could provide the size of the separation bubbles.

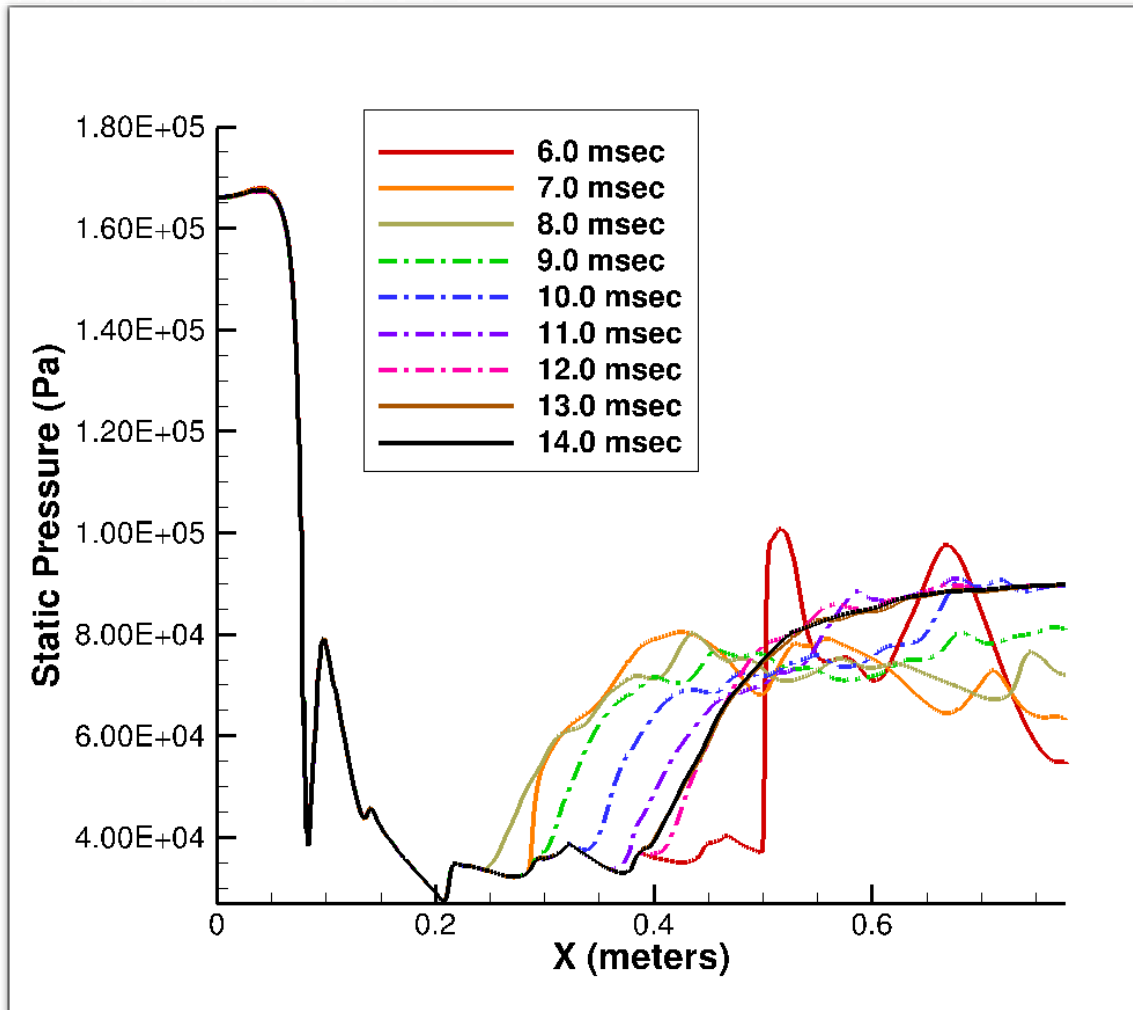


Figure 113. Time history for 89.6 kPa back pressure 0.5 inches from the S1 / S4 corner

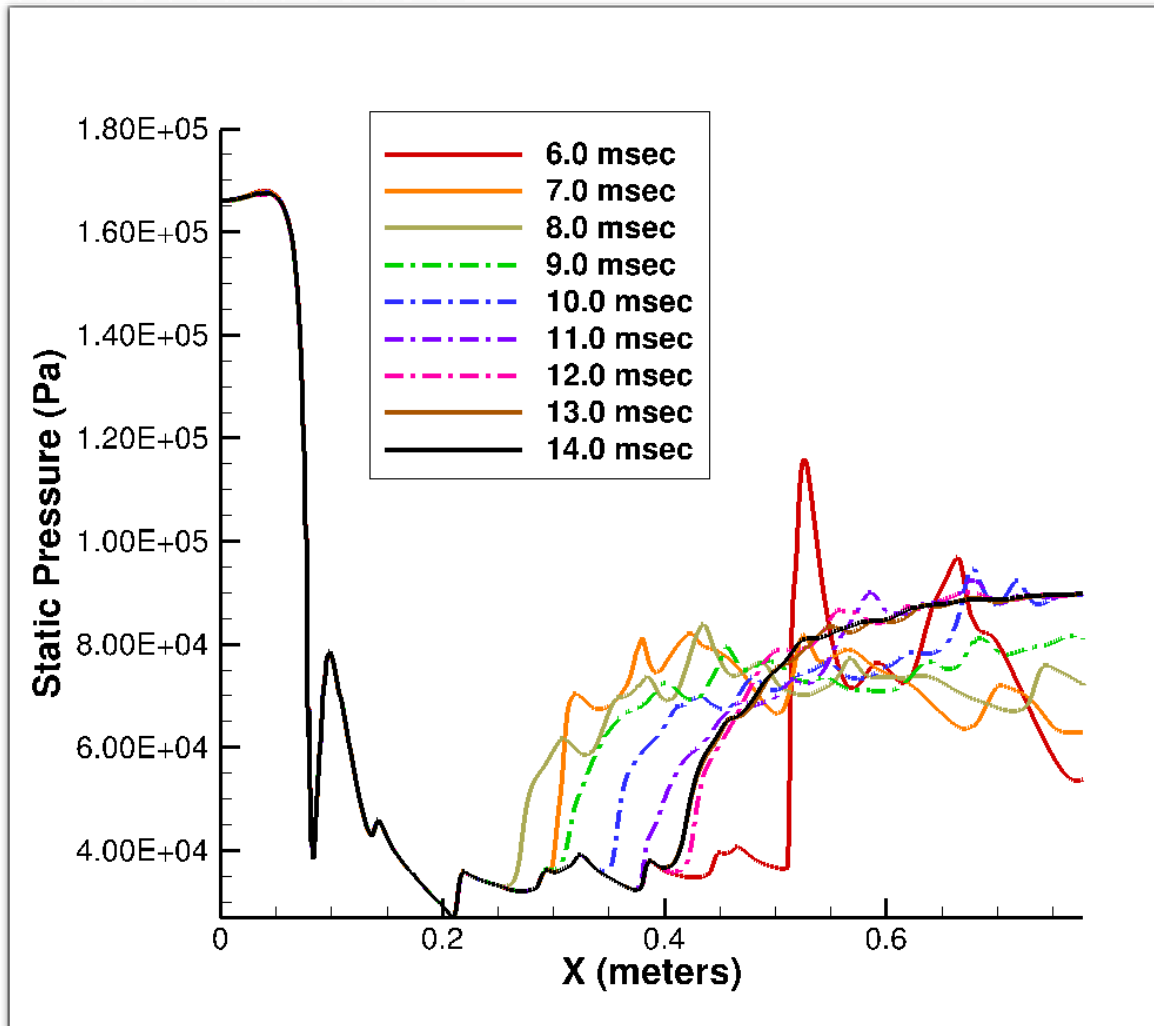


Figure 114. Time history for 89.6 kPa back pressure 1 inch from the S1 / S4 corner

Friction Stress Analysis

Wall friction, sometimes called skin friction, is an important parameter. As a wall property, skin friction can be measured experimentally without complicated, weighty, or bulky flow diagnostics, even on flight vehicles. Skin friction reflects the state of the boundary layer and can be used to detect separation, which occurs when skin friction reaches zero or becomes negative. For these reasons, an understanding of the skin friction field is a valuable aid to the development of scramjet control systems. VULCAN calculates and reports the friction force on each cell in the x, y and z directions.

VULCAN also calculates the area of each cell. If the friction force is divided by the area for each cell wall, the result is the friction stress in the streamwise (x), vertical (y) and transverse (z) directions. Figure 115 shows the friction stress for the x, y, and z directions for the bottom centerline of the stepped 89.6 kPa back pressure case when the shock train has reached its final location. The y-direction friction stress has a spike at the beginning as a result of the nozzle geometry and then goes to zero. Since there is no vertical friction stress component at the wall, it does not provide any information. Similarly, the z-direction friction stress is zero, so the z-direction also does not provide any useful information, except for the slight fluctuation at 39.7 cm, identifying the leading edge of the PCST. The x-direction friction stress has an increase in pressure (resulting from the nozzle geometry) followed by a decrease (as it enters the constant area isolator) from 0 to 25 cm. From 25 to 40 cm, the x-direction friction stress hovers at around 160 Pa. At the leading edge of the PCST where the pressure changes (see Figure 60), the friction stress suddenly decreases, but does not go below zero. If there had been a negative value, the x-direction friction stress would have indicated there was separation of the boundary layer at the location of the leading edge of the PCST. After the drop at 50 cm, the friction stress slowly starts to increase. The increase is due to the boundary layer thickness increasing further downstream in the isolator, increasing the static pressure. Other centerlines (S2, S3, and S4) were also analyzed, and they showed the same decrease in friction stress at the leading edge of the shock train without going to zero, followed by an increase due to the boundary layer thickness. In summary, the other centerlines showed the same tendency toward separation without actual separation.

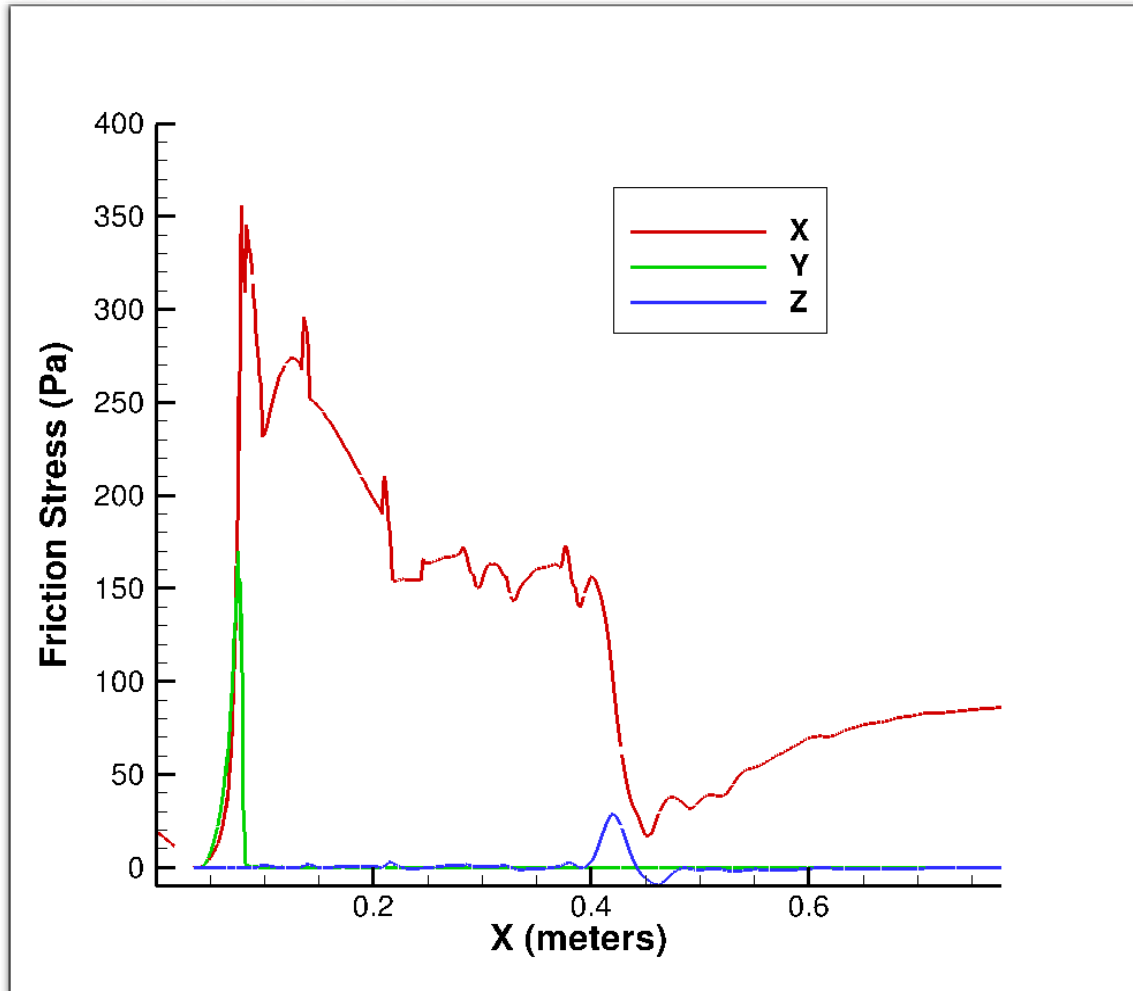


Figure 115. Friction Stress along bottom centerline (S1) for 89.6 kPa back pressure

In Figures 116-120, the same type of profile for both before and after the PCST leading edge for the x-direction friction stresses is seen in the other five simulations. The y-direction friction and z-direction friction stress profiles from Figure 115 are also present in Figures 116-120.

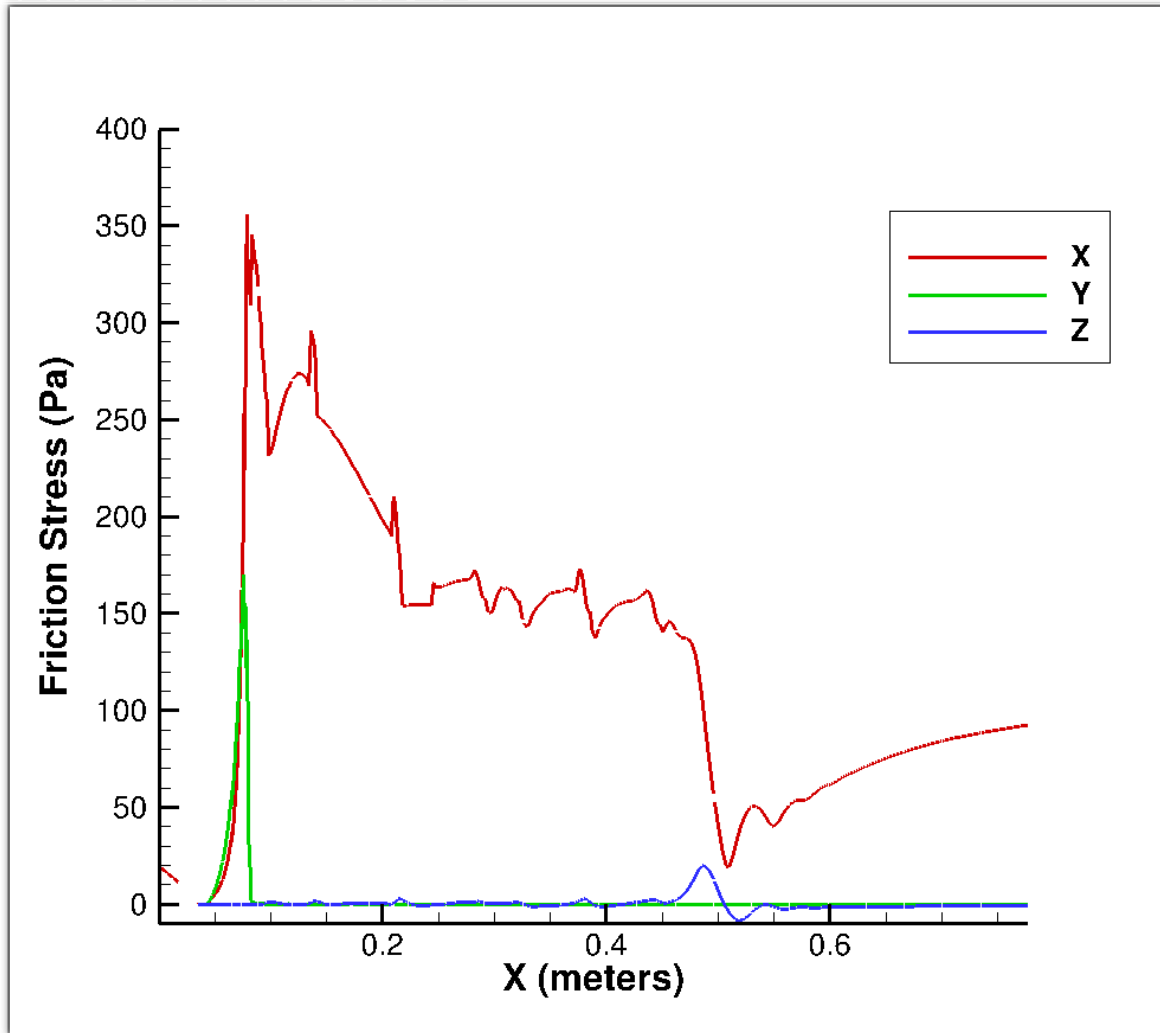


Figure 116. Friction Stress along bottom centerline (S1) for 85.0 kPa back pressure

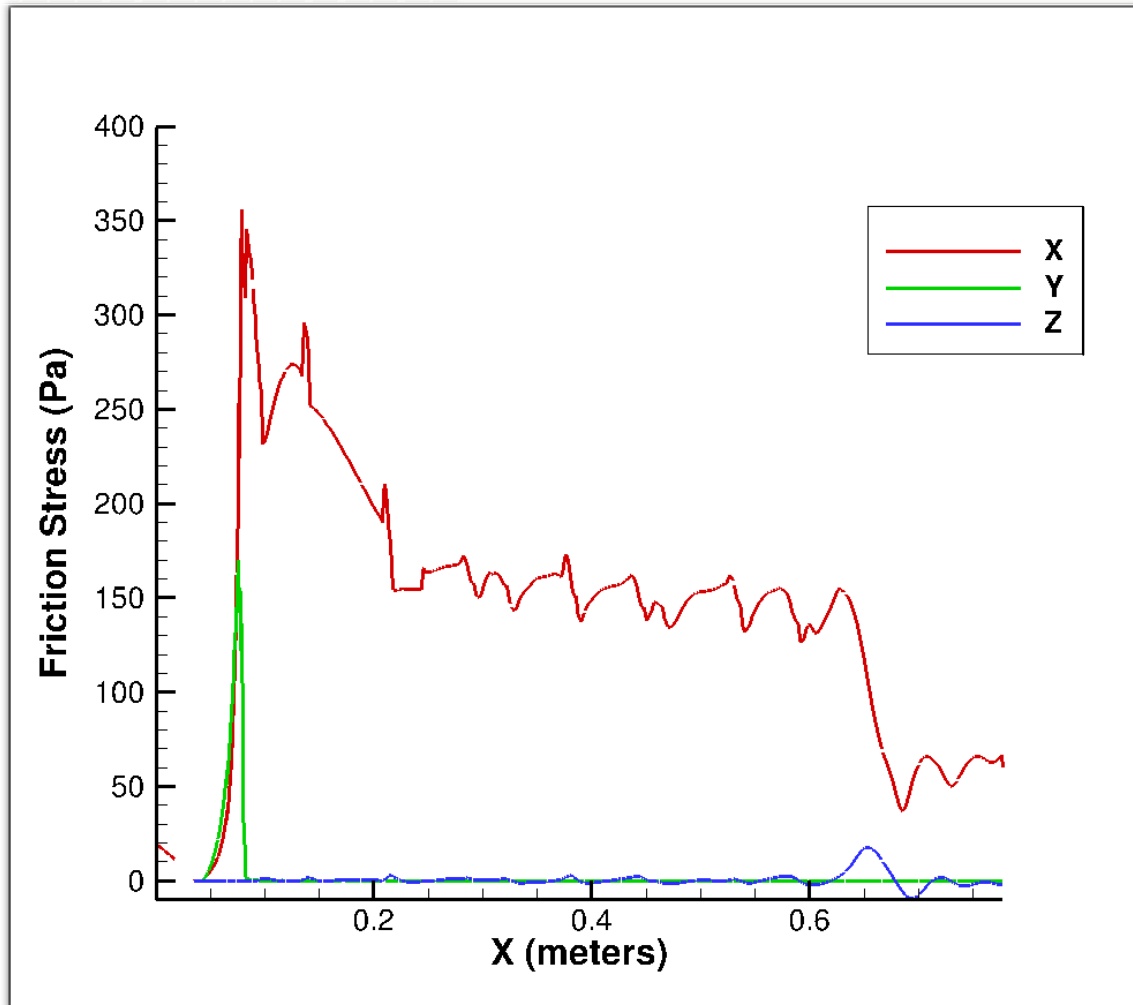


Figure 117. Friction Stress along bottom centerline (S1) for 75.0 kPa back pressure

Figure 118 has the same back to inflow pressure ratio (0.533) as in Figure 115, but a different inflow pressure (140.6 kPa). A comparison of these two figures for the friction stress shows the same profile, with increases and decreases at the same locations on the x-axis. The only difference between Figures 115 and 118 is the values of the y-axis, where in Figure 115 the values of the friction stress are higher since the inflow pressure is 168.2 kPa, while in Figure 118, the friction stress values are lower since the inflow pressure is 140.6 kPa.

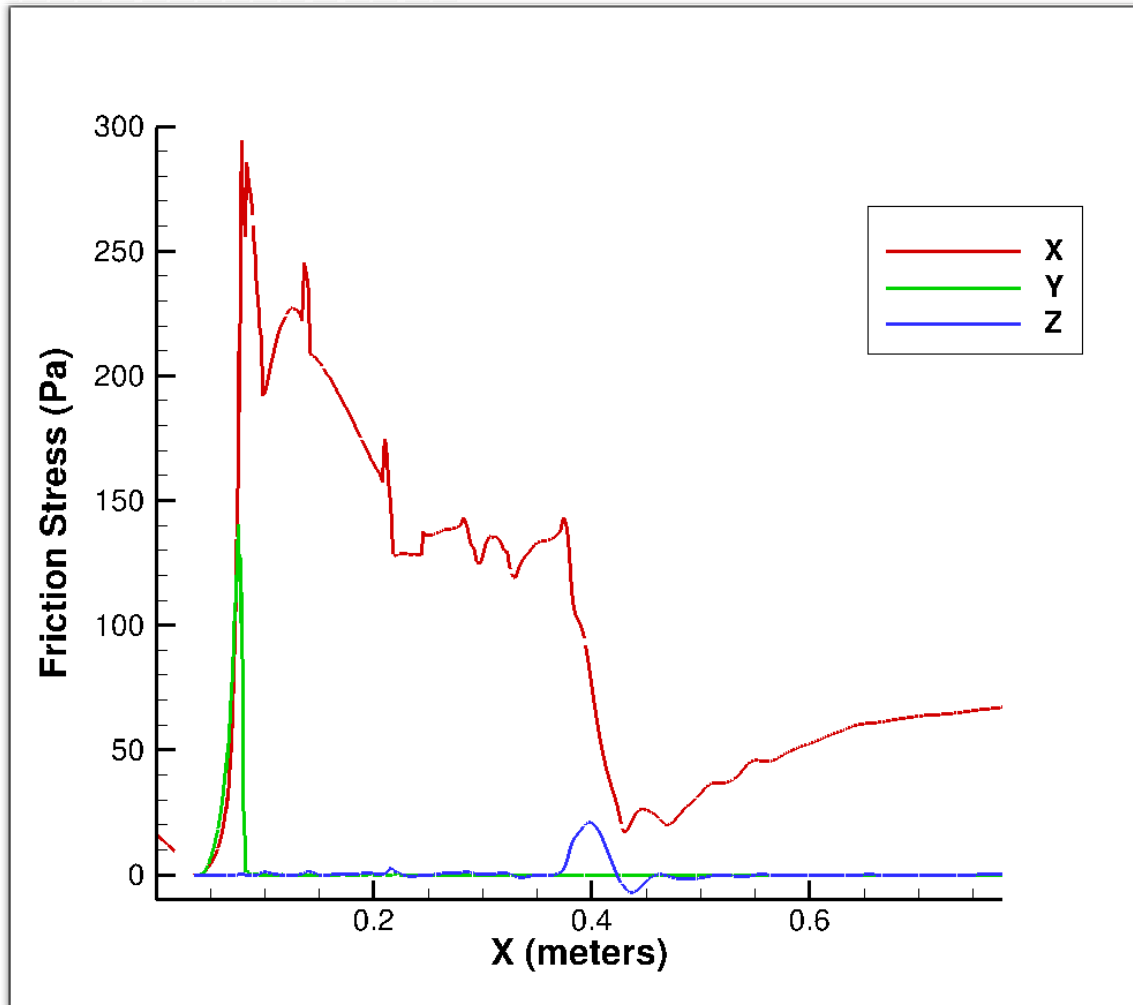


Figure 118. Friction Stress along bottom centerline (S1) for 75.0 kPa back pressure (140.6 kPa inflow)

The same lack of information from the y- and z-direction friction stresses and the same increases and decreases in x-direction friction stresses seen in Figures 115 and 118 for the same back to inflow pressure ratio are also present in Figures 116 and 119 (for the back to inflow pressure ratio of 0.506), and in Figures 117 and 120 (for the back to inflow pressure ratio 0.446).

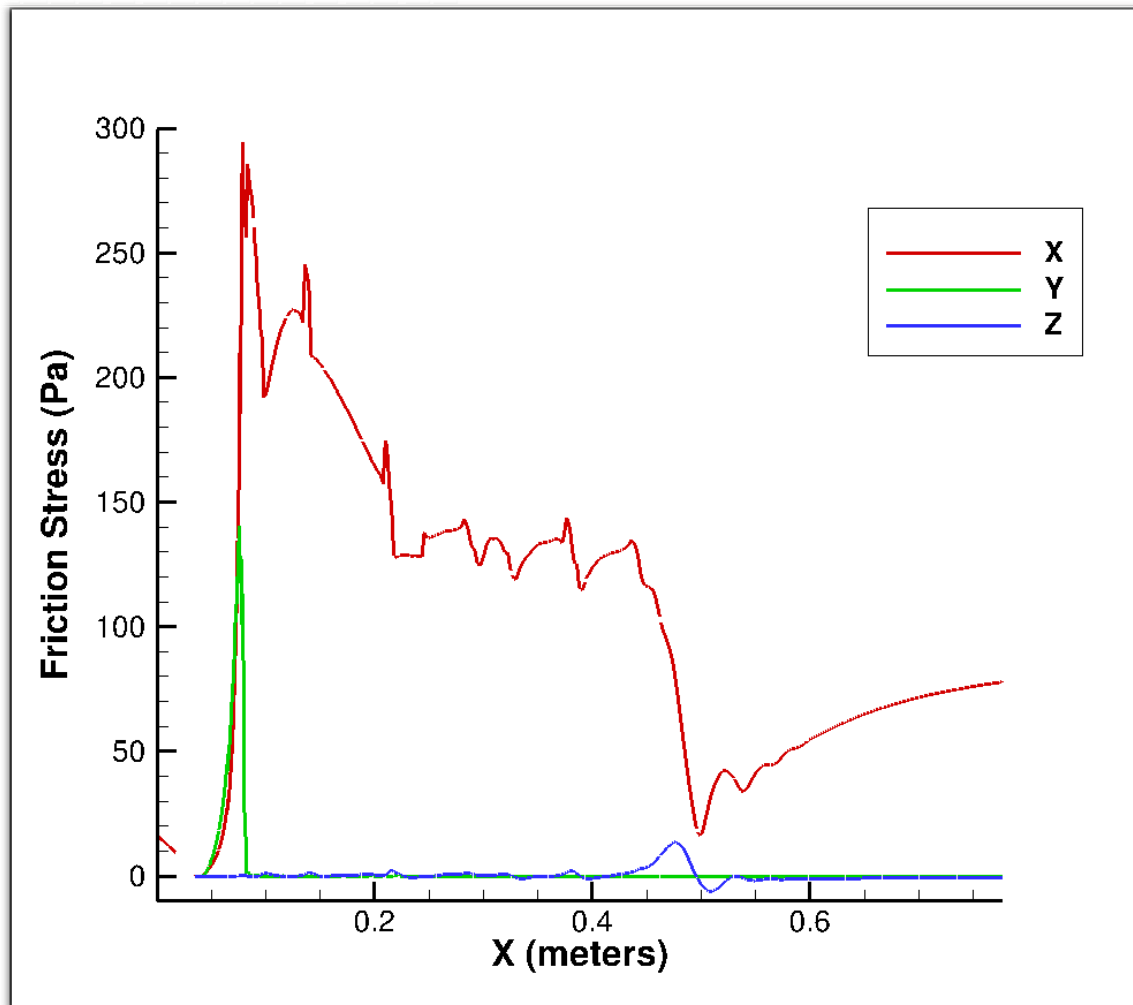


Figure 119. Friction Stress along bottom centerline (S1) for 71.1 kPa back pressure

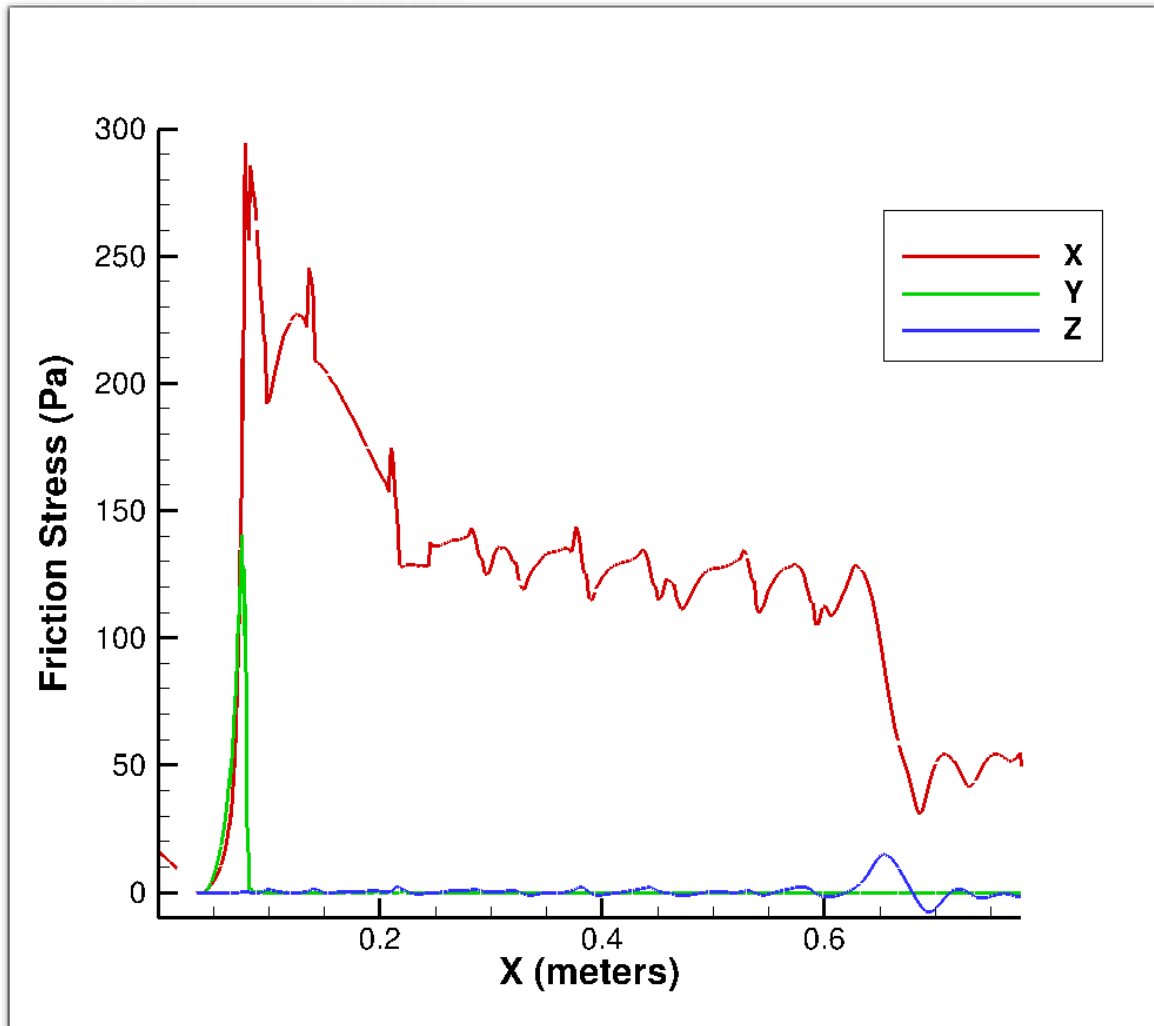


Figure 120. Friction Stress along bottom centerline (S1) for 62.78 kPa back pressure

CFD and Experiment Comparison

The CFD results provided in this research used the nozzle and isolator dimensions in the AFIT experiment (Hutzel, 2011). A comparison between the CFD results and the results from the AFIT experiment was accomplished to compare the final locations of the leading edge of the PCST. Some comparisons are between the CFD results and the AFIT experiment results that have similar back pressure and inflow pressure values, while others are comparisons of similar back to inflow pressure ratios, but with different back pressure and inflow pressure values. For better comparison of all the results, Figures 121-

126 have both the CFD static pressure results and the AFIT experiment static pressure results divided by their respective inflow pressures to create normalized results. Figure 121 shows the final locations of the leading edge of the shock train for the CFD cases (both instantaneous and gradual back pressure applications) where the inflow pressure was 168.2 kPa and the back pressure was 89.6 kPa (0.533 back pressure ratio) and the AFIT experiment where the inflow was 167.91 kPa and the back pressure was 88.5 kPa (back pressure ratio of 0.527). The AFIT experiment measured pressure via 13 transducers with 3.01 cm spacing along the center of the bottom wall of the isolator. There was no way to tell how fast or where the difference in pressure changed from one transducer to the next. The leading edge was located somewhere between two of these transducers, and was considered to be located at 50% of the distance between the two transducers. The spacing between the transducers means the leading edge could have an error as much as 1.50 cm in the experimental data. The CFD cases shown are the results along line S1, the bottom wall for 3-D, and the bottom for 2-D. In Figure 121, the experimental transducer results are shown by the red dashed line which starts at 0.3 meters (the start of the isolator duct). The CFD lines track the static pressure from the start of the nozzle to the end of the isolator. The 3-D CFD case shows a more gradual pressure rise along the isolator than either the AFIT experiment or the 2-D CFD cases. The final location of the leading edge of the 3-D CFD case is 12.3 cm from the final location of the AFIT experiment. The causes for the difference in final locations between the 3-D CFD and the AFIT experiment will be explained later in this section. Figure 122 displays the comparison between the CFD where the back pressure was 85.0 kPa (with a ratio of 0.506) and the AFIT experiment with a back pressure of 82.9 kPa (a ratio of

0.494). The difference between the leading edges of the 3-D CFD case and the AFIT experiment in Figure 122 is 11.4 cm, compared to the difference of 12.3 cm in Figure 120. The differences in Figures 121 and 122 indicate that the results of 3-D CFD are closer to the results of the AFIT experiments for lower back pressure cases.

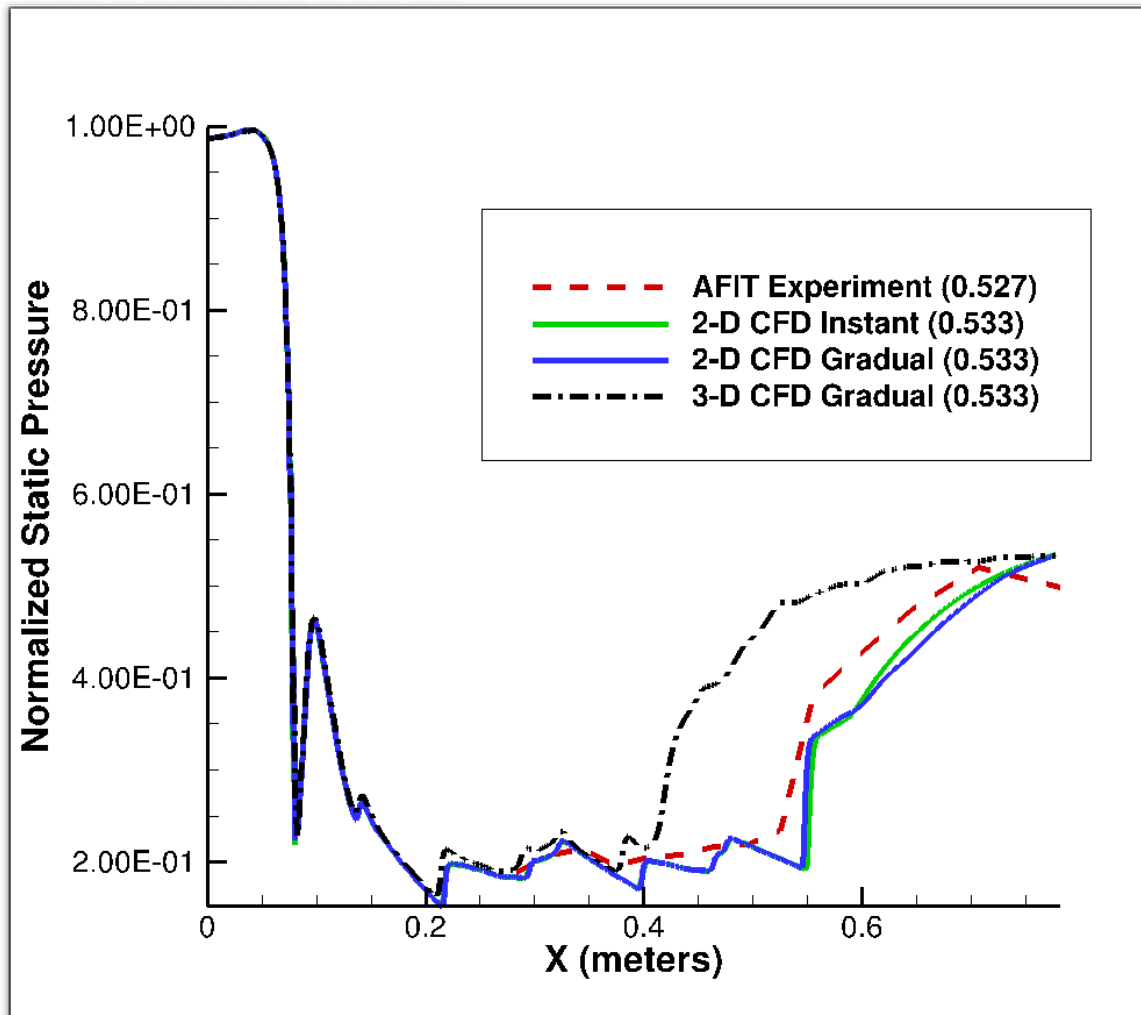


Figure 121. Comparison of CFD (0.533) with AFIT Experiment (0.527)

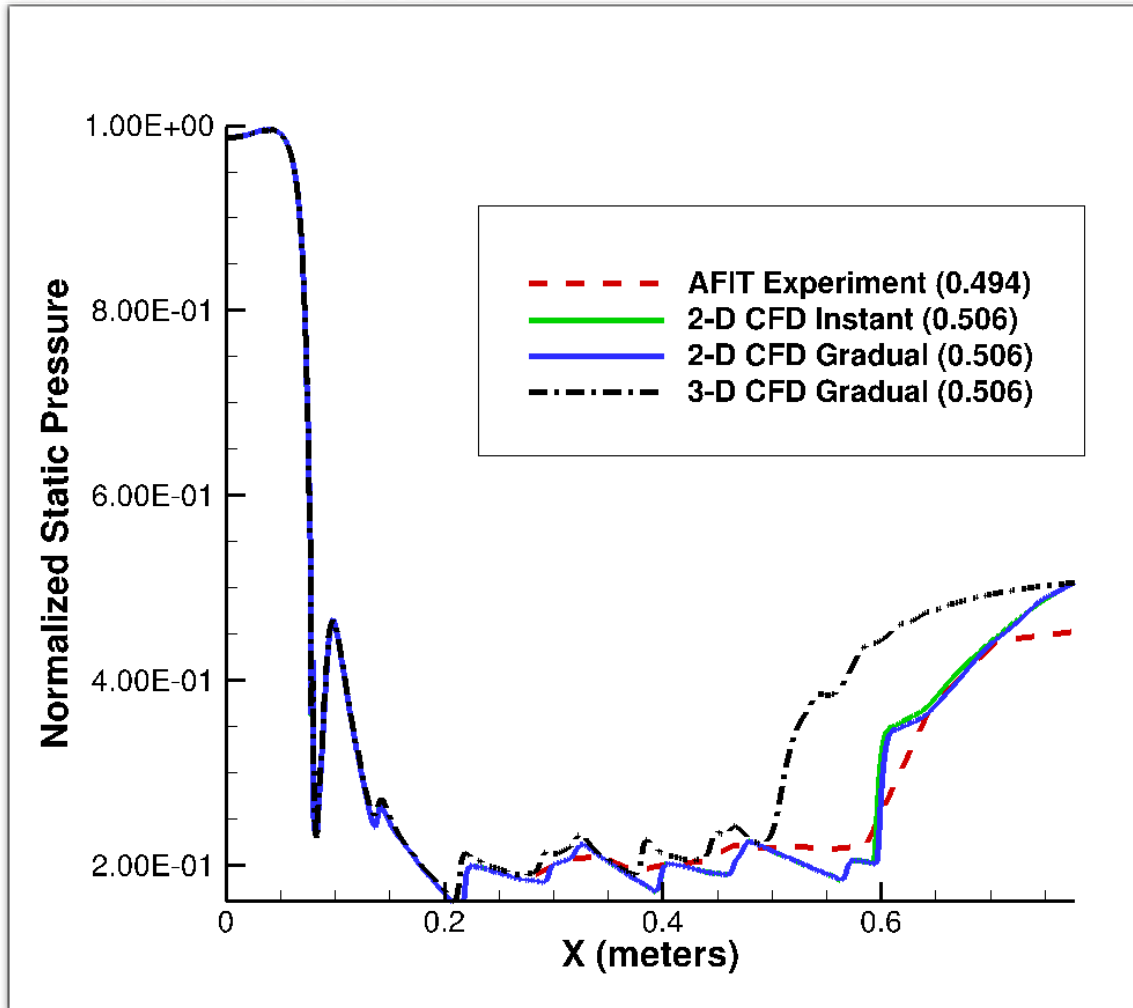


Figure 122. Comparison of CFD (0.506) with AFIT Experiment (0.494)

Figure 123 shows the comparison between the CFD where the back pressure was 75.0 kPa (with a ratio of 0.446) and the AFIT experiment where the back pressure was 75.9 kPa (with a ratio of 0.452). The 3-D CFD case in Figure 123 is now even closer to both the AFIT experiment and the 2-D CFD cases than in Figures 121 or 122, with a difference between leading edges of only 2.1 cm. The leading edge difference confirms that the results from lower back pressure cases are closer to the results of the AFIT experiments. The next step in the CFD/experiment comparison is to determine if the

trend still exists where similar back to inflow pressure ratios are used, but with different back pressure and inflow pressure values.

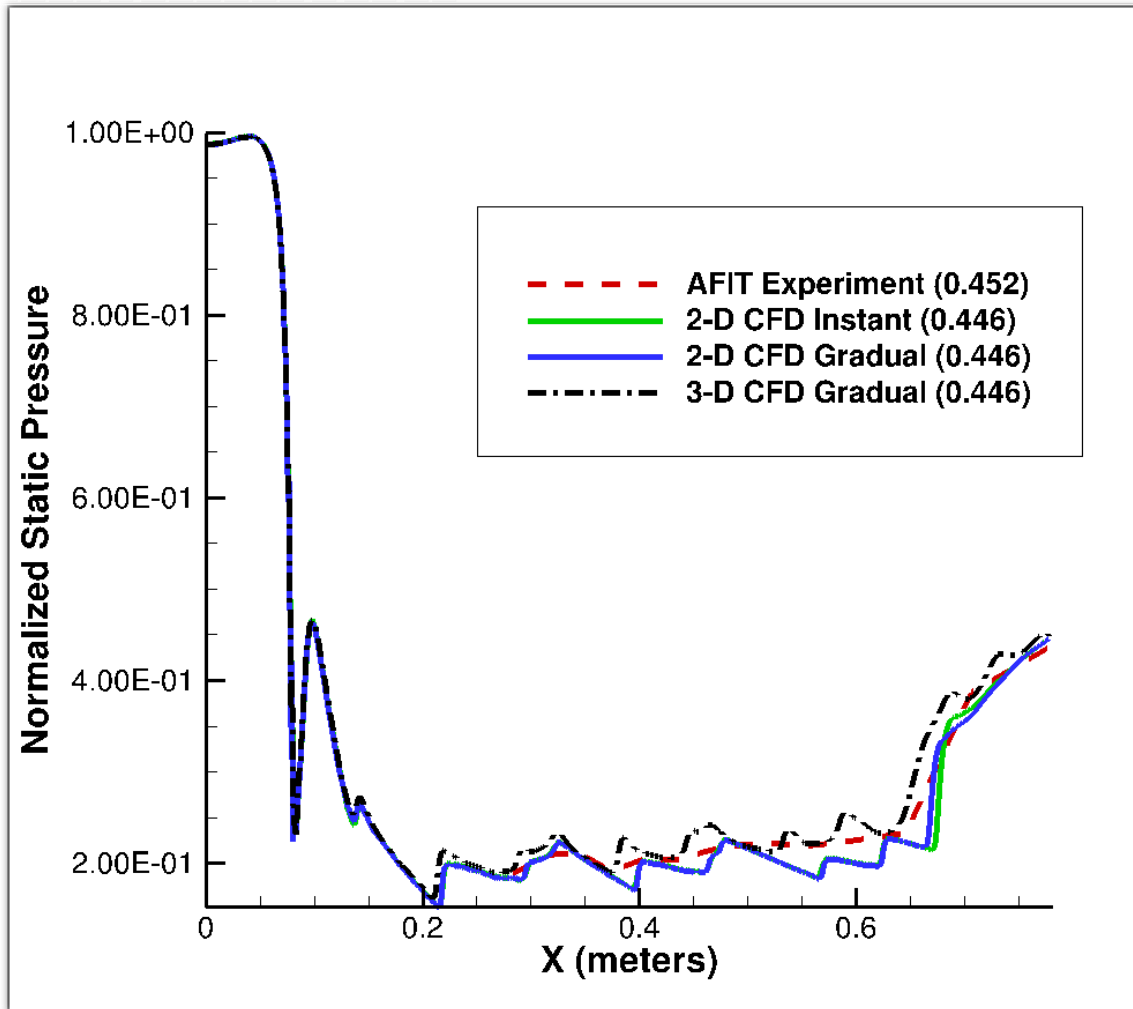


Figure 123. Comparison of CFD (0.446) with AFIT Experiment (0.452)

In addition to the AFIT experiment runs shown in Figures 121-123, three runs were accomplished with an inflow pressure of 112.9 kPa and back pressures of 58.7 kPa, 56.5 kPa, and 49.9 kPa. The three back pressures represent back to inflow pressure ratios of 0.520, 0.492, and 0.442, respectively. The ratios are similar to the ratios used in the CFD cases where the inflow pressure was 140.6 kPa and the back pressures were 75.0 kPa (0.533), 71.1 kPa (0.506) and 62.78 kPa (0.446). Figure 124 shows the final location

of the leading edge of the shock train between the 2-D and 3-D CFD cases where the inflow pressure was 140.6 kPa and the back pressure was 75.0 kPa (0.533) and the AFIT experiment where the inflow was 112.9 kPa and the back pressure was 58.7 kPa (0.520). The difference in the leading edges of the shock trains between the 3-D CFD and the AFIT experiment seen in Figure 121 is present again in Figure 124. A more thorough explanation of the difference between 3-D CFD and AFIT experiment is presented later in this section.

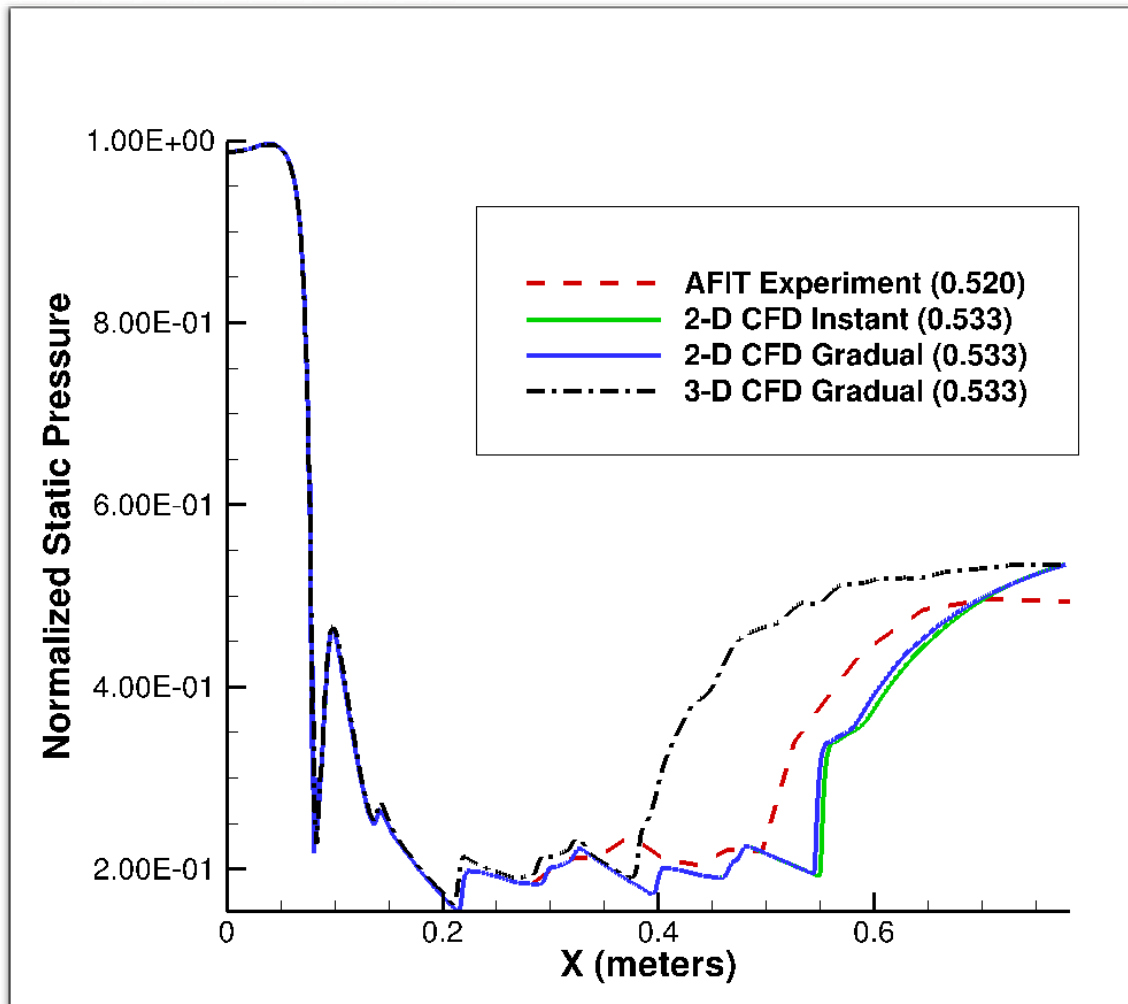


Figure 124. Comparison of CFD (0.533) with AFIT Experiment (0.520)

Figure 125 shows the comparison between the CFD where the back pressure was 71.1 kPa for an inflow pressure of 140.6 kPa (0.506), and the AFIT experiment where the back pressure was 56.5 kPa for an inflow pressure of 112.9 kPa (0.492). Compared to Figure 122, Figure 125 is following the earlier trend, identified in Figures 122 and 123, that lower back pressure cases are closer to the AFIT experiment results.

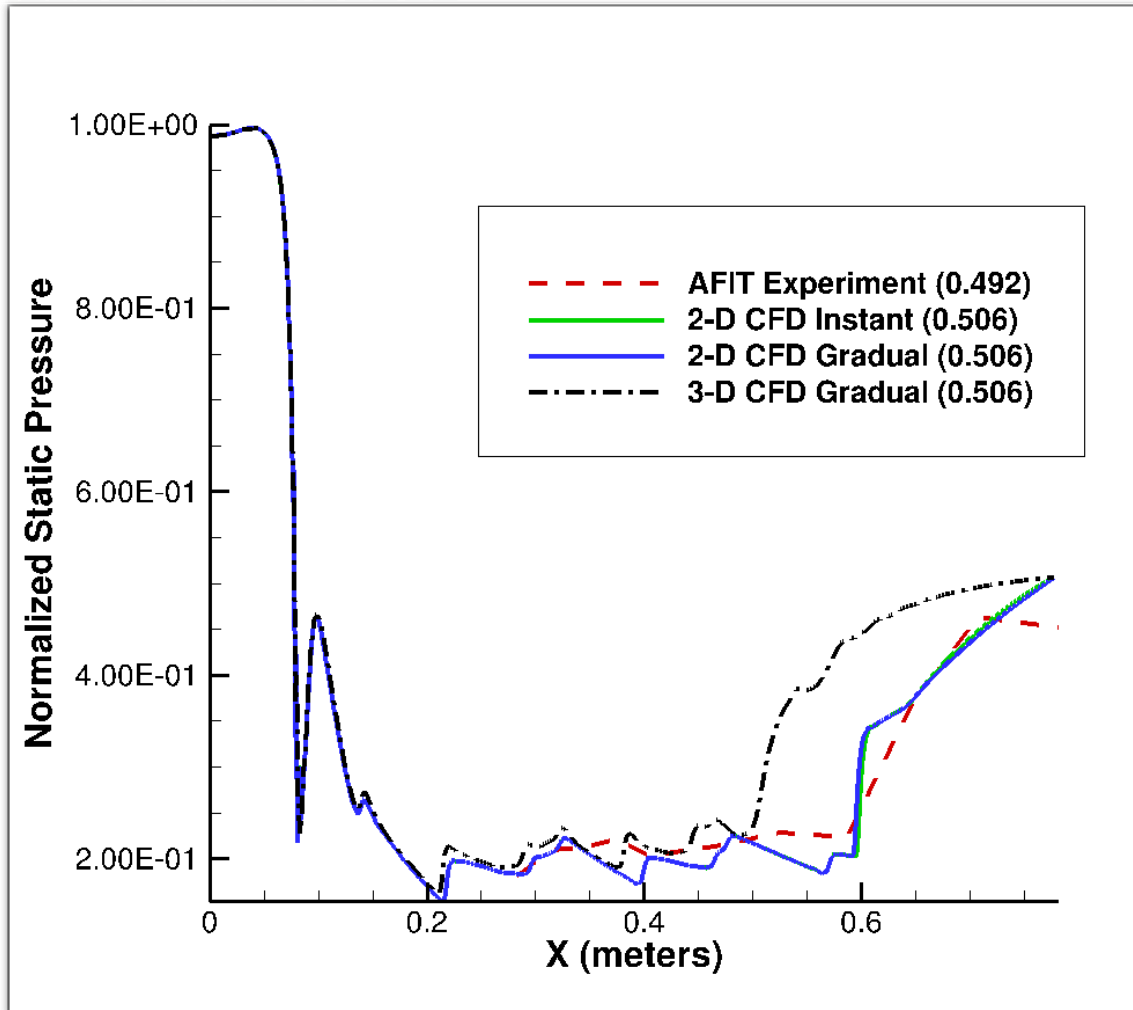


Figure 125. Comparison of CFD (0.506) with AFIT Experiment (0.492)

Figure 126 shows the comparison between the CFD where the back pressure was 62.78 kPa for an inflow pressure of 140.6 kPa (0.446) and the AFIT experiment where the back pressure was 49.9 kPa for an inflow pressure of 112.9 kPa (0.442). The largest

difference in Figure 126 is between the 2-D CFD results and the experimental results (3.8 cm). Note in Figures 121-126 that the 2-D CFD results show almost a vertical line where the rise in pressure at the leading edge of the shock train occurs, while the 3-D CFD results show a more gradual pressure rise. This difference between 2-D and 3-D confirms the earlier observation originally in Figure 120 that the 3-D CFD simulations show more detail for the changes in pressure along the isolator than the 2-D simulations. The 3-D CFD case in Figure 126 is closer to both the AFIT experiment and the 2-D CFD cases than in Figures 124 or 125. The decrease in difference between 3-D CFD and the AFIT experiment in Figures 121-123 is also present in Figures 124-126, indicating that lower back to inflow pressure ratios, not the values, are the variables that result in smaller differences in leading edges between 3-D CFD and the AFIT experiment. The reasons for the leading edge differences are explained later in this section.

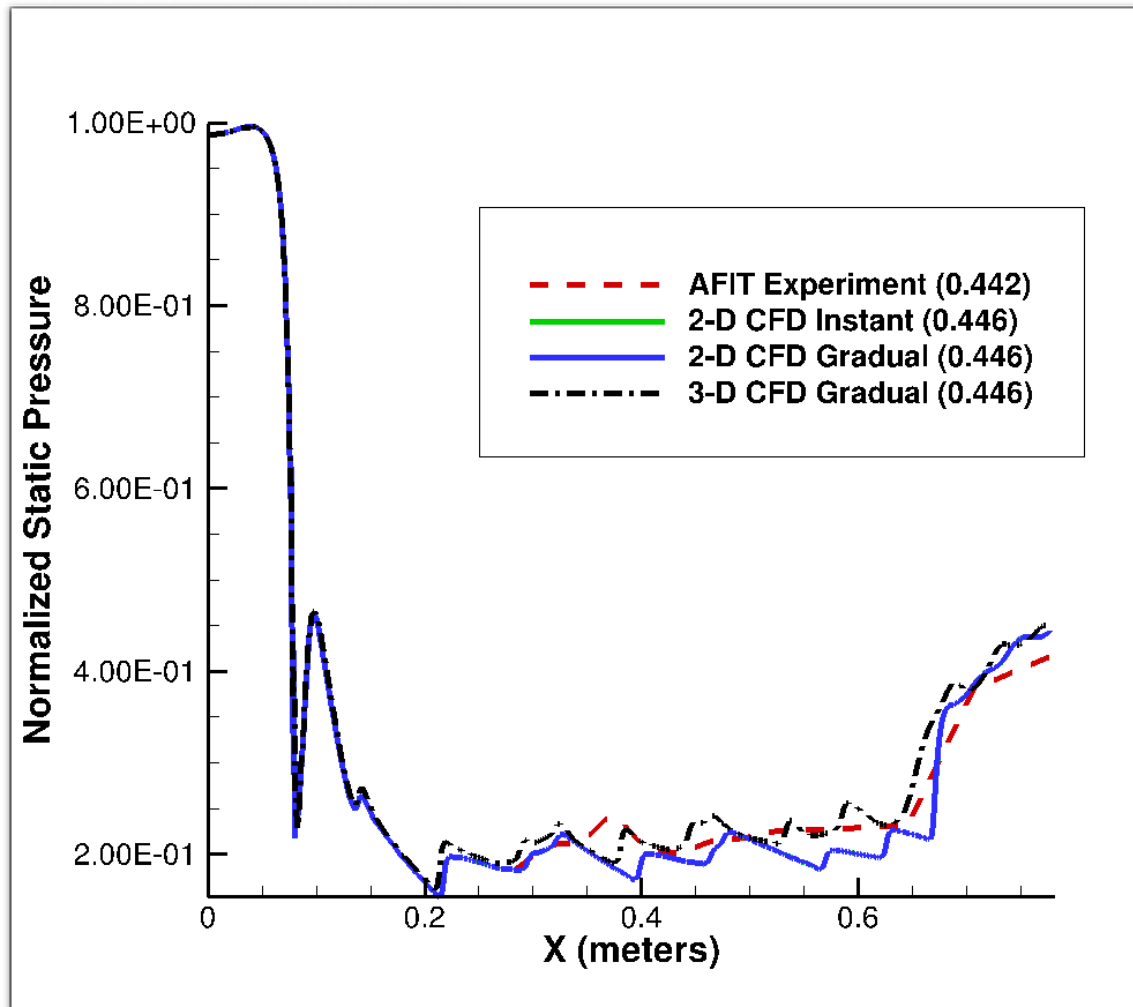


Figure 126. Comparison of CFD (0.446) with AFIT Experiment (0.442)

Table 6 shows a summary of the results of both CFD and the AFIT experiment. All data show the expected result of leading edges farther upstream for higher back to inflow pressure ratios. Both 2-D and 3-D CFD results show that, for a given back to inflow pressure ratio and dimensionality but different inflow conditions, the final shock location varies by no more than 1.0 cm. The final shock location confirms the ratio as a key parameter in predicting shock placement. The 2-D simulations predict experimental shock locations with errors no larger than 6 cm (one isolator duct height) or 20% of the experimental shock train length. For 3-D simulations, errors were as large as 12 cm (two isolator duct heights), or 40% of the experimental shock train length. The larger errors

corresponded to higher ratios; as mentioned previously, agreement was better for lower ratios. For the lowest ratio, the error was no higher than 13%. To put all these errors in context, one should consider the canonical data used in Billig's correlation, shown in Figure 108. The data in that figure shows that for a given back to inflow pressure ratio, the experimentally determined, non-dimensional shock length varied by as much as a factor of two.

Table 6. Comparison of final location between CFD results and experimental results

CFD Results (2-D)		CFD Results (3-D)		AFIT Experiment	
Po = 168.2		Po = 168.2		Po = 167.91	
Back Pressure (kPa) / Ratio	Final Location (cm) (Instant/Gradual)	Back Pressure (kPa) / Ratio	Final Location (cm)	Back Pressure (kPa) / Ratio	Final Location (cm)
89.6 / 0.533	54.3 / 54.3	89.6 / 0.533	39.7	88.5 / 0.527	52
85.0 / 0.506	59.2 / 59.8	85.0 / 0.506	49.7	82.9 / 0.494	58
75.0 / 0.446	67.8 / 67.8	75.0 / 0.446	62.9	75.9 / 0.452	65
Po = 140.6		Po = 140.6		Po=112.9 kPa	
Back Pressure (kPa) / Ratio	Final Location (cm) (Instant/Gradual)	Back Pressure (kPa) / Ratio	Final Location (cm)	Back Pressure (kPa) / Ratio	Final Location (cm)
75.0 / 0.533	54.6 / 54.4	75 / 0.533	38.2	58.7 / 0.520	49
71.1 / 0.506	59.3 / 59.0	71.1 / 0.506	49.9	56.5 / 0.492	58
62.78 / 0.446	67.8 / 67.2	62.78 / 0.446	62.8	49.9 / 0.442	64

Figure 127 presents a comparison of the final location of the PCST leading edge to the back pressure to inflow pressure ratio for the 2-D CFD, 3-D CFD and AFIT experiment results. Horizontal bars on the figure indicate experimental uncertainty, assumed to be half of the streamwise distance between the pressure transducers. The results in Figure 127 with the 168.2 kPa inflow pressure have a Reynolds number of 2.3×10^7 and are identified in Figure 126 as Re_1 . The results in Figure 127 with the 140.6 kPa inflow pressure have a Reynolds number of 1.9×10^7 and are identified in Figure 127 as Re_2 . The AFIT experiment results in Figure 127 with the 112.9 kPa inflow pressure have

a Reynolds number of 1.6×10^7 and are identified in Figure 127 as Re_3 . The CFD results in Figure 127 show very little sensitivity to Reynolds number. Experimental sensitivity is larger, but within the bounds of uncertainty.

The 2-D CFD, 3-D CFD, and AFIT experimental data show reasonable agreement for the lowest pressure ratios, though even around the 65 cm PCST final location, the low pressure ratio data shows some scatter. As Figure 108 show, scatter is inherent even in the canonical data upon which the Billig correlation is based, probably because the leading edges of PCSTs tend to be unsteady (Lindstrom, et al., 2009). Small changes in pressure ratio can result in relatively large changes in isolator performance, as the lowest-pressure experimental data in Figure 127 shows. Unsteadiness, typical of PCSTs, can also add uncertainty and scatter to the data. Additionally, two-equation turbulence models have a known weakness in the area of shock placement, and errors of one to two duct heights (6 to 12 cm in this case) are not uncommon (Lin, et al., 2006). Note that for these lowest pressure ratios, all data points lie within the uncertainty of the experimental data.

In general, the experimental data are bounded by 3-D CFD data on the left (longer shock trains) and by 2-D CFD on the right (shorter shock trains), which is consistent with the earlier observation that a 3-D isolator has a much larger surface area, along which subsonic boundary layers propagate information upstream. The placement of the 3-D CFD data to the left of the experiment suggests that the CFD may be over-predicting corner separation and other propagation mechanisms.

The 3-D simulations show a linear relationship between pressure ratio and shock position (or length). For the 2-D simulations, the relationship is non-linear, with relatively little shock movement for lower pressure ratios and larger movement once the

ratio becomes higher. The difference between the 2-D and 3-D simulations may relate to the more limited mechanisms by which a 2-D isolator can propagate information upstream. While a 3-D isolator will always have subsonic flow along the sidewalls and especially in the corners, a 2-D isolator has only attached, primarily supersonic flow, analogous to the centerline of the 3-D isolator, until the pressure ratio is high enough to induce separation. The discontinuity in the 2-D data may correspond to the formation of that flow separation, which enables much more rapid movement of the shock. The experimental data on the subject in Figure 127 are mixed, with one Reynolds number showing a linear relationship, as does the 3-D CFD, and the other showing an inflection point like the 2-D CFD. Given the uncertainty of the experimental shock locations, the significance of the experimental data trends in Figure 127 are difficult to determine.

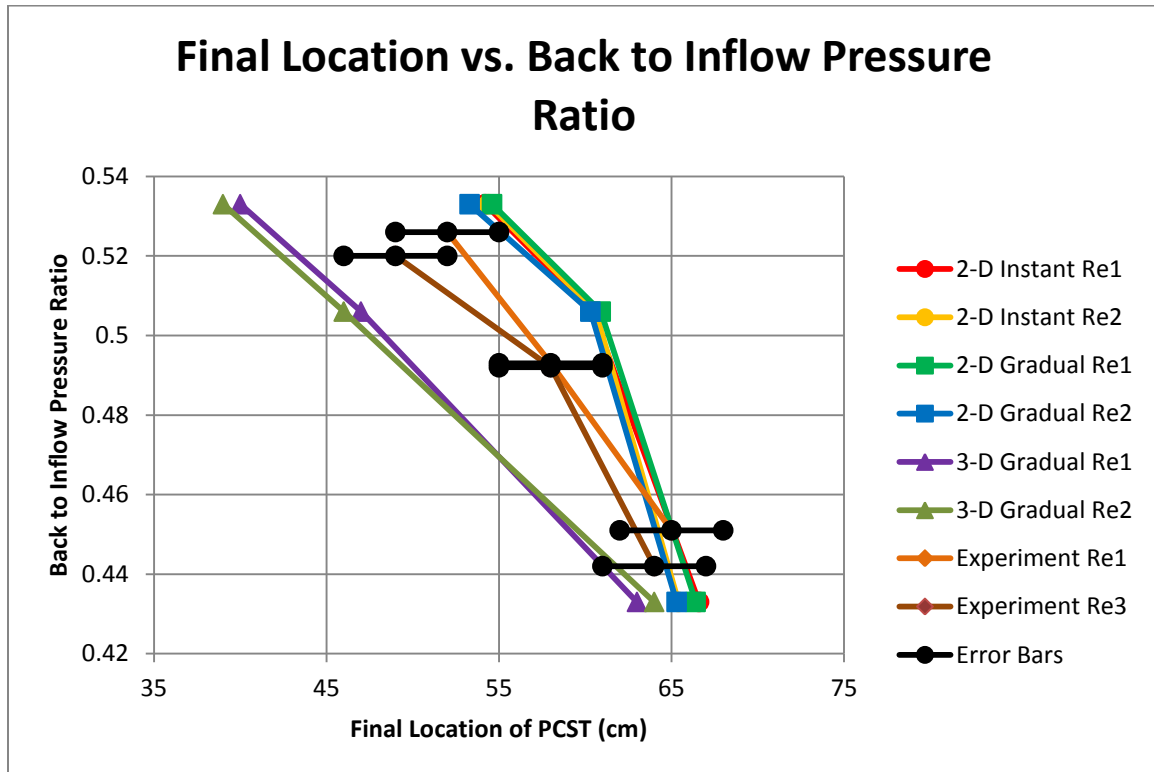


Figure 127. Comparison of final locations based on back to inflow pressure ratio

The difference in final locations between the 3-D CFD and AFIT experiment in Figures 121-126 (and confirmed in Figure 127) is larger than the difference between the 2-D CFD and the AFIT experiment. While the back pressure ratios in Figures 121-126 are not exactly the same, the differences between them are not large enough to be the only reason for the differences in final locations between the 3-D CFD and the AFIT experiment. Four causes have been identified that contributed to some degree to the difference between the 3-D CFD and the experiment, but may not have impacted 2-D CFD which is why 2-D CFD results are closer to the AFIT experiment.

The first two causes are based on the differences between the 2-D and 3-D simulations. First, there are separation bubbles at the corners in the 3-D simulation, as in experiments and applications. These separation bubbles will force the shock train to reverse and obtain final locations further upstream than with no corners, as in a 2-D simulation. The second cause of the difference between 2-D and 3-D simulations was the different turbulence models used. Recall that the 2-D simulations used the Menter-SST model and the 3-D simulations used the $k-\omega$ model. If the 2-D had used the $k-\omega$ model, the differences between 2-D and 3-D would be much larger (see Figure 12). The difference in turbulence models between 2-D and 3-D simulations could cause different results between 2-D and 3-D simulations.

The other two causes were based on the differences between 3-D simulations and the AFIT experiment. One cause is the application method of the back pressure. The differences between the stepped (Figure 66) and the ramped (Figure 97) back pressure cases in 3-D indicate that the method of back pressure application changes the results between the time the back pressure is initially applied and the shock train forms until the

time the shock train reaches its final location. Further, the back pressure was applied in CFD uniformly throughout the exit plane of the isolator, while the AFIT experiment may have not applied the back pressure uniformly at the isolator exit. Since the experimental transducers were placed only along the bottom of the isolator, there is no way to determine exactly how the back pressure was applied in the experiment. Application of the back pressure in a more realistic manner, either temporally, spatially, or both, might improve the results of future simulations. The other cause of the differences between 3-D simulations and the AFIT experiment is the sensitivity of the simulations to the incoming boundary layer profile. Recall that since the inflow boundary layer thickness from the AFIT experiments was unavailable, a CFD simulation was used to develop a boundary layer profile in the isolator based on the reference conditions. This boundary layer should be close to the real boundary layer in the experiment, but may not exactly represent the real boundary layer, so the boundary layer profile CFD created could affect the simulations results.

Distortion Analysis

To ensure that there are no other distortion effects in the flow due to the nozzle design, the boundary layer was analyzed at the nozzle exit using both the pitot and total pressures and Mach number with no back pressure obstacle in the flow. In VULCAN, the post-processor uses standard pitot equations to calculate the pitot pressure. Figure 128 displays the pitot pressure, total pressure and Mach number at the nozzle exit along the y-axis (from top to bottom of the isolator) for an inflow of 168.2 kPa.

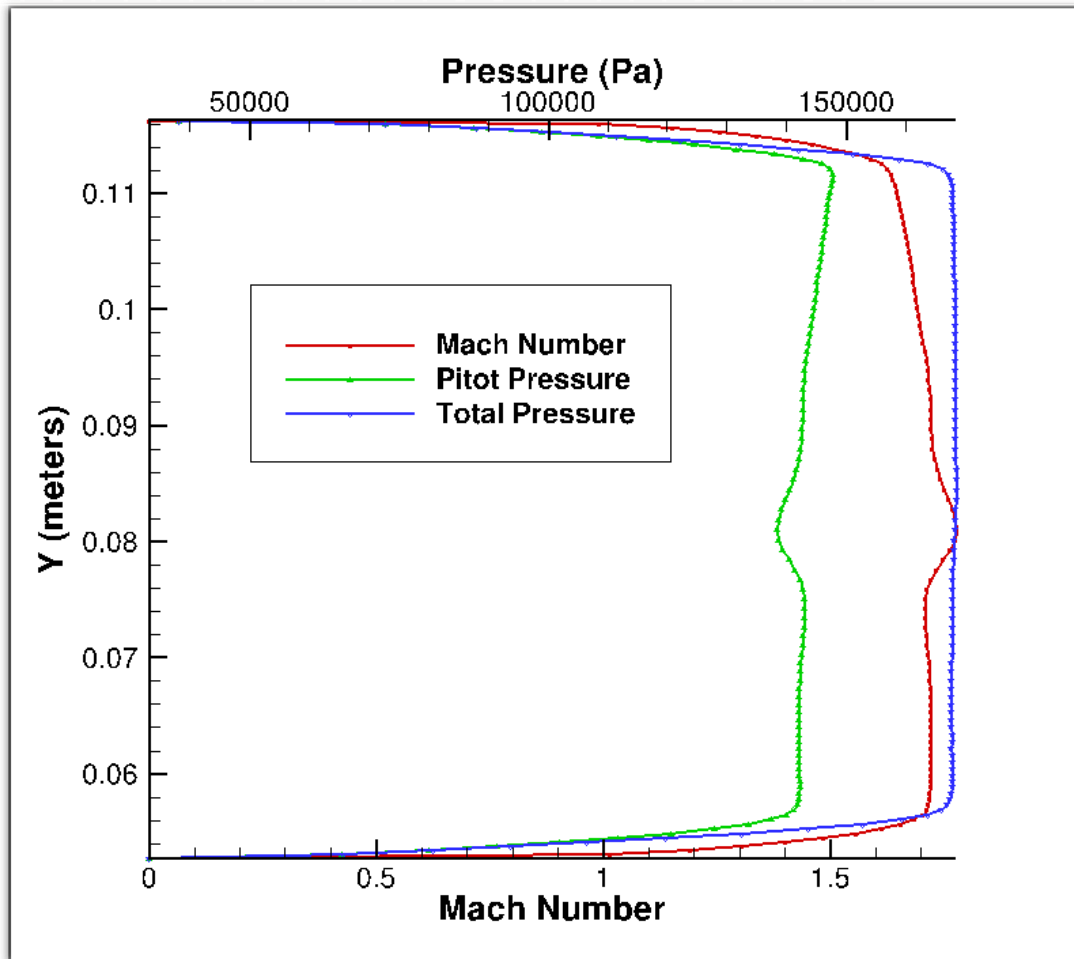


Figure 128. Pitot pressure, total pressure and Mach number for 168.2 kPa inflow with no back pressure

Both the top and bottom of both the pitot and total pressures in Figure 128 are identical and symmetric in terms of the pattern and profile, indicating no distortion effects. The only indication of asymmetry is the slight bump in the pitot pressure and Mach number in the middle, which is a result of the geometry of the nozzle.

Figure 129, a close up of the bottom section of Figure 128, has both the pitot pressure and total pressure diverging as the Mach number approaches one. In the subsonic region before a unity Mach, the flow is stagnated with minimal loss of pressure. Since pitot pressure is measured in a stagnant environment in an open tube, there is no divergence

between pitot and total pressure until the flow goes supersonic. Figures 130 and 131 show the same results as Figures 128 and 129 for an inflow pressure of 140.6 kPa.

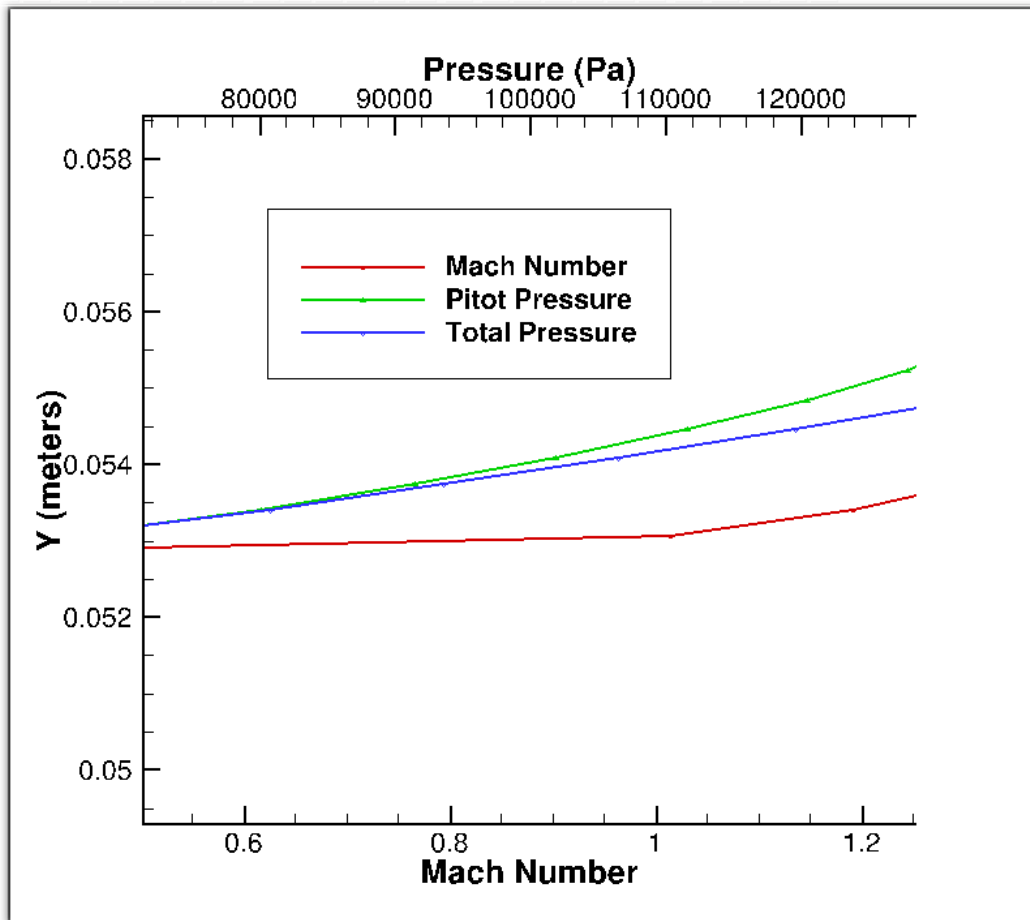


Figure 129. Close up of Figure 128

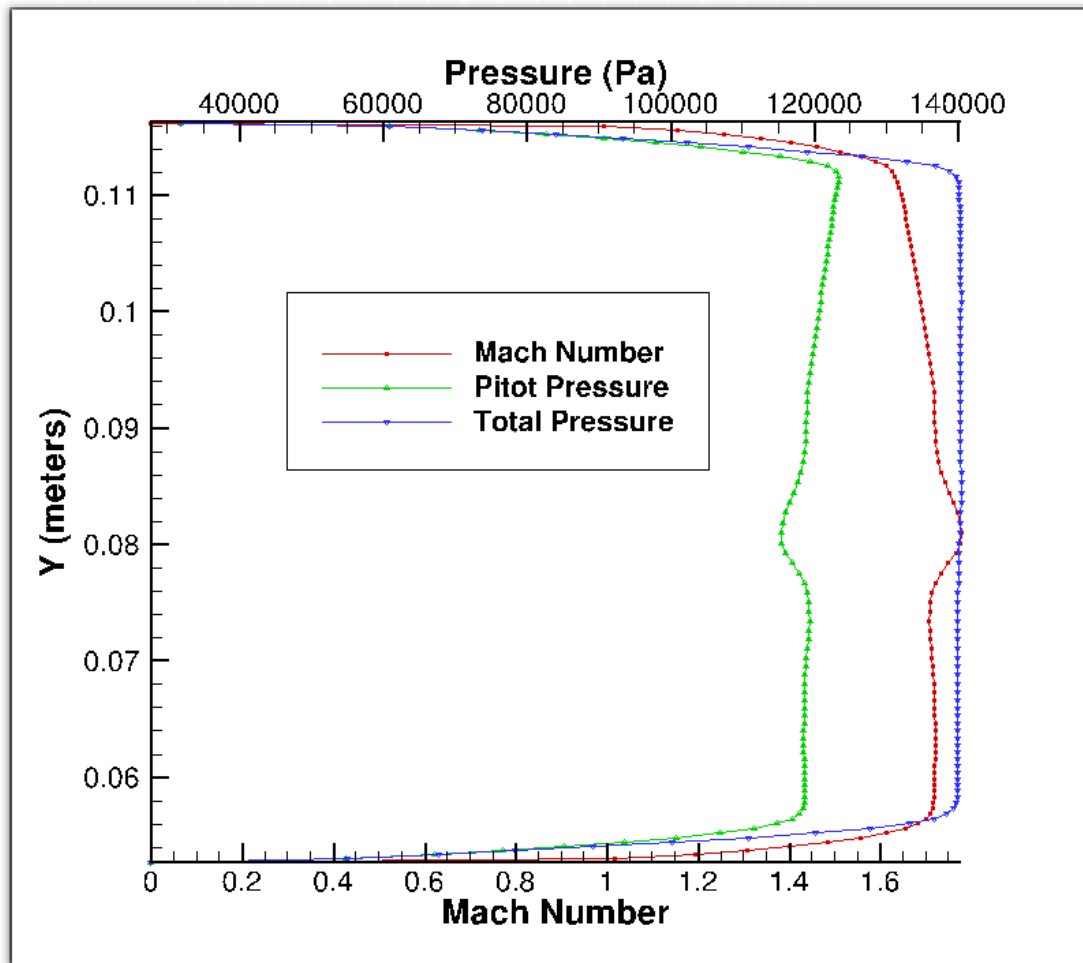


Figure 130. Pitot pressure, total pressure and Mach number for 140.6 kPa inflow with no back pressure

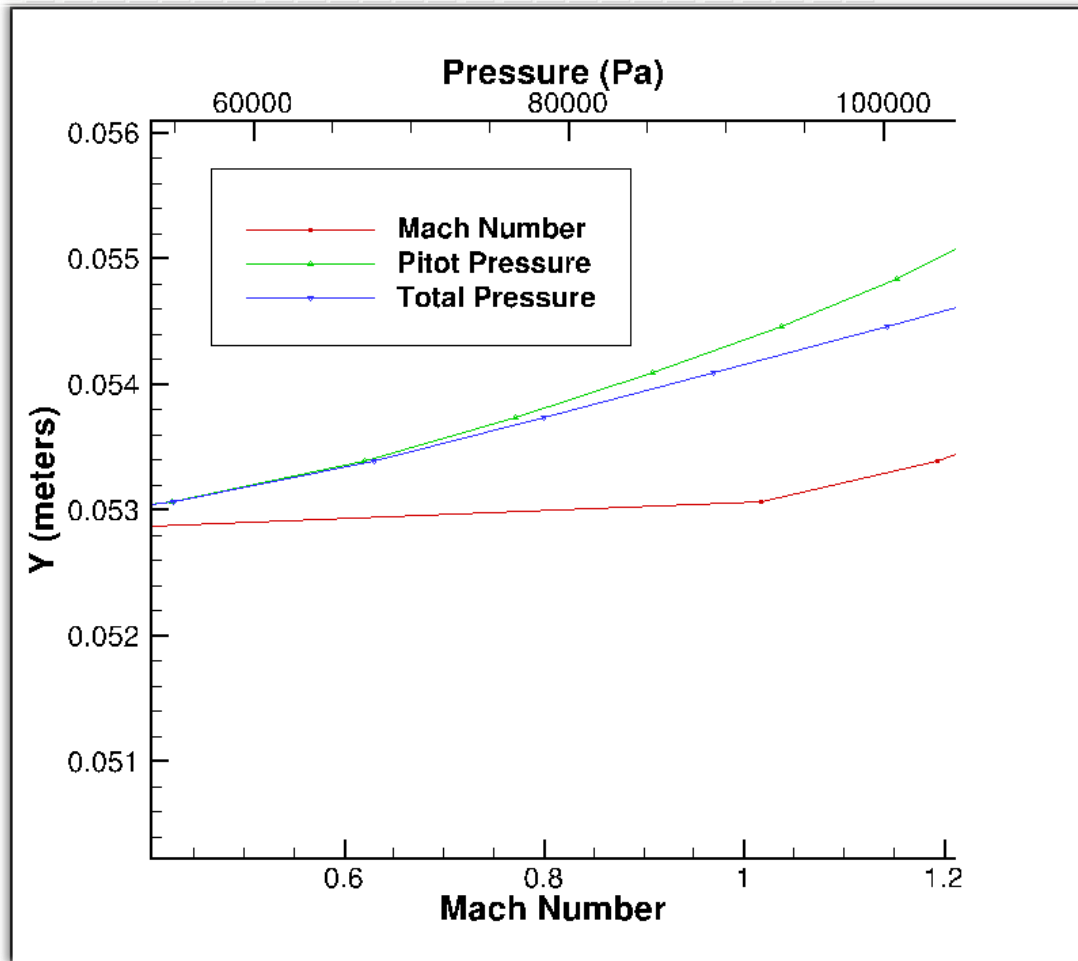


Figure 131. Close up of Figure 130

Summary

Comparison of the six 2-D cases with the Billig correlation indicated that the 2-D cases were systematically higher than the correlation, but both 2-D and 3-D cases were within the same scatter range as was seen in the original Billig correlation data. Analysis of the shock speed indicated an initially upstream movement between 250-350 m/s followed by a decrease to zero in speed before reversing direction and moving downstream at a speed between 0-50 m/s to its final location. An analysis of other locations off the centerline of the isolator walls indicated the same trend of movement as the centerline, but with lower magnitude as the pressure was measured closer to the

corners of the isolator walls than in the middle of the walls. The friction stress results from VULCAN showed both the final location of the leading edge of the PCST in the x and z-directions, and indicated a tendency towards separation without actual separation occurring in the CFD cases. A comparison of both experimental runs and both the 2-D and 3-D CFD cases was presented. One set of three experimental runs was similar (in terms of the inflow and back pressure values used) to three 2-D and three 3-D CFD cases, while another set matched only the back to inlet pressure ratios to another three 2-D and three 3-D CFD cases. The comparison between 2-D CFD and 3-D CFD showed similar movement both upstream and down, and in terms of the final location being further upstream at higher ratios. The CFD cases and the experimental runs in Figures 121-126 were reasonably close matches. When CFD cases and experimental runs were compared, either through the same pressure values or ratios, the 2-D CFD results were within one duct height of the experimental runs, and the 3-D CFD results were within two duct heights. Four causes were identified for the difference between the 3-D CFD simulations and the AFIT experiment. Two were based on the differences between 2-D and 3-D CFD simulations, while the other two were based on the differences between 3-D CFD and the AFIT experiment. Finally, analysis of the boundary layer in the isolator while there is no back pressure indicated no distortion effects as a result of nozzle design.

VII. Conclusions and Recommendations

Conclusions

Recent short duration flights of NASA's X-43 and the multi-minute flights of the USAF's X-51 are proof that scramjet engine design and development are improving. There remain, however, significant problems in the area of engine unstart in which the formation of shock waves in the isolator travel forward and exit the inlet, resulting in vehicle or mission failure. Prior to the X-43/51 flights, there was slow growth in research in active control of scramjet engines, and therefore, there have been very few time-accurate CFD simulations of scramjet engine transients. The need for accurate control models coupled with an increase in CPU capabilities has created an active research area in transient dynamics of a scramjet engine via CFD simulations.

This report addressed the unstart problem from a CFD perspective, focusing on the transient dynamic shock movement caused by perturbations in downstream back pressure. First-ever transient 2-D and 3-D CFD simulations of the pre-combustion shock train (PCST) were run using geometry from the nozzle and isolator of an AFIT experiment for comparison purposes. What was sought was identification of the controlling parameter(s) for shock train development and a discovery of the time transients involved in shock formation, movement and stabilization. Such information would be of practical use in the development of an electro-mechanical control system.

A variety of applied back pressures in both 2-D and 3-D transient simulations showed that the back-to-inflow total pressure ratio is the governing parameter, independent of the magnitude of either the back or inflow pressure. For any variation in back-pressure waveform, whether sudden or gradual, a critical back-to-inflow pressure

ratio above 0.40 for 2-D, or 0.31 for 3-D, caused a PCST to form at the isolator exit (combustor entrance), while for a ratio greater than 0.53, the flow would unstart. The critical ratio difference between 2-D and 3-D is due to the tendency of the boundary layer in 3-D to separate in the corners of the isolator walls (boundary layer separation is the mechanism which leads to the formation of a PCST initially at the isolator exit). Below either 0.4 or 0.31, apparently the axial gradient in static pressure in the boundary layer is too low to initiate a localized boundary layer displacement of sufficient thickness to cause a blockage-induced shock. Slightly above the critical ratio (0.4 or 0.31), a PCST forms, travels upstream, reverses direction and moves downstream to a final stabilized location in the isolator. For a back-to-inflow pressure ratio near unstart, the overshoot past the final, stable location was about two duct heights while for the lower pressure ratios, the overshoot was about five duct heights. All the shock plane overshoots (2-D and 3-D) were in excess of experimental observations, which were less than one duct height. As explained earlier in the Analysis section, the CFD may be over-predicting corner separation and propagating excessive separation upstream, leading to the larger shock plane overshoot as well as to disagreement in final, stabilized location.

For increasing back-to-inflow pressure ratio between critical and 0.53, the final stabilized location of the shock train moves farther upstream from the perturbation (combustor) region. In comparison with AFIT (3-D) experiments, the 2-D CFD transient stabilized PCST locations agreed within one isolator duct height of the experiment. The 3-D simulations agreed within two isolator duct heights. In all cases the lower back pressure ratios better matched the final stable shock location seen in the AFIT

experiment. Given the reported difficulty in locating the shock front plane in the AFIT experiment, the CFD results are in good agreement.

CFD backpressure was applied (as shown in Figure 35) incrementally in time for the gradual and ramped back pressures. Unlike an instantaneous pressure ratio application, gradual and ramped applications allow CFD solutions in both 2-D and 3-D to track the shock train. The best experimental match of shock position occurred at low pressure ratios nearer to the critical ratio. In scramjets, lower pressure ratios occur at lower fuel flow rates experienced at a flight Mach number less than five, the ram mode of the scramjet engine. (For flight Mach numbers greater than five, the early scram and full scram modes, a PCST does not form since the flow is resistant to separation due to the higher momentum of the incoming flow). During a lower Mach number acceleration or climb, the fuel flow rate is higher, resulting in more energetic combustion, larger combustion pressure, and a higher back to inflow pressure ratio. For higher pressure ratios (nearer to unstart), the CFD solutions matched the AFIT experiment less well. A more realistic approach for the higher CFD backpressure application could yield a better match. One approach for improved fidelity with the AFIT experiment would be smaller increments in pressure, incrementing the pressure at every iteration (time step) instead of discrete real-time increments. Such an approach, however, would require hundreds of hours of human interface as the program is currently constructed. Another approach would be to selectively apply the back pressure boundary value to certain cells in the outflow boundary condition in the CFD grid, simulating the ramp deployed in the AFIT isolator, which created a back pressure that increased monotonically in magnitude until full deployment. A spatially non-uniform back pressure would mimic the AFIT

experimental backpressure development. A third approach would be to model the AFIT ramp gridwise. Instead of incrementally increasing back pressure to simulate the ramp effect, a series of sequential grids would model the actual ramp-tunnel cross-section. This last approach, while tedious, could yield a more realistic modeling of back pressure.

Turbulence modeling is one of the more significant parameters in the determination of shock location and there is no way to determine a priori which turbulence model is best for a given simulation. For both the 2-D and 3-D simulations, different turbulence models resulted in different shock placements. Of the three turbulence models available in VULCAN, the Menter-SST model placed the shock train furthest upstream (the most conservative result) for both 2-D and 3-D simulations and is the one for which data is given in this report. The shock train location occurred furthest downstream (least conservative) with the Menter model (in 2-D) or the $k-\omega$ model (in 3-D), mainly because 2-equation turbulence models produce separation based on turbulent kinetic energy and dissipation, while the more conservative Menter-SST uses turbulent kinetic energy, dissipation, and shear stress transport, all of which result in larger regions of separated flow and location of the shock train further upstream. For example, in 2-D, the Menter-SST was about 0.79 or 1.26 duct heights further upstream than the Menter or $k-\omega$ model, respectively. The 2-D Menter-SST results were also closest to the experimental results. In 3-D, the Menter-SST was 2.05 or 3.15 duct heights further upstream than the Menter or $k-\omega$ model, respectively. In the 3-D case, however, the $k-\omega$ model agreed best with the experiment, which, as stated earlier, is mainly due to the 3-D CFD over-predicting corner separation and propagating excessive separation upstream

due to a much larger surface area. Based on the foregoing, the author suggests that for predicting final location of the shock train, the Menter-SST model is the best choice.

Grid density and choices of integration schemes (temporal and spatial) are parameters that affect the accuracy of the solutions and thus the shock location also. These parameters were varied during the simulations to ensure accuracy of the solutions shown in this study. Three different grids were considered, each denser than the previous by a factor of 8 (twice as many cells in each direction). The fine grid was found to offer no advantage over the medium grid in terms of final shock location. Variations in the integration schemes included the use of a time-accurate, five-stage Runge-Kutta integration scheme in the simulation in place of a three-stage Runge-Kutta scheme. There was no change in the final shock location with either scheme.

Other features of the isolator flow were investigated with an eye toward a practical control methodology. To this end, analysis of the 3-D simulations included an off-centerline analysis and a friction stress analysis to determine if precursors to shock formation were evident. It was seen that shock-induced pressure rise tended to extend farther upstream near the corners of the isolator than near the centerline due to boundary layer separation bubbles in the corners. Thus, in practice, off-centerline pressure readings could provide advanced warning of shock movement and potential unstart. Decreased friction stress accompanied increased susceptibility to separation near the leading edge of the shock train (though the friction stress remained above zero, indicating no separation on the centerline). Therefore, both friction stress and wall pressure values can provide an indication of shock location, though pressure sensing would continue to be the preferred control option due to the simplicity of the sensing method.

Both the 2-D and 3-D results showed that the time needed to reach the stabilized stopping criteria was on the order of tens of milliseconds following a downstream pressure perturbation. Such a time scale would require sensors and actuators to operate at a kilohertz level for control purposes, well within modern day sensing instrumentation capabilities, but posing a difficult and not fully solved problem for mechanical actuators. Nevertheless, the techniques developed in this study have proven useful in working toward understanding the required capabilities of an active control scheme for scramjet engines. With transient CFD, a better understanding of the time scales involved in unstart and possible sensor locations have been identified, both essential to the creation of an effective control system.

Recommendations

It is recommended that the following steps be taken to continue this research. First, a Mach 3 nozzle exists for the AFIT experiment. A second set of both 2-D and 3-D CFD runs using this nozzle for Mach 3 runs with varying backpressure cases would be useful for expanding this knowledge base, for comparison with the Mach 1.8 cases, and for further analysis of the scram mode in the isolator. Experimental runs would need to be accomplished first to determine what range of pressure values and what range of the back to inlet pressure ratios would work. The information from the experimental runs would then be used to run CFD simulations with the same values and the same ratios for comparison.

Another recommendation is to monitor, record, and track the transient data of the shock train in CFD inside the isolator in addition to lines S1, S2, S3, and S4 for comparison. The off-center analysis showed that there were differences between the lines

in the middle of the isolator walls compared to the lines closer to the corners of the isolator walls. Further analysis can be accomplished to analyze different areas inside the isolator to examine the non-uniformity more closely or to determine if there are any other differences occurring between the walls and the interior of the isolator. This information may be useful in the future for operating a scramjet engine.

A third recommendation is to apply the back pressure in a more realistic manner. The runs accomplished and presented in this dissertation were done with the back pressure applied as a subsonic outflow boundary condition uniformly at the isolator exit. In the AFIT experiment, the ramp started increasing the pressure from the bottom of the isolator, moving upward. Runs should be made with the back pressure applied more like the AFIT experiment. Another simulation improvement worth trying is with the ramp added in the grid. To simulate the ramp deployment, multiple grids can be created with the ramp added at different stages of deployment. During the run, the grids would be changed out to simulate the ramp deploying in the isolator.

Finally, four causes contributing to the difference between the 3-D CFD and the AFIT experiment in the Analysis section were discussed. Further analysis can be done on these causes. Recall that two causes were based on the differences between 2-D and 3-D CFD simulations, while the other two were based on the differences between 3-D CFD and the AFIT experiment. A study could be accomplished to determine the amount each of the two causes between 2-D and 3-D simulations contribute to the difference between 2-D and 3-D while another study could determine the amount each of the two causes between 3-D and the AFIT experiment contribute to the difference the 3-D and the AFIT experiment. Once those two studies are completed, a follow-on study could determine

how the two causes between 2-D and 3-D simulations contribute to the difference between the 3-D and the AFIT experiment. Separate studies could also be done on all four causes to try to eliminate them. If it not possible to eliminate them, then work can be done to minimize their impact on the differences identified in the simulations.

Bibliography

AFRL DSRC website

<http://www.afrl.hpc.mil>

Allen, Jeffrey B., Thomas Hauser, and C-J John Tam. "Numerical Simulations of a Scramjet Isolator Using RANS and LES Approaches," *45th AIAA Aerospace Sciences Meeting and Exhibit*. AIAA 2007-115, Reno NV, 9-11 January, 2007.

Anderson, John D., Jr. *Hypersonic and High-Temperature Gas Dynamics*. Reston, VA: AIAA, Inc., 2006.

Anonymous. "To Adapt - Or Not to Adapt – That is The Question!" *FLUENT NEWS*, Vol. 10, No. 1 (2001), pp. 18-19.

Bagaveyev, Nadir T., William A. Engblom, Vishal and A. Bhagwandin. "Parametric Investigation of Racetrack-to-Circular Cross-Section Transition of a Dual-mode Ramjet Isolator," *48th AIAA Aerospace Sciences Meeting Including The New Horizons Forum and Aerospace Exposition*. AIAA 2010-942, Orlando FL, 4-7 January, 2010.

Balu, G., S. Panneerselvam, and E. Rathakrishnan. "Computational Studies on the Performance of an Isolator for a Dual Mode Scramjet Engine," *International Journal of Turbo and Jet Engines*, Vol. 22, 2005: 255-263.

Baurle, R.A., and D.R. Eklund. "Analysis of Dual-Mode Hydrocarbon Scramjet Operation at Mach 4-6.5," *37th AIAA/ASME/SAE/ASEE Joint Propulsion Conference and Exhibit*. AIAA 2001-3299, Salt Lake City, UT, 8-11 July, 2001.

Benson, Rusty A., and D. Scott McRae. "Numerical Simulations of the Unstart Phenomenon in a Supersonic Inlet/Diffuser," *29th AIAA/ASME/SAE/ASEE Joint Propulsion Conference and Exhibit*. AIAA 93-2239, Monterey, CA, 28-30 June, 1993.

Billig, F.S. "Research on Supersonic Combustion," *Journal of Propulsion and Power*, Vol. 9, No. 4, July-Aug 1993: 499-514.

Blazek, J. *Computational Fluid Dynamics: Principles and Applications*. San Diego, CA: Elsevier Inc., 2005.

Chang, Juntao, Yi Fan, Wen Bao, Daren Yu and Yi Shen. "Unstart Margin Control of Hypersonic Inlets," *Acta Astronautica*, Vol. 66, Issue 1-2 (2010): 78-87.

Cockrell, Charles E., Jr., Aaron H. Auslender, R. Wayne Guy, Charles R. McClinton and Sharon S. Welch. "Technology Roadmap for Dual-Mode Scramjet Propulsion to Support Space-Access Vision Vehicle Development," *AIAA/AAAF 11th*

- International Space Planes and Hypersonic Systems and Technologies Conference*. AIAA 2002-5188, Orleans, France, 29 September - 4 October, 2002.
- Corbin, Christopher R., OhioLINK Electronic Theses and Dissertations Center. *Design and Analysis of a Mach 3 Dual Mode Scramjet Combustor*. MS thesis. School of Graduate Studies, Wright State University, Dayton, OH, 2008.
- DoD HPCMP Web Site
<http://www.hpcmp.hpc.mil>
- Donbar, Jeffrey M, Graham J. Linn and Maruthi R. Akella. "High Frequency Pressure Measurements in Scramjet Isolators." 88ABW-2009-4772.
- Donbar, Jeffrey M. "Investigation of Scramjet Isolator SWBLIs." White Paper to Dr. John Schmisser, AFRL/RZAS, 2010.
- Edwards, Jack R. "A Low-Diffusion Flux-Splitting Scheme for Navier-Stokes Calculations," *Computers and Fluids*, Vol. 26, No. 6, 1997: 635-659.
- Hank, Joseph M. "Air Force Research Laboratory Hypersonic Propulsion Research Programs," *43rd AIAA/ASME/SAE/ASEE Joint Propulsion Conference & Exhibit*. AIAA 2007-5371, Cincinnati OH, 8-12 July, 2007.
- Heiser, William H., and David T. Pratt. *Hypersonic Airbreathing Propulsion*. Washington, DC: AIAA Education Series, AIAA, Inc., 1994.
- Hirsch, Charles. *Numerical Computation of Internal and External Flows, Fundamentals of Computational Fluid Dynamics*. Boston, MA: Elsevier, Inc., 2007.
- Hoffman, Klaus A., and Steve T. Chiang. *Computational Fluid Dynamics, Volume I*. Wichita, KS: Engineering Education System™, 2004.
- Hoffman, Klaus A., and Steve T. Chiang. *Computational Fluid Dynamics, Volume III*. Wichita, KS: Engineering Education System™, 2000.
- Hutzel, John R. PhD Candidate, Air Force Institute of Technology, Wright-Patterson AFB OH. Personal Correspondence. 6 June 2011.
- Jones, W.P., and B.E. Launder. "The Calculation of Low-Reynolds-Number-Phenomena with a Two-Equation Model of Turbulence," *International Journal of Heat Mass Transfer*, Vol. 16, 1973, pp. 1119-1130.
- Kim, Sang Dug, and Dong Joo Song. "Modified Shear-Stress Transport Turbulence Model for Supersonic Flows," *Journal of Aircraft*, Vol. 42, No. 5, Sept-Oct 2005: 1118-1125.

- Le, Daniel B. "Scramjet Isolator Flow Studies," *2005 Virginia Space Grant Consortium (VSGC) Student Research Conference*. Newport News, VA, 1 April 2005.
- Le, D.B., C.P. Goyne, R.H.Krauss and J.C. McDaniel. "Shock Train Leading-Edge Detection in a Dual-Mode Scramjet," *44th AIAA Aerospace Sciences Meeting and Exhibit*. AIAA 2006-815, Reno NV, 9-12 January, 2006.
- Lin, K.-C., C.-J. Tam, K.R. Jackson, D.R. Ecklund and T.A. Jackson. "Characterization of Shock Train Structures inside Constant-Area Isolators of Model Scramjet Combustors," *44th AIAA Aerospace Sciences Meeting and Exhibit*. AIAA 2006-816, Reno NV, 9-12 January, 2006.
- Lin, Kuo-Cheng, Chung-Jen Tam, Kevin Jackson, Paul Kennedy and Robert Behdadnia. "Experimental Investigations on Simple Variable Geometry for Improving Scramjet Isolator Performance," *43rd AIAA/ASME/SAE/ASEE Joint Propulsion Conference & Exhibit*. AIAA 2007-5378, Cincinnati OH, 8-12 July, 2007.
- Lin, Pei, G.V.R. Rao and George M. O'Connor. "Numerical Analysis of Normal Shock Train in a Constant Area Isolator," *27th AIAA/SAE/ASME/ASEE Joint Propulsion Conference*, Sacramento, CA, 24-26 July 1991.
- Lindstrom, Chadwick D., Doug Davis, Skip Williams and Chung-Jen Tam. "Shock-Train Structure Resolved with Absorption Spectroscopy Part 2: Analysis and CFD Comparison," *AIAA Journal*, Vol. 47, No. 10, October 2009.
- Maicke, Brian A., and Joseph Majadalani. "Evaluation of CFD Codes for Hypersonic Modeling," *46th AIAA/ASME/SAE/ASEE Joint Propulsion Conference and Exhibit*. AIAA 2010-7184, Nashville, TN, 25-28 July, 2010.
- McDaniel, James C., Christopher P. Goyne, Elliott B. Bryner, Daniel B. Le, Chad T. Smith and Roland H. Krauss. "Dual-Mode Scramjet Operation at a Mach 5 Flight Enthalpy in a Clean Air Test Facility," *Rarefied Gas Dynamics: 24th International Symposium*, Bari, Italy, 10-16 July 2004, pp. 1277-1282.
- Menter, Florian R. "Zonal Two Equation $k-\omega$ Turbulence Models for Aerodynamic Flows," *24th Fluid Dynamics Conference*, AIAA 1993-2906, Orlando, FL, 6-9 July, 1993.
- NASA Web Site
http://www.nasa.gov/centers/langley/images/content/142861main_x43a_intscramjet_550.gif
- Neaves, Michael Dean, D. Scott McRaem and Jack R. Edwards. "High-Speed Inlet Unstart Calculations Using an Implicit Solution Adaptive Mesh Algorithm," *39th AIAA Aerospace Sciences Meeting and Exhibit*. AIAA 2001-0825, Reno, NV, 8-11 January, 2001.

- Pointwise, Inc., Gridgen User Manual, Version 15, Volume 1, 2003.
- Pratt, David T. and William H. Heiser. "Isolator-Combustor Interaction in a Dual-Mode Scramjet Engine," *31st AIAA Aerospace Sciences Meeting and Exhibit*. AIAA 1993-0358, Reno NV, 11-14 January, 1993.
- Rice, Tharen. "High Aspect Ratio Isolator Performance for Access-to-Space Vehicles," *12th AIAA International Space Planes and Hypersonic Systems and Technologies*. AIAA 2003-7041, Norfolk, VA, 15-19 December, 2003.
- Roe, Philip L. "Discrete Models for the Numerical Analysis of Time-Dependent Multidimensional Gas Dynamics," *Journal of Computational Physics*, Vol. 63, No. 2, April 1986: 458-476.
- Tam, Chung-Jen, Dean Eklund and Robert Behdadnia. "Influence of the Downstream Boundary Conditions on Scramjet-Isolator Simulations," *26th AIAA Applied Aerodynamics Conference*. AIAA-2008-6929, Honolulu, HI, 18-21 August, 2008.
- Tecplot, Inc., Tecplot 360™ User's Manual, 2011.
- Torrez, Sean M., Nathan A. Scholten, Daniel J. Micka, James F. Driscoll, Micahel A. Bolender, David B. Doman and Michael W. Oppenheimer. "A Scramjet Engine Model Including Effects of Precombustion Shock and Dissociation," *44th AIAA/ASME/SAE/ASEE Joint Propulsion Conference & Exhibit*. AIAA 2008-4619, Hartford CT, 21-23 July, 2008.
- Tu, Jiyuan, Guan Heng Yeoh and Chaoqun Liu. *Computational Fluid Dynamics: A Practical Approach*. Boston, MA: Elsevier, Inc., 2008.
- Van Leer, Bram. "Towards the Ultimate Conservative Difference Scheme V. A Second Order Sequel to Gudunov's Method," *Journal of Computational Physics*, Vol. 32, No. 1, July 1979: 101-136.
- VULCAN Home Page
<http://vulcan-cfd.larc.nasa.gov/>
- Waltrup, P.J., and F.S. Billig. "Prediction of Precombustion Wall Pressure Distributions in Scramjet Engines," *Journal of Spacecraft and Rockets*, Vol. 10, 1973: 620-622.
- Waltrup, P.J., and F.S. Billig. "Structure of Shock Waves in Cylindrical Ducts," *AIAA Journal*, Vol. 11, No. 10, 1973: 1404-1408.
- Weber, R.J., and J.S. MacKay. "An Analysis of Ramjet Engines Using Supersonic Combustion," NACA TN 4386, NACA Lewis Flight Propulsion Laboratory, 1958.

White, J.A., and J.H. Morrison. "A Pseudo-Temporal Multi-Grid Relaxation Scheme for Solving Parabolized Navier-Stokes Equations," *14th Computational Fluid Dynamics Conference*, AIAA 1999-3360, Norfolk, VA, 28 June – 1 July, 1999.

Wilcox, David C. "Turbulence Modeling: An Overview," *39th Aerospace Sciences Meeting & Exhibit*. AIAA 2001-0724, Reno NV, 8-11 January 2001.

Wilcox, David C. *Turbulence Modeling for CFD*. San Diego, CA: DCW Industries, Inc., 2000.

Wilcox, David C. "Wall Matching, A Rational Alternative to Wall Functions," *27th Aerospace Sciences Meeting*. AIAA 1989-0611, Reno NV, 9-12 January 1989.

REPORT DOCUMENTATION PAGE				Form Approved OMB No. 0704-0188	
<p>The public reporting burden for this collection of information is estimated to average 1 hour per response, including the time for reviewing instructions, searching existing data sources, gathering and maintaining the data needed, and completing and reviewing the collection of information. Send comments regarding this burden estimate or any other aspect of this collection of information, including suggestions for reducing this burden to Department of Defense, Washington Headquarters Services, Directorate for Information Operations and Reports (0704-0188), 1215 Jefferson Davis Highway, Suite 1204, Arlington, VA 22202-4302. Respondents should be aware that notwithstanding any other provision of law, no person shall be subject to any penalty for failing to comply with a collection of information if it does not display a currently valid OMB control number.</p> <p>PLEASE DO NOT RETURN YOUR FORM TO THE ABOVE ADDRESS.</p>					
1. REPORT DATE (DD-MM-YYYY) 07-09-2012		2. REPORT TYPE Dissertation		3. DATES COVERED (From — To) Aug 2008 - Sep 2012	
4. TITLE AND SUBTITLE CFD Transient Simulation of an Isolator Shock Train in a Scramjet Engine				5a. CONTRACT NUMBER N/A	
				5b. GRANT NUMBER N/A	
				5c. PROGRAM ELEMENT NUMBER N/A	
6. AUTHOR(S) Hoeger, Troy C., Lieutenant Colonel, USAF				5d. PROJECT NUMBER N/A	
				5e. TASK NUMBER N/A	
				5f. WORK UNIT NUMBER N/A	
7. PERFORMING ORGANIZATION NAME(S) AND ADDRESS(ES) Air Force Institute of Technology Graduate School of Engineering and Management (AFIT/ENY) 2950 Hobson Way WPAFB OH 45433-7765				8. PERFORMING ORGANIZATION REPORT NUMBER AFIT/DS/ENY/12-18	
9. SPONSORING / MONITORING AGENCY NAME(S) AND ADDRESS(ES) Air Force Research Laboratory Aerospace Propulsion Division 1950 Fifth Street Wright-Patterson AFB, OH 45433-7251 Dr. Jeffrey M. Donbar (937) 255-1996; Jeffrey.Donbar@wpafb.af.mil				10. SPONSOR/MONITOR'S ACRONYM(S) AFRL/RQH	
				11. SPONSOR/MONITOR'S REPORT NUMBER(S) N/A	
12. DISTRIBUTION / AVAILABILITY STATEMENT APPROVED FOR PUBLIC RELEASE; DISTRIBUTION UNLIMITED					
13. SUPPLEMENTARY NOTES This material is declared a work of the U.S. Government and is not subject to copyright protection in the United States					
14. ABSTRACT For hypersonic flight, the scramjet engine uses an isolator to contain the pre-combustion shock train formed by the pressure difference between the inlet and the combustion chamber. If this shock train were to reach the inlet, it would cause an engine unstart, disrupting the flow through the engine and leading to a loss of thrust and potential loss of the vehicle. Prior to this work, a Computational Fluid Dynamics (CFD) simulation of the isolator was needed for simulating and characterizing the isolator flow and for finding the relationship between back pressure and changes in the location of the leading edge of the shock train. In this work, the VULCAN code was employed with back pressure as an input to obtain the time history of the shock train leading location. Results were obtained for both transient and steady-state conditions. The simulation showed a relationship between back-to-inlet pressure ratios and final locations of the shock train. For the 2-D runs, locations were within one isolator duct height of experimental results while for 3-D runs, the results were within two isolator duct heights.					
15. SUBJECT TERMS Hypersonics, Scramjet, Isolator, Computational Fluid Dynamics					
16. SECURITY CLASSIFICATION OF:			17. LIMITATION OF ABSTRACT	18. NUMBER OF PAGES	19a. NAME OF RESPONSIBLE PERSON
a. REPORT	b. ABSTRACT	c. THIS PAGE			19b. TELEPHONE NUMBER (Include Area Code)
U	U	U	UU	220	Dr. Paul I. King, CIV, ADVISOR (937)255-3636, ext 4628 (Paul.King@afit.edu)

Standard Form 298 (Rev. 8-98)
Prescribed by ANSI Std. Z39.18